FERMILAB-THESIS-2001-46

Thesis

Search for first generation leptoquarks in the evjj and eejj Decay Channels in pp□collisions at √s = 1.8 TeV

STRUMIA MICHELINI, Federica

Abstract

La recherche des particules exotiques suggérée dans les scénarios prévus par les théories qui vont au delà du Modèle Standard est un domaine d'investigation très étudié lors de ces dernières années dans la physique des particules élémentaires. Le sujet de cette thèse est la recherche des leptoquarks scalaires et vectoriels de première génération produits en couple dans des collisions proton-antiproton à une énergie du centre de masse de √s = 1.8 TeV et se désintégrant dans les canaux evjj et eejj. L'analyse a été conduite sur les données récoltées par l'experience CDF (Collider Detector at Fermilab) pendant la période 1992-1995.

Reference

STRUMIA MICHELINI, Federica. *Search for first generation leptoquarks in the evjj and eejj Decay Channels in pp̄ collisions at √s = 1.8 TeV*. Thèse de doctorat : Univ. Genève, 2001, no. Sc. 3311

DOI : 10.13097/archive-ouverte/unige:95303

UNIVERSITÉ DE GENÈVE
Département de physique nucléaire et corpusculaire

FACULTÉ DES SCIENCES
Professeur Allan G. Clark

Search for First Generation Leptoquarks in the $e\nu jj$ and $eejj$ Decay Channels in $p\bar{p}$ Collisions at $\sqrt{s} = 1.8$ TeV

THÈSE

présentée à la Faculté des sciences
de l'Université de Genève
pour l'obtention du grade de Docteur ès sciences,
mention physique

par

Federica STRUMIA
de Forlì, Italie

Thèse No 3311

GENÈVE
Atelier de reproduction de la Section de physique
2001

La Faculté des sciences, sur le préavis de Monsieur A.G. CLARK, professeur ordinaire et directeur de thèse (Département de physique nucléaire et corpusculaire), Madame M.-N. KIENZLE, professeur ordinaire (Département de physique nucléaire et corpusculaire), Messieurs T. MUELLER, professeur (Universiät Karlshruhe, Institut für Experimentelle Kernphysik - Deutschland) et X. WU, docteur (Département de physique nucléaire et corpusculaire), autorise l'impression de la présente thèse, sans exprimer d'opinion sur les propositions qui y sont énoncées.

Genève, le 12 décembre 2001

Thèse - 3311 -

Le Doyen, Jacques WEBER

To see a World in a Grain of Sand
And a Heaven in a Wild Flower,
Hold Infinity in the palm of your hand
And Eternity in an hour.

William Blake, "Auguries of Innocence"

Contents

Chapter 1

Résumé

La recherche des particules exotiques suggérée dans les scénarios prévus par les théories qui vont au delà du Modèle Standard est un domaine d'investigation très étudié lors de ces dernières années dans la physique des particules éleméntaires. Le sujet de cette thèse est la recherche des leptoquarks scalaires et vectoriels de première génération produits en couple dans des collisions proton-antiproton à une énergie du centre de masse de $\sqrt{s} = 1.8$ TeV et se désintégrant dans les canaux $e\nu jj$ et $eejj$. L'analyse a été conduite sur les données récoltées par l'expérience CDF (Collider Detector at Fermilab) pendant la période 1992-1995.

La thèse comporte trois parties:

(i) une introduction théorique, traitée dans le Chapitre 2, résume les succès mais aussi les limites du Modèle Standard, la théorie qui a trouvé à ce jour le plus de confirmations dans le domaine de la physique des hautes énergies;

(ii) le Chapitre 3 détaille la structure de l'accélérateur de protons et antiprotons Tevatron et du détecteur CDF qui a collecté les données analysées dans cette thèse;

(iii) l'analyse est commentée dans les Chapitres 4, 5, 6, 7, 8 et dans les Annexes. Les échantillons de données réelles et celles simulées par Monte Carlo ainsi que la façon de sélectionner les électrons sont décrits dans le Chapitre 4. Dans le Chapitre 5 figure la recherche des leptoquarks scalaires dans les canaux $e\nu jj$ et $eejj$. Dans le Chapitre 6 on trouvera la recherche des leptoquarks vectoriels avant de combiner les résultats des deux canaux dans le Chapitre 7. Le Chapitre 8 contient les conclusions, à savoir une comparaison avec les résultats actuellement disponibles par d'autres expériences, et les projections des recherches des leptoquarks pour le futur.

1.1. Introduction théorique

Le Modèle Standard des interactions électro-faibles et fortes décrit les interactions entre les particules élementaires dans le cadre de la théorie quantique relativiste des champs. Elle est répresentée par le groupe de jauge SU(3) $\times$ SU(2) $\times$ U(1), qui exprime une symétrie spontanément brisée par l'introduction d'une particule scalaire massive, le boson de Higgs,

à travers un mécanisme qui permet de justifier la masse des bosons intermédiaires W et Z, découverts au CERN en 1983, ainsi que des fermions. Aujourd'hui le boson de Higgs reste la seule particule prévue par le Modèle Standard a ne pas avoir été détectée.

Le Modèle Standard a rencontré un véritable succès avec la vérification expérimentale de ses prédictions, notamment dans les expériences menées pendant les années '80-'90 au LEP, SLC et Tevatron, qui n'ont pas trouvé de signaux de nouveaux phénomènes. Le Modèle Standard n'est pas tout de même considéré comme une théorie satisfaisante, parce que elle laisse ouvertes des questions fondamentales, comme l'origine des masses des particules, la prédiction du nombre de familles fermioniques, la quantification de la charge électrique, le nombre des couleurs.

Les théories modernes cherchent à répondre à ces questions, tout en englobant le Modèle Standard qui reste valide jusqu'à une énergie de l'ordre de $\mathcal{O}(100$ GeV).

A des énergies de plus en plus élevées, l'idée de l'unification des interactions électromagnétiques, faibles et fortes est prise en compte par des modèles élégants comme les Grand Unified Theories (GUT's), où les trois forces possèdent le même couplage à une énergie de l'ordre de $M_{GUT} \sim 10^{17}$ GeV/c^2, et se trouvent ainsi unifiées à la force gravitationelle à une échelle d'énergie, dite échelle de Planck, $M_P \sim 10^{19}$ GeV/c^2.

Dans ce contexte, leptons et quarks deviennent indistincts. Cette symétrie suggère, dans plusieurs théories, l'existence des particules, appellées leptoquarks, pour justifier la transition quark-lepton.

Ces particules, qui ont la caractéristique de posséder, en même temps, un nombre barionique et un nombre leptonique, différent en fonction du modèle théorique considéré. En général, ils sont bosons triplets de couleur, et peuvent avoir spin=0 (leptoquarks scalaires) ou spin=1 (leptoquarks vectoriels). Une hypothèse qui est normallement acceptée, pour ne pas générer des courants neutres avec changement de couleur, est que les leptoquarks se lient seulement dans la même famille, ce qui justifie leur classification en première, deuxième et troisième génération. La recherche illustrée dans cette thèse porte sur les leptoquarks de première génération, qui peuvent se coupler seulement avec des électrons, des neutrinos électron et des quarks *up* ou *down*.

Dans l'hypothèse que les nombres barionique et leptonique soient conservés séparémment, on peut aussi supposer l'existence des leptoquarks avec une masse accessible aux collisionneurs actuels. Au Tevatron, le collisionneur protons-antiprotons à une énergie du centre de masse $\sqrt{s} = 1.8$ TeV, les leptoquarks peuvent être produits directement, seuls ou en couple, dans les réactions: $p\bar{p} \rightarrow Lq + X$, $p\bar{p} \rightarrow Lq\bar{L}q + X$.

Le processus de production d'un seul leptoquark a une section efficace très petite à l'énergie du Tevatron et devient difficilement détectable.

Toute l'attention dans les recherches actuelles aux collisionneurs hadroniques va à la production en couples, qui a l'avantage d'une section efficace presque indépendante du couplage entre quark, lepton et leptoquark λ et, dans le cas du Tevatron, fonction de la constante de couplage forte et donc calculable. Les leptoquarks sont produits en couple par annihilation quark-antiquark ou par fusion des gluons, comme il est montré dans la Figure (1.1). La section efficace de production des leptoquarks scalaires est totalement déterminée, tandis que dans les cas vectoriels elle dépend par des couplages anomales,

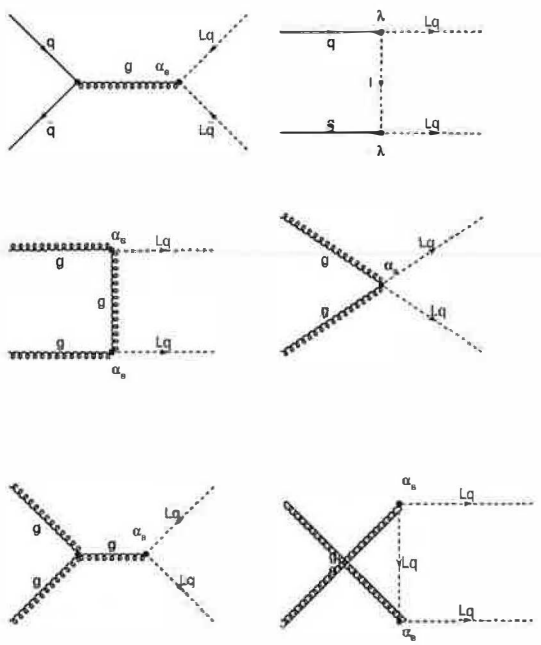

Figure 1.1: *Diagrammes de Feynman pour la production des leptoquarks en couple aux collisionneurs hadroniques.*

indiqués avec k_G et λ_G, qui dépendent du moment magnétique anomal et du moment de quadrupole électrique des leptoquarks dans le champ de couleur. La section efficace dans le cas vectoriel est plus élevée que celle dans le cas scalaire: par exemple dans la production d'un couple de leptoquarks de masse égale à 200 GeV/c^2 on a que $\sigma(p\bar{p} \to \mathrm{S1}\bar{\mathrm{S1}}) \sim 0.2$ pb et que $\sigma(p\bar{p} \to \mathrm{V1}\bar{\mathrm{V1}}) \sim 10$ pb.

Chaque leptoquark de première génération peut se désintégrer uniquement soit en eq avec taux de branchement $Br(Lq \to eq) = \beta$ ou en $\nu_e q$ avec taux de branchement $Br(Lq \to \nu q) = (1 - \beta)$. La production de couples des leptoquarks a lieu avec les taux suivants: β^2 pour le canal de désintégration $eeqq$, $2\beta(1-\beta)$ pour le canal $e\nu qq$ et $(1-\beta)^2$ pour le canal $\nu_e\nu_e qq$.

1.2. Le détecteur

L'expérience plurifonctionnelle CDF (*Collider Detector at Fermilab*) est une des deux expériences construites sur l'accélérateur circulaire Tevatron situé au Fermilab (Fermi National Accelerator Laboratory) à Batavia, aux Etats-Unis, pour étudier la physique des collisions proton-antiproton à une énergie du centre de masse $\sqrt{s} = 1.8$ TeV.

Les données analysées dans cette thèse ont été récoltées pendant les périodes 1992-93 (run 1a) et 1994-95 (run 1b): ils correspondent à une luminosité intégrée de $\int \mathcal{L}dt = (110 \pm 4)$ pb^{-1}.

CDF a une structure cylindrique, et ses sous-détecteurs sont disposées en gros par

couches concentriques, en donnant, autour du point d'interaction, une couverture sur tout l'angle solide. Le détecteur est décrit en détail dans le Chapitre 3 de cette thèse et dans les publications auxquelles il fait référence.

Dans le système de coordonnées employé à CDF, l'axe z est orienté dans la direction du faisceau des protons, l'axe x s'éloigne du centre du Tevatron et l'axe y est perpendiculaire au plan du Tevatron. L'origine se trouve dans le point d'interaction. En étant donnée sa géométrie cylindrique, le système de coordonnées polaires est le plus souvent employé, où r est la distance du point d'interaction, l'angle azimutale ϕ se trouve dans le plan $x - y$ et l'angle polaire ϑ rentre dans la définition de *pseudorapidité* η, définie comme $\eta = -\log\tan(\vartheta/2)$.

La structure de l'expérience peut être répartie en trois parties: (i) les systèmes de trajectographie, à l'intérieur d'un champ magnétique de 1.4 T produit par un aimant solénoïdale, qui reconstruisent les traces des particules chargées pour la mesure de leur impulsion; (ii) les calorimètres, qui mesurent l'énergie totale déposée par les électrons, les photons et les hadrons; (iii) le système de détection des muons.

Les sous-détecteurs les plus importantes pour conduire les recherches décrites dans cette thèse sont le détecteur central de traces (CTC), décrit brièvement dans la suite, et le calorimètres électromagnétiques central (CEM) et plug (PEM) et les calorimètres hadroniques central, endwall, plug et forward (CHA, WHA, PHA et FHA), dont les caractéristiques principales sont illustrées dans la Table (1.1).

Situé immédiatement à l'extérieur d'un système de chambres à projection temporelle (VTX), qui entourent le détecteur du vertex au silicium (SVX) et, plus à l'intérieur, le tube à vide du faisceau, la CTC est une chambre à dérive qui permet la reconstruction en trois dimensions des traces des particules chargées. En particulier pour les électrons la mesure de l' impulsion est possible grâce à la correspondance des traces avec la position des dépôts d'énergie dans le CEM.

La CTC, qui couvre 2π en azimut, est longue 3.2 m, ce qui correspond à une couverture en pseudorapidité $|\eta| < 1.2$. Elle est constituée par 84 couches de fils de mesure, groupés en 9 super-couches (*superlayers*): 4 de ces 9 superlayers ont les fils disposés avec un rangement stéréo par rapport à la direction du faisceau, ce qui permet la reconstruction des traces dans la direction z. La précision dans la mesure de la position dans le plan $r - \phi$ est d'environ 200 μm et celle dans la direction z est de l'ordre de 5 mm, tandis que dans la mesure de l'impulsion la résolution de la CTC est $\frac{\delta P_t}{P_t} \sim 0.002\ P_t$ GeV/c.

CDF emploie un système de déclenchement en trois niveaux pour une sélection des événements en temps réel acte à réduire la quantité des données à enregistrer. Le premier niveau utilise une information basée sur les dépôts d'énergie dans les *tours* des calorimètres et sur les segments de trace reconstruits dans les détecteurs des muons. Le deuxième niveau raffine la sélection, en insérant aussi l'information donnée par la CTC, et, par conséquence, en utilisant un déclenchement donné par un système de reconnaissance de traces rapide, le *Central Fast Tracker* (CFT), qui associe le signal du système de trajectographie à l'information des calorimètres ou des chambres des muons. Le troisième niveau utilise un software qui est très similaire aux programmes d'analyse offline.

Les événements utilisés pour cette analyse ont été sélectionnés avec les déclenchements

Calorimeter		$\|\eta\|$ coverage	Tower size $\Delta\eta \times \Delta\phi$	Energy resolution GeV	Thickness
Central	EM	$\|\eta\| < 1.1$	$\sim 0.1 \times 15°$	$13.7\%/\sqrt{E_T} \oplus 2\%$	18 X_0
	Had	$\|\eta\| < 0.9$	$\sim 0.1 \times 15°$	$50\%/\sqrt{E_T} \oplus 3\%$	4.5 λ_0
Endwall	Had	$0.7 < \|\eta\| < 1.3$	$\sim 0.1 \times 15°$	$75\%/\sqrt{E_T} \oplus 4\%$	4.5 λ_0
Endplug	EM	$1.1 < \|\eta\| < 2.4$	$\sim 0.09 \times 5°$	$22\%/\sqrt{E_T} \oplus 2\%$	18-21 X_0
	Had	$1.3 < \|\eta\| < 2.4$	$\sim 0.09 \times 5°$	$106\%/\sqrt{E_T} \oplus 6\%$	5.7 λ_0
Forward	EM	$2.2 < \|\eta\| < 4.2$	$\sim 0.1 \times 5°$	$26\%/\sqrt{E_T} \oplus 2\%$	25 X_0
	Had	$2.4 < \|\eta\| < 4.2$	$\sim 0.1 \times 5°$	$137\%/\sqrt{E_T} \oplus 3\%$	7.7 λ_0

Table 1.1: *Calorimétrie à CDF: λ_0 est l'épaisseur des calorimétres hadroniques en longueur d'interaction et X_0 est celui des calorimétres électromagnétiques en longueur de radiation.*

recherchant des électrons de haute impulsion transverse. Pour ces déclenchements, au premier niveau au moins une tour du CEM ou du PEM est requise. Au deuxième niveau on détermine les groupements (*clusters*) d'énergie dans les calorimètres. En utilisant le CFT, il est demandé une association entre le cluster du CEM et une trace dans le CTC. En outre, le rapport entre le dépôt d'énergie dans le cluster du calorimètre hadronique et celui dans le calorimètre électromagnétique doit être suffisamment petit (< 0.125). Au troisième niveau sont sélectionnés seulement les événements caractérisés par des clusters électromagnétiques de haute énergie: plus en détail, dans le CEM on demande des clusters avec $E_T > 18$ GeV et associés à des traces de haute impulsion, $p_T > 13$ GeV/c, tandis que dans le PEM, où l'on a pas de correspondance avec la CTC, il est requis $E_T > 20$ GeV et $\not\!\!E_T > 20$ GeV.

1.3. Stratégie de l'analyse

L'analyse illustrée dans cette thèse est une recherche des leptoquarks de première génération produits en couples dans des collisions $p\bar{p}$ à une énergie du centre de masse $\sqrt{s} = 1.8$ TeV et qui se désintègrent dans les canaux $e\nu+$ 2 jets et ee + 2 jets.

La signature des événements recherchés est la suivante: un électron énergétique et isolé de l'activité des autres particules, deux jets hadroniques de haute énergie et de l'énergie transverse manquante (missing transverse energy $\not\!\!E_T$) dans le canal $e\nu jj$ et deux électrons isolés et de haute énergie, ainsi que deux jets de haute énergie dans le canal $eejj$. La même sélection est appliquée dans la recherche des leptoquarks scalaires et vectoriels, puisque la topologie des événements est similaire dans les deux cas.

Les sources principales de bruit de fond dans le canal $e\nu jj$ sont des événements (W + jets), où la W se désintègre en $e\nu$, et des événements $t\bar{t}$, où un quark top se désintègre semileptoniquement en quark bottom. Ces événements peuvent être distingués par rapport aux événements du signal en demandant un anti-B tagging qui élimine les jets générées par des quarks bottom, ou à travers des coupures sur les variables cinématiques des événements, ou sur la masse transverse de l'électron et du neutrino, $M_T(e,\nu)$, qui est distribuée différemment pour les événements avec W et pour les événements du signal.

CUT	Tight (Central)	Loose (Central or Plug)
Had/Em	< 0.05	< 0.1
E/p	< 1.8	< 4.0
Isolation	< 0.1	< 0.1
$\|\Delta x\|$	≤ 1.5 cm	*none*
$\|\Delta z\|$	≤ 3.0 cm	*none*
$Lshr$	< 0.2	*none*
χ^2_{str}	< 10.0	*none*
$\chi^2_{3\times3}$	*none*	≤ 3.0
$\|Z_v - Z_e\|$	≤ 5.0 cm	*none*
$\|Z_v\|$	≤ 60.0 cm	*none*
Conversion	yes	yes
Fiducial	yes	*none*

Table 1.2: *Liste de coupures strictes et larges appliquées pour l'identification des électrons.*

Pour la recherche dans le canal $eejj$ le bruit de fond est constitué par les événements de type Drell-Yan, où une Z ou un photon, produits par annihilation quark-antiquark, en association avec des jets provenant de la radiation du gluon, se désintègrent en électrons. L'autre source de bruit de fond sont des événements $t\bar{t}$ où les deux quarks top se désintègrent semileptoniquement en bottom. Une coupure sur la masse invariante des deux leptons dans la fenêtre $[76, 106]$ GeV/c^2 est utile pour éliminer la partie des événements Drell-Yan correspondants au pic du Z, et c'est surtout grâce aux coupures cinématiques que l'on élimine la grand partie du bruit restant.

1.3.1. La sélection des électrons

Les données analysées constituent la totalité des événements collectés par l'expérience CDF pendant les runs 1a (1992-93) et 1b (1994-95). Un sous-groupe des ces données, appellé *high p_t inclusive electron sample*, a été utilisé : il correspond à environ 27000 événements dans le run 1a et à 130000 événements dans le run 1b ($\int \mathcal{L}dt \sim 110$ pb^{-1}) et il est caractérisé par la présence d' au moins un électron avec $E_T > 20$ GeV dans chaque événement.

Pour la recherche dans le canal $e\nu jj$ l'électron doit être détecté par le calorimètre électromagnétique central (CEM) et doit satisfaire les conditions *strictes* de la Table (1.2), tandis que pour la recherche dans le canal $eejj$ l'électron plus énergétique doit être détecté par le CEM et satisfaire les conditions *strictes* de la Table (1.2) et le deuxième électron plus énergétique doit être détecté soit par le CEM ou par le calorimètre électromagnétique plug (PEM) et satisfaire les conditions *larges* de la Table (1.2). L'identification des électrons à travers cette sélection a une efficacité de l'ordre du 70% pour le canal $e\nu jj$ et de 62% pour le canal $eejj$, évaluée sur des événements du signal de leptoquark simulées avec le générateur Monte Carlo Pythia et confirmées par une comparaison avec les données.

1.3.2. Recherche des Leptoquarks scalaires dans le canal $e\nu jj$

Sélection des événements

Les événements produits par la réaction:

$$p\bar{p} \rightarrow \mathrm{S1\bar{S}1} + \mathrm{X} \rightarrow \mathrm{e\nu jj} + \mathrm{X}$$

sont sélectionnés selon les critères suivants:

- au moins un électron avec $E_T(e) > 30$ GeV
- au moins deux jets avec $E_T^C(jet1), E_T^C(jet2) > 30, 15$ GeV, où on a appliqué des corrections sur les énergies des jets pour tenir compte et de la présence des événements sous-jaçants (*underlying events*) et des pertes de partie de la gerbe électromagnétique
- énergie manquante transverse de l'événement $\not\!\!E_T > 20$ GeV
- les événements avec un deuxième lepton chargé $(e^{\pm}, \mu^{\pm})$ sont exclus
- les événements avec des hadrons de saveur B sont exclus
- les événements avec $\Delta\phi(\not\!\!E_T, jet) < 10°$ si $\not\!\!E_T/\sqrt{\sum E_T} < 4$ GeV$^{1/2}$ sont exclus, ou $\Delta\phi(\not\!\!E_T, jet)$ est la distance angulaire, en azimut, entre la direction du $\not\!\!E_T$ et celle du jet et $\not\!\!E_T/\sqrt{\sum E_T}$ représente le poids de la $\not\!\!E_T$ par rapport à l'énergie transverse visible totale de l'événement
- $E_T^C(jet1) + E_T^C(jet2) > 60$ GeV
- $E_T^C(jet1) + E_T^C(jet2) + \not\!\!E_T > 100$ GeV
- $LOG3 < -10.5$, où la variable $LOG3$ exprime la probabilité relative pour un événement d'être bruit de fond par rapport au signal: elle est définie comme $LOG3 = \log(r(M_T e, \nu)) + \log(r(\sqrt{(E_T^C e + E_T^C \nu)^2 + (E_T^C(jet1) + E_T^C(jet2))^2}) + \log(r(\not\!\!E_T))$, où $r(x) = P_B(x)/P_S(x)$ est une fonction calculée comme rapport entre la fonction $P_B(x)$, qui exprime la distribution de la variable x sur le bruit de fond (W + jets et $t\bar{t}$), et la fonction $P_S(x)$, qui exprime la distribution de la variable x sur le signal (leptoquarks avec $M_{Lq} = 180$ GeV/c^2). Les énergies transverses des électrons sont corrigées en tenant compte des valeurs des énergies mesurées dans des tests de faisceau ou de la masse de la W reconstruite sur les données. La distribution de la variable $LOG3$ est illustrée dans la Figure (1.2), où les points représentent les données, l'histogramme avec traits le signal et l'histogramme blanc le bruit de fond normalisé à la luminosité des données.

Résultats

L'efficacité de cette sélection est d' environ 19% pour une masse de leptoquark de 180 GeV/c^2. Dans la détermination de l'efficacité plusieurs sources d'erreur systématique ont été considerées: (i) dans la définition du jet et de son énergie, (ii) dans le nombre d'événements

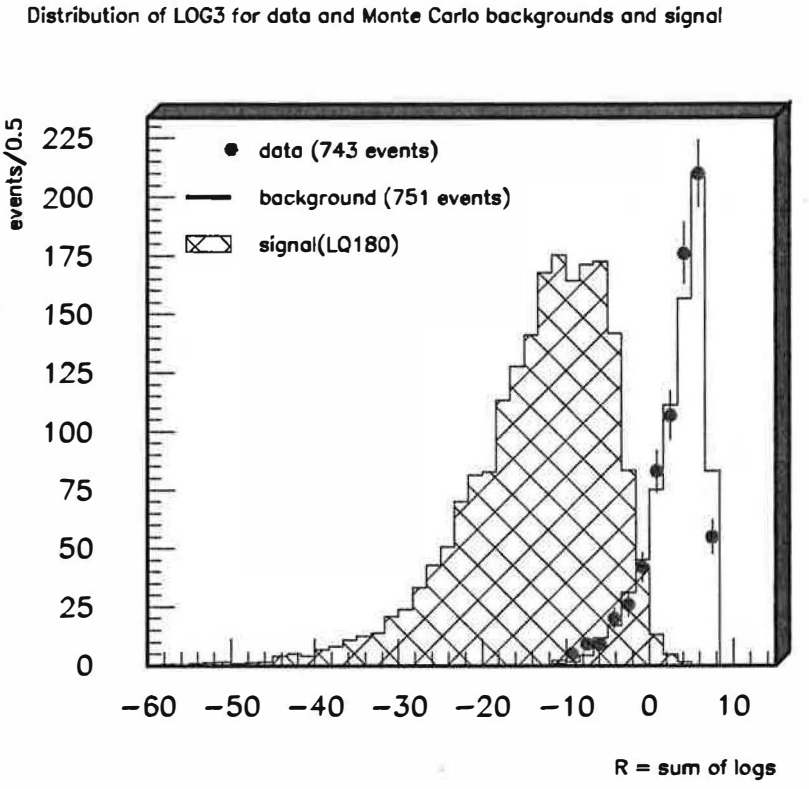

Figure 1.2: *Distribution de la variable LOG3 pour des événements du signal* (M_{S1} = 180 GeV/c^2, *histogramme avec les traits), bruit de fond (histogramme blanc) et données (points).*

Monte Carlo du signal générés, (iii) dans la simulation de la radiation du gluon dans l'état initial ou final, (iv) dans le choix de la fonction de distribution pour le parton, (v) dans le choix de l'échelle d'impulsion du parton Q^2 et (vi) dans la détermination de l'efficacité d'identification des électrons. Tous ces sources, dont (i) est la principale, donnent un erreur systématique qui, additionnée en quadrature avec l'erreur systématique dans la mesure de la luminosité à CDF, qui est d'environ 4%, donne un total de 15%.

Le nombre d'événements de bruit de fond que l'on attend après avoir appliqué cette sélection sur des événements générés avec des programmes de simulation Monte Carlo (Vecbos pour le W + jets, Pythia pour les $t\bar{t}$), et normalisés à la luminosité des données, est de (1.0 ± 0.6). Aucun événement ne survit dans les données.

1.3.3. Recherche des Leptoquarks scalaires dans le canal $eejj$

Sélection des événements

Les événements produits par la réaction:

$$p\bar{p} \rightarrow S1\bar{S1} + X \rightarrow eejj + X$$

sont sélectionnés selon les critères suivants:

- un électron *stricte* avec $E_T(e1) > 40$ GeV
- un électron *large* avec $E_T(e2) > 15$ GeV [1]
- les événements dont la masse invariante des deux électrons $M_{e1,e2} \in [76, 106]$ GeV/c^2 sont éliminés
- $E_T^C(e1) + E_T^C(e2) > 85$ GeV, où les énergies transverses des électrons sont corrigées selon des valeurs calculées dans des tests de faisceau ou dans la reconstruction de la masse de la W sur les données
- $E_T^C(jet1) + E_T^C(jet2) > 85$ GeV
- $\sqrt{(E_T^C(e1) + E_T^C(e2))^2 + (E_T^C(jet1) + E_T^C(jet2))^2} > 200$ GeV

La sélection est basée sur les caractéristiques cimématiques des événements, qui sont un discriminant très important entre événements du signal et du bruit de fond. Dans ce sens, la variable $\sqrt{(E_T^C(e1) + E_T^C(e2))^2 + (E_T^C(jet1) + E_T^C(jet2))^2}$ est la plus importante: elle représente le rayon d'un cercle avec comme centre l'origine du plan $E_T^C(e1) + E_T^C(e2)$ versus $E_T^C(jet1) + E_T^C(jet2)$, et dans la Figure (1.3) elle est dessinée pour le signal (leptoquarks de masse 220 GeV/c^2) et pour le bruit de fond (Drell-Yan et $t\bar{t}$).

Résultats

L'efficacité de cette sélection est d' environ 35% pour une masse de leptoquark de 220 GeV/c^2. Les sources d'erreur systématique restent les mêmes que celles trouvées dans le canal $e\nu jj$ et, quand cette contribution est additionnée en quadrature avec l'erreur systématique du 4% sur la mesure de la luminosité, un erreur total du 10% est obtenu.

Le nombre d'événements de bruit de fond attendues après cette sélection sur des événements générés par le programme Pythia de simulation Monte Carlo et normalisés à la luminosité des données est de (1.8 ± 0.6). Comme dans l'analyse précédente, aucun événement ne survit dans les données.

[1] Les deux électrons sélectionnés ne doivent pas forcément posséder une charge électrique opposée: cette information n'est pas utilisée, puisque la détermination de la charge électrique pour particules de haute impulsion transverse n'est pas fiable.

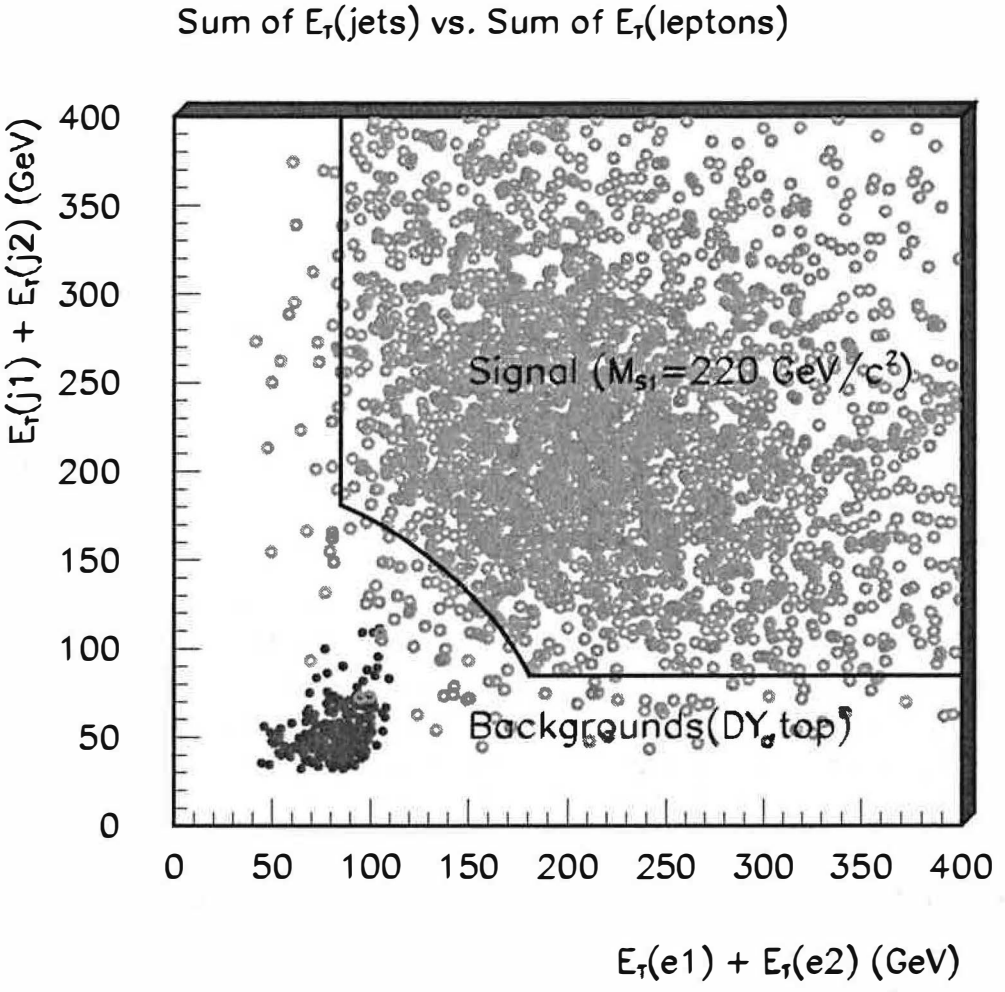

Figure 1.3: *Cette figure illustre la distribution de la somme des énergies transverses corrigées des deux électrons les plus énergétiques dans l'événement versus la somme des énergies transverses corrigées des deux jets les plus énergétiques dans l'événement pour le signal (leptoquarks de masse* $M_{S1} = 220\ \mathrm{GeV/c^2}$*) et pour le bruit de fond (Drell-Yan et top). Les lignes droites montrent les coupures sur ces variables à 85 GeV et la ligne circulaire représente la coupure à 200 GeV sur la variable* $\sqrt{(E_T^C(e1) + E_T^C(e2))^2 + (E_T^C(jet1) + E_T^C(jet2))^2}$.

1.3.4. Recherche des Leptoquarks vectoriels

Sélection des événements et résultats

La cinématique de désintégration des leptoquarks vectoriels est la même que celle des leptoquarks scalaires, et c'est la raison pour laquelle les mêmes coupures des sélection utilisées dans le cas scalaire peuvent être appliquées pour la recherche des leptoquarks de spin 1 dans les deux canaux $e\nu jj$ et $eejj$.

Les efficacités de sélection ont été evaluées sur des échantillons des leptoquarks vectoriels simulés avec Pythia dans les deux cas de couplage anomal $k_G = 0, \lambda_G = 0$ et $k_G = 1, \lambda_G = 0$. Elles sont les valeurs utilisées pour la détermination des limites sur la section efficace de production.

Les résultats de la sélection sur les données, ainsi que les expectations du bruit de fond dans les deux canaux, restent les mêmes.

1.3.5. Calcul des limites et leur combinaison

La limite supérieure sur la section efficace de production des leptoquarks à un niveau de confiance du 95%, $\sigma_{95}(M_{Lq})$, est définie dans la façon suivante:

$$\sigma_{95}(M_{Lq}) = \frac{N_{95}(M_{Lq})}{\int \mathcal{L}dt \cdot \varepsilon(M_{Lq}) \cdot Br}$$

où $N_{95}(M_{Lq})$ est la limite supérieure, calculée avec une méthode statistique Bayesienne, sur le nombre d'événements observés pour chaque valeur de masse de leptoquark, et qui dans ce cas est, pour chaque M_{Lq}, la limite supérieure sur zéro; $\mathcal{L}$ est la luminosité intégrée, $\varepsilon(M_{Lq})$ l'efficacité de la sélection evaluée sur les événements simulés du signal pour chaque masse de leptoquark et $Br = 2\beta(1-\beta)$ dans le canal $e\nu jj$ et $Br = \beta^2$ dans le canal $eejj$. Les valeurs obtenues pour chaque masse de leptoquark et pour $\beta = 0.5$ dans la recherche dans le canal $e\nu jj$ sont comparées avec les valeurs théoriques calculées à l'ordre d'approximation NLO (Next-to-Leading Order): la valeur de la limite inférieure sur la masse de leptoquark est obtenue à 182 GeV/c^2. La même chose, pour $\beta = 1$ et dans le canal $eejj$, donne une limite inférieure sur la masse à 220 GeV/c^2.

Ces résultats peuvent être généralisés pour des valeurs de $\beta \in [0., 1.]$ dans la recherche dans les deux canaux et dans la combinaison des résultats, en appliquant une méthode statistique Bayesienne, comme illustré en Figure (1.4).

Pour ce qui concerne la recherche des leptoquarks vectoriels, en procédant de la même façon pour chaque canal on peut déterminer les limites supérieures sur la section efficace pour $\beta = 0.5$ ($e\nu jj$) et pour $\beta = 1$ ($eejj$) et, par comparaison avec les valeurs théoriques les limites inférieures sur la masse, en faisant la distinction appropriée entre les valeurs du couplage anomal $k_G = 0, \lambda_G = 0$ et $k_G = 1, \lambda_G = 0$. Les limites sur les masses sont $M_{V1} > 300,250$ GeV/c^2 ($k_G = 0, k_G = 1$) dans le canal $e\nu jj$ et pour $\beta = 0.5$ et $M_{V1} > 330,280$ GeV/c^2 ($k_G = 0, k_G = 1$) dans le canal $eejj$ et pour $\beta = 1$.

Même pour le cas vectoriel on peut généraliser le résultat pour des valeurs de β dans l'intervalle [0.,1.] et obtenir les limites inférieures sur la masse en fonction du rapport

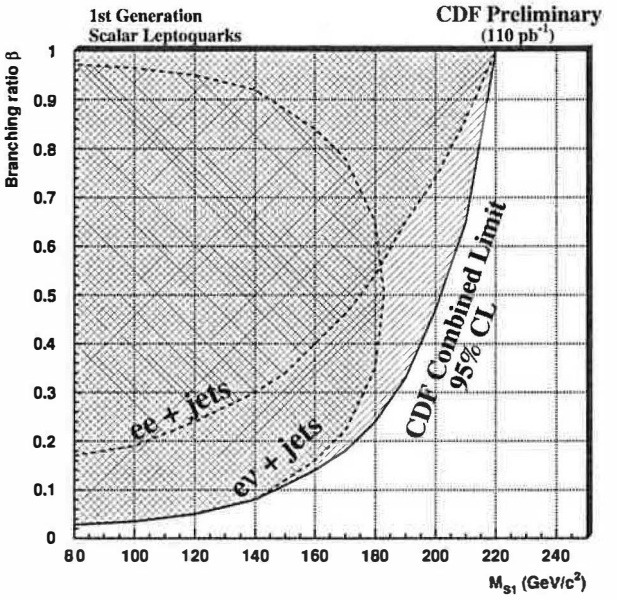

Figure 1.4: *Cette figure résume tous les résultats trouvés dans la recherche des leptoquarks scalaires produits en couples dans les canaux $e\nu jj$ et $eejj$ dans la forme β versus M_{S1}. Les résultats sont donnés pour chaque canal et pour leur combinaison.*

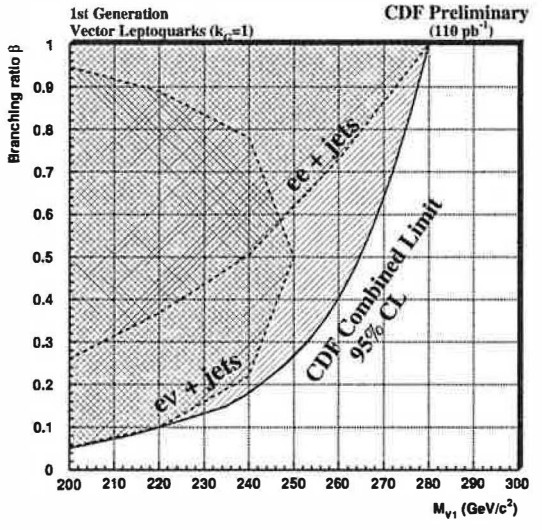

Figure 1.5: *Résultats dans la recherche des leptoquarks vectoriels dans le cas de couplage anomal $k_G = 1, \lambda_G = 0$.*

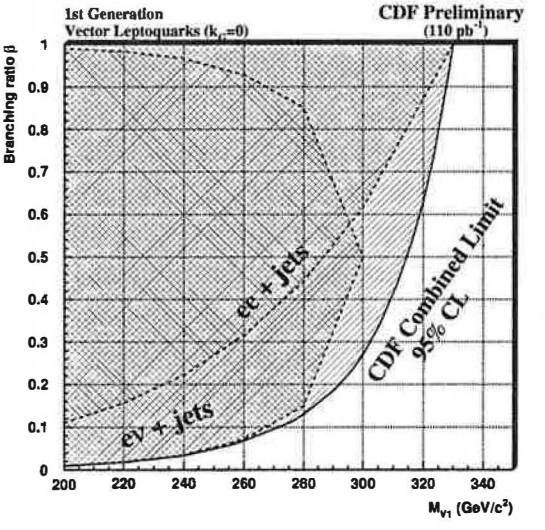

Figure 1.6: *Résultats dans la recherche des leptoquarks vectoriels dans le cas de couplage anomal $k_G = 0, \lambda_G = 0$.*

de branchement: cela est illustré dans les Figures (1.5) et (1.6) pour diverses valeurs du couplage anomal.

Ces limites sont en accord avec les valeurs trouvées par l'autre expérience du Tevatron, DØ. Dans le prochain run du Tevatron, qui vient de commencer, on pourra rejoindre des limites inférieures sur les masses des leptoquarks de l'ordre des 300 GeV/c^2. Au LHC, ainsi que dans les collisionneurs linéaires prévus dans les prochaines décades, ces limites pourront rejoindre l'ordre du Tev/c^2, qui représente aussi l'ordre de grandeur d'une éventuelle découverte.

Part I

Theoretical Motivation

Chapter 2

Standard Model and beyond

Introduction- *During last century a big effort has been made by physicists in trying to answer questions about the basic and fundamental components of the matter, questions which always have interested men and scientists searching for simple solutions in terms of the number of building blocks of Nature.*
Thanks to a series of experiments and theoretical works embracing the fields of atomic, nuclear, cosmic-ray and high-energy physics we have now some answers and we can see a world made by quarks, leptons and gauge bosons. This chapter, after a short historical summary, will briefly (i) introduce the most successfull theory actually describing the elementary particles and their interactions, the Standard Model, then (ii) it will talk about the unanswered questions of the Standard Model and about leptoquarks, particles naturally present in models which go beyond it.

2.1. Brief historical overview

The end of the 19th and the beginning of the 20th centuries were dense with discoveries in the field of atomic and sub-atomic physics. In that period the atoms were supposed to be held together in various combinations to form matter by a very complicated force [1]. The year 1895 was crucial for the beginning of the atomic physics. From studies about the nature of cathodic rays, J. J. Thomson and W. Crookes [2] in England and J. Perrin [3] in France discovered that they are constitued by charged particles, the electrons. Thomson [4] in addition measured the e/m ratio between electron charge and mass and demonstrated that electrons are all identical, whatever their provenience, and that they are the same kind of particles present in atoms. Thanks to this new picture, the atoms became easier to understand and the successfull investigations of Rutherford in 1911, in studies about the properties of α particles [5], gave the confirmation that they have a nucleus at the center, which is positively electrically charged and very massive, and that the nucleus is surrounded by a certain number of electrons which are very light and negatively charged. Therefore the bonds between electrons and nuclei to form atoms, and between atoms to form molecules, have their origin in the Coulomb interaction.

In the early 1930's the hypothesis that the nucleus could be seen as conglomerate of protons and neutrons was made by Chadwick as consequence of the discovery of the neutron [6]. But protons and neutrons are not ultimate components or fundamental particles. In more recent years, in the 1960's, Gell-Mann and Zweig introduced the quark model [7] according to which quarks, with three possible flavours, *up, down* and *strange*, are the constituents of protons, neutrons and of all those particles initially seen in cosmic rays experiments. In particular, quarks with flavours up and down are the constituents of nucleons: protons are uud states and neutrons are udd states. Following the discovery, at the high-energy accelerators, of hadronic resonances like the J/ψ [8], [9] and Υ [10], the model has been enlarged to include the *charm*, the *bottom* and, finally, after its discovery at Tevatron in 1991 [11], the *top* flavours.

The electrons and the quarks *up* and *down* are the components of the ordinary matter. The other basic constituents are non-stable particles seen in cosmic rays or produced in particle accelerators and are listed in Table (2.1). As leptons are indicated the electrically charged electron, muon (μ) and tau (τ), these two latters of the same kind as the electron,

LEPTON	Charge (e)	Mass (Mev/c^2)	QUARK	Charge (e)	Mass (Mev/c^2)
e	± 1	0.511	**u**(p)	$\pm 2/3$	1 to 5
ν_e	0	$< 3 \cdot 10^{-6}$	**d**(own)	$\mp 1/3$	3 to 9
μ	± 1	106	**c**(harmed)	$\pm 2/3$	1150 to 1350
ν_μ	0	$< 0.19(90\% C.L.)$	**s**(trange)	$\mp 1/3$	75 to 170
τ	± 1	1777	**t**(op)	$\pm 2/3$	(174.3 ± 5.1) GeV/c^2 [16]
ν_τ [2]	0	$< 18.2(95\% C.L.)$	**b**(ottom)	$\mp 1/3$	4000 to 4400

Table 2.1: *The classification in leptons and quarks according to the Standard Model.*

but much more massive, and the uncharged, almost massless neutrinos ν_e, ν_μ and ν_τ. Neutrinos were first hypothesized in 1933 by W. Pauli [12] to explain the continuum energy spectrum of electrons in nuclear β decays. This classification of particles, summarized in Table (2.1), is given by the Standard Model, the most successfull theory describing the interactions between elementary particles up to now, which will be explained in some more detail in a dedicated section. The *top* quark mass value reported in Table (2.1) is the best known up to now and it comes from the combination of the $D\emptyset$ and CDF experiments at Fermilab's Tevatron direct measurements [11] [1].

The early 1900 was also very productive by the point of view of the theoretical physics, for the birth of the quantum mechanics and of the special relativity, which lead to a new interpretation of particles and interactions: Newton's laws were considered inapplicable in the world of atoms. In quantum mechanics particles behave like waves and waves like particles and the determinism given in the classical mechanics is lost. In quantum mechanics the idea that a particle has a definite location and a definite momentum is no longer valid, as expressed in the Heisenberg's uncertainty principle $\Delta x \Delta p \geq \not{h}$, where h is the Planck's constant: the uncertainty of the momentum and the uncertainty of the position are complementary, and the product of the two is constant. Moreover, from the relation $\Delta E = \Delta p/c$, which gives $\Delta x \geq \not{h}/c\Delta E$, follows that to investigate at smaller and smaller dimensions on the subatomic world, higher and higher energies are needed, and this is one of the basic principles used at the particle accelerators.

Quantum mechanics and special relativity, merged together, give the relativistic quantum field theory, which represents the modern theoretical framework for the description of particle physics. The Quantum Electro-Dynamics (QED) is the first example of this kind of theory. It is a quantized and relativistically invariant description of the electromagnetic interactions of electrons and photons. The interaction between particles is viewed in terms of the exchange of specific quanta with integer spin (bosons) associated with the particular

[1] The most precise measurements come from the reaction $p\bar{p} \to t\bar{t}X$, with both top's going to b's through the decay $t\bar{t} \to W^+bW^-\bar{b} \to \ell\nu_\ell q\bar{q}'b\bar{b}$. Given its very high mass, the *top* has a short lifetime, so it is expected to decay before top-flavoured hadrons bound states can form.

[2] The direct evidence for the third neutrino type, has been recently announced at the DONUT (Direct Observation of Nu Tau) experiment at Fermilab after five months of exposing a photografic-emulsion target to an intense neutrino beam from the Tevatron [13]. Four ν_τ interactions have been identified.

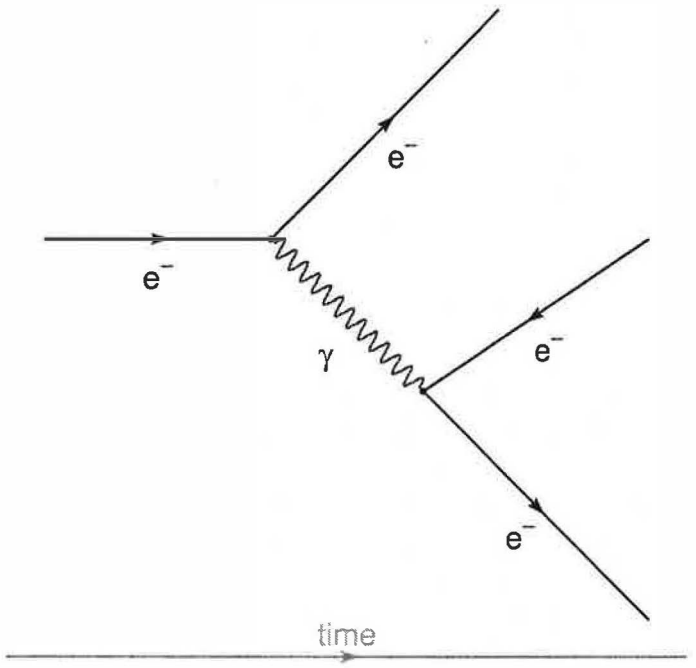

Figure 2.1: *This diagram represents the electromagnetic interaction between two electrons as interpreted by QED and seen as exchange of a photon, which is emitted by one electron and absorbed by the other. The photon carries part of the energy-momentum of the emitting electron, and it travels for a finite time interval Δt, given by the uncertainty principle expressed in the form $\Delta E \Delta t \geq \hbar$.*

type of interaction: in QED it is the photon (see picture in Figure (2.1)). Since the quantum carries part of the energy and momentum of the interacting particle, the conservation laws can be satisfied only if the process takes place over a time interval Δt limited by the uncertainty principle expressed in the form $\Delta E \Delta t \geq \hbar$. Indeed, the range R of the interaction depends on the mass m of the quantum to be exchanged: from $\Delta t \geq \hbar/mc^2$ follows that $R = c\Delta t \geq \hbar/mc$. For a quantum whose mass is zero, as is the case for the photon in QED, the range of the interaction is infinity.
The fundamental interactions on atomic and sub-atomic scales are the electromagnetic, the weak and the strong interactions:

- the electromagnetic interaction takes place between electrically charged particles: it can be attractive or repulsive. Its carrier is the spin 1 photon,which is massless, thus the range is infinite.
- the weak interaction is responsible, for example, for the β decay of the neutron into proton in the nucleus. It is a short range interaction, mediated by the spin 1, very massive particles $W^{\pm}$ and Z.

INTERACTION	Vector Boson(s)	Mass (GeV/c^2)
Electromagnetic	photon	M_γ=0
Weak	$W^\pm$	$M_W = (80.42 \pm 0.05)$[16]
	Z	$M_Z = (91.188 \pm 0.002)$[16]
Strong	8 gluons	$M_{gluon} = 0$

Table 2.2: *List of the interactions occurring at atomic and sub-atomic scale with the corresponding carriers, or exchange particles, spin-1 bosons.*

- the strong interaction confines quarks into hadrons. It is mediated by 8 massless, bicoloured, spin 1 gluons: colour charge is the equivalent to the electric charge of the Coulomb interaction.

Gravitation is not considered for the usual mass scales in high-energy physics because the gravitational coupling is negligible. Gravity becomes strongly interacting at the so called Planck mass scale, $M_P = 10^{19}$ GeV/c^2. In parallel with the other three interactions, since it has an infinite range it is supposed to occur due to the exchange of a massless, spin 2 particle called graviton.

Charged leptons ($e^\pm, \mu^\pm, \tau^\pm$) experience electromagnetic and weak interactions, neutrinos only weak interaction, quarks can experience all of the three. Particles which can interact through strong interaction are called hadrons: the mesons are $q\bar{q}$ states, and the baryons are qqq bound states. In Table (2.2) are listed the interactions and their corresponding carriers.

2.2. The Standard Model

The Standard Model for the electroweak and strong interactions is a trial of a comprehensive theory of the particle physics, and is a renormalizable local gauge theory describing the interactions between elementary particles. It offers a description of phenomena in the framework of the relativistic quantum field theory. It makes use of a special class of theories, called *gauge* theories: QED itself is the simplest example of such a theory. The weak and strong interaction of quarks and leptons are both believed to be described by gauge theories: the unified electroweak model and the Quantum Chromo-Dynamics (QCD).
The Standard Model identifies the basic constituents of matter - quarks and leptons, grouped in 3 generations which have exactly the same interactions - and describes all the forces of nature relevant at accessible energies - the strong, weak and electromagnetic interactions.
- Quarks and leptons -
In the Standard Model quarks and leptons, which are spin 1/2 fields satisfying the Dirac equation, are arranged in a kind of periodic table as represented in Table (2.1). Their masses are not predicted by the model and come from measurement. Charged leptons have masses which increase rapidly through the three generations: $M_e = 0.511$ MeV/c^2, $M_\mu =$ 106 MeV/c^2 , $M_\tau = 1777$ MeV/c^2. Neutrinos are almost massless: recently limits on the ν_e and ν_μ masses have been set from observations of $\nu_\mu \rightarrow \nu_e$ oscillations by the LSND [14]

and the Super-Kamiokande [15] experiments. Quarks are particles with fractionary electric charge and carrying one of three possible colour numbers, usually denoted with the names of the primary colours blue, red and green. Colour charge is the equivalent of electric charge in QED, and it has been introduced to overcome problems in the Fermi-Dirac statistics of states like the $\Delta^{++} = uuu$ and to explain why states like qq or $\bar{q}\bar{q}$ are not observed. Quarks are confined inside the hadrons and since free-quarks have never been observed their mass should be thought of simply as a parameter to be determined in principle by the experiment and from non-perturbative QCD calculations [16]. Estimations are reported in the Table (2.1). The number of fermion families is not predicted by the Standard Model. Experimentally, it has been found equal to three: this has been an important result of LEP running at a center of mass energy corresponding to the peak of the Z gauge boson, $\sqrt{s} = 91$ GeV, and gave $N_\nu = 2.984 \pm 0.008$ as number of light neutrinos ($m_\nu < Z/2$) [17]. More recently it has also been excluded the existence of a fourth family [18].

- Fundamental interactions -

As mentioned in previous section, there are three possible kind of interactions on nuclear and sub-nuclear scale: the electromagnetic, the weak and the strong. The Standard Model is based on the belief that all particle interactions are dictated by *local gauge symmetries.* In field theory one talks about fields (scalar, vector, Dirac fields) instead of particles. These fields are quantized. A symmetry corresponds to a field transformation which leaves invariant the action $\mathcal{S}$ of the system, defined as: $\mathcal{S} = \int d^4x \mathcal{L}(\phi, \partial_\mu \phi)$ where $\mathcal{L}$ is the Lagrangian density. The generic $\mathcal{L}$ for free, massless, scalar (spin=0) and spinorial (Dirac, spin=1/2) fields ϕ^i and ψ_L, ψ_R [3] is given by:

$$\mathcal{L} = \frac{1}{2}(\partial_\mu \phi^i)(\partial^\mu \phi^i) + i\bar{\psi}_{LI}\gamma^\mu \partial_\mu \psi_L^I + i\bar{\psi}_{RJ}\gamma^\mu \partial_\mu \psi_R^J \tag{2.1}$$

where the γ^μ's are the Dirac matrices. When the field transformation depends on the space-time point x it is called *local.* A phase field transformation is called *gauge* transformation and is expressed by:

$$\phi^j \rightarrow \phi^{j\prime} = U_k^j \phi^k = e^{i\alpha T_k^j} \phi^k \tag{2.2}$$

It is local if α differs from space-time point to point, that is $\alpha = \alpha(x)$. The U matrices satisfying the Equation (2.2) form the gauge group, and the T matrices are the generators of the algebra of the transformation. The Lagrangian density $\mathcal{L}$ of a free field, of Equation (2.1), is not invariant under local gauge transformation of the fields. If the ordinary derivatives are replaced by covariant derivatives, defined by the introduction of a massless [4] extra vector field, A_μ, called gauge field, the invariance of $\mathcal{L}$ can be maintained for local gauge transformations. The covariant derivative is defined as:

$$D_\mu \phi^i = \partial_\mu \phi^i - iA_\mu (T)_j^i \phi^j \tag{2.3}$$

[3] the labels L and R indicate the left and right helicities of the spinor. A generic spinor ψ can be seen as composed by ψ_L and ψ_R. The spin polarization of particles is often referred to by the term helicity. A particle with spin S and momentum $\vec{p}$ has helicity defined as the projection of the spin S in the direction of the momentum, and it is measured through the operator $H = \frac{\vec{p}\vec{S}}{|\vec{p}|}$.

[4] a mass term for the gauge field in the lagrangian would not respect the invariance under gauge transformations: for each gauge symmetry there is a gauge boson without mass.

The properties of the gauge field A_μ are defined by requiring that the transformation over $D_\mu\phi$ acts as over ϕ itself, that means:

$$D_\mu\phi^i \rightarrow D_\mu\phi^{i\prime} = (e^{i\alpha T})^i_j D_\mu\phi^j \tag{2.4}$$

The local gauge theory with which we are most familiar is QED, describing the electromagnetic interaction, which is invariant under the phase transformations expressed in the abelian $U(1)$ gauge group. The gauge field A_μ associated to $U(1)$ is the massless, spin 1, photon field.

The Quantum Chromo-dynamics (QCD), the theory which explains the strong interaction, has been obtained in analogy with QED. The group of local gauge transformations is $SU(3)_C$, where the label C indicates that the transformations expressed in this theory depend only on the colour charge. The requirement of local conservation of the Lagrangian density by gauge transformation generates 8 massless gluons. A feature which is typical of a non-abelian theory as QCD and has no analogue in QED is that in the lagrangian of QCD there is self-interaction between the gauge bosons, that means that gluons carry colour charge. For this reason quarks are expected to be confined inside hadrons and have never been seen as free particles. Another important implication of the direct coupling of gluons is that the interaction has an asymptotic freedom at very short distances, that means also that for large momentum transfers the quark looks like a free field without interaction.

2.3. Electroweak Symmetry Breaking

The local gauge invariance expressed in QED and in QCD through the $U(1)$ and $SU(3)$ group transformations is satisfied at the price of the introduction of the gauge fields A_μ (the photon in QED and the gluons in QCD), whose masslessness comes from the requirement of local gauge invariance. Problems arise when it is attempted to explain weak interactions in the framework of the local gauge transformations. How to reconcile the fact that this theory requires, to be invariant, a massless gauge boson, with the experimental fact that, since the range of the weak force is very short, its carrier must be obviously massive? And how to explain the discovery of the massive bosons $W^\pm$ and Z [19] without introducing a mass term in the Lagrangian? A mass term $M^2 W_\mu W^\mu$ for the gauge field, introduced in the lagrangian density of Equation (2.1), has the consequence of destroying its invariance even after replacing the ordinary derivatives with covariant derivatives. The theory emerging from this assumption would be unrenormalizable.
A way, formally very elegant, to proceed, and which is the basis of the Glashow-Weinberg-Salam [20], [21], [22] model of electroweak interaction, is the spontaneous symmetry breaking mechanism.
Assume a Lagrangian density, for which the minima are searched, of the form [23]:

$$\mathcal{L} = \frac{1}{2}(\partial_\mu\phi)^2 - (\frac{\mu^2}{2}\phi^2 + \frac{\lambda}{4}\phi^4) = T - V \tag{2.5}$$

The field ϕ has been taken, for simplicity, to be scalar, and the parameter λ is positive. $\mathcal{L}$ is symmetric under transformation $\phi \rightarrow -\phi$. The term in ϕ^2 is usually recognized as the mass term, with $\mu^2 > 0$ and μ is the mass of the field. In this case the potential V has

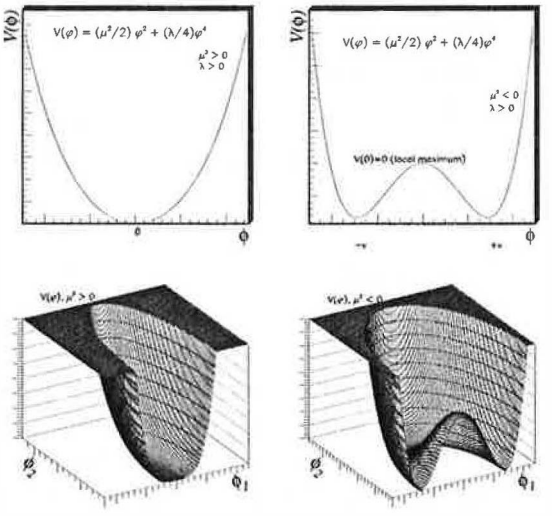

Figure 2.2: *In the two plots on the top the potential $V = V(\phi)$ is represented with the assumptions $\mu^2 > 0$ and $\mu^2 < 0$ respectively. In the first case the potential is symmetric with respect to the ground state $\phi = 0$, while in the second case it has a local maximum at $\phi = 0$. Two minima are found for $\phi = \pm v = \pm\sqrt{-\mu^2/\lambda}$. The same features can be found for the complex, scalar field $\phi = \frac{1}{\sqrt{2}}(\phi_1 + i\phi_2)$, for which the two cases are plotted in the figures at the bottom.*

the form shown in Figure (2.2) (top,left) and has one ground state corresponding to $\phi = 0$, with respect to which it is symmetric. One can disregard the natural assumption $\mu^2 > 0$ and take $\mu^2 < 0$. The parameter μ cannot be interpreted as the mass of the field. The minima of the potential $V(\phi)$, which is plotted in Figure (2.2) (top,right), are found by the equation $\partial V(\phi)/\partial\phi = 0$, from which follows:

$$(\mu^2 + \lambda\phi^2)\phi = 0 \tag{2.6}$$

The point $\phi = 0$ is a local maximum of the function, therefore it is not considered since the physical interest is in the minima of the function. There are two possible minima that can be taken as ground states: they are $\phi = \pm v = \pm\sqrt{-\mu^2/\lambda}$. These two minima are not symmetric for the function $V(\phi)$, contrary to $\phi = 0$ in the case $\mu^2 > 0$ of Figure (2.2) (top,left). An infinitesimal transformation over ϕ around one of the possible ground states, for example $\phi = +v$, can be expressed as:

$$\phi \rightarrow \phi' = +\sqrt{\frac{-\mu^2}{\lambda}} + \eta(x) \tag{2.7}$$

where $\eta(x)$ is a scalar field expressing a small variation around the minimum. This transformation, when applied to the Lagrangian density, gives:

$$\mathcal{L}' = \frac{1}{2}(\partial_\mu\eta)^2 - \lambda v^2\eta^2 - \lambda v\eta^3 - \frac{1}{4}\lambda\eta^4 + ... \tag{2.8}$$

$\mathcal{L}'$ is equivalent to $\mathcal{L}$: the physics behind both of them is the same and $\mathcal{L}'$, as $\mathcal{L}$, is invariant under transformations in η. From $\mathcal{L}'$ one can deduce that the field $\eta(x)$ is massive and that the mass term, $\lambda v^2\eta^2$, has the right sign, so that:

$$m_\eta = \sqrt{2\lambda v^2} = \sqrt{-2\mu^2} \tag{2.9}$$

This procedure reveals a massive, scalar field η which allows to preserve the invariance by transformation. This process, whose result is the generation of masses, is called spontaneous symmetry breaking: the symmetry is broken at the moment one makes a choice between $+v$ and $-v$ as the ground state around which performing the transformation.

2.3.1. Spontaneous breaking of a global gauge symmetry: Goldstone's theorem

The spontaneous symmetry breaking works well for a real scalar field ϕ whose Lagrangian is invariant under the transformation $\phi \to -\phi$. What happens if ϕ is complex? It has the form:

$$\phi = \frac{1}{\sqrt{2}}(\phi_1 + i\phi_2) \tag{2.10}$$

and the lagrangian density is:

$$\mathcal{L} = (\partial_\mu\phi)^*(\partial_\mu\phi) - \mu^2\phi^*\phi - \lambda(\phi^*\phi)^2 \tag{2.11}$$

$\mathcal{L}$ is invariant under global gauge transformation $\phi \to e^{i\alpha}\phi$, which means that $\mathcal{L}$ has a $U(1)$ global gauge symmetry. $\mathcal{L}$ can be written as:

$$\mathcal{L} = \frac{1}{2}(\partial_\mu\phi_1)^2 + \frac{1}{2}(\partial_\mu\phi_2)^2 - \frac{1}{2}\mu^2(\phi_1^2 + \phi_2^2) - \frac{1}{4}\lambda(\phi_1^2 + \phi_2^2)^2 \tag{2.12}$$

The case $\eta^2 > 0, \lambda > 0$ is illustrated in Figure (2.2) (bottom, left) and does not lead to symmetry breaking. When considering the case $\eta^2 < 0, \lambda > 0$, in the plane ϕ_1, ϕ_2 the function $V(\phi)$ has, as minima, all the points belonging to a circle of radius v such that $v^2 = \phi_1^2 + \phi_2^2$ with $v^2 = -\mu^2/\lambda$, as shown in Figure (2.2) (bottom, right). In this case as well there is no symmetry of the function with respect to the minimum. A minimum can be in the point $\phi_1 = v, \phi_2 = 0$. As in previous section, $\mathcal{L}$ can be expanded around it if an infinitesimal transformation of ϕ around (ϕ_1, ϕ_2) is considered:

$$\phi(x) = \sqrt{\frac{1}{2}}[v + \eta(x) + i\chi(x)] \tag{2.13}$$

expressed through the real, scalar fields $\eta(x)$ and $\chi(x)$ to be substituted in $\mathcal{L}$:

$$\mathcal{L}' = \frac{1}{2}(\partial_\mu\chi)^2 + \frac{1}{2}(\partial_\mu\eta)^2 + \mu^2\eta^2 + const. + ... \tag{2.14}$$

The term $\mu^2\eta^2$ has the form of a mass term $-1/2m_\eta^2\eta^2$ for the field η. From that it follows that $m_\eta = \sqrt{-2\mu^2}$ as in previous section. In Equation (2.14) there is also a kinetic term for the field $\chi(x)$, but there is no mass term corresponding to it. This is a general property:

in the case of global gauge transformations another field is introduced, the massless scalar field $\chi(x)$. It is also called *Goldstone's boson*, its existence is stated by the *Goldstone's theorem*: " Massless scalars occur whenever a continuos symmetry of a physical system is spontaneously broken".
The aim of these calculations was to demonstrate the existence of massive gauge bosons by considering a global gauge transformation on a massless scalar field ϕ. For the moment the calculation has given a massive, scalar η field and a massless, scalar χ field. When the same calculations are made for local gauge transformations the results change.

2.3.2. Spontaneous breaking of a local $SU(2)$ gauge symmetry: the Higgs mechanism

This paragraph concludes this brief theoretical overview with a last effort to obtain the mechanism which, thanks to the spontaneous breaking of $U(1)$ and $SU(2)$ gauge symmetries, leads to the Glashow-Weinberg-Salam electroweak model which incorporates the massive gauge bosons.
First of all, here is introduced the *Higgs mechanism* in the spontaneous breaking of the $U(1)$ local gauge symmetry. The $U(1)$ local gauge transformations are like:

$$\phi \rightarrow e^{i\alpha(x)}\phi \tag{2.15}$$

By introducing the covariant derivative D_μ to replace ∂_μ:

$$D_\mu = \partial_\mu - ieA_\mu \tag{2.16}$$

where A_μ is the gauge field which transforms as:

$$A_\mu \rightarrow A_\mu + \frac{1}{e}\partial_\mu \alpha \tag{2.17}$$

the Lagrangian density $\mathcal{L}$ can be written as:

$$\mathcal{L} = (\partial^\mu + ieA^\mu)\phi^*(\partial_\mu - ieA_\mu)\phi - \mu^2\phi^*\phi - \lambda(\phi^*\phi)^2 - \frac{1}{4}F_{\mu\nu}F^{\mu\nu} \tag{2.18}$$

$F_{\mu\nu}$ is the field strength tensor here defined as: $F_{\mu\nu} = \partial_\mu A_\nu - \partial_\nu A_\mu$. $\mathcal{L}$ is the QED lagrangian for a charged scalar field ϕ with mass μ when one assumes $\mu^2 > 0$. Here the interest is in taking $\mu^2 < 0$, to break the symmetry and generate masses. By substituing, again, $\phi(x) = \sqrt{\frac{1}{2}}[v + \eta(x) + i\chi(x)]$ in the lagrangian $\mathcal{L}$, the resulting $\mathcal{L}'$ is:

$$\mathcal{L}' = \frac{1}{2}(\partial_\mu\chi)^2 + \frac{1}{2}(\partial_\mu\eta)^2 - v^2\lambda\eta^2 + \frac{1}{2}e^2v^2A_\mu A^\mu - evA_\mu\partial^\mu\chi - \frac{1}{4}F_{\mu\nu}F^{\mu\nu} + \text{inter. terms} \tag{2.19}$$

The scalar field η represents a particle with mass $m_\eta = \sqrt{2\lambda v^2}$; χ is massless.
There is a positive result in this calculation: it has been generated a mass $m_A = ev$ for the gauge boson A_μ, which was "hidden" in the initial $\mathcal{L}$. The negative point is that there

is still a Goldstone's boson with mass zero. A new transformation can be introduced to eliminate this problem. Since:

$$\begin{aligned}\phi &= \sqrt{\frac{1}{2}}(v+\eta+i\chi) \\ &\simeq \sqrt{\frac{1}{2}}(v+\eta)e^{i\chi/v}\end{aligned}$$

at the lowest order in χ, if a new set of real fields h, ϑ and A_μ is taken such that:

$$\phi \rightarrow \sqrt{\frac{1}{2}}(v+h(x))e^{i\vartheta(x)/v} \tag{2.20}$$

$$A_\mu \rightarrow A_\mu + \frac{1}{ev}\partial_\mu\vartheta \tag{2.21}$$

and is substituted in the original $\mathcal{L}$, this gives:

$$\mathcal{L}'' = \frac{1}{2}(\partial_\mu h)^2 - \lambda v^2 h^2 + \frac{1}{2}e^2v^2A_\mu^2 - \lambda v h^3 - \frac{1}{4}\lambda h^4 + \frac{1}{2}e^2A_\mu^2h^2 + ve^2A_\mu^2h - \frac{1}{4}F_{\mu\nu}F^{\mu\nu} \tag{2.22}$$

In $\mathcal{L}''$ there is no Goldstone's boson. Indeed, $\mathcal{L}''$ describes two fields, the scalar h which has mass $m_h = \sqrt{2\lambda v^2}$ and which is called Higgs boson, and a vector gauge boson A_μ with mass $m_A = ev$. A_μ and h are reciprocally interacting.
In this section the $U(1)$ local gauge symmetry has been broken as the result of the introduction of a massive vector gauge boson field A_μ interacting with a scalar, massive field h, the Higgs particle.

The same procedure can be repeated for local $SU(2)$ gauge symmetry. The Lagrangian density here is:

$$\mathcal{L} = (\partial_\mu\phi)^\dagger(\partial^\mu\phi) - \mu^2\phi^\dagger\phi - \lambda(\phi^\dagger\phi)^2 \tag{2.23}$$

with ϕ given by:

$$\phi = \begin{pmatrix}\phi_\alpha \\ \phi_\beta\end{pmatrix} = \sqrt{\frac{1}{2}}\begin{pmatrix}\phi_1+i\phi_2 \\ \phi_3+i\phi_4\end{pmatrix} \tag{2.24}$$

ϕ is an $SU(2)$ doublet of complex scalar fields ϕ_α and ϕ_β. The global $SU(2)$ phase transformation under which $\mathcal{L}$ is invariant is:

$$\phi \rightarrow \phi' = e^{i\alpha_a\tau_a/2}\phi \tag{2.25}$$

By taking the local phase transformation, with $\alpha = \alpha(x)$, the invariance of the lagrangian is maintained by introducing the covariant derivative and three gauge fields $W_\mu^a, a = 1, 2, 3$. The gauge invariant lagrangian, whose very complicated form will be omitted here, has a potential $V(\phi)$ of the form:

$$V(\phi) = \mu^2\phi^\dagger\phi + \lambda(\phi^\dagger\phi)^2 \tag{2.26}$$

For $\mu^2 < 0, \lambda > 0$ it has minima for all those values of ϕ_1, ϕ_2, ϕ_3 and ϕ_4 satisfying $|\phi| = \sqrt{\phi^\dagger\phi} = \sqrt{-\mu^2/2\lambda}$ and by expanding $\phi(x)$ around a particular minimum ϕ_0 that could be

$\phi_1 = \phi_2 = \phi_4 = 0$ and $\phi_3 = -\mu^2/\lambda = v^2$, from which it follows that $\phi_0 = \sqrt{\frac{1}{2}} \begin{pmatrix} 0 \\ v \end{pmatrix}$, the $SU(2)$ symmetry is broken. The infinitesimal transformation around ϕ_0 is now:

$$\phi(x) = \sqrt{\frac{1}{2}} \begin{pmatrix} 0 \\ v + h(x) \end{pmatrix} \tag{2.27}$$

which can be substitued in the lagrangian giving a new one which is locally $SU(2)$ invariant and which describes only three massive gauge fields $W_\mu^1, W_\mu^2, W_\mu^3$ and one massive scalar h. This calculation concludes the $SU(2)$ local symmetry breaking section. The $U(1)$ and the $SU(2)$ local gauge theories, which are renormalizable, are the ingredient for the construction of the Standard Model of electroweak interactions.

2.4. The Glashow-Weinberg-Salam Standard Model for the electroweak interaction

The Standard Model for weak and electromagnetic interactions is a renormalizable gauge theory, $U(1) \times SU(2)$, constitued by the two groups, each with an independent coupling strength. In this sense one cannot really talk about "unification" of electromagnetic and weak interactions. This model contains four gauge bosons: one is massless, the photon (γ), the other three (Z, W^+, W^-), are massive. The masses of the gauge fields, as well as of all the fermions of the Standard Model, are generated by spontaneous symmetry breaking of local gauge symmetry, even if their numerical value is not predicted.
To express the interaction terms of the electroweak lagrangian, one can consider the parallel with the QED interaction between electromagnetic current $(j^{em})^\mu$ with a photon field A^μ, which has the form $-ie(j^{em})^\mu A_\mu$ and write the term $-ig(J^i)^\mu W_\mu^i - ig'/2(j^Y)^\mu B_\mu, i = 1, 2, 3$ as the basic term for the electroweak interaction. Here the weak isospin current J^i is coupled, with strength g, to the three vector fields W_μ^i and the weak hypercharge current y^Y is coupled with strength $g'/2$ to the single vector field B_μ. The fields W_μ^i define the massive charged bosons $W_\mu^\pm$:

$$W_\mu^\pm = \sqrt{\frac{1}{2}}(W_\mu^1 \mp iW_\mu^2) \tag{2.28}$$

and W_μ^3 and B_μ mix each other to give the mass eigenstates of the neutral fields, that is the physical states A_μ (photon) and Z_μ (Z):

$$\begin{aligned} A_\mu &= B_\mu \cos\vartheta_W + W_\mu^3 \sin\vartheta_W \qquad [\gamma] \\ Z_\mu &= -B_\mu \sin\vartheta_W + W_\mu^3 \cos\vartheta_W \qquad [Z] \end{aligned}$$

where ϑ_W is the Weinberg weak mixing angle, which satisfies:

$$g \sin\vartheta_W = g' \cos\vartheta_W = e \tag{2.29}$$

and is such that:

$$\cos\vartheta_W = \frac{M_W}{M_Z} \tag{2.30}$$

In 1983 the $W^{\pm}$'s and the Z bosons have been discovered at the CERN $p\bar{p}$ collider [19] in the reactions:

$$\begin{aligned} p\bar{p} &\rightarrow W^{\pm}X \rightarrow (e^{\pm}\nu)X \\ p\bar{p} &\rightarrow Z\,X \rightarrow (e^{+}e^{-})X \end{aligned}$$

from which the mass determination has been $M_W = (81 \pm 2)$ GeV/c^2 and $M_Z = (93 \pm 2)$ GeV/c^2. The value of the ratio between these mass values is in excellent agreement, according to the relation of Equation (2.30), with the measurements of the Weinberg angle. Since then, these mass values have been largely confirmed and the measurements are much more precise, being actually $M_W = (80.42 \pm 0.06)$ GeV/c^2 and $M_Z = (91.188 \pm 0.002)$ GeV/c^2 [16].

2.5. Beyond the Standard Model

Today the Glashow-Weinberg-Salam theory accurately describes electroweak phenomena, while Quantum Chromo-Dynamics is accepted as the theory of the strong interactions. Ten years of precision measurements of electroweak observables at LEP, SLC and the Tevatron have failed to find any fundamental departures from Standard Model predictions. In some cases, theoretical predictions have been checked with an accuracy of one part in a thousand or better. The global analysis of electroweak observables provides a superb fit to the predictions of this model, which is based on the $SU(3) \times SU(2) \times U(1)$ gauge theory, but there is still no direct experimental evidence for the underlying dynamics responsible for the electroweak symmetry breaking, the spin zero Higgs boson, whose mass, as the mass of the other particles, is not predicted by the model. The minimal model contains 19 arbitrary parameters [5] [23], too many for a fundamental theory which should be simple and elegant and should have predictability. The parameters are:

- three gauge couplings for the three gauge groups g_s, g' and g. Usually they are expressed through other measured variables:
  - $\alpha_s = \frac{g_s^2}{4\pi}$
  - $\sin\vartheta_W = \frac{g'}{\sqrt{g^2+g'^2}}$
  - $\alpha = \frac{e^2}{4\pi} \sim (1/137), e = g\sin\vartheta_W$

  where ϑ_W is the Weinberg angle and α is the fine structure constant
- M_W, the mass of the weak bosons $W^{\pm}$, or the Fermi constant G_F; at the lowest order of the perturbative theory these two quantities are correlated by the expression:

$$\frac{g^2}{8M_W^2} = \frac{1}{\sqrt{2}}G_F \tag{2.31}$$

[5] Here the assumption is that there are no right-handed neutrinos and that there is no strong CP violation.

- two parameters representing the Higgs sector, even in the absence of fermions
- nine masses for the six quarks (u, d, c, s, t, b) and the three charged leptons (e, μ, τ) of the three generations. The nine mass values are spread over at least five orders of magnitude
- three generalized Cabibbo angles and one Kobayashi-Maskawa phase for the quark sector.

These parameters are not predicted by the model, and many questions cannot be answered by this theory, like the origin and pattern of particle masses, the number of families, the quantization of the electric charge, the number of colours. The Standard Model is clearly a very good description of the physics of elementary particles and their interactions at an energy scale of $\mathcal{O}(100)$ GeV/c^2 and below. The actual belief is that it is a low-energy approximation of a fundamental theory. Theories going beyond the Standard Model should give a solution to all these problems and provide the formalism to answer fundamental questions like the unification of strong, electroweak and gravitational interactions (the Grand Unifid Theories, GUT's), and the consequent hierarchy problem, which emerges from the introduction of new energy scales, the GUT scale ($M_{GUT} \sim 10^{17}$ GeV/c^2) or the Planck scale ($M_P \sim 10^{19}$ GeV/c^2), at which electroweak and strong interactions or all four interactions should have, respectively, the same strength.

2.6. Unification theories and the hierarchy problem

The fact that strong, weak and electromagnetic interactions appear to be well described by gauge theories offers the prospect that perhaps all three can be understood as somehow different aspects of a single gauge theory. Partial unification of weak and electromagnetic interactions has been achieved in the Glashow-Salam-Weinberg theory, in which there are still two independent gauge coupling constants. It is natural to try to include the strong interaction as well in a grand unified scheme. Interactions can be in reality very similar, but the similarity can be hidden by the phenomenon of spontaneous symmetry breaking, as is the case for the $SU(2) \times U(1)$ symmetry, which only becomes apparent at mass scales $\gg \mathrm{M_W}, \mathrm{M_Z}$. An unified theory (Grand Unified Theory [24]) of all three interactions would involve only one gauge coupling constant, which would imply, at some energy, that all three interactions should have the same strength. Since the couplings are very different at a scale of approximately 10^2 GeV/c^2, and since they vary logarithmically with energy, this unification scale is very large: $M_{GUT} \sim 10^{17}$ GeV/c^2. Given the large uncertainty in this scale, the question arises as to whether gravity, whose effects should come into play at the Planck mass $M_P \sim 10^{19}$ GeV/c^2 can indeed be neglected.

In a world in which the different interactions have the same intrinsic strength, quarks and leptons become indistinguishable, because what differentiates the one from the other is that quarks undergo strong interaction and leptons do not. For this reason grand unified theories allow transitions between quarks and leptons.
In this framework, strong, weak and electromagnetic interactions are described by a single gauge group G, big enough to contain the $SU(3)$ and $SU(2) \times U(1)$ groups as subgroups.

This gauge group G will have an unique gauge constant g_G and will be able to describe all the interactions. The requirement that G contains electromagnetism means that the photon must be one of the gauge bosons of G. Hence, the electric charge operator Q_{ch} must be one of the generators of G. Since all generators are represented by traceless matrices, $\mathrm{Tr}(Q_{ch})=0$, that means the sum of the electric charges of all particles in a given representation vanishes. This requirement is satisfied by the members of each fermion family, and thus gives a relationship between the charges of quarks and leptons. This is not the case if leptons and quarks are considered separately, so G must contain bosons which can transform leptons to quarks and vice versa. Hence, non-conservation of both baryon and lepton numbers B and L is possible, and the proton decay is allowed. The smallest group with the required properties is SU(5), first considered by Georgi and Glashow in 1974 [25]. Together with the vector bosons of electroweak and strong interactions, the model introduces 12 other gauge bosons, indicated with X and Y, with fractionary charge $Q_X = \pm 4/3$ and $Q_Y = \pm 1/3$ and with very high masses of the order or higher than $2 \times 10^{14} \sim 10^{15}$ GeV/c^2, which is the energy scale at which the symmetry breaking from SU(5) to $SU(3) \times SU(2) \times U(1)$ happens. They mediate the interactions which violate the conservation of B, in particular allowing the proton decay which must be very slow to maintain its lifetime higher than the actual limits. These superheavy particles are leptoquark-like, if by leptoquark one means every boson which couples both to quarks and to leptons.

The SU(5) theory is an elegant model, but its predictions, when extrapolated to the energy scales where the Standard Model works, are not completely in agreement with the experimental results. Moreover, it doesn't give a solution to the so called hierarchy problem. The hierarchy problem comes from the difficulty in field theory in keeping the observed states light in presence of new physics at very large mass scale. In GUTs there are at least two stages of spontaneous symmetry breaking: one that provides the grand unification scale, $M_{GUT} \sim 10^{17}$ GeV/c^2, and one that gives the electroweak unification scale, $M_W \sim 10^2$ GeV/c^2. What seems very striking is the big difference between the two scales:

$$M_W/M_{GUT} \sim 10^{-15} \tag{2.32}$$

because such a disparity in scales is very difficult first to be produced and then to be maintained in field theories. The spontaneous symmetry breaking occurs thanks to the Higgs mechanism, but then the scale at which that happens is more or less the same to the mass of the Higgs particle. This mass gets radiative corrections which are quadratically divergent requiring a cut-off Λ which gives $m_H^2 = 2\mu^2 + c\Lambda^2$, where μ^2 is the vacuum expectation value of the Higgs potential $V_H = -\mu^2\phi^\dagger\phi$ and c is a constant. The cut-off represents the scale where new physics occurs. If the Standard Model would be valid all the way up to the GUT scale without any intervening new physics, then Λ would be equal to M_{GUT}. In this case the electroweak scale would be driven to the GUT scale, which is obviously wrong. On the other hand, fixing the electroweak scale at its real order of magnitude, one could arrange the Higgs mass in the electroweak region by a cancellation between the μ^2 and the Λ^2 terms. However, this requires a fine tuning to 22 decimal places, which is unnatural. This is a very strong theoretical hint for the existence of new physics beyond the Standard Model and simple GUTs models, like SU(5), cannot solve it. A way to avoid the hierarchy problem is either by using a theory in which there are no point-like couplings to fundamental scalars, like composite models such as technicolor, or by

cancelling the divergence directly with additional particles, as is the case for supersymmetry. Technicolor [26] is a model of electroweak symmetry breaking based on the postulate of new strong interactions at the electroweak scale. It has been introduced to explore the possibility that some, or all, of the elementary particles supposed as such today in the Standard Model may be composite. Supersymmetry [27] represents the best motivated known extension of the Standard Model, offering an elegant solution to the hierarchy problem, being consistent with present experimental data and predicting new particles to be discovered in the current generation of collider experiments. In its minimal form, each Standard Model particle has one supersymmetric partner: the partners of the gauge bosons (gauginos) have spin 1/2, the partners of the fermions (sfermions) have spin 0 and the partners of the Higgs fields (higgsinos) have spin 1/2. This theory involves transformations changing fermions to bosons and vice versa. In supersymmetry the hierarchy problem is solved because there are no quadratic divergences in the theory, and this occurs via cancellations in the Feynman diagrams which are insured by requiring the presence of the supersymmetric partners to the ordinary particles. This solution predicts that new physical phenomena must exist at a scale of the order $\mathcal{O}(1$ TeV) or below. In the case of supersymmetry, this new physics consists of a spectrum of new supersymmetric particles which have masses not greater than about 1 TeV/c^2 and in some cases may be substantially lighter.

In the context of supersymmetry, the relevant symmetry is a continuous global symmetry called R-symmetry, which leads to a multiplicative quantum number called R-parity. All ordinary particles are assigned an R-parity of +1, whereas the supersymmetric partners have an R-parity equal to -1. Formally, the R-parity of any particle with spin j, baryon number B and lepton number L is $R = (-1)^{3B+L+2j}$. If R-parity is conserved, the consequences are first that supersymmetric particles must be produced in pairs, since in laboratory experiments the initial state contains no supersymmetric particles the final state must contain an even number of such particles; second, there must be a stable lightest supersymmetric particle, which cannot decay into only non-supersymmetric particles. In case of supersymmetry with R-parity violation the theory assumes particular significance in view of the particles which will be treated in the following: in fact the R-parity violation would allow the squarks to have leptoquark-like interactions.

2.7. Hypothesis for a new particle: the leptoquark

A common feature of theoretical models trying to imagine possible scenarios for new physics is the symmetry between quarks and leptons suggested by the Standard Model, and the search of a more fundamental relation between them. Theories like the grand unification or R-parity violating supersymmetric models introduce the idea of quark to lepton transitions: whenever quarks and leptons are allowed to couple directly to each other, particles which carry both lepton and baryon quantum numbers can also exist, with unknown λ coupling to lepton and quark, that are called leptoquarks, and which assume different forms according to the constraints of the model. So, for example, the superheavy X and Y gauge bosons of $SU(5)$ and the squarks in R-parity violating supersymmetry are leptoquark-like particles.

A general classification of leptoquark states is in the Buchmüller-Rückl-Wyler model [28], where leptoquarks are indicated as all the possible states coupling to quark and lepton

Model	F	Charge Q	β	Coupling	Squark
S_0^L	2	-1/3	0.5	$\lambda_L(e_L u)$, $-\lambda_L(\nu d)$	$\tilde{d}_R$
S_0^R	2	-1/3	1	$\lambda_R(e_R u)$	
$\tilde{S}_0$	2	-4/3	1	$\lambda_R(e_R d)$	
$S_{1/2}^L$	0	-5/3	1	$\lambda_L(e_L \bar{u})$	
		-2/3	0	$\lambda_L(\nu \bar{u})$	
$S_{1/2}^R$	0	-5/3	1	$\lambda_R(e_R \bar{u})$	
		-2/3	1	$-\lambda_R(e_R \bar{d})$	
$\tilde{S}_{1/2}$	0	-2/3	1	$\lambda_L(e_L \bar{d})$	$\tilde{\bar{u}}_L$
		+1/3	0	$\lambda_L(\nu \bar{d})$	$\tilde{\bar{d}}_L$
S_1	2	-4/3	1	$-\sqrt{2}\lambda_L(e_L d)$	
		-1/3	0.5	$-\lambda_L(e_L u)$, $-\lambda_L(\nu d)$	
		+2/3	0	$\sqrt{2}\lambda_L(\nu u)$	
$V_\circ^L$	0	-2/3	0.5	$\lambda_L(e_L d)$, $\lambda_L(\nu \bar{u})$	
$V_\circ^R$	0	-2/3	1	$\lambda_R(e_R \bar{d})$	
$\tilde{V}_\circ$	0	-5/3	1	$\lambda_R(e_R \bar{u})$	
$V_{1/2}^L$	2	-4/3	1	$\lambda_L(e_L d)$	
		-1/3	0	$\lambda_L(\nu d)$	
$V_{1/2}^R$	2	-4/3	1	$\lambda_R(e_R d)$	
		-1/3	1	$\lambda_R(e_R u)$	
$\tilde{V}_{1/2}$	2	-1/3	1	$\lambda_L(e_L u)$	
		+2/3	0	$\lambda_L(\nu u)$	
V_1	0	-5/3	1	$\sqrt{2}\lambda_L(e_L \bar{u})$	
		-2/3	0.5	$-\lambda_L(e_L \bar{d})$, $\lambda_L(\nu \bar{u})$	
		+1/3	0	$\sqrt{2}\lambda_L(\nu \bar{d})$	

Table 2.3: *A general classification of leptoquark states in the Buchmüller-Rückl-Wyler model [28]. This table implies charge conjugation symmetry, as well as the global replacement of first-generation particles with corresponding ones in second or third generation. Listed are the leptoquark fermion number F (see the text for definitions), the electric charge Q, in units of elementary charges, the branching ratio β to electron-quark, or electron-antiquark, and the lepton-quark couplings. Also shown are possible squark assignements to the leptoquark states in the minimal supersymmetric theories with broken R-parity.*

in different models as listed in Table (2.3), carrying both lepton and baryon numbers, and which are colour triplet bosons with spin 0 or 1 and have fractionary charge. There are fourteen different models allowed, seven for scalar (spin=0) and seven for vector (spin=1) leptoquarks. All these models are, however, based on new interactions which should respect the $SU(3) \times SU(2) \times U(1)$ symmetry of the Standard Model. In the table the S (V) denotes a scalar (vector) leptoquark, and the subscript denotes the weak isospin. The superscript indicates whether the leptoquark couples to left-handed (L) or right-handed (R) leptons, and a tilde differentiates between leptoquarks that differ by two units of hypercharge [6]. The fermion number is defined as F=L + 3B, where L is the lepton number (L=+1 for electrons) and B is the baryon number (B=+1/3 for quarks). The electric charge Q is indicated in units of electron charge and λ is the unknown leptoquark coupling to the quark and lepton. It is assumed to be chiral to take into account of very strong bounds from rare decays like $\pi \rightarrow e\nu_e$, from which follows that leptoquarks with masses of order of 100 $\mathrm{GeV/c^2}$ can have sizeable couplings only to either left- or right-handed leptons. An important assumption in this models is that the coupling conserves separately both baryon and lepton numbers: the consequence is that leptoquarks can be light, with leptoquark mass $\mathrm{M_{LQ}} \sim \mathcal{O}(\mathrm{M_W})$, still avoiding conflicts with rapid proton decay, and family diagonal, that is the leptoquarks couple only to one generation, to exclude flavour changing neutral currents. This last assumption gives rise to the classification in first, second or third generation. This table implies charge conjugation symmetry, as well as the global replacement of first-generation particles with the corresponding ones in second or third generation.

The model gives the conditions which induce the couplings to the gauge bosons of the Standard Model, that enter in the calculation of the production cross section: for example in the case of direct leptoquark production at hadron colliders (see the diagrams in Figures (2.3) and (2.4)) the bosonic couplings of scalar leptoquarks with gluons are assumed to be the ordinary strong coupling. As a consequence, in the case of scalar leptoquarks the production cross section is completely predicted, whereas in the case of vector leptoquarks the ordinary Yang-Mills couplings may be supplemented by anomalous couplings. These latters appear to take into account the hypothesis that vector leptoquarks with mass M_V could be some low energy manifestation of a more fundamental theory at a higher scale and that these particles may even be composite. Two possible anomalous couplings are usually described in the literature by the parameters k_A and λ_A, with $\mathrm{A} = \gamma, \mathrm{g}, \mathrm{W}^{\pm}$ and Z. Since the bosonic couplings of leptoquarks produced at hadron colliders is with gluons, only the couplings $\mathrm{K_G}$ and λ_G between vector leptoquark and gluon field are involved. The two anomalous couplings are real parameters and are related to the anomalous magnetic moment μ_V and to the electric quadrupole moment q_V of the leptoquarks in the color field like [29]:

$$\begin{aligned} \mu_{V,G} &= \frac{\alpha_s}{2M_V}(2 - k_G + \lambda_G) \\ q_{V,G} &= -\frac{\alpha_s}{M_V^2}(1 - k_G - \lambda_G) \end{aligned}$$

[6] The hypercharge Y is the combination of baryon number B and strangeness S of the quark. Each quark has B=+1/3, while S = -1 for the quark s, +1 for the quark $\bar{s}$, and 0 for the other quarks. Y is defined as equal to B+S

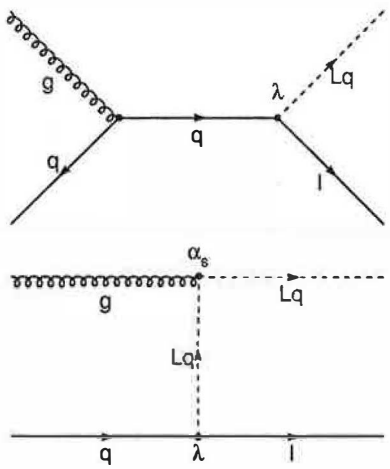

Figure 2.3: *Feynman diagrams for single production of leptoquark at hadron colliders.*

There are no direct bounds on the parameters λ_G and K_G, on which the hadronic production cross section results are strongly dependent. Usually the theoretical production cross sections to which one compares the experimental results are those calculated with Yang-Mills type couplings, $k_G = \lambda_G = 0$, and with minimal vector couplings, $k_G = 1, \lambda_G = 0$.

2.7.1. Leptoquarks production at Tevatron

If baryon and lepton numbers are assumed to be separately conserved, leptoquarks may exist with a mass accessible to present colliders. At the Tevatron, where the available center of mass energy $\sqrt{s}$ is very high, leptoquarks can be produced directly, singly or in pairs: in Figures (2.3) and (2.4) are shown the leading order Feynman diagrams. In the case of the single production processes the cross sections are proportional to λ^2, where λ is the coupling between leptoquark, lepton and quark which is present in each diagram, and amount to 0.4 to 1.3 fb at Tevatron energies for fermionic couplings of the order $(\lambda/e)\sqrt{\beta} \sim 0.075$ [30], where $\beta = Br(Lq \to eq)$, and are too small to be detected currently.

The pair production has the advantage that its cross section is almost independent on the λ fermionic coupling, depending only on the strong coupling, therefore it is calculable [30]. The processes responsable for pair production are quark-antiquark annihilation and gluon-gluon fusion (see Figure (2.4)). Only the lepton exchange process depends on λ, but if one takes for λ the electromagnetic coupling strength, then its contribution will be only about 1% of the total cross section. The hadronic production cross section can be calculated starting from the effective Lagrangian density describing the interaction of the scalar and vector leptoquarks with gluons:

$$\mathcal{L} = \mathcal{L}_S^g + \mathcal{L}_V^g \tag{2.33}$$

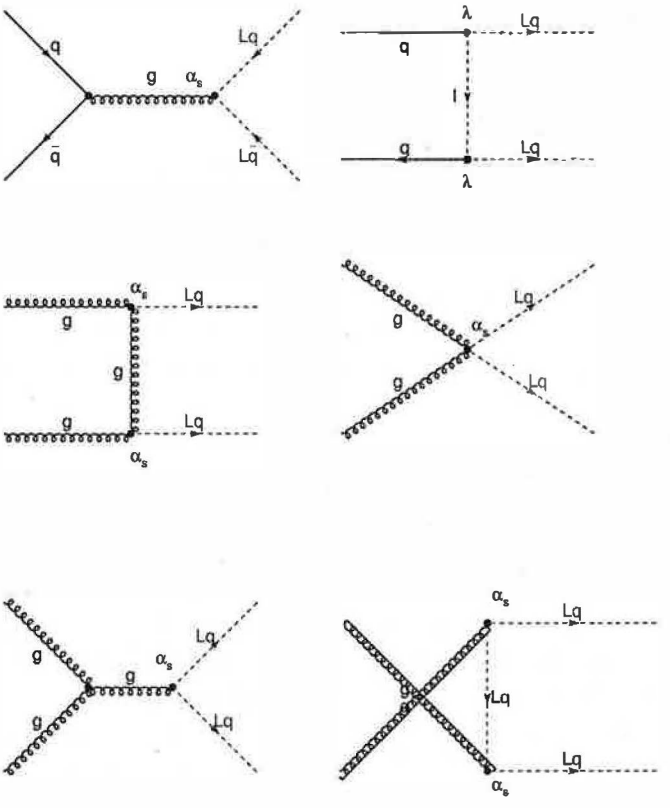

Figure 2.4: *Feynman diagrams for pair production of leptoquarks at hadron colliders.*

where

$$\begin{aligned}
\mathcal{L}_S^g &= \sum_{scalars} (D_{ij}^{\mu}\Phi^j)^{\dagger}(D_{\mu}^{ik}\Phi_k) - \mathrm{M}_{\mathrm{S1}}^2\Phi^{\mathrm{i}\dagger}\Phi_{\mathrm{i}} \\
\mathcal{L}_V^g &= \sum_{vectors} -\frac{1}{2}G_{\mu\nu}^{i\dagger}G_i^{\mu\nu} + \mathrm{M}_{\mathrm{V1}}^2\Phi_{\mu}^{\mathrm{i}\dagger}\Phi_{\mathrm{i}}^{\mu} \\
&\quad -ig_s((1-k_G)\Phi_{\mu}^{i\dagger}t_{ij}^a\Phi_{\nu}^j\mathcal{G}_a^{\mu\nu} + \frac{\lambda_G}{\mathrm{M}_{\mathrm{V1}}^2}G_{\sigma\mu}^{i\dagger}t_{ij}^aG_{\nu}^{j\mu}\mathcal{G}_a^{\nu\sigma})
\end{aligned}$$

Here, g_s is the strong coupling constant, t^a are the generators of $SU(3)_c$, M_{S1} and M_{V1} are the scalar and vector leptoquark masses and k_G and λ_G are the anomalous couplings. The field strength tensors of the gluon and vector leptoquark fields are:

$$\begin{aligned}
\mathcal{G}_{\mu\nu}^a &= \partial_{\mu}\mathcal{A}_{\nu}^a - \partial_{\nu}\mathcal{A}_{\mu}^a + g_s f^{abc}\mathcal{A}_{\mu b}\mathcal{A}_{\nu c} \\
G_{\mu\nu}^i &= D_{\mu}^{ik}\Phi_{\nu k} - D_{\nu}^{ik}\Phi_{\mu k}
\end{aligned}$$

where the covariant derivative is given by:

$$D_{\mu}^{ij} = \partial_{\mu}\delta^{ij} - ig_s t_a^{ij}\mathcal{A}_{\mu}^a$$

The total hadronic production cross section for leptoquark pair production in $p\bar{p}$ collisions can be expressed as in [30]:

$$\sigma(p\bar{p} \to Lq\bar{L}q + X) = \int_0^1\int_0^1 dx_a dx_b F_i^{(a)}(x_a,\mu^2)F_j^{(b)}(x_b,\mu^2)\sigma^{ij}(s)\Theta(s - 4\mathrm{M}_{\mathrm{LQ}}^2)$$

where F_i and F_j are the parton densities convoluted with the corresponding cross sections σ^{ij}, Θ is the delta function for the energy conservation and μ is the factorization scale. The leading-order (LO) differential and integral cross section for pair produced scalar leptoquarks from quark-antiquark annihilation can be parametrized as follows as a function of the leptoquark mass M_{S1} [30] [31]:

$$\begin{aligned}
\frac{d\sigma_{S\bar{S}}^{q\bar{q}}}{d\cos\vartheta} &= \frac{\pi\alpha_s^2}{18\hat{s}}\beta^3\sin^2\vartheta \\
\sigma_{LO}^{scalar}(q\bar{q}) &= \frac{2\pi\alpha_s^2}{27\hat{s}}\beta^3
\end{aligned}$$

and from gluon fusion:

$$\begin{aligned}
\frac{d\sigma_{S\bar{S}}^{gg}}{d\cos\vartheta} &= \frac{\pi\alpha_s^2}{6\hat{s}}\beta\frac{1}{32}(25 + 9\beta^2\cos^2\vartheta - 18\beta^2) - \frac{1}{16}\frac{(25 - 34\beta^2 + 9\beta^4)}{1 - \beta^2\cos^2\vartheta} + \frac{(1-\beta^2)^2}{(1-\beta^2\cos^2\vartheta)^2} \\
\sigma_{LO}^{scalar}(gg) &= \frac{\pi\alpha_s^2}{96\hat{s}}(\beta(41 - 31\beta^2) + (18\beta^2 - \beta^4 - 17)\log\frac{1+\beta}{1-\beta})
\end{aligned}$$

where $\hat{s}$ is the squared of the center of mass system energy of the process, $\beta = (1 - 4\mathrm{M}_{\mathrm{S1}}^2/\hat{s})$ is the speed of the produced leptoquarks in their center of mass system, $\alpha_s = g_s^2/4\pi$ and ϑ the leptoquark scattering angle in the parton-parton center of mass system. All quark flavours are supposed to be massless. For vector leptoquarks the production cross sections

depend also on the values of the anomalous couplings k_G and λ_G. The differential cross section for quark-antiquark annihilation and gluon fusion respectively are given by [30] [31]:

$$\frac{d\sigma_{V\bar{V}}^{q\bar{q}}}{d\cos\vartheta} = \frac{2\pi\alpha_s^2}{9M_{V1}^2}\beta^3\sum_{i=0}^{5}\chi_i^q(k_G,\lambda_G)G_i(\hat{s},\beta,\cos\vartheta)$$

$$\frac{d\sigma_{V\bar{V}}^{gg}}{d\cos\vartheta} = \frac{\pi\alpha_s^2}{192\hat{s}}\beta\sum_{i=0}^{14}\chi_i^g(k_G,\lambda_G)\frac{F_i(\hat{s},\beta,\cos\vartheta)}{(1-\beta^2\cos^2\vartheta)^2}$$

where the functions χ_i^g, χ_i^q, F_i and G_i are given in [30]. The total cross section can be calculated in the case of anomalous couplings equal to zero as follows:

$$\sigma_{LO}(q\bar{q}\to V\bar{V}) = \frac{\alpha_s^2\pi}{27\hat{s}}\frac{\beta^3}{1-\beta^2}(23-3\beta^2+\frac{4}{1-\beta^2})$$

$$\sigma_{LO}(gg\to V\bar{V}) = \frac{\alpha_s^2\pi}{24\hat{s}}\frac{1}{1-\beta^2}(\beta(\frac{523}{4}-90\beta^2+\frac{93}{4}\beta^4) - \frac{3}{4}(65-83\beta^2+19\beta^4-\beta^6)\log\frac{1+\beta}{1-\beta})$$

The quark terms yield the largest contributions to the scalar leptoquark production cross section at the Tevatron in the mass range $M_{S1} > 100$ GeV/c^2. Also for the vector leptoquarks, even if there is a sizeable dependance of the cross section on the value of both the anomalous couplings k_G and λ_G, the quarks contributions dominate. In Figure (2.5) is shown the pair production cross section for scalar leptoquarks at the Tevatron from quark-antiquark annihilation and gluon gluon fusion [30]. For vector leptoquarks production, the pair production cross sections are shown in Figure (2.6), which depends on the anomalous couplings k_G and λ_G.

The production cross section in the vector case is higher than in the scalar case for the same mass value. In Figure (2.7) are plotted the leading order cross sections for single and pair production of scalar and vector leptoquarks: in the vector case are shown the values calculated assuming vanishing anomalous couplings of vector leptoquarks to gluons. More detailed calculations and plots can be found, for example, in [30], [31] and [32]. For a leptoquark mass of 200 GeV/c^2, $\sigma(p\bar{p}\to S\bar{S}) \sim 0.2$ pb and $\sigma(p\bar{p}\to V\bar{V}) \sim 10$ pb, and even if the anomalous couplings are chosen such as to minimize the cross section, the total rate for vector leptoquark pair production still remains a factor of two larger than that for scalar leptoquarks. For the leading order process the first generation scalar leptoquark pair production cross section is the same as the leading order cross section for squark-pair production in the infinite gluino mass limit $m_{\tilde{g}}\to\infty$ [33]. For finite values $m_{\tilde{g}} \leq 1$ TeV/c^2, t-channel gluino exchange significantly contributes to the partonic squark cross section: taking $m_{\tilde{g}} = m_{\tilde{q}} = 200$ GeV/c^2, the $\tilde{u},\tilde{d}$ pair production at the Tevatron is enhanced by almost an order of magnitude as compared to scalar leptoquark pair production. Indeed, for second and third generation scalar leptoquarks, the production cross sections for pair production is completely coincident with those of $\tilde{c},\tilde{b}$ and $\tilde{t}$.

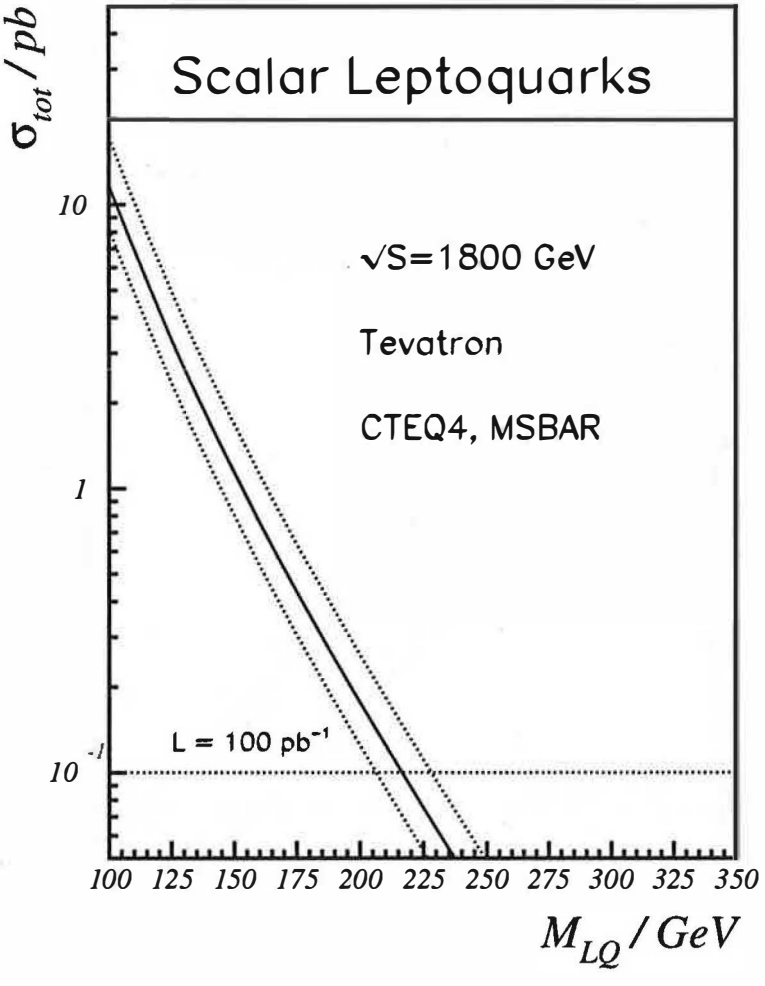

Figure 2.5: *Production cross section for pair-produced scalar leptoquarks at the run 1 energy of Tevatron. The full line represents the theoretical calculation for a renormalization and factorization scale* $\mu = \mathrm{M_{LQ}}$, *while the dotted lines contain the range of the scale variation* $\mu \in [\mathrm{M_{LQ}}/2, 2\mathrm{M_{LQ}}]$. *From [30].*

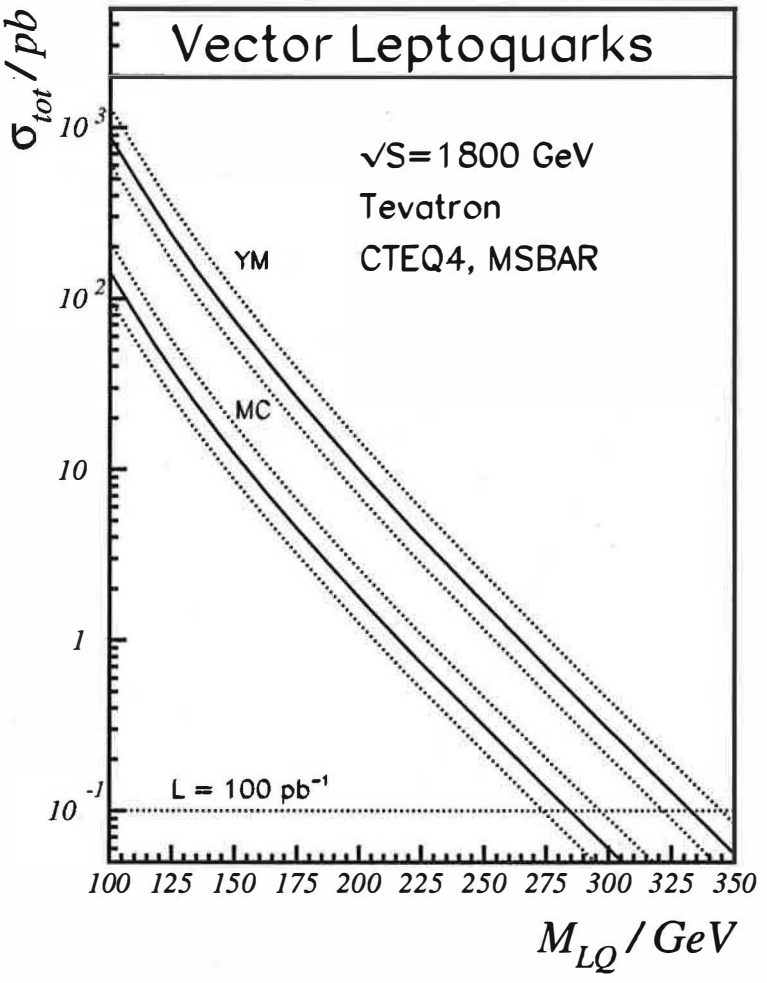

Figure 2.6: *Production cross sections for vector leptoquarks pair production at the Tevatron for the Yang-Mills type coupling (YM) and minimal coupling (MC) at 1.8 TeV. The full line represents the theoretical calculation for* $\mu = \mathrm{M_{LQ}}$*, while the dotted lines contain the range of the scale variation* $\mu \in [\mathrm{M_{LQ}}/2, 2\mathrm{M_{LQ}}]$*. From [30].*

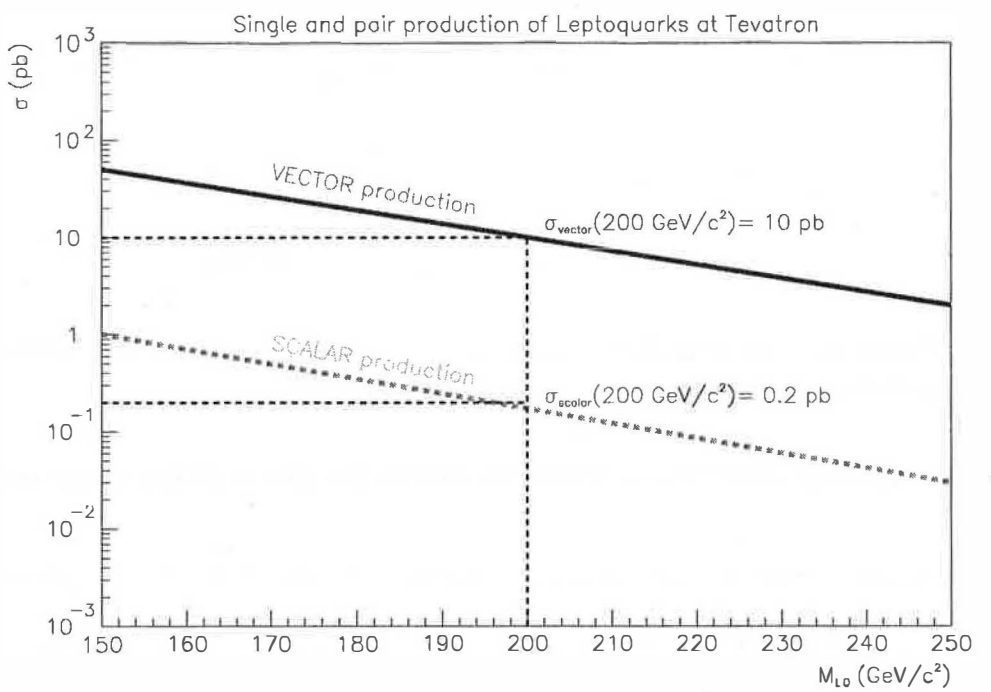

Figure 2.7: *Leading-order cross sections for single and pair production cross sections of scalar and vector leptoquarks at the Tevatron as a function of the leptoquark mass* M_{LQ} *[31]. The CTEQ4L [91] parton densities have been adopted and the renormalization and factorization scale has been set to* $\mu = M_{LQ}$.

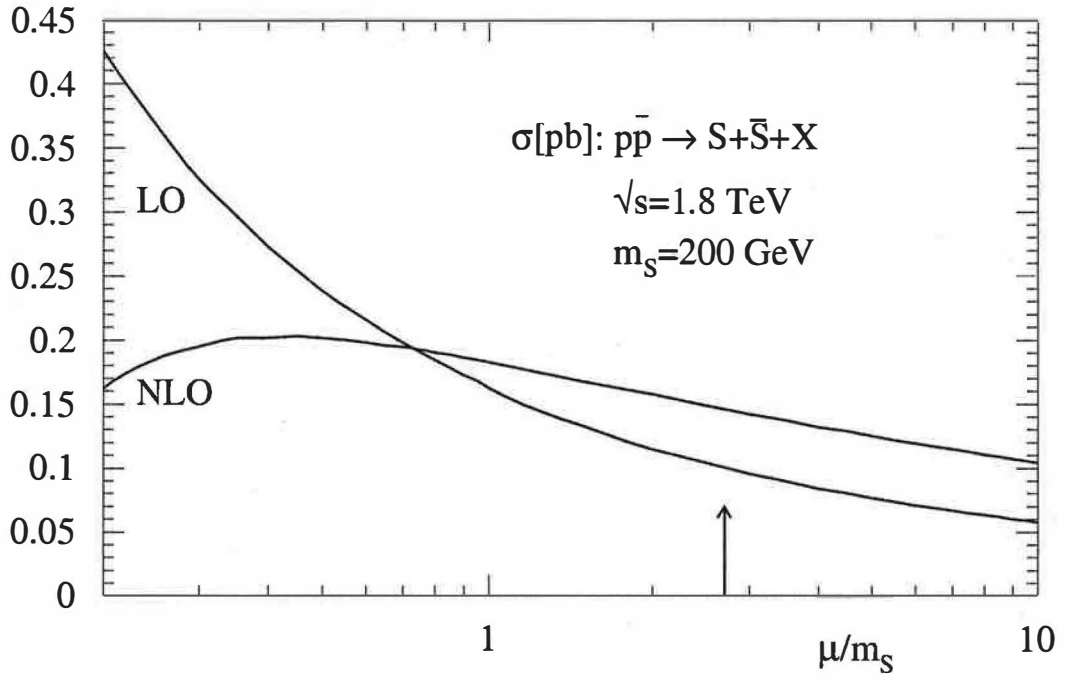

Figure 2.8: *Renormalization and factorization scale dependence of the cross section* $\sigma(p\bar{p} \to S\bar{S} + X)$ *at the Tevatron energy* $\sqrt{s} = 1.8\ TeV$. *From [31].*

2.7.2. Next-to-leading order corrections to the scalar production cross section

The vector leptoquark production cross sections are large, of the order of $\mathcal{O}(1-10)\ pb$, and this is the reason to consider the search of vector leptoquarks only marginal with respect to the search of the scalar leptoquarks. The most powerful competitor in the actual scenario of the high-energy colliders is thus pair production of scalar leptoquarks. The leading-order predictions on their production cross sections depend on the choice of the parton density function and on the parameters μ, the renormalization and factorization scale $\alpha_s(\mu)$ and $F(\mu)$. Changing scale from $\mu = 2M_{LQ}$ to $\mu = M_{LQ}/2$ changes the leading-order cross section by about 100%. These calculations have become inadequate for the Tevatron experiments to compete with other experiments, in particular after the anomaly observed in 1997 by H1 [34] and ZEUS [35] at HERA in deep-inelastic e^+p scattering at very large Q^2, which could be interpreted as the production of a narrow state of mass 200 GeV/c^2 with leptoquark couplings. To extract reliable mass limits from Tevatron data a NLO calculation has become important. The calculation has been performed in [31] and allows an improvement in the evaluation of the cross section, which becomes more independent from the factorization or renormalization scales, and is almost uniform in μ, as shown in Figure (2.8), where there is a comparison with the corresponding leading-order calculations. A variation from $\mu = 2M_{S1}$ to $\mu = M_{S1}/2$ in the next-to-leading order cross section gives a 30% variation, a considerable improvement in the stability of the theoretical prediction.

$M_{S1}(GeV/c^2)$		$\sigma_{q\bar{q}}$ (pb)	σ_{gg} (pb)	σ_{tot} (pb)	K
150	LO	0.741	0.244	0.985	
	NLO	0.722	0.490	1.184	1.20
200	LO	0.142	0.022	0.164	
	NLO	0.141	0.047	0.184	1.12
250	LO	0.030	0.003	0.033	
	NLO	0.030	0.006	0.035	1.08

Table 2.4: *Leading-order and next-to-leading order results for the total cross section* $p\bar{p} \to S + \bar{S} + X$ *at the Tevatron energy* $\sqrt{s} = 1.8$ *TeV for various values of the leptoquark mass* M_{S1}. *The quantities* $\alpha_s(Q^2)$, *the parton densities and the partonic cross sections have been calculated consistently in leading order and next-to-leading order, respectively. Also shown is the K factor defined as* $K = \sigma_{NLO}/\sigma_{LO}$. *From [31].*

Based on previous experience from the production of squarks pairs in hadron collisions [33], it is expected that higher-order QCD corrections increase the production cross section compared to the predictions at the Born level. Experimental mass bounds are therefore shifted upwards. The QCD radiative corrections to the order α_s include virtual corrections, the bremsstrahlung of gluons and contributions from gluon-quark collisions. The cross section at $p\bar{p}$ colliders is found by folding the parton cross sections σ_{ij} with the gluon and quark luminosities in $p\bar{p}$ collisions, where the σ_{ij} are defined as [31]:

$$\sigma_{ij}(s, M_{S1}^2) = \frac{\alpha_s^2(\mu^2)}{M_{S1}^2}[f_{ij}^{(0)}(\eta) + 4\pi\alpha_s(\mu^2) f_{ij}^{(1)}(\eta, r_t) + \bar{f}_{ij}^{(1)}(\eta) \ln(\frac{\mu^2}{M_{S1}^2})] \qquad (2.34)$$

with $i, j = g, q, \bar{q}$ denoting the initial-state partons. The scaling functions f's depend on the invariant parton energy $\sqrt{s}$ through $\eta = s/4M_{S1}^2 - 1$ and, very mildly, on the ratio of the particle masses $r_t = m_{top}/M_{S1}$.

Some values of the cross section are listed in Table (2.4), where is also reported the corresponding value of the K-factor, defined as $K = \sigma_{NLO}/\sigma_{LO}$, with all quantities calculated consistently in next-to-leading order and leading-order respectively. The impact of the next-to-leading order QCD corrections on the present experimental lower mass limits for scalar leptoquarks is illustrated in Figure (2.9). In the plot are compared the results for next-to-leading order calculations, done using the CTEQ4M [91] parton density function and setting $\mu = M_{S1}$ with those for the leading-order cross section used in the earlier analyses, to show how these new calculations can improve the limits on leptoquark mass. They can increase by about 15 GeV/c^2. The shaded band in the plot represents the remaining theoretical uncertainty at next-to-leading order due to the choice of the renormalization and factorization scale when μ changes in the range of values $M_{S1}/2 \leq \mu \leq 2M_{S1}$. In the interesting mass region $M_{S1} \geq 150$ GeV/c^2 the cross section is dominated by quark-antiquark contribution, for which the variation between different parton density functions is less than 5%.

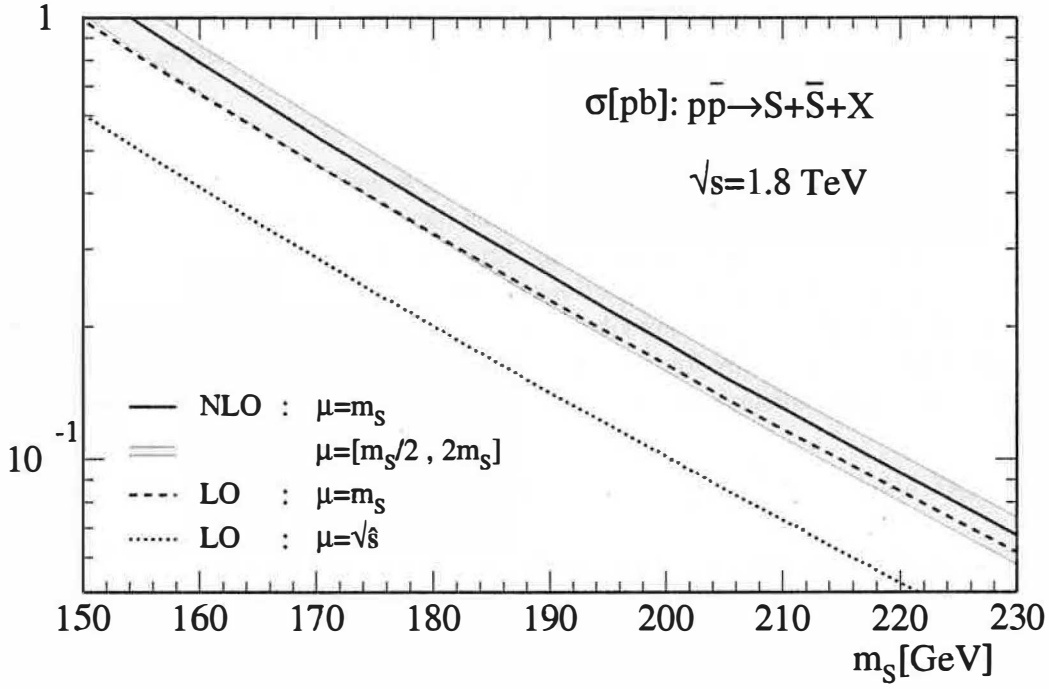

Figure 2.9: *The cross section for the production of scalar leptoquark pairs at the Tevatron energy* $\sqrt{s}$ = 1.8 *TeV as a function of the leptoquark mass* M_{LQ}. *The NLO result is compared with the LO calculations. The shaded band indicates the variation of the NLO cross section with the value of the renormalization and factorization scale. The CTEQ4 [91] parton densities are used. From [31].*

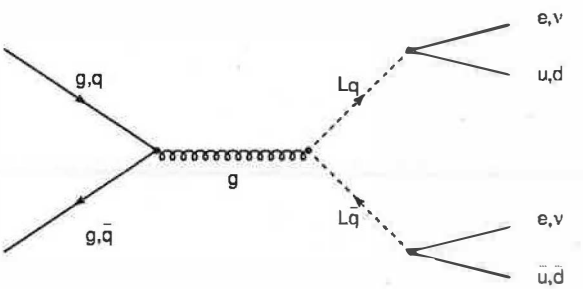

Figure 2.10: *Decay of first generation leptoquarks produced, at Tevatron, by quark-antiquark annihilation or gluon fusion.*

2.7.3. Experimental signatures

There are three possible final states in the decay of pairs of leptoquarks, since each leptoquark can decay into a lepton and a quark: $\ell\ell$ + jets, $\ell\nu$ + jets and $\nu\nu$ + jets, where ℓ is a charged lepton and ν is its associated neutrino. If β is the decay branching fraction of a leptoquark to a charged lepton, $\beta = Br(Lq \rightarrow \ell q)$, the three final states appear with rates proportional to $\beta^2, 2\beta(1-\beta)$ and $(1-\beta)^2$, respectively.

The searches performed in this thesis are for pair produced, first generation scalar and vector leptoquarks, decaying into the final states $e\nu jj$ or $eejj$, as sketched in the plot of Figure (2.10). Final states for scalar leptoquark pairs and vector leptoquark pairs are identical and the experimental acceptance is similar. The interesting events to be selected in this analysis are characterized by one or two high energy, isolated electrons, two high energy jets and eventually, for the decay channel with the neutrino, by a considerable amount of missing transverse energy.

2.7.4. Current limits

Many results on first generation leptoquark searches have been published during the last few years, in particular after 1997, when the H1 [34] and ZEUS [35] experiments at the HERA accelerator at DESY reported an excess of events with large squared momentum transfer Q^2 in deep inelastic neutral current and charged current electron-proton scattering compared to QCD expectations. The plot of the cross sections for $Q^2 > Q^2_{min}$ versus Q^2_{min} found at HERA is shown in Figure (2.11) [46], where there is evidence of an excess of events with respect to the Standard Model predictions in high Q^2 events. One possible explanation for these events was the production of first generation scalar leptoquarks with masses of about 200 GeV/c^2 for $\beta = 1$.
This hypothesis was quickly rejected after the results of prompt CDF and DØ searches

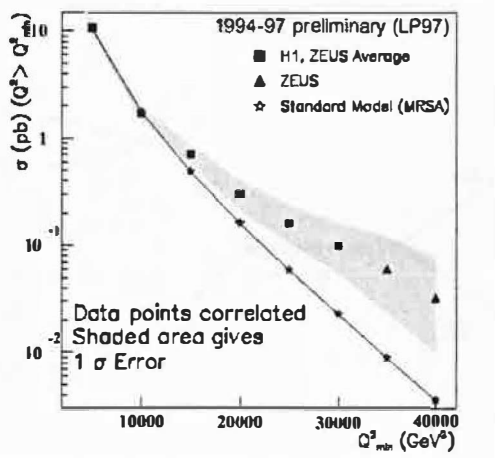

Figure 2.11: *Cross sections for $Q^2 > Q^2_{min}$ with $Q^2_{min} > 5000\ GeV^2$ in neutral current events in e^+p collisions with the HERA accelerator at DESY [46]. Shown are the combined ZEUS and H1 results (squares) and the corresponding one-sigma error band (shaded region). The triangles in the domain $Q^2 \geq 35000\ GeV^2$ are the ZEUS cross sections and contain no averaging with the zero events observed by H1 in this region.*

for possible signals in dielectron plus jets events: CDF searched for first generation scalar leptoquarks in the $eejj$ channel and obtained a lower limit at 95% confidence level on M_{S1} at 213 GeV/c^2 for $\beta = 1$ [36], [37], while DØ searched for first generation scalar leptoquarks in all three decay channels and obtained for M_{S1} limits at 225 GeV/c^2 in the $eejj$ channel for $\beta = 1$ [38], at 175 GeV/c^2 in the $e\nu jj$ channel for $\beta = 0.5$ and at 204 GeV/c^2 by combining limits from the $eejj$, $e\nu jj$ and $\nu\nu jj$ decay channels for $\beta = 0.5$ [41] . DØ set also the limit for $\beta = 0$ at 79 GeV/c^2 [40] by combining the results of all channels. These are the most recent results of DØ up to date. The combination of the three channels performed by DØ, in terms of limits on M_{S1} as a function of β, is illustrated in Figure (2.12) for the single channels and for their combination. After the publication of the respective results, the two Tevatron experiments combined their limits in the $eejj$ channel for $\beta = 1$ and obtained a limit at 242 GeV/c^2 [39], which is the most stringent limit on M_{S1} to date.
All the most recent results of scalar searches published by CDF and DØ are summarized in Table (2.5). DØ has recently published the results of the searches for vector leptoquarks as well [41], whose mass limits are listed in Table (2.6) and illustrated in Figure(2.13).

All these results certainly disclaimed the hypothesis of the HERA experiments about leptoquark states observation. In the meantime H1 and ZEUS data samples have almost doubled and a very good agreement between measured and expected cross section is generally observed. The excess has not been corroborated by the new data but is still present in the combined data samples. The HERA experiments, having found no evidence for leptoquarks, have set new limits on their masses, which are dependent on the value of the λ coupling and are shown in the Table (2.7) for scalar leptoquark searches for $\lambda = 0.3$.

The LEP experiments have also results on searches for first generation leptoquarks mainly produced through the reaction $eq \rightarrow Lq$ where a photon, radiated by one of the beam electrons, serves as source of quarks through its fluctuations into hadronic states.

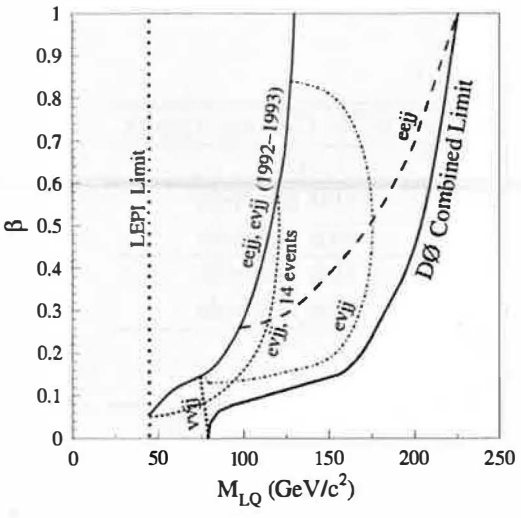

Figure 2.12: 95% *confidence level limits on the mass of first generation scalar leptoquarks at the DØ experiment as a function of* β *for the individual* $eejj$, $e\nu jj$ *and* $\nu\nu jj$ *channels, and for the combined analysis [41].*

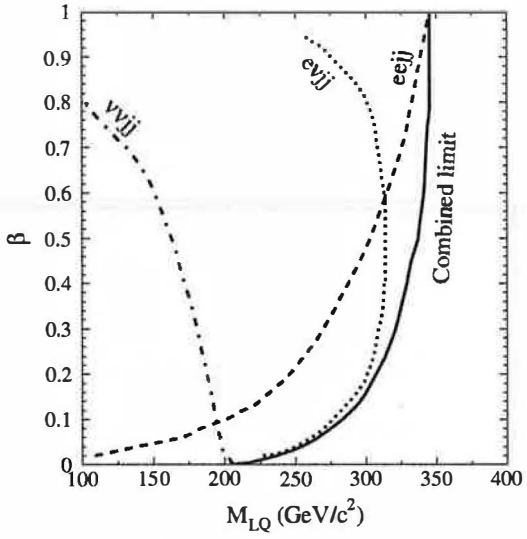

Figure 2.13: 95% *confidence level limits on the mass of first generation vector leptoquarks at the DØ experiment as a function of* β *for the individual* $eejj$, $e\nu jj$ *and* $\nu\nu jj$ *channels, and for the combined analysis [41].*

Decay channel	Scalar Lq's Searches - TEVATRON Current Limits		
	CDF	DØ	CDF + DØ
$eejj$ ($\beta = 1$)	213 GeV/c^2 [37] + this analysis	225 GeV/c^2 [38]	242 GeV/c^2 [39]
$e\nu jj$ ($\beta = 0.5$)	this analysis	175 GeV/c^2 [41]	
$\nu\nu jj$ ($\beta = 0$)		79 GeV/c^2 [40]	
All 3 channels ($\beta = 1$)	this analysis ($ee + e\nu$)	225 GeV/c^2 [41]	
All 3 channels ($\beta = 0.5$)	this analysis ($ee + e\nu$)	204 GeV/c^2 [41]	
All 3 channels ($\beta = 0$)		79 GeV/c^2 [41]	

Table 2.5: *Values of the* 95% *confidence level lower limits on the masses of first generation scalar leptoquarks from CDF [37] and DØ [38], [39], [41]. It is also indicated where this analysis will insert new limits or improve the previous ones.*

Decay channel	Vector Lq's Searches - TEVATRON Current Limits	
	DØ	CDF
$eejj$ ($\beta = 1$)	340 GeV/c^2($K_G = 0$) [41]	this analysis
	290 GeV/c^2($K_G = 1$) [41]	this analysis
$e\nu jj$ ($\beta = 0.5$)	315 GeV/c^2($K_G = 0$) [41]	this analysis
	260 GeV/c^2($K_G = 1$) [41]	this analysis
$\nu\nu jj$ ($\beta = 0$)	206 GeV/c^2($K_G = 0$) [41]	
	154 GeV/c^2($K_G = 1$) [41]	
All 3 ($\beta = 1$)	345 GeV/c^2($K_G = 0$) [41]	this analysis($ee + e\nu$)
	292 GeV/c^2($K_G = 1$) [41]	this analysis($ee + e\nu$)
All 3 ($\beta = 0.5$)	337 GeV/c^2($K_G = 0$) [41]	this analysis($ee + e\nu$)
	282 GeV/c^2($K_G = 1$) [41]	this analysis($ee + e\nu$)
All 3 ($\beta = 0$)	206 GeV/c^2($K_G = 0$) [41]	
	159 GeV/c^2($K_G = 1$) [41]	

Table 2.6: *Values of the 95% confidence level lower limits on first generation vector leptoquarks from DØ [41]. The analysis performed in this thesis will give the first CDF limits on vector leptoquark searches.*

Scalar Lq's Searches - HERA Current Limits	H1	ZEUS
F=2 (e^-p, 1998/1999), $\lambda = \sqrt{4\pi\alpha_{em}} = 0.3$	290 GeV/c^2 [42]	280 GeV/c^2 [44]
F=0 (e^+p, 1999/2000), $\lambda = \sqrt{4\pi\alpha_{em}} = 0.3$	200 GeV/c^2 [43]	204 GeV/c^2 [45]

Table 2.7: *Recent results of searches for leptoquarks at HERA ([42], [43], [44] and [45]).*

DELPHI [47] analysed the single scalar and vector leptoquark production setting limits on the mass ranging from 134 to 171 GeV/c^2 at an e^+e^- center of mass energy $\sqrt{s} = 183$ GeV and for a Yukawa coupling $\lambda > \sqrt{4\pi\alpha_{em}}$, while OPAL [48] has set mass limits ranging from 121 to 175 GeV/c^2 (149 to 188 GeV/c^2) for scalar (vector) leptoquarks depending on β for $\lambda > \sqrt{4\pi\alpha_{em}}$ at an energy of 189 GeV.

Part II

The Experimental Setup

Chapter 3

The Collider Detector at Fermilab

Introduction- *The general purpose detector CDF (Collider Detector at Fermilab [49], built in 1984) has been designed to study the physics of $p\bar{p}$ collisions with center of mass energies up to $\sqrt{s} = 2$ TeV at the Tevatron accelerator, originally called Energy Doubler, in the large experimental area of the Fermi National Accelerator Laboratory situated in Batavia, Illinois, about 60 km far from Chicago. First collisions were produced and detected in 1985, while the first physics results were obtained in 1987, in an engineering run, and in 1988-89, in a year-long run called run 0, at $\sqrt{s} = 1.8$ TeV. Then in spring 1996 the collider ended its first long physics run, called run 1, with a total luminosity of 110 pb^{-1} recorded on tape: 20 pb^{-1} in the run 1a (1992-93) and 90 pb^{-1} in the run 1b (1994-95).*
Analyses of experimental data resulted in the publication of more than 70 papers among the most cited ones in the high-energy physics community and about 400 papers in total. CDF provided the first experimental evidence of the top quark [50] and measurements of its production cross section [97], precision electroweak measurements, such as m_W [52], and determination of important parameters in the field of the b-physics [53].
In this chapter, after a short overview on the Fermilab Accelerators complex, the main components of the CDF experiment will be passed in review. A particular emphasis in the description will be given to the structure of CDF during the run 1, corresponding to the detector used to collect the data analysed in this thesis. A few words will be spent to describe the main changes to which Tevatron and CDF have undergone after the shutdown in 1996 to increase the center of mass energy, the luminosity and the detector acceptance, in prevision of the new physics run started in March 2001 at $\sqrt{s} = 2$ TeV.

3.1. The Tevatron colliding ring

The first generation of colliders accelerated electrons and positrons: it wasn't until the early 1980's that CERN first collided protons with antiprotons. Since the proton is much more massive than the electron, higher energy collisions could be achieved. The SPS (Super Proton Synchrotron) accelerator at CERN was used as their first collider. The center of mass energy of the collisions was initially 540 GeV (270 GeV on 270 GeV), then was later increased to 630 GeV (315 GeV on 315 GeV). With the switch to colliding beams, the SPS became the highest energy accelerator surpassing Fermilab's Main Ring, which was by then a 400 GeV fixed target machine.

The Tevatron began operation as an 800 GeV fixed target machine, but the eventual goal was to use it as a proton-antiproton collider. Building on the CERN innovations and experiences, Fermilab began construction of its own antiproton source. The first colliding beams in the Tevatron were established late in 1985 during a study period following a fixed target run. The complex has two major modes of running, collider and fixed target. In the former mode, beams of protons and antiprotons are brought into collisions at a center of mass energy of 1800 GeV. In the latter mode, protons are accelerated to 800 GeV and delivered to a number of experiments at the ends of various extraction beamlines. The accelerator complex consists of a preaccelerator plus a 400 MeV Linac, an 8 GeV Booster, a 150 GeV Main Ring, a 900 GeV superconducting Tevatron and associated transfer and extraction beamlines as sketched in Figure (3.1) . Features of each accelerating system are listed in Table (3.1). In addition, there is an Antiproton Source containing two 8 GeV

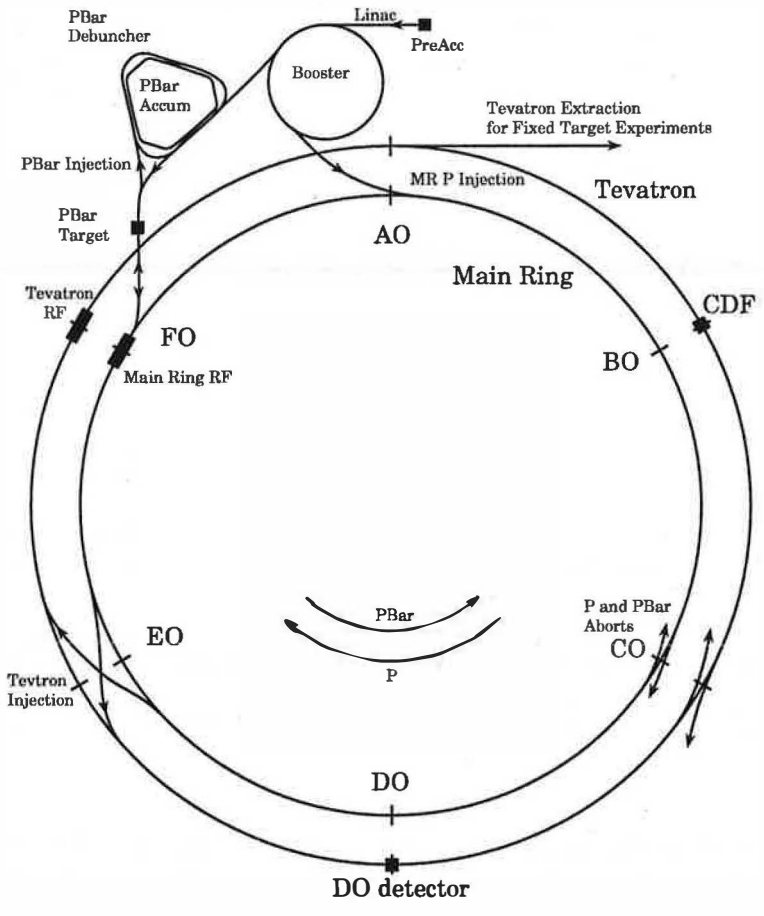

Figure 3.1: *Schematic draw of the Fermilab accelerator complex.*

synchrotrons, the Debuncher and the Accumulator. The Main Ring supplies the 120 GeV proton beam to generate antiprotons that are then accumulated in the Antiproton source. Here follows a summary description of the accelerators [54].

1. **Preaccelerator**
   The Cockcroft-Walton pre-accelerator is really the first of the accelerators. It is the source of the negatively-charged hydrogen ions accelerated by the linear accelerator. The Preaccelerator consists of the source housed in an electrically-charged dome. The source converts hydrogen gas H_2 to ionized hydrogen gas (H^-). The dome is charged to a potential of -750 kV. The ionized gas is allowed to have an electrostatic acceleration through a column from the charged dome to the grounded wall, and in doing so is accelerated to an energy of 750 keV.

2. **Linac**
   The Linear Accelerator, or Linac, is the next level of acceleration for the negatively-charged hydrogen ions. It accelerates ions with an energy of 750 keV to an energy of 400 MeV through a system of 14 cylindrical accelerating radio-frequency (RF) cavities arranged colinearly. The Linac itself was upgraded in 1993, increasing its energy from

ACCELERATOR	Initial Beam energy	Final Beam energy	Destination of beam
Preaccelerator	0 keV	750 keV	Linac
Linac	750 keV	400 MeV	Booster, dumps
Booster	400 MeV	8 GeV	Main Ring, dumps Antiproton Source
Main Ring	8 GeV	120 GeV for $\bar{p}$ production	Antiproton Source
		150 GeV for Tevatron injection	Tevatron
Tevatron	150 GeV	800 GeV for fixed target	Switchyard
		900 - 1000 GeV for Collider	Stays in Tevatron
$\bar{p}$ **Source**	8 GeV	8 GeV	Main Ring
Switchyard	800 GeV	800 GeV	Proton, Meson, Neutrino and Muon beamlines

Table 3.1: *Table of the injection and extraction energies of the various accelerators at Fermilab.*

200 MeV to 400 MeV; this made it possible, during run 1b, to double the number of protons per bunch, and to increase by about 50% the production rate of antiprotons.

3. **Booster**
   The Booster accelerator ring is the next level of acceleration, taking the 400 MeV negative hydrogen ions, stripping the electrons off leaving only the proton core. In the Booster the protons attain an energy of 8 GeV and are formed into bunches before being injected into the Main Ring. The Booster is the first circular accelerator, or synchrotron, in the acceleration chain. It consists of a series of magnets arranged around a 75 meter radius circle, with 17 RF cavities interspersed. The accelerated proton beam in Booster can be directed to four different locations depending on the need, one of these is the Main Ring, another is the antiproton source.

4. **Main Ring**
   The Main Ring is a circular synchrotron of radius 1000 meters, originally built to provide 400 GeV protons to Fermilab's fixed target experiments. It can accelerate protons from the Booster from 8 GeV to either 120 GeV or 150 GeV, depending on their destination. The proton beam that is accelerated to 120 GeV can be sent to the Antiproton source. As well as accepting protons from Booster, the Main Ring can accept antiprotons from the antiproton source at 8 GeV and accelerate them to 150 GeV. Once the protons (or the antiprotons) in Main Ring are accelerated to 150 GeV, they can be sent to the Tevatron after being coalesced into one bunch. For 6 bunch operation this procedure is repeated 6 times.

5. **Antiproton Source**
The antiprotons are a lot more difficult and time consuming than protons to produce. The Antiproton Source is comprised of a target station, two rings called the Debuncher and Accumulator and the transport lines between those and the Main Ring.
a. Target
The antiproton target station is where the target for making antiprotons is located. 120 GeV protons coming from Main Ring hit a Tungsten target to produce secondary particles, some of which are antiprotons which are focussed with a Lithium lens. These antiprotons are directed to the Debuncher.
b. Debuncher
The Debuncher is one of the two synchrotrons that makes up the antiproton source. The Debuncher is a rounded triangular-shaped synchrotron with a mean radius of 90 meters. It can accept 8 GeV protons from Main Ring or Booster for beam studies, and 8 GeV antiprotons from the target station. Its primary purpose is to reduce the momentum spread of the antiprotons by stochastic cooling. The cooling is accomplished by picking up a signal from the circulating antiprotons on one side of the ring, then amplifying the signal, and applying that signal to the antiproton beam at another part of the ring. The Debuncher does not accelerate beam in the same sense as the other accelerators, but maintains the beam at a constant energy of 8 GeV. There are three RF systems used in the Debuncher: one for rotating the bunches of antiprotons and thereby cooling the beam, one for maintaining the beam energy at 8 GeV, and the third for diagnostics and beam studies. The antiproton beam is then transferred to the Accumulator.
c. Accumulator
The Accumulator is the second synchrotron of the antiproton source. It is a triangular-shaped synchrotron of radius 75 meters, and is housed in the same radiation enclosure as the Debuncher. It is the storage ring for the antiprotons: all of the antiprotons made are stored here at 8 GeV and cooled until needed and then sent to the Main Ring, where they are accelerated to 150 GeV.

6. **Tevatron**
The Tevatron is the only cryogenically cooled accelerator at Fermilab. It is a circular synchrotron of radius 1000 meters that has the same basic layout and shares the same radiation enclosure as the Main Ring. The RF section of the accelerator consists of 8 accelerating cavities with 5.7 T superconducting dipole magnets. The Tevatron accepts both protons and antiprotons from Main Ring and accelerates them from 150 GeV to 900 GeV in different orbits and opposite directions. It is loaded with six intense proton bunches and six intense antiproton bunches. The proton and antiproton bunches are injected onto electrostatically separated orbits. Beams are then accelerated to Tevatron flattop. Strong focusing low beta quadrupoles on either side of each interaction region squeeze down the beam spot size and the beams are then brought into collisions at the centers of the two collider detectors. At this point the Tevatron provides collisions at the two experiments, CDF and DØ, and the Main Ring and the Antiproton Source are reconfigured to produce and accumulate antiprotons. Shot setup typically takes 2.5 hours and the stores last about 16 hours.

7. **Switchyard**
   The Switchyard is not really an accelerator, but is a collection of beam lines that can be used to re-direct proton beam from the Tevatron to various experiments during Fixed Target. It consists of four primary beamlines: proton beams are supplied to the various beam lines at the required intensities.

3.2. The Luminosity

An important physical quantity used in the accelerators is the luminosity, which is directly connected with the amount of collisions produced at the machine. The expression for the Tevatron's luminosity $\mathcal{L}$ is given by [55]:

$$\mathcal{L} = \frac{3\gamma f N_p (B N_{\bar{p}})}{\beta^* (\varepsilon_p + \varepsilon_{\bar{p}})} F(\sigma_z/\beta^*, \phi) \tag{3.1}$$

where γ is the relativistic factor, f is the revolution frequency, B is the number of bunches in each beam, N_p ($N_{\bar{p}}$) is the number of protons (antiprotons) in a bunch, $\varepsilon_p(\varepsilon_{\bar{p}})$ is the 95% normalized transverse beam emittance, σ_z is the rms bunch length, β^* is the beta function at the interaction point, and F is a form factor dependent on the ratio of the bunch length to β^* and on crossing angle, ϕ, which ideally should be equal to zero. Potential limitations on the value of $\mathcal{L}$ are related to the number of protons per bunch, N_p, and the total number of antiprotons in the collider, $BN_{\bar{p}}$. While the number of protons per bunch is limited due to beam-beam effects, the primary performance limitation in the Tevatron is, and will remain, the availability of antiprotons.

Through a series of improvements to Fermilab's accelerators, there has been a steady increase in the Tevatron luminosity every run from the 0.07 pb^{-1} delivered in the first three month long collider run in 1987. In the 1988-89 run typical initial instantaneous luminosities of 0.16×10^{31} $cm^{-2}s^{-1}$ were seen and the integrated luminosity in that 14 month run was 9.6 pb^{-1}. At that point the luminosity in the Tevatron was limited by the beam-beam tune shift: the installation of electrostatic separators prior to run 1a reduced the number of beam crossings from twelve to two. This enabled Tevatron to reach typical luminosities of 0.54×10^{31} $cm^{-1}s^{-1}$ and integrate a total of 32 pb^{-1} at two interaction regions, corresponding to the CDF and DØ experimental areas. The collider luminosity was now limited by the available proton beam that could be injected in the Booster and, hence, be used for antiproton production and for proton injection into the Tevatron. The limit in the Booster was due to space charge effects at injection from the 200 MeV Linac. After the Linac upgrade, with an increase in the injection energy to 400 MeV, the performance of the collider complex improved. This improved performance has been demonstrated in run 1b which has seen typical luminosities of 1.89×10^{31} $cm^{-2}s^{-1}$ and which has delivered more than 100 pb^{-1} to each of the two experiments at the two interaction regions.

With the addition of the Main Injector during the run 2 phase and other accelerator improvements, the luminosity is expected to increase by another factor of 4 during next years. The addition of the Recycler Ring should bring further improvements, perhaps as much as another factor of 2.

3.2.1. The Tevatron upgrade for Run 2

In March 2001 Tevatron started running again in colliding mode, with early stages of data taking, at $\sqrt{s} = 2$ TeV with as stated goal the accumulation of 2 fb^{-1} within the first two years using instantaneous luminosities up to 2×10^{32} $cm^{-2}s^{-1}$. The Fermilab Tevatron is the highest energy collider operating in the world today and will remain so until the initiation of LHC operations at CERN. The goal of the Tevatron collider program over the upcoming decade is to exploit the capabilities of this facility to the fullest extent possible.

The experimental program is directed by the potential of revealing new physics [56]. The precise analysis of processes whose cross section is several orders of magnitude lower than the $p\bar{p}$ cross section will be allowed partially thanks to the increase of the center of mass energy provided by the accelerator and to the luminosity enhancement. The increase in energy affects the detector performance only marginally, instead having an important impact on the physics: for example the $t\bar{t}$ yield increases by 40 %. In support of this goal a new proton accelerator, the Fermilab Main Injector, and a new antiproton storage ring, the Recycler Ring, have been constructed.

During run 1 the performance of the Main Ring has been insufficient, being not able to make full use of the Booster's capabilities, like for example the apertures, which for the Main Ring was only 60 % of the Booster's aperture. Built at the place of the Main Ring, the **Main Injector** is a 3 km circular accelerator which brings protons and antiprotons energies from 8 to 150 GeV. Thanks to its flexibility, it can be used in several modes: for the antiprotons production, for the proton and antiproton boosting before the injection into the Tevatron in collider mode, for antiproton deceleration to recover antiprotons not used in collisions at Tevatron, and for proton and antiproton acceleration for fixed target experiments. The primary source of improved performance relative to run 1b is an increase in the number of antiprotons in the collider.

During run 2 the antiprotons are transferred every about half an hour from the accumulator to the **Recycler Ring**, which allows to keep the total beam current in the Accumulator small. The Recycler Ring provides much higher proton and antiproton intensities. It is so called because it is used to recycle antiprotons which remain after the end of a run, instead of being dumped and lost as was happening during run 1. At the end of a store, about 75% of the antiprotons are expected to be still circulating in the Tevatron, and the opportunity of using even just 2/3 of them can increase the average luminosity of a factor of two. Moreover, in the past it had been found that the antiproton accumulator had some failures and tipically once a week the entire store was lost.
The Recycler Ring is built with permanent magnets, which assures the maintain of the produced flux of antiprotons, since they don't suffer the common causes of loss of particles, like for example the power loss due to lightning. In Table (3.2) are listed the Tevatron's operational parameters during the first physical runs, while in Table (3.3) are there comparisons between typical accelerator performances during the run 1b and the projections on run 2. In Table (3.3) two sets of run 2 parameters are shown: one based on operations with 36 proton and 36 antiproton bunches and a second based on 140 proton and 121 antiproton bunches. In Figure (3.2) is represented the average number of interactions per crossing as a function of the total luminosity in different bunch configurations. The bunch configurations

Run	1989	1a (1992-93)	1b (1994-95)
p /bunch	7.00E+10	1.20E+11	2.32E+11
$\bar{p}$/bunch	2.90E+10	3.10E+10	5.50E+10
p emittance (mm rad)	25	20	23
$\bar{p}$ emittance (mm rad)	18	12	13
Beta @ IP (m)	0.55	0.35	0.35
Energy (GeV/particle)	900	900	900
Bunches	6	6	6
Bunch length (rms, m)	0.65	0.55	0.60
Form Factor	0.71	0.62	0.59
Typical $\mathcal{L}$ (cm^{-2} s^{-1})	1.60E+30	5.42E+30	1.58E+31
Best $\mathcal{L}$ (cm^{-2} s^{-1})	2.05E+30	9.22E+30	2.50E+31
$\int \mathcal{L}dt$ (pb^{-1}/week)	0.32	1.09	3.18
Bunch spacing (ns)	3500	3500	3500
Interactions/crossing	0.25	0.85	2.48
Improvements		Separators $\bar{p}$ improvements	Linac Upgrade

Table 3.2: *Evolution of Tevatron parameters during the first physical runs.*

Run	1b (6 × 6)	Run 2 (36 × 36)	Run 2 (140 × 121)	
Protons/bunch	2.3E+11	2.7E+11	2.7E+11	
Antiprotons/bunch	5.5E+10	3.0E+10	3.0E+10	
Total antiprotons	3.3E+11	1.1E+12	3.6E+12	
Pbar production rate	6.0E+10	2.0E+11	2.0E+11	hr^{-1}
Proton emittance	23 π	20π	20π	mm rad
Antiproton emittance	13π	15π	15π	mm rad
β^*	35	35	35	cm
Energy	900	1000	1000	GeV
Antiproton bunches	6	36	121	
Bunch lenght (rms)	0.60	0.37	0.37	m
Crossing angle	0	0	136	μrad
Typical Luminosity	0.16E+31	0.86E+32	1.61E+32	$cm^{-2}s^{-1}$
Integrated Luminosity	3.2	17.3	32.5	pb^{-1}/week
Bunch Spacing	3500	396	132	ns
Interactions/crossing	2.5	2.3	1.3	

Table 3.3: *Evolution of Tevatron parameters from run 1 to run 2. The typical luminosity is quoted at the beginning of a store and translates to integrated luminosity with a* 33% *duty factor.*

during run 2 will be chosen to maintain fewer than three interactions per crossing as seen by the two experimental detectors, CDF and DØ.

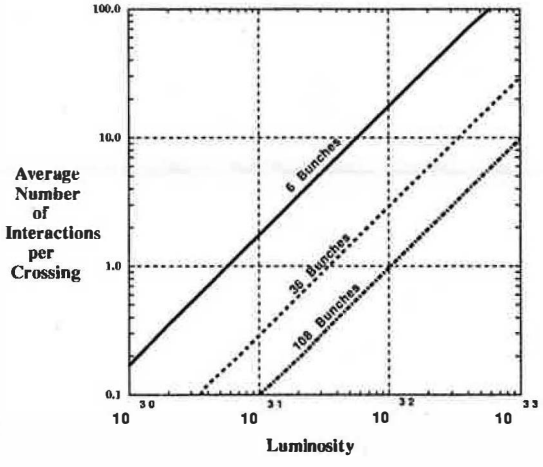

Figure 3.2: *The average number of interactions per crossing for various conditions at CDF. 36 bunches is equivalent to 396 ns crossings, while 108 bunches means 132 ns crossings.*

3.3. The experimental apparatus

The Collider Detector at Fermilab (CDF) is a multipurpose experiment for high energy physics conceived to measure the energies and momenta of the particles produced in $p\bar{p}$ collisions and, when possible, identify them.

The structure of CDF is illustrated in Figures (3.3), (3.4) and (3.5). It is constituted by a 2000 tons, cylindrical detector which forms its central structure, and by two identical forward/backward detectors on both sides of the barrel. The interaction point is in the center of symmetry of this structure, and the proton and antiproton beams come, in opposite directions, along the symmetry axis of the central cylinder.

In the CDF frame system, the $\hat{z}$ axis is oriented along the proton beam direction, the $\hat{x}$ axis points away from the center of the Tevatron, and the $\hat{y}$ axis points up. The origin is at the interaction point. Given its cylindrical geometry, the coordinates are usually expressed in terms of r, the distance from the interaction point, of azimuthal angle ϕ in the $x-y$ plane, given with respect to the positive $\hat{z}$ direction, and of *pseudorapidity* η, defined in terms of polar angle ϑ as $\eta = -\log\tan(\frac{\vartheta}{2})$, with ϑ measured starting from the positive $\hat{z}$ axis. The pseudorapidity is the massless approximation of the *rapidity* which is a natural variable for particles at relativistic energies since it is additive under Lorentz boosts. The pseudorapidity is equal to zero at a $\vartheta = 90°$ and has positive values in the proton direction. The transverse energies (E_T) and momenta (p_T) are defined as the projections of energy and momentum on the plane perpendicular to the beam direction, which is the $r-\phi$ plane, such that: $E_T = E \cdot \sin\vartheta$ and $p_T = p \cdot \sin\vartheta$, with E and p energy and momentum of the particle and ϑ polar angle of its trajectory. The overall design of CDF is dictated by the manner in which different types of particles interact with matter. It has been

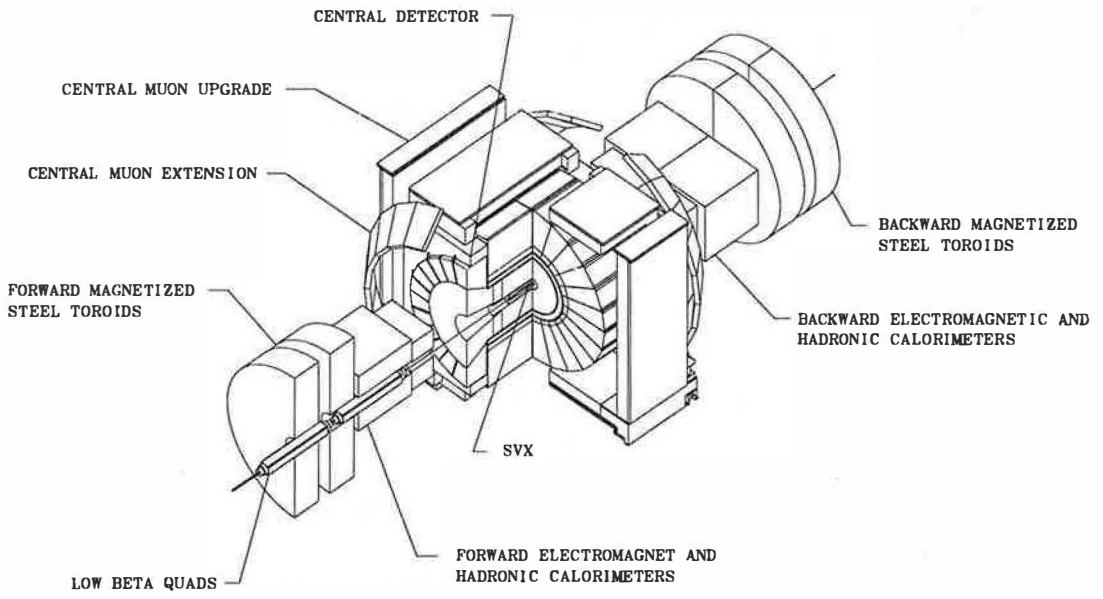

Figure 3.3: *Isometric view of the CDF detector illustrating its cylindrical and backward-forward symmetry. Protons and antiprotons beams come along the symmetry axis of the structure and collide at the center of the detector.*

conceived to be totally hermetic with a 4π coverage around the interaction point with enough sensitive material to stop all the detectable particles produced in the interaction. It is constituted by three main functional sections: after the thin wall Berillium vacuum chamber which constitutes the beam pipe, there is (i) the tracking system, located inside the field produced by an axial 1.4 T solenoidal magnet, which aims to the track reconstruction for momentum measurement of charged particles down to 2 mrad from the beam direction; (ii) the calorimeters, for the measurement of the total energy released by electrons, photons and hadrons, which has a polar angle coverage from 2° to 178° and full azimuthal coverage; and (iii) the muon chambers, the most external ones of the apparatus, covering the range $56° < \vartheta < 124°$ and ranging in ϑ from 3° to 16° and from 164° to 177° in the forward regions. In Table (3.4) are listed the detector components with their abbreviations.

In the following sections a description of the original structure of CDF as it was during run 1 will be given. A paragraph with a summary on the upgrade of the detector will conclude the description.

3.4. Tracking System

The tracking system allows the reconstruction of the trajectory of charged particles, from which the track parameters, the interaction vertex position and eventual secondary vertices positions in the event can be determined . It is surrounded by a 1.5 m radius superconducting solenoidal coil producing a 1.4 T axial magnetic field able to bend the trajectories of the charged particles: the radius of curvature in the $r - \phi$ plane allows the measurement

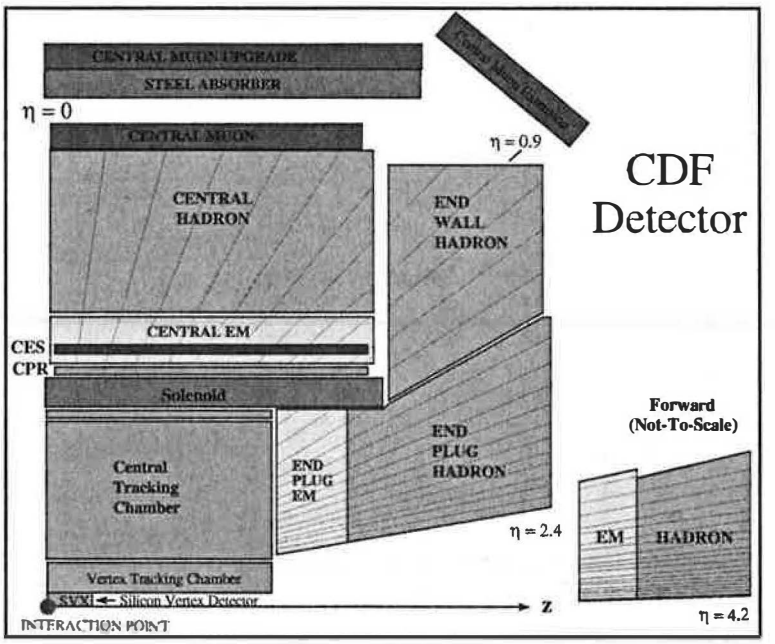

Figure 3.4: *Cross section of one quarter of the run 1 CDF detector, with emphasis on the central detector and the projective geometry of the calorimeter towers. For scale, the radial distance from the beamline to the inner surface of the Central Electromagnetic Calorimeter is 1.73 m.*

of their momentum and electric charge.
The tracking detectors are, going outside from the beampipe, the silicon vertex detector (SVX), the vertex time projection chambers (VTX) and the central tracking chamber (CTC).

Silicon Vertex detector

The silicon vertex detector for CDF was designed to operate in the environment imposed by the Tevatron Collider and the general principles for which firstly SVX in 1992 [57], then SVX' in 1995 [58], have been installed are the necessity of a detector allowing a good reconstruction of secondary vertices from b decays, which is also called *b-tagging*, and having inner radius as small as possible to obtain the best impact parameter resolution. B-tagging is also useful in cross-checking the top quark production estimates since top quarks decay almost exclusively to a final state containing a b quark. Not much different from the SVX geometry, SVX' is 51 cm long along the beam direction and consists of two independent, cylindrical modules of equal length with a 2 cm gap at the center of the detector, mounted inside the VTX. Due to the 30 cm spread of the z location of the interaction point, the consequent track acceptance is about 60% for $p\bar{p}$ collisions. Each barrel is divided azimuthally into 12 wedges and radially it consists of four concentric cylindrical layers of silicon strip detectors bonded in groups of three, called *ladders*: the inner layer in SVX' has a radius of 2.86 cm, which improves the resolution in the determination of the impact parameter with respect to SVX, whose innermost layer had a radius of 3 cm, the outer layer of about 8 cm, therefore covering the pseudorapidity region $|\eta| < 1.9$.

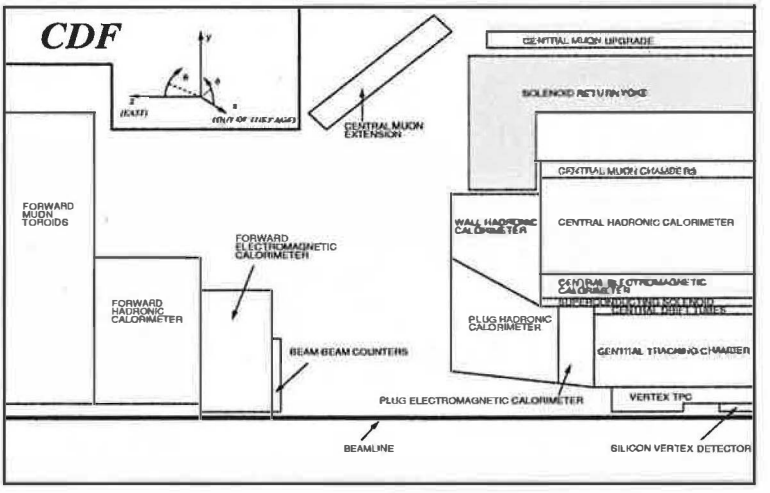

Figure 3.5: *Longitudinal view of one quarter of the detector. The interaction point is on the beam line, on the right corner on the bottom of the figure.*

Detector		Name
Tracking	SVX	Silicon VerteX detector
	VTX	VerTeX detector
	CTC	Central Tracking Chamber
Calorimetry	CES	Central Electromagnetic Strip chamber
	CEM	Central ElectroMagnetic
	CHA	Central HAdronic
	WHA	Wall HAdronic
	PEM	Plug ElectroMagnetic
	PHA	Plug HAdronic
	FEM	Forward ElectroMagnetic
	FHA	Forward HAdronic
Muon Detectors	CMU	Central MUon
(tracking)	CMP	Central Muon uPgrade
	CMX	Central Muon eXtension
	FMU	Forward MUon

Table 3.4: *The abbreviations and names of the CDF elements.*

The SVX' uses silicon microstrip technology to provide track measurements in the $r-\phi$ plane with 10 μm precision, and to avoid the creation of secondary particles, pair conversion and multiple scattering, the amount of material used has been minimized. The reason for the SVX replacement, in run 1b, with the SVX', has been its radiation damage at the end of run 1a, which was at the origin of an increase of leakage current and of a significant degradation in hit efficiency. The SVX' AC coupled silicon microstrip detectors replace the single sided DC coupled devices to reduce leakage current and coherent noise. Moreover the readout chips were upgraded to be radiation hard for the increased luminosity of run 1b.

Vertex time projection chambers

Immediately outside the silicon detectors, extending out to a radius of 22 cm and with a pseudorapidity coverage of $|\eta| < 3.25$, is the VTX [59], formed by eight vertex time projection chambers, optimized to provide a good pattern recognition in the $r-z$ view, required to locate the event vertex, with a spatial resolution per hit of 200 μm. The VTX identifies the z-position of the collision to calculate the $\sin\vartheta$ of the energy released by the particle in the calorimeter, therefore allowing the measurement of the transverse energy $E_T = E \cdot \sin\vartheta$. Another important feature of VTX is the capability of reconstructing multiple vertices, which permits to correct for the contamination of energy in the calorimeters due to extra interactions. The gas chambers of the VTX are segmented azimuthally into 8 wedges, the endcaps of which consist of wires perpendicular to the beam line and the radial centerline of the wedges. The drift velocity of the gas is parallel to the beam line so that the drift time is converted to a z position of the ionizing particle while the radial coordinate is determined by the radial position of a sense wire. Each octant of a drift chamber samples the particle trajectory at 24 points. Pattern recognition software collects the individual wire hits to reconstruct the track of the ionizing particle. Multiple tracks which converge to a common origin identify the vertex.

Central tracking chamber

This 3.2 m long cylindrical drift chamber surrounds both the SVX and the VTX and corresponds to a pseudorapidity coverage of $|\eta| < 1.2$ and to a 2π azimuthal coverage [60]. For the analysis performed in this thesis the central tracking chamber is important since its information allows three-dimensional track reconstruction providing the measurement of electron's momentum and its identification and energy measurement through the matching between the track with the position of its energy deposit in the electromagnetic calorimeter. The curvature of charged particle trajectories due to the 1.4 T solenoidal field is in the transverse plane so that the precision transverse tracking translates to precision transverse momentum measurements of charged particles. The resolution for momentum measurements is a function of the curvature of the track and therefore of the transverse momentum of the particle: for the CTC alone, it is $\frac{\delta P_t}{P_t} \sim 0.002\ P_t$ GeV/c, while when information from SVX is additionally used in the track reconstruction the transverse momentum resolution improves to $\frac{\delta P_t}{P_t} \sim 0.001\ P_t$ GeV/c.

The Central Tracking Chamber has large drift cells arranged in superlayers, whose cells provide the $r-\phi$ information with a resolution of 200 μm and whose stereo layers give information about the $r-z$ view, with a z resolution of about 5 mm, equal to the position

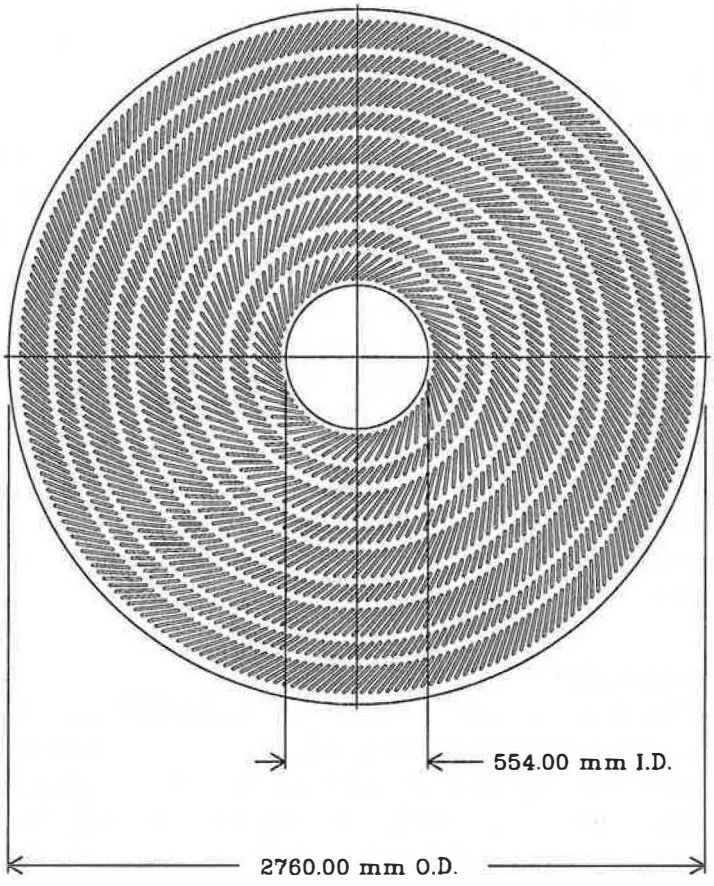

Figure 3.6: *End-view of the Central Tracking Chamber showing the wires disposition in 9 superlayers and their position in cells tilted by 45° with respect to the radial direction.*

resolution in the calorimeters.
Since the drifting electrons produced in the gas ionization move at a Lorentz angle β with respect to the electric field direction due to the magnetic field and to the 1350 V/cm electric drift field, the cells are tilted by 45° with respect to the radial direction, so that the drift trajectories are approximately azimuthal. This is well visible in the schematic view of the CTC shown in Figure (3.6), which offers a global picture in the $r - \phi$ plane.

The CTC is constituted by 84 cylindrical layers of sense wires, which are grouped in 9 superlayers: 5 of these each contain 12 layers of sense wires which are parallel to the beam line, and they are interleaved with the other 4 superlayers containing each 6 stereo wire layers in which the angle between the sense wires and the beam line alternates between ±3°. The stereo arrangement allows the reconstruction of the third dimension. The CTC provides 84 individual wire hits out to a radius of 1.4 m for use in track reconstruction. The gas drift direction is in the ϕ direction around the beam line. This configuration optimizes for track measurements in the plane transverse to the beam line.

3.5. The Calorimeters

The calorimeters are used extensively in the search for leptoquark pairs decaying into the channels $e\nu jj$ and $eejj$, where isolated electrons, high energy jets and neutrinos are demanded, since in particular they perform the energy measurement of electrons and jets and allow the reconstruction of the missing transverse energy of the event. The electromagnetic calorimeters are used to determine the electrons energies, with the hadron calorimeters they are used to find jets and to determine jet energies, while the complete set of calorimeters is used to measure the imbalance of transverse energy, which gives the missing transverse energy of the event, $\not\!\!E_T$.

The calorimeters correspond to the idea that every device that totally absorbs an incoming particle also measures its energy if it is deposited in the sensitive volume of the detector. According to the kind of particle one can use electromagnetic calorimeters, which measure photons and electrons energies released by electron-positron pair production and bremsstrahlung respectively, and hadron calorimeters, which measure the energy deposited by hadrons by strong interaction with the detector material. After traversing the tracking chambers, electrons and photons shower in the electromagnetic calorimeter by depositing their energies; hadrons release their energy in both the electromagnetic and the hadronic calorimeters.

The subdetectors constituting the calorimetric system are the central, plug and forward electromagnetic and hadron calorimeters and the endwall hadron calorimeter. Their main features are summarized in Table (3.5) and explained below. They are *sampling* calorimeters, constructed by alternating ladders of passive material, like lead or iron, where the particles shower, with ladders of material where the released energy is measured. Together the calorimeters offer a 2π azimuthal coverage and a pseudorapidity coverage of $|\eta| < 4.2$. For all calorimeters it has been chosen a projective tower geometry: a tower, which points to the interaction region, corresponds to a segmentation of the detector volume which is 0.1 units of η wide by 15° (5°) in the central (plug and forward) regions in azimuth. Each

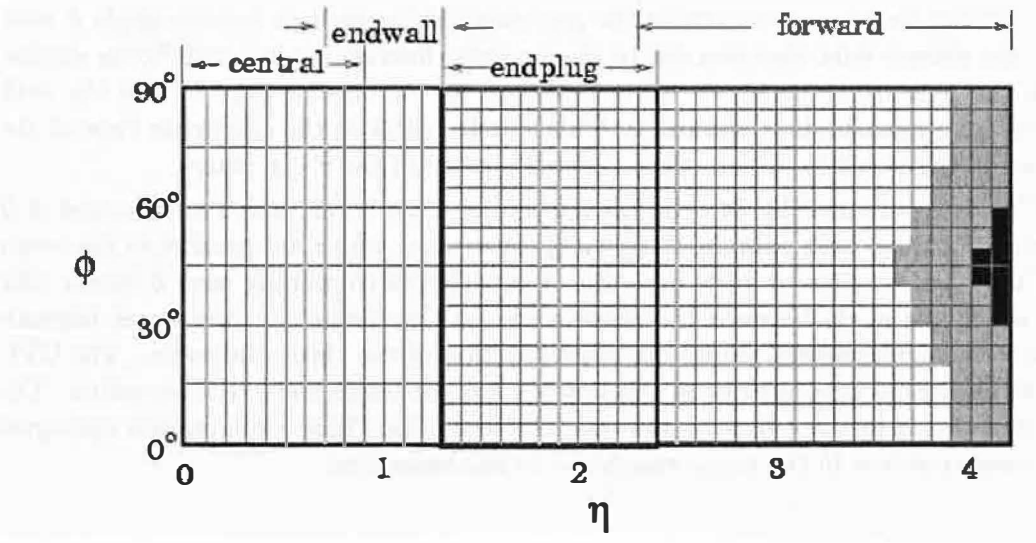

Figure 3.7: *Schematic map of the hadronic calorimeter towers in one of eight $\eta - \phi$ quadrants ($\delta\phi = 90°, \eta > 0$). The black areas are not covered, while the shaded area has only partial coverage due to geometrical obstruction by the low beta quadrupoles. The thicker lines indicate module or chamber boundaries.*

tower has an electromagnetic shower counter in front of a corresponding hadron calorimeter, so that one can make a detailed comparison of electromagnetic to hadronic energy on a tower-by-tower basis. The physical size of a tower ranges from about 24.1 cm × 46.2 cm ($\eta \times \phi$) in the central region to 1.8 cm × 1.8 cm in the forward region. The coverage of the calorimeter towers in $\eta - \phi$ space is shown in Figure (3.7).

Central electromagnetic calorimeter

The CEM [61] is a sampling calorimeter with 31 layers of 5 mm thick scintillator alternated with 30 layers of 3 mm lead. Its thickness in radiation lengths is about 18 X_0. A gas proportional wire chamber with cathode strips (CES) allows more precise measurements of shower position and shape inserted in each CEM wedge, at a depth corresponding to the maximum average transverse electromagnetic shower development ($\sim 6X_0$). The usage of this latter in the run 1 trigger decreased the fake electron trigger rate by a factor of two [62]. Another wire chamber is placed immediately in front of the calorimeter, to act as a pre-shower detector which uses the tracker and the solenoid coil as radiators.
The energy resolution of this calorimeter is given by $\sigma(E)/E = 13.5\%/\sqrt{E_T(\text{GeV})} \oplus 2\%$, where the two terms are added in quadrature, while the position resolution is ±2 mm for 50 GeV/c electrons [63].

The CEM, located outside the solenoid at a radius of 173 cm and 35 cm thick, has an overall dimension of 4.9 m along the beam direction, with a separation into two sides at $\eta = 0$. Each side is furtherly divided in two arches each of which consists of 12 modules with $\Delta\phi = 15°$. The basic layout of each module is shown in Figure (3.8). Each module forms a single unit called wedge. The segmentation in pseudorapidity forms calorimeter projective

	Central		Endwall	Plug		Forward	
	EM	Hadron	Hadron	EM	Hadron	EM	Hadron
$\|\eta\|$ coverage	0-1.1	0-0.9	0.7-1.3	1.1-2.4	1.3-2.4	2.2-4.2	2.3-4.2
Number of modules	48	48	48	2	24	8	8
Tower size $\Delta\eta \times \Delta\phi$	0.1 $\times$15°	0.1 $\times$15°	0.1 $\times$15°	0.09 $\times$5°	0.09 $\times$5°	0.1 $\times$5°	0.1 $\times$5°
Number of towers/module	10	8	6	1152	72	360	360
Active medium	polystyrene scintillator	acrylic scintillator	acrylic scintillator	Proportional tube chambers with cathode pad readout		Proportional tube chambers with cathode pad readout	
Scintillator thickness or proportional tube size	0.5 cm	1.0 cm	1.0 cm	0.7 $\times$ 0.7 cm^2	1.4 $\times$ 0.8 cm^2	1.0 $\times$ 0.7 cm^2	1.5 $\times$ 1.0 cm^2
Number of layers	31	32	15	34	20	30	27
Absorber	Pb	Fe	Fe	Pb	Fe	94% Pb, 6% Sb	Fe
Absorber thickness (cm)	0.32	2.5	5.1	0.27	5.1	0.48	5.1
Depth	18 X_0	4.7 λ_0	4.5 λ_0	18 X_0	6 λ_0	24 X_0	8 λ_0
Typical PM or wire voltage (V)	-1100	-1500	-1100	+1700	+2120	+1900	+2200
Typical PM or wire gain	1.2E+5	6.0E+5	1.0E+6	2.0E+3	2.0E+4	5.0E+3	1.0E+4
Energy resolution	$\frac{13.7\%}{\sqrt{E_T}} \oplus 2\%$	$\frac{50\%}{\sqrt{E_T}} \oplus 3\%$	$\frac{75\%}{\sqrt{E_T}} \oplus 4\%$	$\frac{22\%}{\sqrt{E_T}} \oplus 2\%$	$\frac{106\%}{\sqrt{E_T}} \oplus 6\%$	$\frac{26\%}{\sqrt{E_T}} \oplus 2\%$	$\frac{137\%}{\sqrt{E_T}} \oplus 3\%$
Typical position resolution at 50 GeV (cm^2)	0.2 $\times$ 0.2	10 $\times$ 5	10 $\times$ 5	0.2 $\times$ 0.2	2 $\times$ 2	0.2 $\times$ 0.2	3 $\times$ 3

Table 3.5: *Calorimeter properties by system. The thickness is given in radiation length (X_0) for the electromagnetic calorimeters and interaction lengths (λ_0) for the hadronic calorimeters.*

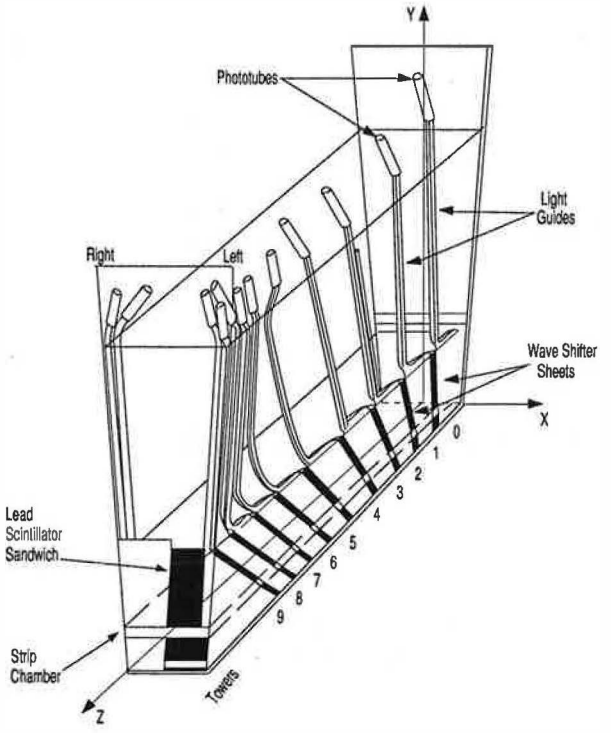

Figure 3.8: *Schematic of a wedge module of the CDF central calorimeter. Shown are the basic components: lead-scintillator sandwich for absorbing and measuring electromagnetic energy, wavelength shifter and light guides to carry the output of the scintillator to the photomultipliers. The ten towers are numbered from 0 to 9 and each cover 0.11 units of η. The coordinate system in the figure is the one used for test beam energy and mapping measurements.*

towers, each covering $\Delta\eta = 0.1$. A total of 10 towers are contained along the z direction in each CEM module. The physical dimensions of a tower are 24 cm in z by 45 cm in ϕ. The CEM towers are directly in front of the towers of the central hadron calorimeter: a cut on the ratio of hadronic over electromagnetic energies is applied for the electron identification performed in this analysis.

Central and Endwall hadron calorimeters

The Central and Endwall hadron calorimeters [64] are sampling detectors in which the showers are initiated from collisions of hadrons with the carbon and iron nuclei of the active medium.

The CHA covers polar angles from 45° to 135°, corresponding to the pseudorapidity region $|\eta| < 0.9$, and 2π in azimuth. It consists of 48 steel-scintillator calorimeters alternating 2.5 cm sampling with 10 cm scintillator.

The endwall calorimeter WHA covers polar angles from 30° to 45° and from 135° to 150°, corresponding to the pseudorapidity coverage $0.7 < |\eta| < 1.3$, and 2π in azimuth. It

contains a conical hole centered around the beam line to accomodate the plug calorimeter; it also serves as part of the magnetic field return yoke, therefore its scintillators and phototubes are influenced by the presence of the magnetic field and their response is corrected to take into account these effects. It is constituted by 48 steel-scintillator calorimeters alternating 5.0 cm sampling with 1.0 cm scintillator.

The energy resolution for incident isolated pions has been measured as equal to $\sigma(E)/E = 75\%/\sqrt{E_T} \oplus 3\%$. For each 15° azimuthal slice there are 24 towers in all, of which 12 are totally in the central calorimeter, 6 totally in the endwall calorimeter, and 6 are shared. The central modules are 32 layers deep and weigh about 12000 kg, while 15 are the layers of the endwall calorimeters modules, weighting 7000 kg.
As the same way as for the CEM, each module is divided into projective towers, each covering approximately 0.1 units in pseudorapidity and 15° in azimuthal angle, matching those of the electromagnetic calorimeter which is in front of it. This segmentation is fine enough to allow quark and gluon jets to spread over more than one tower. This means that they will deposit energy over many towers. Since energy from jets is also tipically deposited in both the electromagnetic and the hadronic towers, the jet reconstruction and energy measurements use both sets of calorimeters.

The Plug and Forward calorimeters

The remaining calorimeters at CDF use, to sample showers by maintaining an high precision in the energy measurement, conductive plastic proportional tubes with cathode pad readout instead of scintillator sandwiched with lead absorber panels. In this case the amount of charge collected on the wires is proportional to the gas ionization which is in turn proportional to the energy released. The tube orientation is perpendicular to the solenoidal magnetic field, therefore its effect on the secondary tracks is negligible. The proportional tubes allow a finer tower segmentation, which becomes necessary in the higher pseudorapidity regions to isolate electron signals and to identify jets with their masses. The segmentation becomes here 0.1 in pseudorapidity and 5° in azimuth, a granularity which provides excellent position resolution. The calorimeters offer a full azimuthal coverage.

The endplug electromagnetic calorimeter (PEM) [65], which performs electrons and photons energy measurements with a resolution equal to $28\%/\sqrt{E_T} \oplus 2\%$, covers both ends of the solenoid which constitutes the central detector system of CDF leaving a concentric conical hole with an opening angle of 10° with respect to the beam axis in either direction. Each of the two calorimeter modules occupies a cylindrical volume with an outer diameter of 280 cm and a depth of 53 cm between 173 and 226 cm in the z-coordinate along the beam axis. The angular coverage is from 10° to about 36° in the polar angle ϑ, or in the pseudorapidity $|\eta|$ from about 1.1 to 2.4. Each of the two modules consists of four quadrants of $\Delta\phi = 90°$ each, and each of the quadrants consists of 34 layers of proportional tube arrays interleaved with 2.7 mm thick lead absorber panels. The material thickness varies inversely proportional to $\cos\vartheta$ up to 30° and ranges from $18X_0$ to $21X_0$.

With this calorimeter the identification of electrons cannot be based on the momentum measurement performed in the tracker, since the accuracy of such a determination is limited by the fact that tracks exit the central tracking chamber without traversing all the wire layers. During the test-beam phase it has been studied the capability of the PEM of

rejecting pions against electrons without relying on the momentum measurement but using a covariant matrix with longitudinal shower correlation. The result was a rejection factor of 500 to 1000 for 100 GeV π's with 60% to 80% efficiency for electrons.

The hadron calorimeter for the same angular region (PHA) [66] has the same geometrical features. Its coverage in pseudorapidity ranges from 1.3 to 2.4. It consists of 20 layers of chambers separated by 5 cm thick iron plates, corresponding to a total depth of 6 interaction lengths λ_0, and is completely shadowed by the FEM described below. Its energy resolution is equal to $\sigma(E)/E = 130\%/\sqrt{E_T} \oplus 3\%$ and the precision in the position measurement is equal to 2 cm.

The forward electromagnetic and hadron calorimeters (FEM and FHA) [67], [68] are both constructed using chambers with essentially the same design. The FEM is located at approximately 6.5 m from the interaction point on both ends of CDF, the FHA at about 7.0 m. The FEM consists of 30 sampling layers, composed of a lead sheet and a chamber of gas tubes, which result in a total depth of about 25 radiation lengths X_0. Its towers cover the polar angle region 2° to 10° at both ends of the detector. This subdetector, which offers a good e/π discrimination based on the analysis of the particle's energy deposition in the absence of momentum measurement due to the lack of information from the tracking system, has a resolution in the energy measurement given by $\sigma(E)/E = 25\ \%/\sqrt{E_T} \oplus 0.5\%$, while the position resolution for single electrons varies between 1 and 4 mm depending on the location in the calorimeter.
The FHA has been designed to detect and measure the energies and positions of hadrons in the pseudorapidity range of $2.2 < |\eta| < 4.2$. Each of the forward and backward calorimeters is segmented into four independent sections composed of 27 steel plates and 27 ionization chambers, corresponding to 8 interaction lengths λ_0. The FHA measures hadron energies with a resolution equal to $130\%/\sqrt{E_T} \oplus 4\%$ and gives also information about the jet position with a precision of about 3 cm.

3.6. Muon Detectors

The only charged particles with enough energy to escape the calorimeters before decaying are muons with $p_T \geq 1.5$ GeV/c, for whose detection have been created the most external devices of the apparatus. The muon system is composed of four sub-systems: the Central Muon System (CMU), the Central Muon Upgrade (CMP) and the Central Muon Extension (CMX) in the central region and the Forward Muon spectrometer (FMU) in the forward region.

In the central region of CDF, corresponding to a coverage in polar angle of $56° < \vartheta < 124°$ and in pseudorapidity $|\eta| < 0.6$, the muon drift chambers are at the end of each section of the hadron calorimeter, located at around 3.5 m from the beam axis [69] as illustrated in Figure (3.9). These are streamer chambers, working outside the CDF magnetic field, constituted by 4 superposed layers of 4 rectangular single wire drift cells in the $r - \phi$ plane. At the center of each cell is a sense wire running the length of the wedge of 2.3 m. Pairs of sense wires are offset from each other by 2 mm, in order to solve left-right ambiguities. The muon detector in the central region is subdivided into wedges opened 13° in azimuth to fit

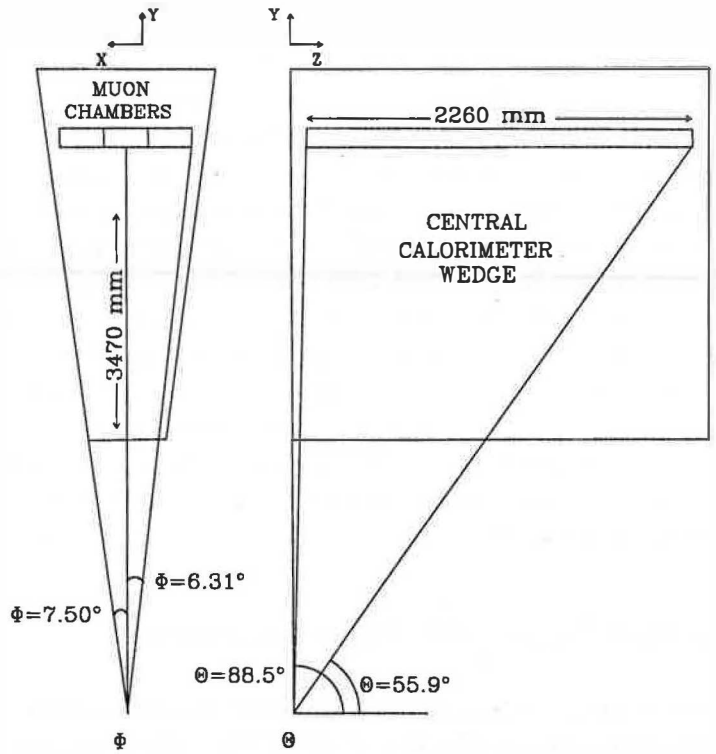

Figure 3.9: *Location of the central muon chambers within a central calorimeter wedge.*

the top of each of the 48 central calorimeter wedges, a geometrical constraint which leaves a gap in the coverage of 2.4° between each wedge. Another gap is given by the boundary between chambers at $\vartheta = 90°$.

The chambers measure position and direction of the μ's in the three dimensions with a resolution of 250 μm in the drift direction, which is the ϕ direction, and a resolution of 1.2 mm along the sense wire, which is parallel to the beam direction, where the position is determined by charge division methods. The subdetector is 100% efficient in the detection of muons with momentum above 3 GeV/c. Their identification requires a matching in position and angle to CTC tracks. Tracks which are measured in at least 3 of the 4 layers form a track segment called a "muon stub".

The central muon extension (CMX) system extends the central muon coverage to the region $0.6 < |\eta| < 1.0$ for azimuthal angles satisfying $\phi < 75°, \phi > 315°$ and $105° < \phi < 225°$. It also consists of 4 layers of drift chambers. The CMP chambers, which cover the regions $\phi < 45°, \phi > 315°$ and $135° < \phi < 225°$ outside the CMU, are constituted by two 60 cm walls of steel running along the sides of the detector at about 540 cm in x providing an extra hadron absorption. The absorbers for the CMP chambers running along the top and the bottom of the detector are provided by the steel return yoke of the solenoid at about 480 cm in y, which is roughly the same thickness as the side walls of the steel. The ϕ gaps in the return yoke mean that the CMP has gaps in the regions $80° < \phi < 100°$ and $260° < \phi < 280°$. The CMP offers the same $|\eta|$ coverage as the CMU and provides coverage over most of the CMU ϕ gaps.

The muon position and the determination of its momentum in the small angle region is done by the forward muon spectrometer, which covers the forward ($3° < \vartheta < 6°$) and backward ($164° < \vartheta < 177°$) regions. It consists of a pair of magnetized iron toroids instrumented with three sets of drift chambers and two planes of scintillation trigger counters, these latters used to trigger events with single and multiple high transverse momentum muons. Four coils excite the toroids to a magnetic field ranging from 2.0 T at the inner radius to 1.6 T at the outer radius. The system is subdivided into 24 wedges in azimuth, each subtending 15°: each wedge is staggered with respect to its neighbors to overlap detector regions eliminating the dead regions at the wedge boundaries. The electrodless drift chambers are located on three layers in the $r - \phi$ plane and they allow the measurement of the muon trajectory with an accuracy of 5° in the ϕ direction and about 200 μm in the r direction, while the momentum resolution is 13% independent on the momentum for μ's with p> 8 GeV/c. The reconstruction of muon tracks is done with a matching with the FTC or the VTX. In case of isolated muons it can be used also the matching with the calorimeters in front of the muon spectrometer.

3.7. Luminosity monitors and trigger counters

The measurement of the integrated luminosity is based on the rate of the *minimum bias trigger* generated by the Beam-Beam Counters (BBC) [70]. The BBC are two planes of scintillator counters which reside on each side, forward and backward, of the detector at about 5.8 m from the nominal interaction point. They are in front of the forward and backward calorimeter shower counters. The counters are arranged in a rectangle around the beam pipe. Each plane consists of 16.2 cm thick scintillator counters, with two phototubes attached to each scintillator, and covers the region of 3.2 to 5.9 in pseudorapidity. The scintillation counters have excellent timing properties, with a resolution $\sigma < 200$ ps, and so provide the best measurement of the time of the interaction. Signal detected in coincidence from both sides of the BBC within a 15 ns gate centered at 20 ns after the beam crossing constitute the minimum bias trigger. The integrated luminosity for a run is calculated using the formula:

$$\int \mathcal{L}dt = N_{BBC}/\sigma_{p\bar{p}}^{BBC} \tag{3.2}$$

where N_{BBC} is the number of minimum bias triggers during the run and $\sigma_{p\bar{p}}^{BBC}$ is the total cross section of $p\bar{p}$ interaction, corrected for the BBC acceptance.

The six proton bunches and the six antiproton bunches circling the Tevatron cross each other every 3.5 μs at the center of CDF, and this corresponds to a bunch crossing rate of 280 kHz. With a luminosity of 2×10^{31} cm^{-2}s^{-1} and with a total inelastic cross section $\sigma \sim 5 \times 10^{-26}$ cm^2 for $p\bar{p}$ collisions at $\sqrt{s} = 1.8$ TeV, a typical interaction rate of 1 MHz is observed at the Tevatron, which translates to an average of over 3 interactions per bunch crossing. It is the bunch crossing rate that defines the maximum rate at which events are produced. The CDF data acquisition system (DAQ) must therefore contend with a few hundred thousand interactions per second. Most $p\bar{p}$ interactions are diffractive, producing minimum bias events that have no high-p_T end-products and are of lesser interest. The more interesting hard-scattering events tend to produce high-p_T particles and have very

small cross sections. For example, the cross section for $t\bar{t}$ pair production is about 5 pb, meaning that one $t\bar{t}$ event is created in beam to beam collisions every 5 hours. Furthermore, due to detector acceptances and efficiencies, only a small fraction of these rare events are actually recorded by the experiment. To limit the amount of data that needs reprocessing, CDF employes a sophisticated online trigger system to select interesting events in real time from the data stream for storage by minimizing the dead time incurred while making a decision. Because not all the information from the detector is immediately available, in order to make a fast decision a 3 level trigger system is employed at CDF to select events with electrons, muons or jets. This system reduces the initial 280 kHz rate to an output event rate to magnetic tape of about 8 Hz during run 1b and of about 5 Hz during run 1a. It is therefore necessary a rejection factor of about $10^4 - 10^5$, while maintaining high trigger efficiencies for the interesting events. Each trigger level processes fewer events than the level preceding it, but it processes them with greater sophistication and hence takes more time per event. The level 1 and level 2 trigger decisions were made by hardware processors, while the level 3 decision was made with software on a farm of Silicon-Graphics computers.

The lowest level triggers are based on the energy deposition in $\Delta\eta \times \Delta\phi = 0.2 \times 15^\circ$ trigger towers for the calorimeter triggers and on the presence of muon track segments for the muon triggers. There is no tracking information available to the level 1 decision. The level 1 triggers incur no dead time, the decisions being made in the 3.5 μs between beam crossings. The level 1 triggers reduce the event rate down to a few kHz, these remaining events being passed on to the level 2 triggers.

The level 2 decision takes about 20 μs and incurs a dead time in the order of a few percent due to the fact that the detector ignores subsequent beam crossings until a level 2 decision is made. Level 2 trigger decisions are based on calorimeter clusters, central stiff tracks and muon candidates. A hardware calorimeter cluster finder provides a list of clusters by searching for seed towers above a threshold, and then all the nearest neighbor towers above a lower threshold, repeating the procedure until no new seed towers are found. For each cluster the E_T is determined together with an average η and ϕ. Stiff CTC tracks are provided by the Central Fast Tracker (CFT) [71], a hardware processor that finds high p_T, $r - \phi$ tracks with high efficiency and computes the p_T with a resolution of $\delta p_T/p_T^2 = 3.5\%$.

Events accepted by level 2 are passed onto the software trigger of level 3 which runs much of the same reconstruction algorithms as used in offline analyses. The tracking algorithms used at this stage are simpler and faster than the ones used in the offline analyses because of the time constraints. Level 3 requires about one CPU second to process an event. Level 3 buffers the events and processes them in parallel, incurring no deadtime. Electrons from level 2 have their tracks fully reconstructed in 3 dimensions, and are required to match a reconstructed electromagnetic cluster. If the event is accepted by level 3, it will be written to tape to make the inclusive electron samples from which the offline data analysis begins.

The events for this analysis were collected using inclusive electron triggers that make use of tracking and calorimeter information. The level 1 calorimeter trigger requires a single trigger tower with $E_T > 6$ GeV (8 GeV) in the CEM (PEM). The central electron trigger at level 2 requires an energy cluster in the CEM with $E_T > 9$ GeV, together with an associated CTC track with transverse momentum $p_T > 9.2$ GeV/c, as measured by the CFT. Since CFT information is available only for $|\eta| \leq 1.0$, the plug electron trigger

at level 2 simply requires either an energy cluster in the PEM with $E_T > 20$ GeV, or $E_T > 15$ GeV and $\not\!\!E_T > 15$ GeV. An electromagnetic cluster is constructed as a set of contiguos CEM(PEM) trigger towers each with $E_T > 7$ GeV (4 GeV), including at least one seed tower with $E_T > 9$ GeV (6 GeV). The ratio of hadronic to electromagnetic energy in the cluster (E_{had}/E_{em}) is required to be less than 0.125. For central electrons, the level 3 algorithm requires that the reconstructed cluster E_T be above 18 GeV and that there be a reconstructed track with $p_T > 13$ GeV/c pointing to it. For plug electrons, the reconstructed E_T is required to be above 20 GeV with $\not\!\!E_T$ >20 GeV. The effect of the electron trigger efficiencies on the total selection efficiencies will be neglected in this analysis, since it has been measured to be greater than 99% efficient [72].

3.8. Measurement of the kinematic variables in the event

As it will be explained more in detail in next chapter, the goal of the analysis is the selection of events with either one energetic electron, two energetic jets and missing transverse energy, for the $e\nu jj$ decay channel, or two energetic electrons and two energetic jets, for the $eejj$ decay channel. The electrons release all of their energy in the electromagnetic calorimeter and, if in the good pseudorapidity range, match a charged track in the CTC. The jets release their energy in both electromagnetic and hadron calorimeters, while the neutrino passes without being detected and takes a part of the total energy, which is missing. The most important kinematic variables to be known in the events are therefore the following:

1. Transverse energy of the electrons (E_T^{ele});
2. Transverse energy of the jets (E_T^{jet});
3. Missing transverse energy of the event ($\not\!\!E_T$).

1. E_T^{ele}, transverse energy of the electrons -
High energy electrons shower in calorimeters through electromagnetic interaction and have as distinctive feature if compared to hadron calorimeters, a characteristic shower profile. Moreover there must be a matching between the position of the energy deposit in the calorimeter and a charged track detected by the tracking system of the apparatus.
The offline reconstruction of electrons begins with the formation of the electromagnetic clusters. All towers with $E_T = E \cdot \sin\vartheta > 3$ GeV are identified as "seed towers" [73]. E is the energy deposit in a tower and ϑ is the polar angle measured from the event vertex to the centroid of the tower. If the towers adjacent to the seed towers in η have $E_T > 100$ MeV, then they are included in the cluster. In the central electromagnetic calorimeter the size of electron showers is typically about one tower. When the E_T of an adjacent tower is greater than the seed tower E_T, the adjacent tower itself is used as the seed tower instead. Final clusters are retained as electron candidates if (i) the total E_T of the towers in the cluster exceeds 5 GeV, and (ii) the ratio of hadronic to electromagnetic energy associated with the cluster is less than 0.125. The maximum size of a CEM cluster is 3 towers in η ($\Delta\eta \sim 0.3$) and 1 tower in ϕ ($\Delta\phi \sim 15^o$), of a PEM cluster is 5 towers in η ($\Delta\eta \sim 0.5$) and 5 in ϕ ($\Delta\phi \sim 25^o$). The size variation takes into account the fact that the physical tower size changes while the shower size remains roughly the same.

The electron energies can be corrected, as it will be done in the analysis, by using the standard CDF routines called CEMFIX [74] and PEMFIX [75]. CEMFIX applies corrections on run 1b central electrons based on corrections determined on the run 1a inclusive electron sample used to calibrate the CEM through the reconstruction of the W mass: in fact W's are prolific enough to allow a preliminary determination of tower gains, time dependence determination and map tuning on a wedge basis. PEMFIX applies corrections to Plug electrons. It consists of a PEM non-linearity correction and a per-quadrant energy scale correction. The first correction derives from the test-beam data while the second one derives from a sample of run 1b central-plug Z's.

2. E_T^{jets}, the transverse energy of the most energetic jets -

The definition of a jet is based on the phenomenology of partonic shower generated by the quarks and the gluons produced in the $p\bar{p}$ collision or during the decay processes in the event. Jet algorithms are used to connect what can be quantified, that is the energy deposited by particles in the calorimeters, with what is not measurable, that is the energy of the initial partons. The role of the algorithm is to group the detected particles in clusters, or jets, whose total energies and momenta can be related to the corresponding properties of the partons produced in the hard scattering process. The term hadronisation indicates the process through which partons form the final jets [76]. Quarks and gluons are confined inside p and $\bar{p}$ by the strong interaction, whose strength is expressed in terms of the QCD coupling constant α_s. α_s changes as Q^2, the transferred quadri-momentum, changes: it decreases as Q^2 increases and increases when Q^2 becomes smaller so that it is lecit to suppose that α_s may become very strong at sufficiently small Q^2. Unfortunately this behaviour is not easy to demonstrate because at small energies the perturbation theory is inapplicable for this same reason. This would imply that as the quarks and gluons become more widely separated, the force holding them together increases, and this could explain their confinement. As a consequence of the strong binding, an energetic parton that is trying to break away from the rest of the system loses its energy by pulling out from the vacuum more partons which then condense into a group of hadrons, that is a jet. By the uncertainty principle, the fluctuation occurs on a distance scale of the order of $1/Q$, and if Q is large the production rate for this short-distance process should be predicted by perturbation theory. Subsequently, the quarks and gluons form themselves into hadrons. This process is called hadronization. Hadronization occurs at a much later time scale characterized by $1/\lambda$, where λ is the scale in α_s, i.e. the scale at which the coupling becomes strong. The interactions which change quarks and gluons into hadrons certainly modify the outgoing state, but they occur too late to modify the original probability for the event to happen, which can therefore be calculated in perturbation theory.

In other words, the jet algorithms allow the observation of the partons through the observation of their final decay products. There are many methods to define jets of hadrons. One is the so called "cone algorithm", which is based on the energy deposition in an angular region, another is the "clustering algorithm", based on combining particle momenta, like the Jade algorithm [77]. At CDF during the run 1 a cone algorithm was used [78], [79], [73] according to which a jet is a concentration of transverse energy $E_T^{jet} = E_T^t$ given by the sum of the transverse energies of the calorimeter towers falling inside a cone of radius $R = \sqrt{(\Delta\eta)^2 + (\Delta\phi)^2}$. $\Delta\eta$ and $\Delta\phi$ are the differences in pseudorapidity and azimuth between the tower position and the jet directions η_{jet} and ϕ_{jet} which are defined by the

E_T-weighted η and ϕ centroids:

$$\eta_{jet} = (\sum_t E_T^t \eta_t)/E_T^{jet} \tag{3.3}$$

$$\phi_{jet} = (\sum_t E_T^t \phi_t)/E_T^{jet} \tag{3.4}$$

As a consequence of this definition, if two partons fall into the same cone of radius R, then they form the same jet, while if they are at a relative distance greater than 2R, then they are considered as two separate jets. Each tower is constituted by the sum of contributions from electromagnetic and hadronic calorimeters and its transverse energy E_T^t is given by:

$$E_T^t = E_{em}^t \sin\vartheta_{em}^t + E_{had}^t \sin\vartheta_{had}^t \tag{3.5}$$

where ϑ_{em}^t and ϑ_{had}^t are the polar angles of the electromagnetic and hadron sections of the tower. The η^t and ϕ^t coordinates of the tower are given by:

$$\eta^t = (\eta_{em}^t E_{em}^t + \eta_{had}^t E_{had}^t)/(E_{em}^t + E_{had}^t) \tag{3.6}$$

$$\phi^t = (\phi_{em}^t E_{em}^t + \phi_{had}^t E_{had}^t)/(E_{em}^t + E_{had}^t) \tag{3.7}$$

where $\eta_{em}^t = -\ln(\tan\vartheta_{em}^t/2)$, $\eta_{had}^t = -\ln(\tan\vartheta_{had}^t/2)$ and ϕ_{em}^t and ϕ_{had}^t are calculated as weighted sum of the azimuthal positions of the right and left edges of the towers. The energy deposits on the towers are called *seeds* when the transverse energy is greater than a threshold value, which at CDF has been fixed at 1 GeV. After finding all the seeds in the event, the algorithm localizes the most energetic one and groups in *preclusters* the seeds which are around it and which lay inside a cone of radius R (R=0.4, 0.7, 1.0 at a choice of the user). This procedure is iterated until all seeds are contained in preclusters. For each precluster the location in the η, ϕ plane is calculated with the Equations (3.3) and (3.4), which give the centroid of the precluster. This direction becomes the axis of new cones of radius R, in which every other tower falling inside and having $E_T > 0.1$ GeV is inglobated: these cones are now called *clusters*. The cone contains all the particles whose trajectories are in an area $A = \pi R^2$ of the $\eta \times \phi$ space ; the axis of this cone, which fixes the jet directions, is given by the vectorial sum of all vectors whose lengths are given by the transverse energy E_T of the particle and direction given by the direction of the particle itself [80]. A paradox of this jet finding algorithm is that it will always find jets in a hadronic final state even when none existed in the first place, for example in the limit case when the hadronic energy is distributed uniformly over the 4π solid angle.
In the case in which a tower is in more than one cluster at the time, then either the two clusters are merged to form an unique one, and this happens when the two clusters share more than 75% of the total energy of the smallest cluster, or the tower will belong to the closest cluster. Once all the clusters will have been defined, they are called *jets*.
Jets energies and momenta are defined as follows:

$$E_J = \sum_{t=1}^{N} E_t \tag{3.8}$$

$$P_{x,J} = \sum_t^N E_t \sin\vartheta_t \cos\phi_t \tag{3.9}$$

$$P_{y,J} = \sum_{t}^{N} E_t \sin\vartheta_t \sin\phi_t \tag{3.10}$$

$$P_{z,J} = \sum_{t}^{N} E_t \cos\vartheta_t \tag{3.11}$$

where the sum is over the number of towers in the cluster. According to this definition, jets are supposed to have a mass. The transverse components are:

$$P_{T,J} = \sqrt{P_{x,J}^2 + P_{y,J}^2} \tag{3.12}$$

$$P_J = \sqrt{P_{x,J}^2 + P_{y,J}^2 + P_{z,J}^2} \tag{3.13}$$

$$E_{T,J} = E_J \frac{P_{T,J}}{P_J} \tag{3.14}$$

Once these energy measurements are made, some detector and physics effects can be taken into account by applying several corrections to the raw measurement [81]:

- Relative corrections: they are applied when the jet is partially lost in cracks of the calorimeter and the energy cannot be completely measured. The corrections normalize the measurement to the response of the fully efficient areas of the detector. These corrections have been calculated using dijet events, for which, in a perfect detector, the two jets should be back-to-back and balanced in E_T;

- Absolute corrections: some hadronic physics processes occurring during an hadron shower, for example energy leakage and nuclear absorption, need to be taken into account when transforming the jet energy into the parton energy. In general the jet energy is an underestimate of the original parton energy. Simulations of the fragmentation are used to calculate the appropriate correction factors to the jet energy;

- Underlying event corrections: the underlying event results either from remnants of the original p and $\bar{p}$ after the collision, that do not participate to the formation of the high p_T process, and remain as spectators, recombined to form low momentum hadrons in the forward direction, or from particles coming from other $p\bar{p}$ interactions in the same bunch-crossing. It is possible that tracks released from these events fall into the jet cone, giving in this way an overestimation of the jet energy. This contribution, to be subtracted from the jet energy, is evaluated using "minimum bias" events from dedicated runs, that is from events which are triggered only by demanding the occurence of a collision and which have soft partons scatterings and for that are very similar to underlying events;

- Out-of-cone corrections: some particles, especially produced by gluon emission, could be directed outside the cone and therefore not included when reconstructing the jet energy. Corrections factors are calculated using Monte Carlo simulations.

3. Missing transverse energy of the event ($\not\!\!E_T$) -
Neutrinos normally traverse the detector without being detected, since their probability of interaction with the material is very low. They carry a fraction of the total event

energy, therefore their presence is inferred from an energy imbalance in the calorimeters. The colliding proton and antiproton have a total energy-momentum quadrivector $p^\mu = (E_{total}, p_{x,total}, p_{y,total}, p_{z,total})$, with $E_{total} = \sqrt{s}$ and $\vec{p}_{total} = 0$. Unfortunately, not the whole energy of the colliding particles is used in the hard collision, because only one parton from each hadron will participate to it with unknown energy and momentum and leaving the other partons as spectators. As a consequence, no conservation rules of E_{total} and $\vec{p}_{total}$ can be applied to the event. However, to a good approximation the total transverse energy and transverse momentum of the two interacting partons should be zero. The total transverse energy of the event can be seen as sum of the visible and the invisible contributions, these latter coming from the neutrino or other non interacting particles. The visible part can be expressed as sum of the deposits in the electromagnetic and hadron calorimeters. In a vectorial form it can be expressed as such that $\vec{E}_T = -\vec{\not{E}}_T$, where $-\vec{\not{E}}_T$ can be therefore written as:

$$\vec{\not{E}}_T = -\sum_{i=1}^{N}(E_i \sin\vartheta_i)\hat{n}_i$$

where N is the total number of calorimeter towers, out to $|\eta| < 3.6$ and with total energy below thresholds fixed for each kind of subdetector, E_i is the measured energy of the i-th tower of the calorimeter, ϑ_i is the polar angle of the tower and $\hat{n}_i$ gives the transverse energy direction from the interaction point to the center of the tower. The magnitude of the vector $\vec{\not{E}}_T$, what is usually called as the missing transverse energy of the event, is given by:

$$|\vec{\not{E}}_T| = \sqrt{(\sum_i E_{T,i}\sin\phi_i)^2 + (\sum_i E_{T,i}\cos\phi_i)^2}$$

In first approximation the $\not{E}_T$ is given by the sum of transverse energy deposits released in the calorimeters by electrons, jets, minimum ionizing particles (muons) or the underlying event, that is:

$$\not{E}_T = -[\sum_{electrons} E_T + \sum_{jets} E_T + \sum_{mips} E_T + \sum_{ue} E_T] \tag{3.15}$$

This $\not{E}_T$ measurement corresponds to the raw missing E_T, and is the variable used in the $e\nu jj$ analysis. Some corrections could be applied to the measurements of the visible energy, to take into account tracks escaping in gaps of the detector before arriving to the calorimeters, branches of the hadron showers lost in cracks of the calorimeters, or unclustered towers. Moreover there can be in general under- or over-estimations of the energies due to calibration errors and since the corrections are average values, they can introduce smearing effects that may actually worsen the resolution. Therefore in analyses like this one, where the absolute $\not{E}_T$ scale is not important, it is decided not to use the corrected missing transverse energy.

3.9. The CDF Upgrade for Run II

Following the Tevatron changes done to provide 20 times greater luminosity than run 1 at a center of mass energy of 2 TeV, CDF has been upgraded [56] to be prepared for the high

radiation and the high crossing rate under this new machine environment. The upgrades of the detector have been also performed to exploit physics goals which in general can be summarized as follows [56]:

1. characterization of the properties of the top quark
2. a global precision electroweak program
3. direct search for new phenomena
4. tests of perturbative QCD at Next-to-Leading order and large Q^2
5. constraint of the CKM matrix with high statistics B decays

These upgrades were designed to give better tracking (silicon, tracking chamber), increased kinematic coverage (muon, silicon) and improved triggering and tagging capabilities (DAQ, software, time-of-flight). Several parts of the detector have been rebuilt from scratch in order to accomodate the higher collision rate during run 2. While the detector has been redesigned, efforts have been made to extend its acceptance. The geometrical coverage has been increased, by adding new detector elements or enlarging the previously existing ones. Detailed documentation about the upgraded systems can be found in [56].

- **Upgrade of the tracking system**
  For the run 2 the entire central tracking volume has been replaced, although the philosophy of using a silicon tracker surrounded by a gas ionization wire tracker which worked so well for run 1 remained. A longitudinal view of the new tracking system is shown in Figure (3.10).
  Central Outer Tracker

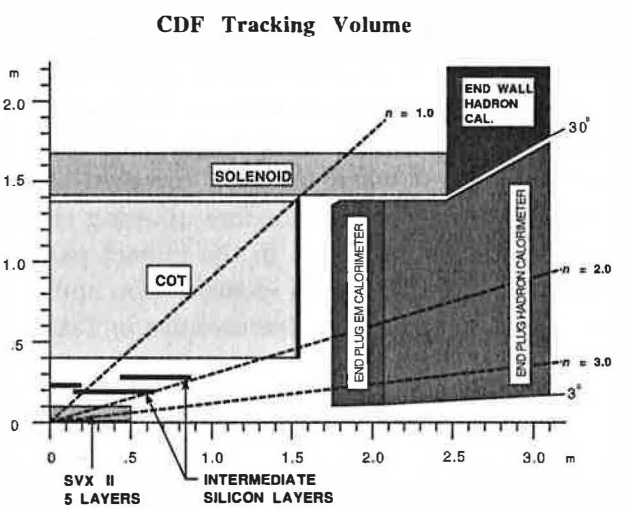

Figure 3.10: *Longitudinal view of the CDF II Tracking System.*

The tracking in the region $|\eta| < 1.0$ will be done with an open cell drift chamber, the COT, replacing the CTC which would suffer from severe occupancy problems at

$\mathcal{L} > 1 \times 10^{32}$ cm^{-2}s^{-1}. The design goal of the COT is to reproduce the functionality of the CTC, but using small drift cells and a fast gas to limit drift times to less than 100 ns. Its main features are listed in Table (3.6).

SVXII

The new silicon device is constituted by the new Silicon VerteX detector (SVXII) and by the Intermediate Silicon Layers (ISL). The system is twice as long than in run 1 to increase the forward coverage and has enough layers - 5 in the SVXII and 2 in the ISL - for a stand-alone tracking out to $|\eta| < 2.0$. This design has over 10 times as many channels as the run 1 detector and a new readout system to accomodate the 132 ns bunch spacing with a fully pipelined readout. In order to do this it has been necessary to mount the readout chips on the silicon itself. Since this would have increased the multiple scattering, a final layer of silicon, the Layer 00, has been installed directly on the beam pipe. This latter will furnish improvements on the impact parameter resolution which will be very important for the B_s oscillation measurements [1]. The SVX II is built in three cylindrical barrels with a total length of 96 cm, covering about 2.5σ of the luminous region and leading to contained b-tagging in almost all the events. Each barrel supports five layers of double sided silicon microstrip detectors: three of the layers combine an $r - \phi$ measurement on one side with 90° stereo measurement on the other and the remaining two layers combine $r - \phi$ with small angle stereo at 1.2°. Its designed position resolution is 12 μm. The radiation level at the inner layer is expected to be about 0.5 MRad per fb^{-1}. In Table (3.6) are summarized some of its parameters.

Intermediate Silicon Layers

The SVX II provides coverage to $|\eta| \sim 2$. In the region $|\eta| < 1$ the combination of the SVX II and the COT can provide full three-dimensional tracking, but it will suffer the amplification of inefficiencies in the reconstruction of tracks in the COT. On the other hand, it will be possible only a two-dimensional reconstruction for $|\eta| > 1$, which will rely only on the SVX II information, and in such a condition the impact parameter resolution for such tracks will be too poor to enable efficient b-tagging. The Intermediate Silicon Layers has been designed to solve both of these problems. It consists of a single layer of silicon placed at a radius of 22 cm from the beam pipe in the central region; in the region $1.0 \leq |\eta| \leq 2.0$, where the COT coverage is incomplete or missing, it is constituted by two layers of silicon, therefore allowing three-dimensional track finding in the plug region and improvement in the impact parameter measurement. The ISL should thus extend tracking, lepton identification and b-tagging capabilities over the full region $|\eta| \leq 2.0$. Details on its features are in Table (3.6).

Time Of Flight

The Time-Of-Flight system [82] will greatly enhance the particle identification capabilities of CDF, by increasing the detector's sensitivity to CP violation and B mixing measurements. Information from the TOF detector will allow an improvement in the flavor tagging technique thanks to an expected resolution of 100 ps, since it is supposed to provide a 2 standard deviation separation between $K^{\pm}$ and $\pi^{\pm}$ with momenta lower than 1.5 GeV/c and therefore complementing the energy loss dE/dx

[1] This kind of measurement constitutes a topic that is likely to be unique to the Tevatron during run 2.

COT	
Radial coverage	44 to 132 cm
Number of superlayers	8
Measurements per superlayer	12
Maximum drift distance	0.88 cm
Resolution per measurement	180 μm
Rapidity coverage	$\|\eta\| \leq 1.0$
Number of channels	30240
Material thickness	1.3%X_0
SVX II	
Radial coverage	2.4 to 10.7 cm, staggered quadrants
Number of layers	5
Readout coordinates	$r - \phi$ on one side of all layers
Resolution per measurement	12 μm (axial)
Total length	96.0 cm
Rapidity coverage	$\|\eta\| \leq 2.0$
Number of channels	405504
Material thickness	3.5%X_0
ISL	
Radial coverage	20 to 28 cm
Number of layers	one for $\|\eta\| < 1.0$; two for $1 < \|\eta\| < 2$
Resolution per measurement	16 μm (axial)
Total length	174 cm
Rapidity coverage	$\|\eta\| \leq 1.9$
Number of channels	268800
Material thickness	2%X_0

Table 3.6: *Main parameters of the baseline tracking systems for CDF II.*

measurement performed with the COT. The TOF consists of 216 bars of Bicron, a scintillator chosen for its long attenuation length $\lambda_{eff} \sim 250$ cm and its fast rise time. It is located at a radius of about 140 cm from the beam between the COT and the cryostat of the superconducting solenoid, giving a pseudorapidity coverage in the region $|\eta| < 1$.

- **Calorimeters Upgrade**
  For the run 2 upgrade, all the gas calorimeters of the plug and forward regions, which would have been incompatible with the high crossing rates, have been replaced with a faster plastic scintillator calorimeter employing optical fibers for readout. It is called Plug Upgrade Calorimeter and covers the region $1.1 < |\eta| < 3.6$. The new plug electromagnetic and hadrons calorimeters are sampling calorimeters with scintillating tiles, alternated with absorber, forming a projective tower geometry. The energy resolution is approximately $16\%/\sqrt{E}$ with a 1% constant term for the electromagnetic section, while it is $80\%/\sqrt{E} \oplus 5\%$ for the hadron section.

- **Upgrade of the muon system**
  The changes on the muon systems represent incremental improvements with respect to run 1, during which they worked well both for the analysis of several physics channels and for calibration. The improvements in the tracking from run 1 to run 2 have a deep impact on muon detection. In fact, during run 1 the momentum of forward muons had to be measured in the muon chambers itself, by resorting to a toroidal magnets, as the central tracker only covered the $|\eta| < 1$ region. For run 2 this feature has been changed: measurement of muon momentum will always be performed in the central tracker, where the multiple scattering effects are smaller, and the toroidal magnets will not be required any longer. Central tracks will be measured in the COT; forward tracks, starting at $|\eta| > 1$, thanks to the SVX upgrade, will be tracked in the silicon only.
  During run 2 the CMU will be reused without major changes; some upgrades started during run 1 (CMP and CSP, the Central Muon / Scintillator Upgrades; CMX and CSX, the Central Muon /Scintillator Extension) will be completed; and a new set of chambers, the Intermediate Muon Detector (IMU), will replace the previous Forward Muon Detectors (FMU), due to a low granularity which translates into high occupancy and uncertain efficiency at the high luminosities of run 2. In Table (3.7) are summarized the informations on the muon subsystems.

- **Upgrade of Data Aquisition and trigger**
  Due to the increase in collision frequency, the DAQ and trigger systems of CDF had to be almost completely replaced. The new three-level architecture, schematized in Figure (3.11), is fully capable of withstanding a 132 ns bunch separation, while keeping dead time as short as possible. The Level 1 trigger takes a decision within 4 μs, while the event's data is still in the pipeline. This makes the first trigger level deadtimeless. The rejection factor is about 150, thus decreasing the event rate from 7.6 MHz to about 50 kHz.
  Level 2 tests each event for about one hundred different triggers. Acceptance rate is dominated by single lepton triggers. The level 2 accept rate is around 300 Hz, with

	CMU	CMP/CSP	CMX/CSX	IMU
$\|\eta\|$ coverage	0.- 0.6	0.- 0.6	0.6 - 1.0	1.0 - 1.5
Drift tube length	226 cm	640 cm	180 cm	363 cm
Max drift time	800 ns	1.4 μs	1.4 μs	800 ns
♯ tubes (run I)	2304	864	1536	none
♯ tubes (run II)	2304	1076	2208	1728
Scintillators thickness		2.5 cm	1.5 cm	2.5 cm
Scintillators width		30 cm	30-40 cm	17 cm
Scintillators length		320 cm	180 cm	180 cm
♯ counters (run I)		128	256	none
♯ counters (run II)		269	324	864
Minimum muon p_T	1.4 GeV/c	2.2 GeV/c	1.4 GeV/c	1.4-2.0 GeV/c
MS resolution	12 cm/p (GeV/c)	15 cm/p	13 cm/p	13-15 cm/p

Table 3.7: *Design parameters of the CDF II Muon detectors. The multiple scattering (MS) resolutions are computed at a reference angle of $\vartheta = 90°$ in CMU and CMP/CSP, at an angle of $\vartheta = 55°$ in CMX/CSX, and on the entire ϑ coverage for the IMU.*

a rejection of about 150. The Silicon Vertex Tracker (SVT) [83] is a level 2 trigger which reconstructs tracks in the vertex detector, measuring their impact parameter to perform efficient b-tagging. Events passing the level 3 cuts are permanently written on tape. Assuming a level 3 input rate of 300 Hz, a rejection factor of 10, and an average event size of 250 kB, CDF II will record about $3{\cdot}10^8$ events per year, corresponding to 75 TB of data.

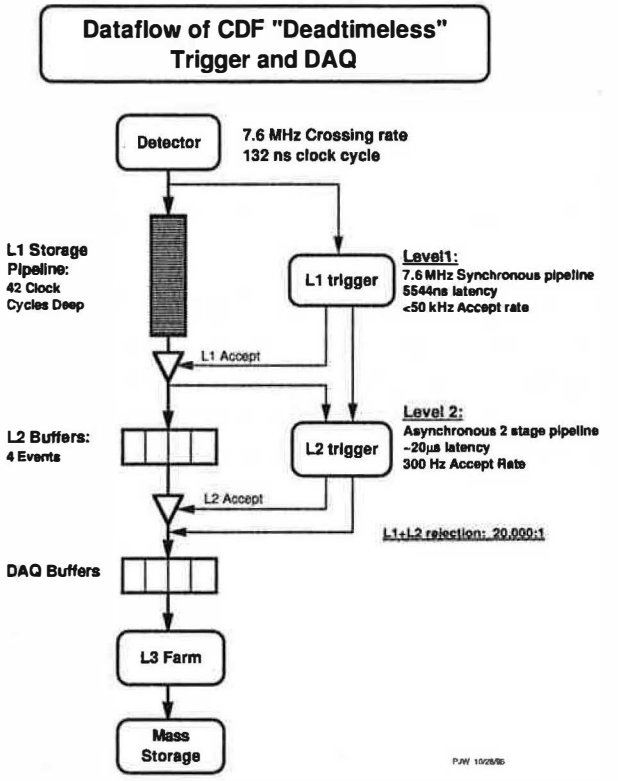

Figure 3.11: *Block diagram of the CDF II data flow.*

Part III

The Analysis

Chapter 4

Data Samples

Introduction- *The Collider Detector at Fermilab has collected a total integrated luminosity of about* 110 pb^{-1} *during the years 1992 to 1995, a period that has been called run 1 and subdivided in two parts, the run 1a, from August 1992 to July 1993 corresponding to about* 20 pb^{-1}, *and the run 1b, from January 1994 to July 1995 corresponding to about* 90 pb^{-1}. *The analyses described in this thesis have used the full run 1 data sample to search for first generation scalar and vector leptoquarks in the decay channels* $e\nu jj$ *and* $eejj$. *Since the event selection for the analysis of this thesis requires events with one or two energetic electrons, a subsample of the entire dataset, the so called high* p_T *inclusive electron sample, has been used. This sample contains about 27000 events from run 1a and 130000 events from run 1b with at least one high energy electron. Selection requirements have been then applied to these events to identify the electrons in the two decay channels.*
In this chapter, after a summary of the principles of the analysis, it will be given a description of the criteria used to define the high p_T *inclusive electron sample and of the simulation packages used to reproduce the signal and the background events.*

4.1. Overview of the analysis

The analysis performed in this thesis looks for events containing the decay products of pairs of scalar or vector leptoquarks produced at the Tevatron by quark-antiquark annihilation or gluon fusion according to the processes illustrated in Figures (2.3) and (2.4). Each first generation leptoquark can decay to electron and quark up or down with Branching Ratio $Br(Lq \to eq) = \beta$ or to neutrino and quark with $Br(Lq \to \nu q) = 1 - \beta$. The Figure (4.1) gives a graphical representation of the production and decay of pairs of first generation leptoquarks at Tevatron. The final state of scalar and vector leptoquark decay is identical and the experimental acceptance is similar. A leptoquark pair can therefore decay into $eeqq$

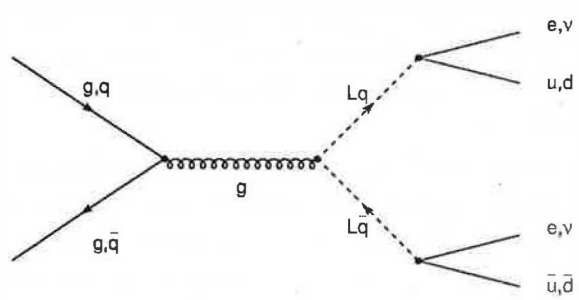

Figure 4.1: *Production and decay of first generation leptoquarks produced at Tevatron by quark-antiquark annihilation or gluon fusion.*

with Br equal to $\beta \cdot \beta = \beta^2$, into $e\nu qq$ with Br equal to $2\,\beta(1-\beta)$ and into $\nu\nu qq$ with Br

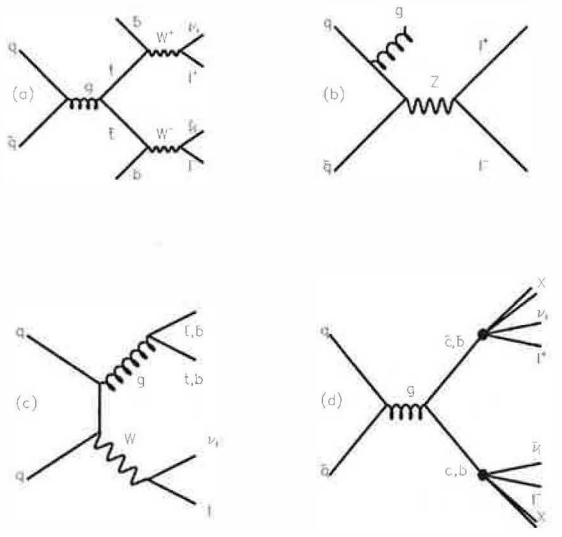

Figure 4.2: *Diagrams of the main backgrounds of the searches in the $e\nu jj$ and $eejj$ decay channels.*

equal to $(1-\beta)^2$.

In this thesis the decay channels under study are the $e\nu jj$ and $eejj$: the final state with $\not\!\!E_T$ + jets, coming from $\nu\nu qq$, was not studied since it suffers from an enormous QCD multijet background, which is very difficult to be estimated in a reliable way. This problem is avoided, for instance, in the search for second and third generation leptoquarks [84] thanks to the use of $c-$ and b-tagging techniques used to eliminate jets from u and d quarks which are the typical QCD jets. The kinematical features of the interesting events for the search in the $eejj$ or $e\nu jj$ decay channels are the presence of one or two isolated and energetic electrons, two high energy jets from quarks fragmentation and missing transverse energy in the decay channels with neutrinos.

The decay products of each possible channel can be mimicked by events with similar kinematical features. For the $e\nu jj$ decay channel the main sources of background are events with (W + jets), where the W decays into $e\nu$, and $t\bar{t}$ events, where one top quark decays semileptonically into bottom. Diagrams of these decays are plotted in Figure (4.2) (a) and (c). Other constributions, given for example by QCD events where jets can be misinterpreted as electrons, have been estimated as negligible, thanks to the very stringent kinematical cuts applied. The main background events, whose production cross section is higher than the leptoquark's cross section, can be eliminated by taking advantage of a few differences in the decay process, like the presence of the W in the background events, which suggests a cut on the electron-neutrino transverse mass $M_T(e,\nu)$, or the presence of b-jets, in $t\bar{t}$ events, which can be eliminated by applying anti-B tagging requirements.

Thanks to the generated Monte Carlo events, it is possible to study the behaviour of

the background events and to estimate the quality of the selection requirements, which are asked to give a good background rejection by maintaining an high selection efficiency.

The main Standard Model sources of background for the search in the $eejj$ channel are Drell-Yan and $t\bar{t}$ events. In the Drell-Yan events a Z or a photon from quark-antiquark annihilation, produced in association with a gluon which fragments into jets, decays into leptons, which in this case are electrons (see Figure (4.2)(b)). At lowest order in perturbation theory, and assuming $M_{e^+e^-} \ll M_Z$, the Drell-Yan cross section is given by the annihilation process $q\bar{q} \to \gamma^* \to e^+e^-$. At higher energies, and in particular at Tevatron, when $M_{e^+e^-} \sim M_Z$, the photon contribution must be supplemented by the additional contribution from the s-channel Z exchange, as is observed at CDF [85]. In terms of dielectron invariant mass (M_{ee}) distribution, the effect is the presence of the resonance peak at around 91 GeV/c^2, as shown in Figure (5.16), where the dots represent the M_{ee} distribution on data. It is, therefore, straightforward to apply a selection cut to eliminate events in a range of the dielectron invariant mass around the Z peak, where the two electrons originate mainly from Drell-Yan events. A second important source of background is given by $t\bar{t}$ events where both quarks decay semileptonically into electrons, which can be rejected thanks to the stringent cuts in transverse energies applied in the selection.

In the following sections it will be given a description of the data samples used in the analysis and of the Monte Carlo samples generated to simulate signal and background events. The procedure used to find the electrons in the events and to estimate the efficiency of the identification cuts will be described. The details of the analyses in the $e\nu jj$ and $eejj$ channels in scalar and vector case are given in next chapters.

4.2. The high p_T inclusive electron sample

To allow people to have samples of manageable size, data sets have been created at CDF which satisfy general selection criteria and can be used for different analyses. One of these is the so called high p_T inclusive electron sample, the one used in these analyses, which has been obtained from the whole runs 1a and 1b and corresponds to a total integrated luminosity of $(110 \pm 4)\text{pb}^{-1}$, with 26882 events from run 1a and 128761 events from run 1b. This sample was created by applying the cuts listed below to the electron sample obtained with the level-3 trigger requirements seen in Section (3.7), which have been evaluated about 100% efficient. The high p_t inclusive electron sample was originally created for top studies in the lepton plus jets decay channel, and it was created by selecting events with a single, high energy electron passing through the central detector. Electron identification in the central region is made powerful by the presence of the central tracking chamber, the central strip chambers and the central preradiator.

To create the sample at least one central electron in the event is required to pass the following cuts [86], whose efficiencies have been evaluated to be of the order of about 80% [11] on $Z \to ee$ events from data :

1. E_T(electron)$>$ 20 GeV
2. E/p $<$ 1.8

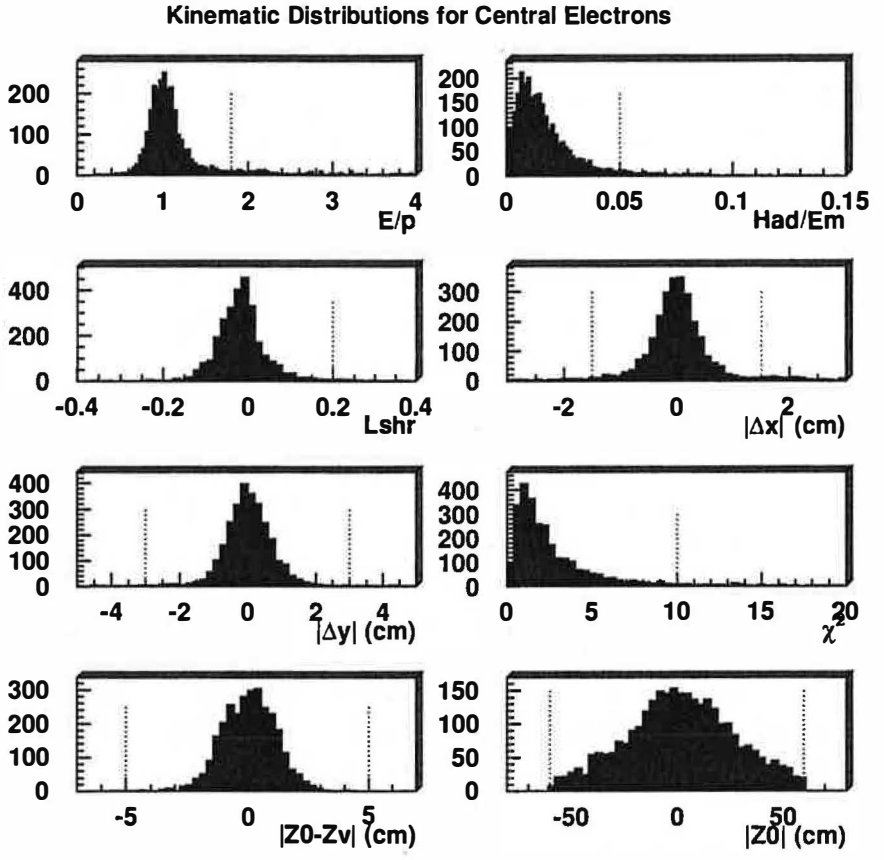

Figure 4.3: *Distributions of the kinematic variables used to define high p_t electrons in the central region of the detector; the dashed lines show the cuts values.*

3. $\frac{Had}{Em}(3 \times 3) < 0.055$
4. $Lshr(3 \text{ towers}) < 0.2$
5. Track Strip Matching: $|\Delta x| < 1.5$ cm
6. Track Strip Matching: $|\Delta z| < 3$ cm
7. $\chi^2_{strip} < 10$
8. $|Z_v - Z_e| < 5.0$ cm
9. $|Z_v| < 60.0$ cm
10. Conversions identified and removed
11. A fiducial Cut

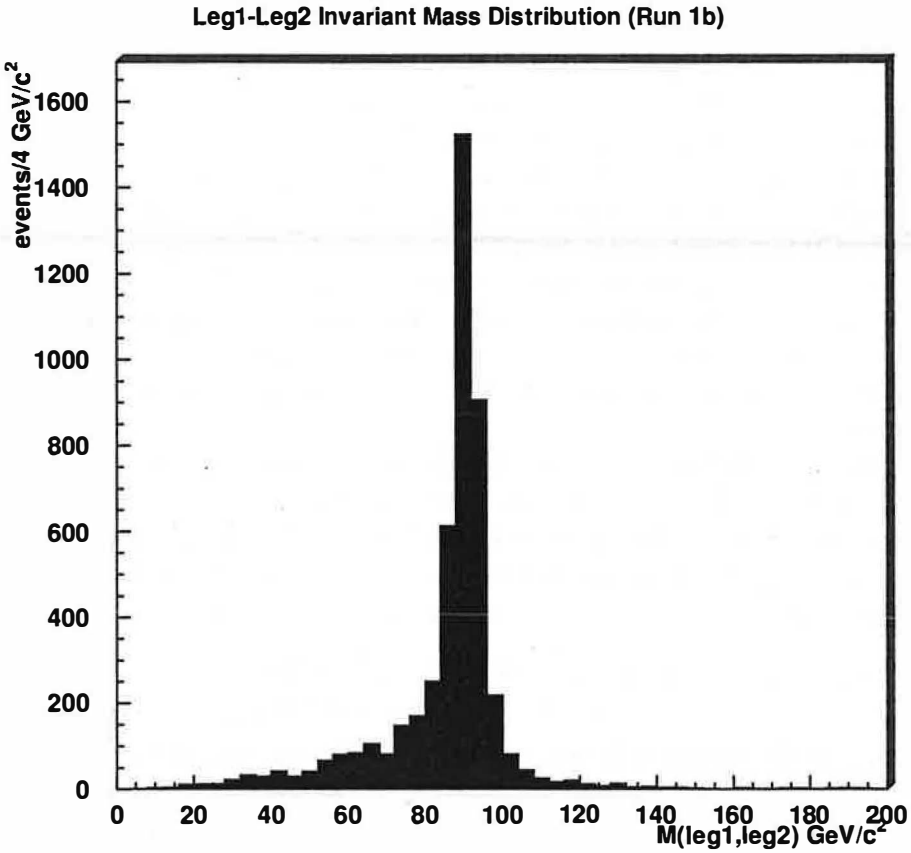

Figure 4.4: *Distributions of the leg1-leg2 invariant mass according to the selection criteria enounced in Section (4.4) before the cut on* $M_{leg1,leg2}$.

The cut on the transverse energy of the electron is required by considering the kinematics of electrons from top decays and is also applicable in leptoquark searches.

The other variables used in this selection are described below and their distributions are plotted in Figure (4.3). They allow a very good discrimination between electron and hadron deposits in the CEM by maintaining an high efficiency in the electron identification. Electrons are expected to release almost all their energy in a single tower of the electromagnetic calorimeter. Their trajectories can be reconstructed in the tracking chambers, and must point to the tower of the calorimeter which has collected the energy. The figure shows the kinematical distributions for the less energetic electron (leg2) in $Z \rightarrow ee$ events from data (run 1b). Leg2's have been found in events where the most energetic electron (leg1) passes the cuts above and where a second electromagnetic calorimeter seed, in the central region, matches a charged track in the CTC and has an invariant mass with leg1 within the Z mass window range [76,106] GeV/c^2. The distribution of the leg1-leg2 invariant mass on run 1b events is plotted in Figure (4.4).

- E/p - This variable estimates the ratio between the electron energy released in the

calorimeter towers and its momentum, measured in the tracking chambers. This value should ideally be distributed around 1, given that the electron mass is small. The E/p distribution has a long tail on the right due to the fact that an electron can radiate photons in the gas of the tracking system and so modify its momentum: in this way the electron momentum is mismeasured while the initial energy is reconstructed correctly, because the emitted photons are usually collected in the same tower as the electron.

• Had/Em - It is the ratio between the hadronic and electromagnetic energies released by the particle in the CHA or WHA and in the CEM respectively. Electromagnetic and hadron calorimeters have been designed according to a tower geometry. Each tower has an electromagnetic shower counter in front of a corresponding hadron calorimeter: in such a way one can perform a direct comparison between the electromagnetic and hadron energies on a tower-by-tower basis. To evaluate this variable, the deposit into three towers along the η direction has been used.

• Lshr - It is defined as lateral energy sharing for the electrons in the central electromagnetic calorimeter and compares the energy deposits in the two adiacent towers in the η direction with the energy collected in the cluster's seed tower. The sharing characteristic is defined as the ratio between the excess energy measured in the adjacent towers over the fluctuations in energy measurement:

$$Lshr = 0.14 \times \frac{M_{TotalShare} - P_{TotalShare}}{\sqrt{(0.14 \times 0.14 * E_{Total} + \sigma^2_{P_{Total}})}} \tag{4.1}$$

where $M_{TotalShare}$ is the energy released on the two adjacent towers to the cluster and $P_{TotalShare}$ is the expected sharing for the given strip chamber coordinate based on test beam results; $0.14 \times \sqrt{E_{Total}}$ is the resolution of the calorimeter and $\sigma_{P_{Total}}$ the uncertainty in the estimation of $P_{TotalShare}$.

• $|\Delta x|$ and $|\Delta z|$ - The matching between CTC tracks with electromagnetic clusters information is the basis for electron identification: these two variables check the alignement of tracks and towers. $|\Delta x|$ is the displacement in the $r - \phi$ plane between extrapolated track from CTC and central electromagnetic tower (CES chamber position) and $|\Delta z|$ is the displacement in the $r - z$ plane, where the track reconstruction uncertainties are larger.

• χ^2_{strip} - This variable is the χ^2 of the comparison between the CES shower profile in the z direction for electrons coming from the interaction and the same quantity measured during the test beams.

• $|Z_v - Z_e|$ and $|Z_v|$ - The cuts on these two variables guarantee on the good quality of the tracks in the event and allow rejection of cosmic rays. The cut on $|Z_v|$ is a cut on the longitudinal z-vertex distribution: the cut at 60 cm corresponds to the requirement that the events fall within the fiducial volume of the vertex time-projection chambers. The cut on $|Z_v - Z_e|$, the longitudinal distance between primary vertex and electron vertex, assures that the electron comes from a $p\bar{p}$ interaction.

• Conversion removal - Electrons may result from pair production following photon conversion, for example in $\pi \rightarrow \gamma\gamma$ decays. They can be removed with high efficiency using tracking information. Any electron that does not have a matching VTX track, or that can be paired with an oppositely charged CTC track to form a small effective mass, is rejected, since it might have come from a photon conversion.

The conversion identification considers the primary electron as a conversion electron if

it has a partner meeting the following requirements:

1. $|\Delta \cot(\vartheta)| < 0.06$
2. $|\Delta(r - \phi)| < 0.3$
3. -20 cm $< R_c <$ 50 cm

.OR.

1. VTX occupancy < 0.2 for the primary electron

where the variable $|\Delta \cot(\vartheta)|$ represents the difference in the polar angle between the primary electron and its partner and $|\Delta(r - \phi)|$ is the azimuthal separation of the two tracks at their point of tangency: conversions should display a peak near zero in both of these variables. The variable R_c is the radial distribution of conversions. The VTX occupancy is a property of the electron track itself and does not require the identification of a partner. The occupancy is defined as the ratio of found to expected VTX hits in a good rotation (away from a radial board), provided that the number of expected VTX hits is at least three. If fewer than three VTX hits are expected, the occupancy variable is defined to be one. The algorithm which performs the conversion removal is about 90% efficient [87].
• Fiducial Cut - This cut takes into account the geometry of the central electromagnetic calorimeter and rejects electron candidates which don't fall within its active volume. The regions of the central electromagnetic calorimeter which are not allowed by this cut are the edges of each module: the electron is required to lie within 21 cm on the tower's center in the $r - \phi$ view so that the shower is fully contained in the active region Also the region $|\eta| < 0.05$, equivalent to the clusters whose $|z|$ coordinate is less than 9 cm, where the two halves of the detector meet, is excluded. There are inactive regions, for example the towers 9 of each module, which are the towers with the largest pseudorapidity, and the 7^{th} tower of the so-called"chimney" modules [1], which are uninstrumented because they are the penetration for the cryogenic connections to the solenoidal magnet.

This cut is suggested by the inactivity of several regions of the detector: to be consistent with the change of acceptance due to the exclusion of these regions, the same requirement has been applied to simulated data in the analysis.

4.3. The Monte Carlo generators: Pythia and Vecbos

As already stated in previous sections, the knowledge of the behaviour of leptoquark and Standard Model background events allows to find a good discrimination between signal and background, optimized to reduce the background by maintaining an high selection efficiency. This knowledge is given by Monte Carlo studies on simulated events. In this section a few

[1]The "chimney" wedge module is a single special module constructed so as to allow access to the CDF superconducting solenoid magnet. The electromagnetic calorimeter in this module consists of normal towers 0-6 and a tower 7 which combines the area of the normal towers 7 and 8. There is no tower 9 in this module.

words will be dedicated to the description of the simulation packages used in this thesis to generate leptoquark and background events: Pythia [88] and Vecbos [89].

Pythia is the Lund Monte Carlo event generator program especially developed for the generation of hadronic physics events at high energies, that is for the description of collisions at high energies between particles such as p and $\bar{p}$, which is our case. Following a "chronological order", the collision and the event generation follow these steps:

(i) The two particles coming one toward the other are characterized by a set of parton distribution functions, which define their partonic substructure in terms of flavour composition and energy sharing. The parton distribution function gives the probability to have a certain parton in the beam particle with a certain fraction of the total momentum and usually depends also on the variable Q^2, the momentum scale, that is a characteristic of the hard process [2];

(ii) An initial state shower can be produced, like $q \rightarrow qg$, from partons of each beam;

(iii) One parton from each of the two beams participates to the hard process to generate the outgoing partons, which are usually two;

(iv) The outgoing partons can eventually emit radiation;

(v) Colour confinement ensures that the outgoing quarks and gluons are not observable and that they fragment into colour singlet hadrons. The process through which coloured partons (quarks and gluons) give colourless hadrons is called fragmentation or hadronization, based on the model of string fragmentation. The hadronization is based on a phenomenological approach, the Lund string model [92], due to the important QCD feature that perturbation theory is only applicable at short distances, due to the value of α_s, while at long distances it becomes strongly interacting and perturbation theory breaks down;

(vi) Unstable hadrons decay further.

In Pythia the perturbative corrections to lowest order diagrams can be made using a matrix-element approach, in which all the Feynman diagrams are exactly calculated to a certain order taking into account the kinematics of the process. Another option, which is usually the default, is the parton shower method which uses approximations derived by simplifications of the kinematics.

It has been necessary to implement the vector leptoquarks production in Pythia, since it is not present by default. Based on the calculations found in [31], it has been possible to insert the differential cross section $d\sigma/d\hat{t}$, which in the vector case is spin dependent and is also function of the anomalous couplings k_G and λ_G. Moreover it has been assumed that also vector leptoquarks, like scalar, decay isotropically.

[2] There is an huge set of pdf's available for the proton, the most recent ones are next-to-leading order evolutions of the Altarelli-Parisi equation, such as the different sets of Martin, Roberts and Stirling (MRS) [90] or a number of versions from the CTEQ collaboration [91].

The other simulation package used to generate events has been Vecbos. It is a leading order QCD Monte Carlo for the production of a W boson plus up to 4 partons or a Z boson plus up to 3 partons. While in Pythia the perturbative corrections to lowest order diagrams are determined with the parton shower, Vecbos is based on exact calculations of matrix element for each process involving a $q\bar{q}$ pair, a vector boson and a fixed number of partons [3]. In Vecbos the events are generated at parton level. This means that the final structure of the event can be determined by using other generators, like Herwig [93], which provide the fragmentation processes for the partons.

To calculate the production cross section of the events generated by Vecbos, an adaptive algorithm is used, which performs multidimensional integrations in the phase space of the event. Vecbos proceeds according the so called *important sampling method*, which automatically concentrates the evaluation of the integral in those regions where the integrand is large in magnitude. To find regions of interest in the phase space it associates to each event a weight proportional to its cross section.

To assign weights to the events, Vecbos must be run twice: the first time it roughly generates many thousands of events, and with their weight it maps the phase space. It produces a *grid* file where the phase space is subdivided in regions, each one characterized by a certain weight, in such a way that when it is run a second time each generated event, according to its kinematical features, will have a weight assigned. This latter will be compared to W_{max}, the maximum weight in the grid, and the event will be accepted or rejected depending on the outcome of the comparison between its weight and W_{max}. In this second step Vecbos reads, in the grid file, the weight W assigned to the event. It compares W, $W_{\max}$ and an uniformly distributed random number η, $0 < \eta \leq 1$. The event is accepted if $W/W_{\max} < \eta$, otherwise it is rejected.

4.3.1. Monte Carlo Simulation of the Detector

There are numerous Monte Carlo generators that attempt to model the physics of $p\bar{p}$ collisions. These usually produce, in suitably formatted arrays, a detailed report on the particles entering and exiting the collision. In order to fully understand what these collision products will look like on data, it is necessary a simulation of the detector that takes the output from the Monte Carlo generators and models the response of the detector to particles passing through it. For this purpose at CDF it is commonly used the "quick" detector simulator, called QFL [94], which doesn't calculate the response of each detector component, but rather models the combined response of the whole detector and the reconstruction algorithms; the model is then tuned to agreement with the data. The output of QFL is in the same format as the processed detector data, so the same programs can be used to analyze both generated and recorded events.

[3] Vecbos has been used to generate (W + jets) events which are the main source of background for the search in the $e\nu jj$ channel. With respect to Pythia, which calculates the exact $2 \rightarrow 2$ process plus one parton to produce one jet, whereas the other jets of the events are obtained via a parton showering process, Vecbos exactly calculates all the matrix elements of these processes.

4.3.2. Monte Carlo samples for signal and background

Simulated events for both signal and background have been generated to understand better the kinematics of the signal and to elaborate methods to discriminate them from the main sources of background. On these samples the final selection efficiencies used for the calculations of the limits on the leptoquark production cross sections have been then evaluated.

For the scalar leptoquarks search in the $e\nu jj$ decay channel, 40000 scalar leptoquark events with masses ranging between 140 and 210 GeV/c^2 have been generated to simulate the signal with Pythia using the CTEQ4L as parton distribution function for the proton and $Q^2 = M^2_{S1}$ as momentum scale. By default the initial and final state radiations have been set on. To reproduce the main backgrounds (W + jets and $t\bar{t}$ events), 13000 (W + 1 jet), 32000 (W + 2 jets) and 11000 (W + 3 jets) events have been generated with Vecbos and 44000 $t\bar{t}$ events have been generated with Isajet.

To search for scalar leptoquarks in the $eejj$ decay channel, 48000 scalar leptoquark events with masses ranging between 100 and 240 GeV/c^2 and the same settings as in the $e\nu jj$ channel have been generated with Pythia to simulate the signal and 30000 Drell-Yan $Z/\gamma \rightarrow eeg$ events and 20000 $t\bar{t}$ events have been generated with Pythia to simulate the main backgrounds.

In addition to these samples vector leptoquark events have been generated with Pythia to evaluate the selection efficiencies for their searches. Since in this case there is a dependence of the production cross section on the anomalous couplings, 4000 events for each M_{V1} between 200 and 400 GeV/c^2 for $\lambda_G = 0$ and $K_G = 0$ as well as for $\lambda_G = 0$ and $K_G = 1$ have been generated, both for the $e\nu jj$ and for the $eejj$ decay channels.

4.4. Electron selection for the search in the $e\nu jj$ and in the $eejj$ channels

Starting from the almost 160000 events of run 1 obtained with the preselection detailed in Section (4.2), requirements for electron's identification in the two decay channels have been applied.

For the search in the electron-neutrino channel the selected electron is taken to be the most energetic object in the bank of the central electromagnetic calorimeter passing the cuts referred as "tight" and listed in Table (4.1): these cuts are the same used to create the pre-sample described in Section (4.2), with the addition of the calorimeter isolation cut. The isolation variable expresses the requirement that the lepton is not surrounded by jet activities, as should be the case in a leptoquark decay. The isolation variable is defined as the ratio between the transverse energy deposited in the electromagnetic calorimeter in a cone, with axis the electron direction and with radius $R = \sqrt{(\delta\eta)^2 + (\delta\phi)^2} = 0.4$, and the electron transverse energy:

$$Isolation = \frac{\Sigma E_T(cone\ R = 0.4)}{E_T(electron)} \tag{4.2}$$

CUT	Tight (Central)	Loose (Central / Plug)
Had/Em	< 0.05	< 0.1
E/p	< 1.8	< 4.0 / *none*
Isolation	< 0.1	< 0.1
$\|\Delta x\|$	≤ 1.5 cm	*none*
$\|\Delta z\|$	≤ 3.0 cm	*none*
$Lshr$	< 0.2	*none*
χ^2_{str}	< 10.0	*none*
$\chi^2_{3\times3}$	*none*	≤ 3.0
$\|Z_v - Z_e\|$	≤ 5.0 cm	*none*
$\|Z_v\|$	≤ 60.0 cm	*none*
Conversion	yes	yes
Fiducial	yes	*none*

Table 4.1: *Electron-ID cuts applied in this analysis: the requirements are a central electron passing the tight cuts in the $e\nu jj$ analysis and a central electron passing tight cuts and a central or plug electron passing looser cuts in the $eejj$ analysis.*

In the electron-electron channel, the requirements for electrons identification are the tight cuts for the most energetic electromagnetic calorimeter bank in the event and the loose cuts for the second most energetic one. The loose cuts are less stringent and applied to electromagnetic clusters deposited in the central region, being or not in the fiducial volume, and in the plug region, where there is no distinction between fiducial or non-fiducial volume. The plug electrons must pass a cut over the variable $\chi^2_{3\times3}$, which characterizes the lateral shower profile in the plug electromagnetic towers: it measures the deviation of the shower from the predicted shower shape from test beam data by using a 3×3 array of the plug electromagnetic calorimeters towers.

4.4.1. Electron identification efficiency

The efficiencies of the cuts for the identification of the electrons, summarized in Table (4.1), have been evaluated on Monte Carlo leptoquark events and then cross-checked on $Z \rightarrow ee$ events from run 1b as explained in Appendix A.

The efficiencies ε's are intended as identification efficiency for single electron (ε_e) in the $e\nu jj$ channel and for dielectrons (ε_{ee}) in the $eejj$ channel. A difference in the results on generated events and real data will be intrinsic, due to the different kinematics of electrons coming from leptoquark decay and electrons in $Z \rightarrow ee$ events.
On simulated leptoquark events the efficiency ε has been defined as:

$$\varepsilon(M_{Lq}) = \frac{N_{passed}}{N_{total}} \tag{4.3}$$

N_{total} is the number of events with one central and fiducial electron with $E_T > 30$ GeV in the $e\nu jj$ channel or with two central or central/plug electrons with $E_T > 40, 15$ GeV,

$M_{S1}(GeV/c^2)$	ε_e "$e\nu jj$"	$M_{S1}(GeV/c^2)$	ε_{ee} "$eejj$"
140	$(72.2 \pm 2.2)\%$	**100**	$(65.9 \pm 1.9)\%$
150	$(72.0 \pm 2.1)\%$	**120**	$(65.2 \pm 1.8)\%$
160	$(72.0 \pm 2.1)\%$	**140**	$(63.7 \pm 1.7)\%$
170	$(70.9 \pm 2.1)\%$	**160**	$(60.3 \pm 1.6)\%$
180	$(69.7 \pm 2.0)\%$	**180**	$(62.9 \pm 1.7)\%$
190	$(70.1 \pm 2.1)\%$	**200**	$(60.8 \pm 1.6)\%$
200	$(67.7 \pm 2.0)\%$	**220**	$(60.3 \pm 1.6)\%$
210	$(69.7 \pm 2.0)\%$	**240**	$(58.5 \pm 1.5)\%$

Table 4.2: *Electron-identification efficiencies evaluated on Monte Carlo leptoquark events for the two analyses in the scalar case.*

the most energetic one in the fiducial region, in the $eejj$ channel matching the generated electrons from the leptoquarks decay. N_{passed} is the number of events, among the N_{total}, with one electron passing the tight selection cuts in the $e\nu jj$ channel or with two electrons passing the tight and loose identification cuts in the $eejj$ channel.
The efficiencies range from about 68 to 72 % in the $e\nu jj$ channel and from about 59 to 66 % in the $eejj$ channel for different masses, as reported in Tables (4.2), for scalar leptoquark events. These values are in agreement with the efficiencies evaluated on real data, according to the procedure explained in Appendix A.

Chapter 5

Search for scalar leptoquarks in the $e\nu jj$ and $eejj$ decay channels

Introduction- *This chapter is dedicated to the description of the procedures used to accomplish the analysis in the $e\nu jj$ and $eejj$ channels from scalar leptoquark decay. In the electron neutrino channel a way to proceed, which will be the chosen one, is based on cuts on a relative likelihood variable built with the kinematic variables of the event. It will be called, in the following, the "relative likelihood analysis". A second procedure, which will be described in Appendix C, is based on a computation performed with a neural network and will be referred to as the " Neural network analysis": it doesn't improve either the efficiency of the other analysis or the expected limit on the leptoquark production cross section, and for this reasons it has not been pursued further. In the dielectron channel the data sample of the $e\nu jj$ search has also been used; in this case the selection requirements have been based exclusively on the kinematical features of the events. The results obtained from these two channels have been combined in Chapter 7 to give stringent limits on the existence of first generation scalar leptoquarks.*

5.1. Selection requirements in the $e\nu jj$ decay channel

The so called "relative likelihood analysis" searches for a pair of leptoquarks decaying into $e\nu jj$, as shown in Figure (2.10), by requiring a highly energetic, isolated electron and two energetic jets; moreover, part of the total energy of the event should be missing, due to the presence of the neutrino.

If β indicates the branching ratio of the decay of a scalar leptoquark S1 into electron plus quark, $\beta = Br(\mathrm{S1} \to \mathrm{eq})$, then the branching ratio in this decay channel will be given by $2\beta(1-\beta)$. As described more in detail in Section (4.1) and illustrated in Figure (4.2), the main backgrounds for the search in the $e\nu jj$ channel are events with two or more jets coming from the semileptonic decay of (W + $\geq$ 2 jets) events where the W decays into electron and neutrino, and from $t\bar{t}$ events with one top decaying semileptonically in electron and neutrino, and the other top decaying hadronically.

The selection cuts applied to data are summarized here and explained in detail below:

1. one electron *tight* with $E_T > 30$ GeV
2. at least two jets with $E_T^C > 30, 15$ GeV
3. $\not\!\!E_T > 20$ GeV
4. no events with 2^{nd} charged lepton ($e^{\pm}, \mu^{\pm}$)
5. no B-tagged events
6. no events with $\Delta\phi(\not\!\!E_T, jet) < 10°$ if $\not\!\!E_T/\sqrt{\sum E_T} < 4$ GeV$^{1/2}$
7. $E_T^C(jet1) + E_T^C(jet2) > 60$ GeV
8. $E_T^C(jet1) + E_T^C(jet2) + \not\!\!E_T > 100$ GeV
9. $LOG3 < -10.5$

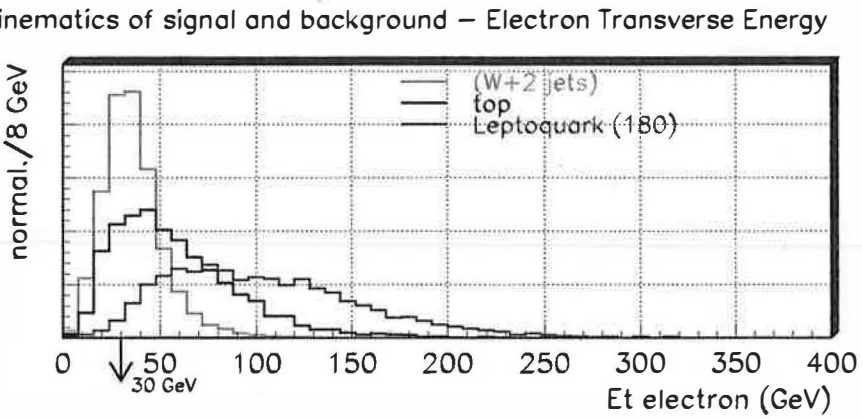

Figure 5.1: *The cut on the transverse energy of the most energetic electron is at 30 GeV. The plot shows the E_T(electron) distribution for the most energetic electron in leptoquark events with* $M_{S1} = 180$ GeV/c^2. *The distributions of the transverse energy for (W + 2 jets) and $t\bar{t}$ events are also shown: all three distributions have been normalized to 1.*

The most important selection requirement is the one at the point 9., where the variable $LOG3$ is defined through the functions describing the distribution of kinematic variables for the signal and for the background interpreted as probability distributions, as will be explained in next section.

Here follows a short explanation of the other selection requirements.

1. To select the events, the electron must pass the tight identification cuts listed in Table (4.1), that means it is identified using the same requirements for the high p_T inclusive electron sample in use here and it is also required to be isolated, according to the definition of isolation variable given in Section (4.4). The distribution of the transverse energy of the most energetic electron of the event is plotted in Figure (5.1) for simulated signal events ($M_{S1} = 180$ GeV/c^2) [1] and, for comparison, for (W + 2 jets) and $t\bar{t}$ events: the three distributions have been normalized to 1. In the selection is applied the cut $E_T > 30$ GeV on the uncorrected transverse energy of the electron.

2. In the Figures (5.2) and (5.3) are plotted for signal and main backgrounds the distributions of the transverse energies of the two most energetic jets corrected for underlying events and for calorimetry/clustering effects. The cone size R of the jets is fixed at the value 0.7. The calorimeter clusters which match towers in the electromagnetic calorimeter, which are not coming from conversion and are isolated are discarded because they are supposed to be electrons (electron-jet veto). The two most energetic jets are required to have $E_T^C > 30, 15$ GeV.

3. In this analysis the uncorrected missing transverse energy of the event, defined in Equation (3.15), is used. An initial cut has been applied at 20 GeV to clean the sample,

[1] This value represents the mass at which has been otpimized the search in the $e\nu jj$ channel in the scalar case.

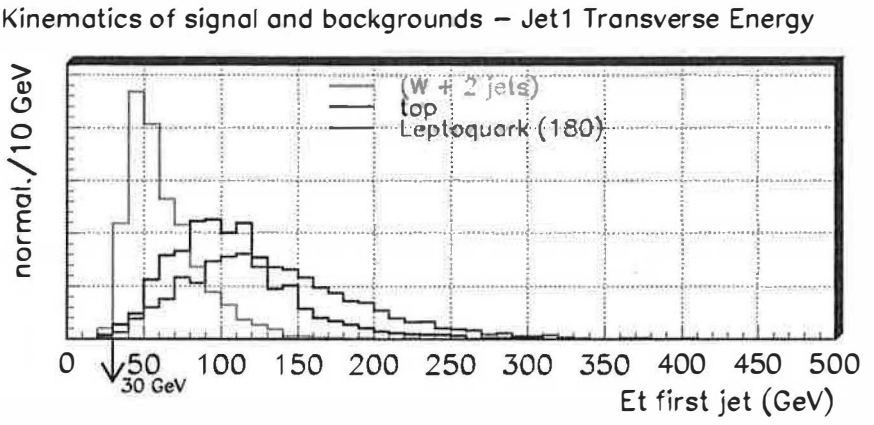

Figure 5.2: *Transverse energy distribution for the most energetic jet in leptoquark events with* $M_{S1} = 180$ GeV/c^2*: the cut on this variable is at 30 GeV. The distributions of the transverse energy for (W + 2 jets) and* $t\bar{t}$ *events are superposed to the signal one: the three distributions have been normalized to 1.*

especially from QCD background, and in the final part of the selection the variable $\not\!\!E_T$ enters in the evaluation of the relative likelihood function, as will be explained below. The distribution of the uncorrected missing energy of the events for signal and background is plotted in Figure (5.4).

4. Events are also required not to have a second charged lepton, either electron or muon, to eliminate background given in particular by Drell-Yan or top dilepton events. These second charged leptons can be electrons with E_T >15 GeV identified with the loose identification cuts of Table (4.1) or can be muons with p_T >15 GeV which leave an energy deposit in the electromagnetic calorimeter lower than 2 GeV and in the hadron calorimeter lower than 6 GeV.

5. It is possible to anti-tag events with jets coming from the fragmentation of second or third generation quarks, in particular with jets containing B-hadrons, coming from $t\bar{t}$ events.

An algorithm used in this analysis is called SECVTX [95], or jet-vertexing, algorithm, which uses the SVX information to reconstruct secondary vertices defined as the point of decay of long-lived B mesons, which originated at the primary vertex. Thanks to their long lifetime, $\tau_0 \sim 10^{-12}$ sec, B-hadrons have a long decay length $c\tau_0 \sim 460$ μm. With the Silicon Vertex detector (SVX) the tracks of charged particles can be reconstructed with a resolution of about 13 μm in the r-ϕ plane, which allows the detection of secondary vertices from B decays with a very good efficiency. The basic idea for this algorithm is to loosen track quality and kinematic cuts to gain efficiency while requiring two or more tracks in a vertex to reject background. The algorithm requires a jet to contain at least two good SVX tracks [2] with $p_T \geq 2$ GeV/c and absolute impact parameter significance $|d|/\sigma_d \geq 3$. Using

[2]The definition of good SVX tracks is given in [11]. As SVX track is defined a CTC track with at least

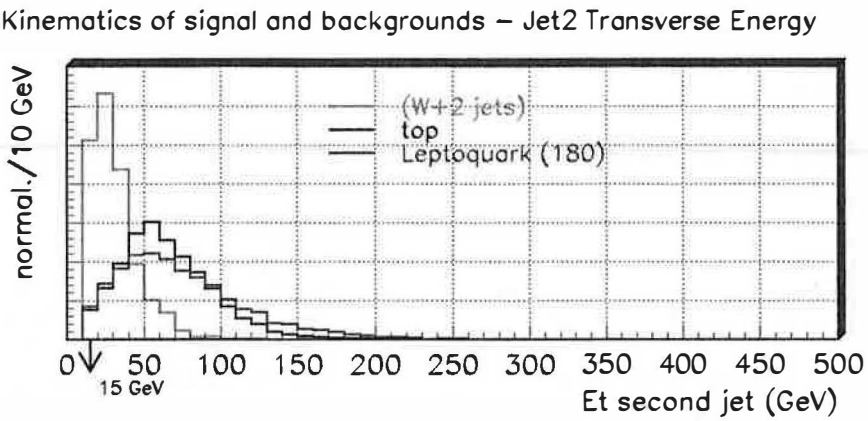

Figure 5.3: *Transverse energy distribution for the second most energetic jet for leptoquark with* $M_{S1} = 180\ GeV/c^2$, *(W+2 jets) and* $t\bar{t}$ *events: the three distributions have been normalized to one. A cut is applied at 15 GeV.*

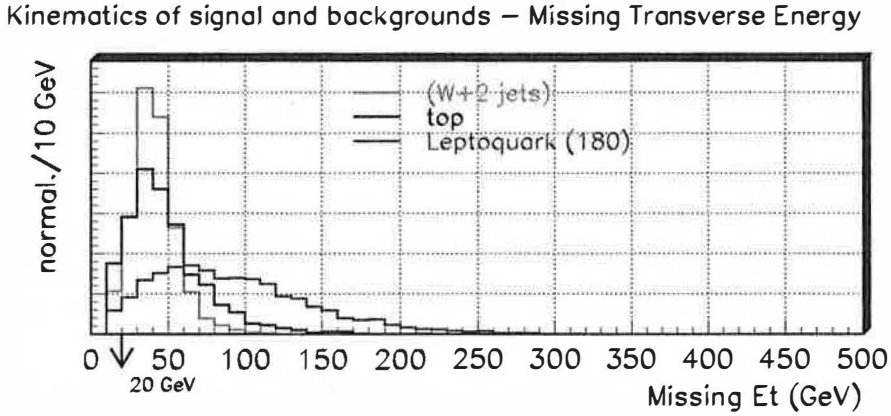

Figure 5.4: *Total missing transverse energy distribution for leptoquark events with* $M_{S1} = 180\ GeV/c^2$ *and for (W+2 jets) and* $t\bar{t}$ *background events. All distributions are normalized to one. A cut at 20 GeV is applied to this variable.*

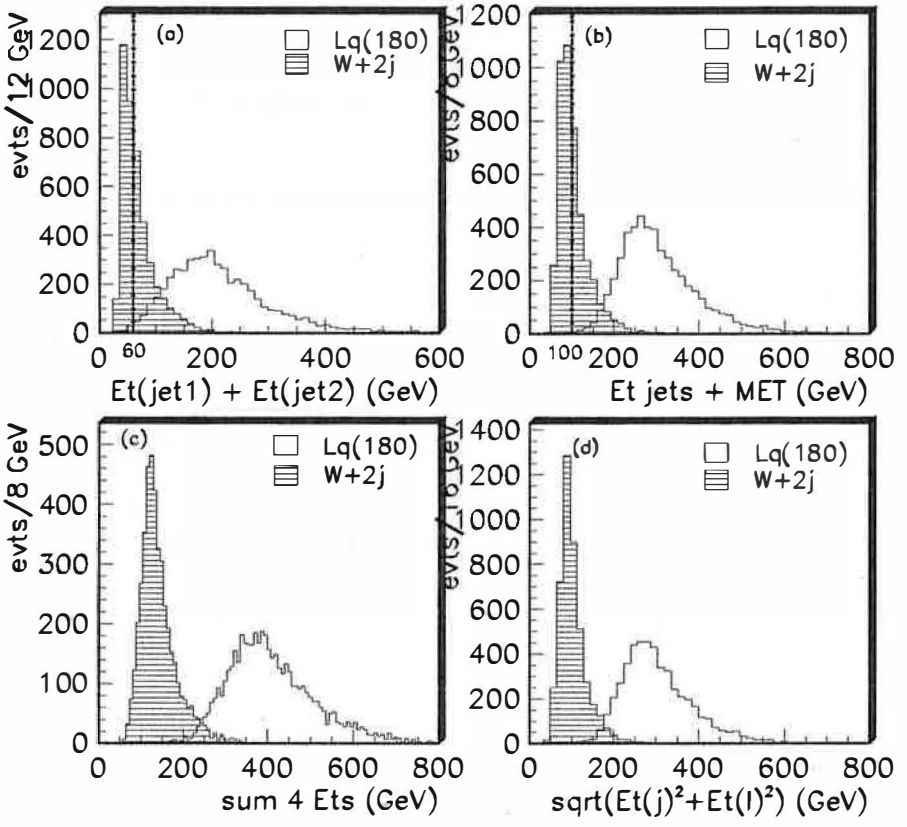

Figure 5.5: *Distribution of the variables (a)* $E_T(j1)+E_T(j2)$, *(b)* $E_T(j1)+E_T(j2)+\not\!\!E_T$, *(c)* $E_T(j1)+E_T(j2)+E_T(e1)+\not\!\!E_T$ *and (d)* $\sqrt{(E_T(e1)+\not\!\!E_T)^2+(E_T(j1)+E_T(j2))^2}$ *for leptoquark* (M_{S1} = 180 GeV/c^2) *and for W + 2 jets Monte Carlo events. Two cuts are applied, as indicated by the vertical lines in the figures: on (a) at 60 GeV and on (b) at 100 GeV.*

these tracks, L_{xy} and its error $\sigma_{L_{xy}}$ are calculated, where L_{xy} is the two-dimensional decay distance to the secondary vertex, measured in the $r-\phi$ plane. The secondary vertex is required to have significance $L_{xy}/\sigma_{L_{xy}} \geq 3$. If these conditions are satisfied, then the jet is classified as b-tagged with the SVX algorithm. Its efficiency is evaluated to be around 40% [11].

A second algorithm for the b-tagging is also used, called SLT (Soft Lepton Tagger)[11] which searches for a lepton in the jet coming from the semileptonic decay of the *b*. It is identified through electromagnetic calorimeter clusters for electrons or stubs in the muon

two associated SVX hits. The SVX χ^2 is then defined to be the increase in the track fit χ^2 when the SVX hits are included in the CTC track fit, divided by the number of included SVX hits. A good SVX track must have $\chi^2 < 6$, at least two of the SVX hits must be associated with exactly one CTC track, there must be no SVX channels with low gain or high noise and the charge profile must be consistent with that of a single particle.

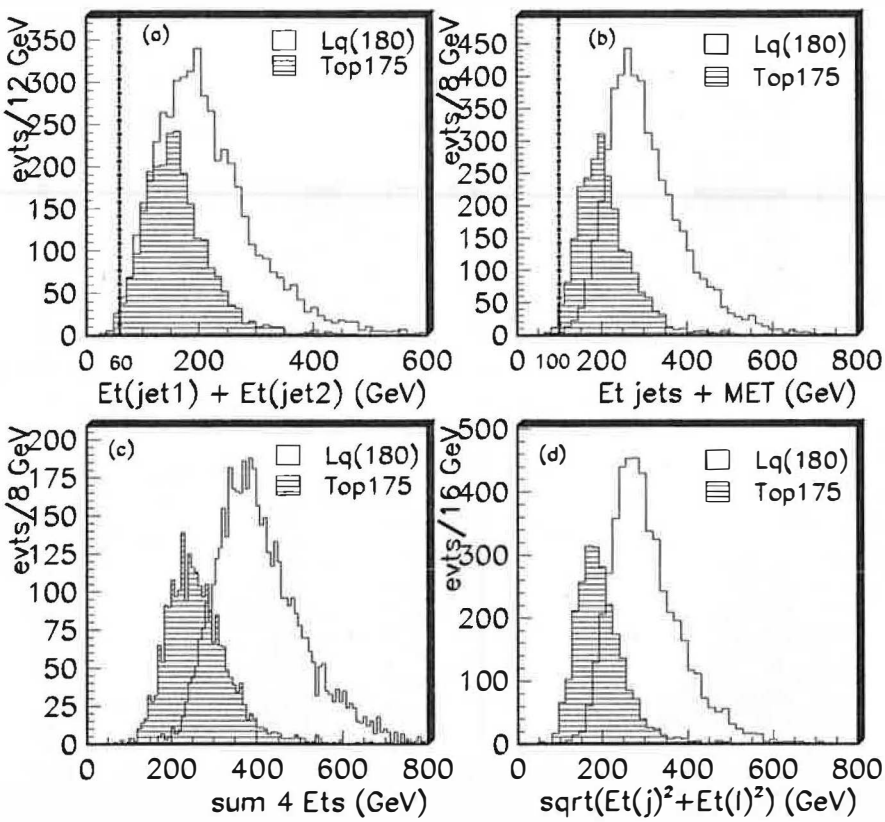

Figure 5.6: *Distribution of the variables (a)* $E_T(j1)+E_T(j2)$*, (b)* $E_T(j1)+E_T(j2)+\not\!\!E_T$*, (c)* $E_T(j1)+E_T(j2)+E_T(e1)+\not\!\!E_T$ *and (d)* $\sqrt{(E_T(e1)+\not\!\!E_T)^2+(E_T(j1)+E_T(j2))^2}$ *for leptoquark* ($M_{S1} = 180$ GeV/c^2) *and for* $t\bar{t}$ *Monte Carlo events. Two cuts are applied, as indicated by the vertical lines in the figures: on (a) at 60 GeV and on (b) at 100 GeV.*

chambers for muons matching a CTC track, and its p_T threshold is kept low (2 GeV/c). The efficiency of this algorithm is lower than the previous method, of about 20% [96], due to the background of hadrons misidentified as leptons and of electrons from non detected photon conversion.

6. Events for which at least one jet is within 10° in ϕ with respect to the $\not\!\!E_T$ direction are not accepted if the $\not\!\!E_T$ significance ($\equiv \not\!\!E_T/\sqrt{\sum E_T}$), that is the weight of the missing transverse energy over the total visible transverse energy, is less than 4 GeV$^{1/2}$. This cut eliminates events in which transverse energy comes from jet mismeasurements due to calorimeter cracks or punch-through's.

7. and 8. Intuitively, if a few kinematic variables are individually able to discriminate background from signal, then their sum may improve their separation and allow a very good background rejection while preserving a high efficiency. Several combinations are shown in Figures (5.5) and (5.6) for backgrounds, compared to leptoquark events. Cuts on the sum

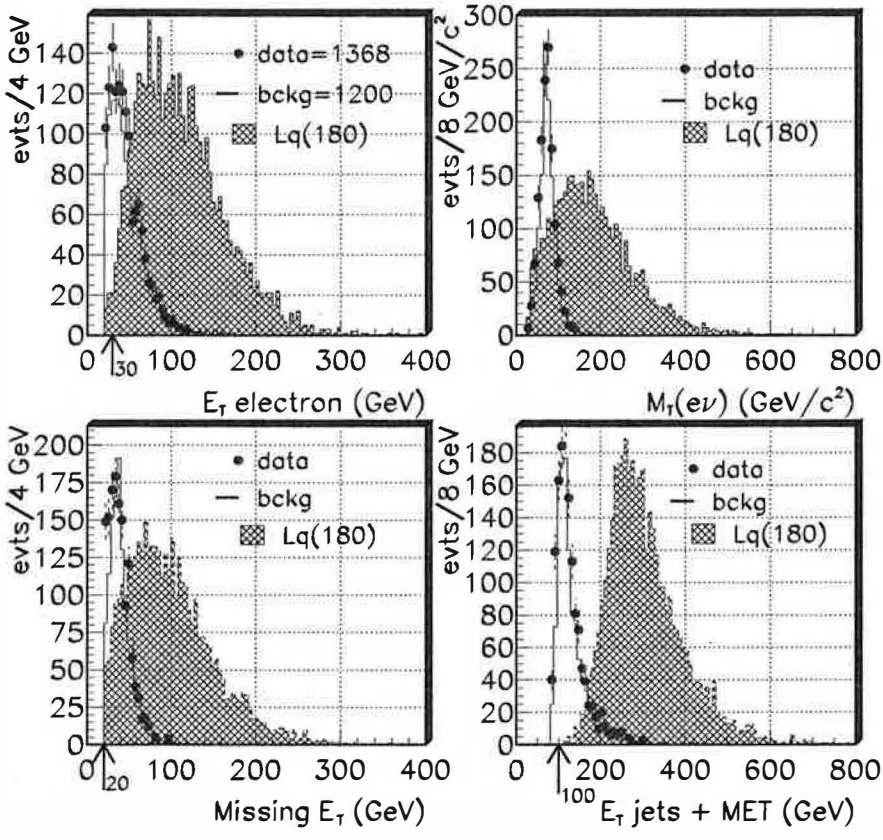

Figure 5.7: *Transverse energy distributions for the most energetic electron, transverse mass of electron and neutrino, missing transverse energy plus transverse energy of jets and missing transverse energy in simulated events (W+ jets) and $t\bar{t}$ normalized to data. Red dots represent run 1a and run 1b data points, the hashed histogram represents the simulated leptoquark events for* $M_{S1} = 180$ GeV/c^2. *The arrows indicate the values of the cuts.*

of the corrected transverse energies of the two most energetic jets and on the sum of the corrected transverse energies of the two most energetic jets with $\not\!\!E_T$ are applied at 60 GeV and 100 GeV respectively.

In Figure (5.7) are shown the distributions of the transverse energies of the most energetic electron, of the $\not\!\!E_T$, of the $M_T(e,\nu)$ and of the variable $E_T^C(j1) + E_T^C(j2) + \not\!\!E_T$ for all backgrounds (W + jets and $t\bar{t}$ events) normalized to the same luminosity of data and, superimposed to them, for data. The normalization factor for the contribution from $t\bar{t}$ events has been estimated by taking the theoretical value $\sigma_{t\bar{t}} = (4.75^{+0.73}_{-0.62})$ pb calculated in [97], while the one from (W + jets) events has been found by using the production cross section calculated by Vecbos. These normalization factors have been corrected by factors determined from a fit on the jet multiplicity distributions for data and for Monte Carlo events [98]. In Figure (5.8) is represented the distribution of the number of jets with $E_T > 15$ GeV

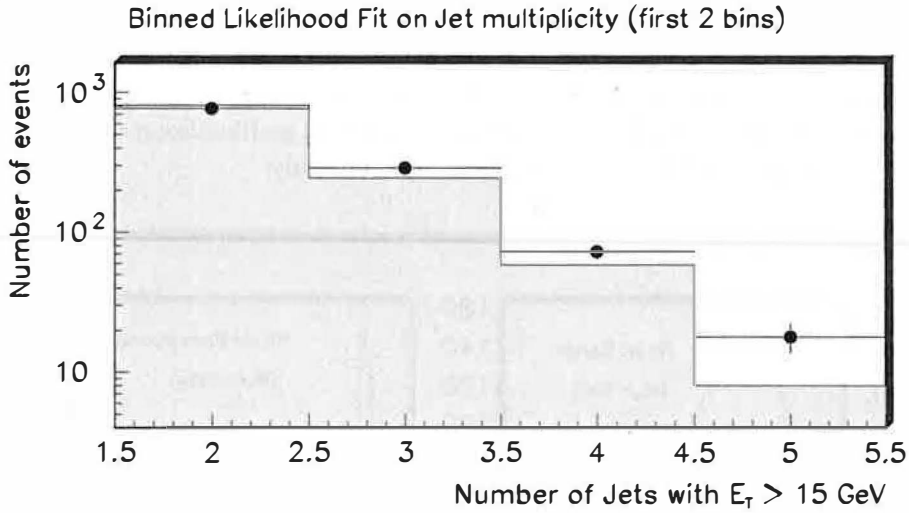

Figure 5.8: *Jet multiplicity distribution of (W + jets) and $t\bar{t}$ events compared with data after a binned likelihood fit performed on the first two bins of the distribution. The (W + jets) events normalization factor has been corrected by a multiplicative term of* (0.643 ± 0.004).

on $W + 1, 2$ and 3 jets and $t\bar{t}$ Monte Carlo events and on data selected by applying a loose selection [3], after a binned likelihood fit on the first two bins. The result of the fit has been a correction parameter of (0.643 ± 0.004) to apply to the (W + jets) events and no correction to apply to the $t\bar{t}$ events.

[3]This loose selection requires, in particular, at least one central, isolated electron with $E_T > 20$ GeV, at least 2 jets with $E_T > 20, 10$ GeV, $\not\!\!E_T > 20$ GeV and $E_T(jet1) + E_T(jet2) + \not\!\!E_T > 100$ GeV.

5.1.1. Relative likelihood studies on kinematical distributions

Let us consider the distribution of a generic variable x of the event, for example the missing transverse energy or the transverse mass of electron and neutrino, $M_T(e,\nu)$, for the Monte Carlo's of the signal and of the background: they can be seen as likelihood distributions for that variable for the signal and for the background respectively.

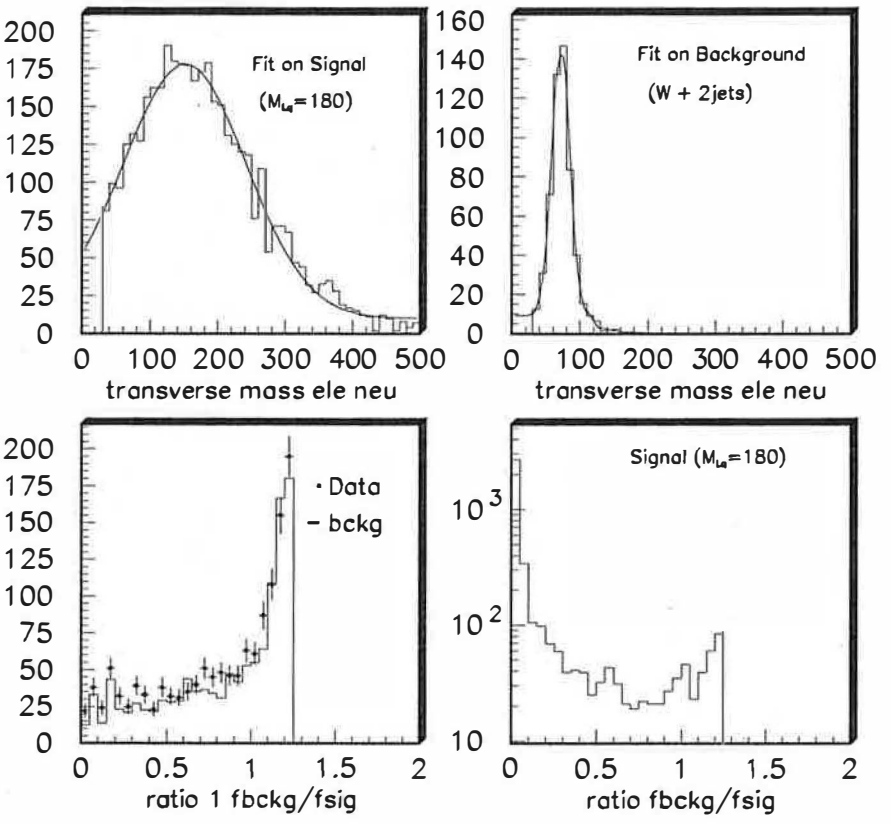

Figure 5.9: *Top: distributions of the variable $x = M_T(e,\nu)$ on the Monte Carlo of signal and of background; the fits give the functions $P_S(x)$ and $P_B(x)$ respectively. Bottom: in the figures are represented the distributions of the ratio $r = r(x) = P_B(x)/P_S(x)$ evaluated for each event on background and on signal respectively.*

The fit of these distributions with an appropriate function for the signal, $P_S(x)$, and for the background, $P_B(x)$, normalized to one in the same range of x can be interpreted as the probability density function of that variable. Through the likelihoods $P_B(x)$ and $P_S(x)$ the variable $r = r(x) = \frac{P_B(x)}{P_S(x)}$ expresses the relative likelihood for the variable x to be background instead of signal. In Figure (5.9)(top) are illustrated the distributions of the variable $x = M_T(e,\nu)$ for signal and background events, and the fits on these distributions with the functions $P_B(x)$ and $P_S(x)$; the ratio r is shown in the two plots on the bottom for events of signal and of background as well as for data, represented by the red dots

superimposed to the r distribution for the backgrounds.

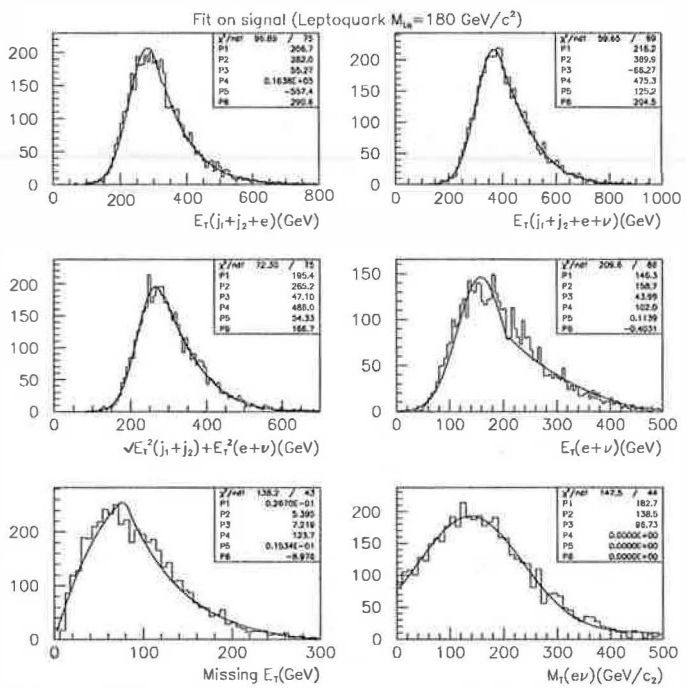

Figure 5.10: *Fits on the kinematical distributions of some variables for the signal* (M_{S1} = 180 GeV/c^2) *and determination of the functions* $P_S(x)$ *listed in Appendix B.*

In the hypothesis that x is well separated for signal and background, the two distributions don't overlap, leading to values for $r(x)$ equal to 0 for each value of x evaluated on the signal and equal to ∞ for x evaluated on the background. In the reality the "x variables" of the events are quite well separated each other for signal and background, but there are points of overlapping in the distributions. Peaks in the r distribution correspond to regions where x is well separated for signal and background.

To take advantage of such a method, one should find suitable "x variables", well separated in signal and background. To illustrate the procedure, in the Figures (5.10) and (5.11) are plotted the distributions of the most common kinematic variables of the event for signal and background respectively, fitted with functions that are described in Appendix B. Corresponding to these plots, in Figure (5.12) are plotted the r distributions evaluated on background and data events.

In this analysis a combination of relative likelihood variables r has been chosen, which is called $LOG3 = \log(r(M_T e,\nu)) + \log(r(\sqrt{(E_T^C(e) + E_T\nu)^2 + (E_T^C(jet1) + E_T^C(jet2))^2}) + \log(r(\not\!\!E_T))$: it depends on the missing transverse energy of the event, $\not\!\!E_T$, on the variable $\sqrt{(\mathrm{E_T^C(e1)} + \not\!\!E_T)^2 + (\mathrm{E_T(j1)} + \mathrm{E_T(j2)})^2}$ and on the electron-neutrino transverse mass $M_T(e,\nu)$.

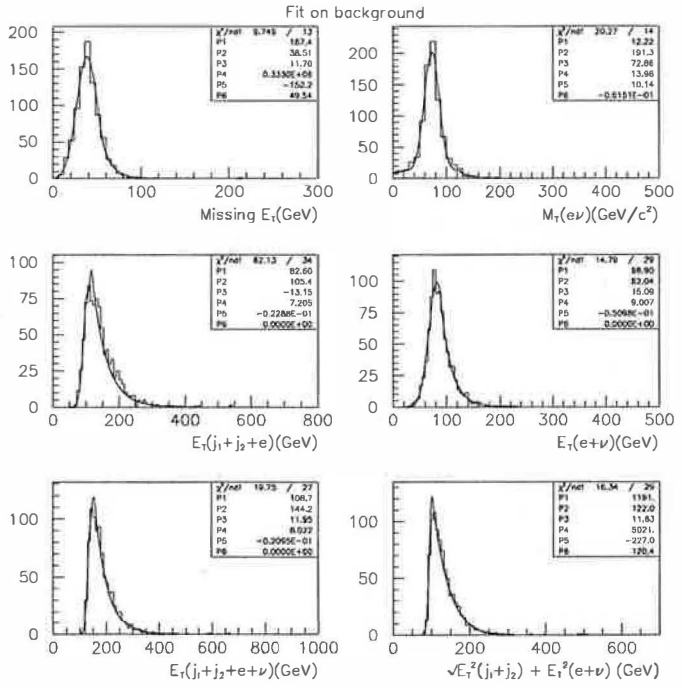

Figure 5.11: *Fits on the kinematical distributions of the same variables of Figure (5.10) for all the backgrounds and determination of the functions $P_B(x)$ as given in Appendix B.*

The variable $\sqrt{(E_T^C(e)+E_T(\nu))^2+(E_T^C(jet1)+E_T^C(jet2))^2}$ represents, in the plane $E_T^C(e)+\not{E}_T$ versus $E_T^C(jet1)+E_T^C(jet2)$, the radius of a circle centered in the origin of the coordinate system. The transverse energy of the electron has been corrected by using factors determined during test beam measurements and through the reconstruction of the W mass on data. The transverse mass $M_T(e,\nu)$ is introduced, rather than the mass, because the informations about neutrinos can be only partially reconstructed, since only the transverse components of its energy and momentum can be measured. The variable $M_T(e,\nu)$, whose distribution is expected to be uniformly spread for electron and neutrino coming from the decay of two different leptoquarks and that should show the typical Jacobian peak for events with a W, is defined as:

$$M_T(e,\nu)=\sqrt{(E_{T,\nu}+E_{T,e})^2-(p_{T,\nu}+p_{T,e})^2} \tag{5.1}$$

The choice of the best combination of relative likelihoods $r(x)$'s to use in the selection has been based on comparisons between the corresponding expected limits on the leptoquark production cross section σ_{exp}^{lim} at $M_{S1} = 180$ GeV/c^2, evaluated as:

$$\sigma_{exp}^{lim}=\frac{(int(N_{bckg})-N_{bckg})^{lim}}{\int \mathcal{L}dt\cdot\varepsilon\cdot Br} \tag{5.2}$$

where the numerator indicates that the estimation is done by assuming that what is pre-

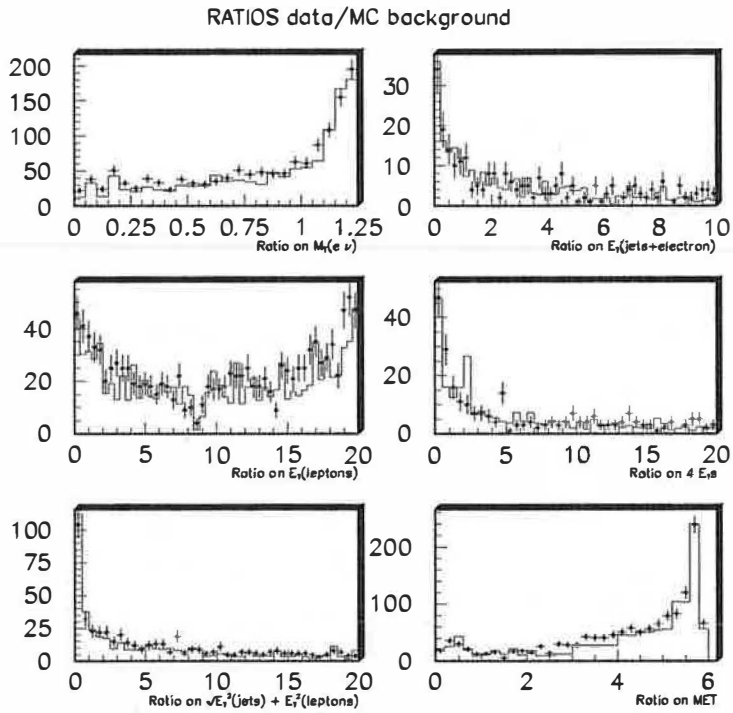

Figure 5.12: *Distributions for background, compared with real data, of* $r(x) = P_B(x)/P_S(x)$ *with* P_B *and* P_S *determined from the fits of Figures (5.11) and (5.10).*

dicted as background is seen on data ($int(N_{bckg})$[4]); the background expectation (N_{bckg}) is then subtracted before determining the upper limit. This upper limit is evaluated by using the Bayesian procedure explained in Appendix D to evaluate upper limits at 95% confidence level. The variable ε is the selection efficiency for that leptoquark mass and Br the Branching ratio for the decay in the studied channel, which in this case is equal to $2\beta(1-\beta)$. The best selection cut is the one which gives the lowest expected upper limit on the cross section, since in principle it minimizes the background, by maintaining an high efficiency. In Table (5.1) are summarized the results of a few checks performed on different combinations of relative likelihood functions, with the corresponding values of selection efficiency evaluated for $M_{S1} = 180$ GeV/c^2, the number of expected background events N_{bckg} and the expected limits on the cross section; Table (5.2) is dedicated to the cuts on the variable $LOG3 = \log(r(M_T e,\nu))+\log(r(\sqrt{(E_T^C(e)+E_T\nu)^2+(E_T^C(jet1)+E_T^C(jet2))^2})+\log(r(\not\!\!E_T))$: it reports the expected limits on the cross section corresponding to different values of the cut. As consistency check between data and background estimation, on all these tables appear also the numbers of real data passing the selection requirements.

A cut at $LOG3 < -10.5$ has been applied. This variable is plotted in Figure (5.13) for all the backgrounds (as white histogram), for data (with red dots), and for leptoquark events with $M_{S1} = 180$ GeV/c^2 (as dashed histogram).

[4]The assumption here is that $int(N_{bckg})$ is equal to the integer number which is closest to N_{bckg}.

Cut	$\varepsilon(\%)$	N_{bckg}	$\sigma \times Br$ (pb)	1a+1b
$\log[r(\not\!\!E_T)]$				
$< -2.$	18.7	(6.6 ± 1.0)	0.40	5
< -2.5	16.9	(4.5 ± 0.8)	0.40	1
$< -5.$	8.5	(0.5 ± 0.1)	0.34	0
$\log[r(M_T(e,\nu))]$				
$< -3.$	21.0	(11.8 ± 1.6)	0.44	19
$< -5.$	15.1	(1.7 ± 0.6)	0.33	2
$< -7.$	9.3	(0.3 ± 0.1)	0.32	0
$\log[r(\not\!\!E_T)] + \log[r(M_T(e,\nu))]$				
$< -5.$	20.2	(3.4 ± 0.7)	0.26	4
$< -7.$	16.6	(1.5 ± 0.2)	0.28	1
$< -9.$	12.9	(0.5 ± 0.1)	0.33	0
$\log[r(\not\!\!E_T)] + \log[r(M_T(e,\nu))] + \log[r(4E_T)]$				
$< -5.$	24.8	(7.8 ± 1.2)	0.31	13
$< -8.$	19.9	(2.5 ± 0.6)	0.29	0
$< -10.$	16.6	(1.5 ± 0.2)	0.28	0
$< -12.$	13.1	(0.5 ± 0.1)	0.33	0
LOG3 + $\log[r(4E_T)]$				
$< -10.$	24.0	(5.9 ± 1.0)	0.29	10
$< -11.$	22.6	(5.1 ± 1.0)	0.28	4
$< -12.$	21.2	(4.5 ± 1.0)	0.32	2
$< -13.$	19.7	(2.7 ± 0.6)	0.28	1
$< -14.$	18.1	(2.0 ± 0.6)	0.27	1

Table 5.1: *List of cuts applied on different relative likelihood variables. For each one are shown the corresponding selection efficiency, the number of expected background events, the expected limit on the leptoquark production cross section and the number of data events surviving the cut. The best cut is the one which gives the lowest upper limit on the cross section, since in principle it minimizes the background, by maintaining an high efficiency.*

Cut	Selection ϵ(%)	N_{bckg}	$\sigma \times Br$ (pb)	1a+1b
LOG3				
$< -8.$	22.8	(5.0 ± 0.9)	0.28	6
< -8.5	22.1	(5.0 ± 0.9)	0.28	6
$< -9.$	21.3	(4.3 ± 0.9)	0.27	4
< -9.5	20.6	(4.1 ± 0.9)	0.29	2
$< -10.$	19.8	(3.2 ± 0.8)	0.27	1
< -10.5	19.0	(1.5 ± 0.6)	0.25	0
$< -11.$	18.1	(1.5 ± 0.4)	0.28	0
< -11.5	17.2	(1.5 ± 0.2)	0.28	0
$< -12.$	15.2	(1.0 ± 0.2)	0.26	0
< -12.5	15.1	(0.8 ± 0.2)	0.27	0
$< -13.$	14.5	(0.8 ± 0.2)	0.28	0
< -13.5	13.8	(0.7 ± 0.2)	0.30	0
$< -14.$	13.2	(0.6 ± 0.1)	0.32	0

Table 5.2: *For different cuts applied to the variable LOG3 are listed the selection efficiencies evaluated for* $M_{S1} = 180$ GeV/c^2, *the expected number of background events, the expected limit on the production cross section and the number of surviving events on data. No events pass the cut at LOG3* < -10.5.

CUT	1a + 1b	Expected background
E_T(j1,j2)> 30,15 GeV	1599	1301
$\not\!\!E_T$ significance	1255	1125
E_T(j1) + E_T(j2)> 60 GeV	900	881
E_T(jets) + $\not\!\!E_T$ > 100 GeV	743	751
LOG3 < -10.5	0	1

Table 5.3: *Results of the selection on data and expectations on the Monte Carlo of backgrounds.*

The total selection efficiency at $M_{S1} = 180$ GeV/c^2 is $\varepsilon = 19.0\%$. With an expected number of background events equal to (1.0 ± 0.6), the expected limit on the cross section is $\sigma^{lim}_{exp} \times Br = 0.25$ pb for $M_{S1} = 180$ GeV/c^2.

The Table (5.3) shows the number of events surviving on data after each kinematical cut compared with the expectations: no events survive the selection requirements.

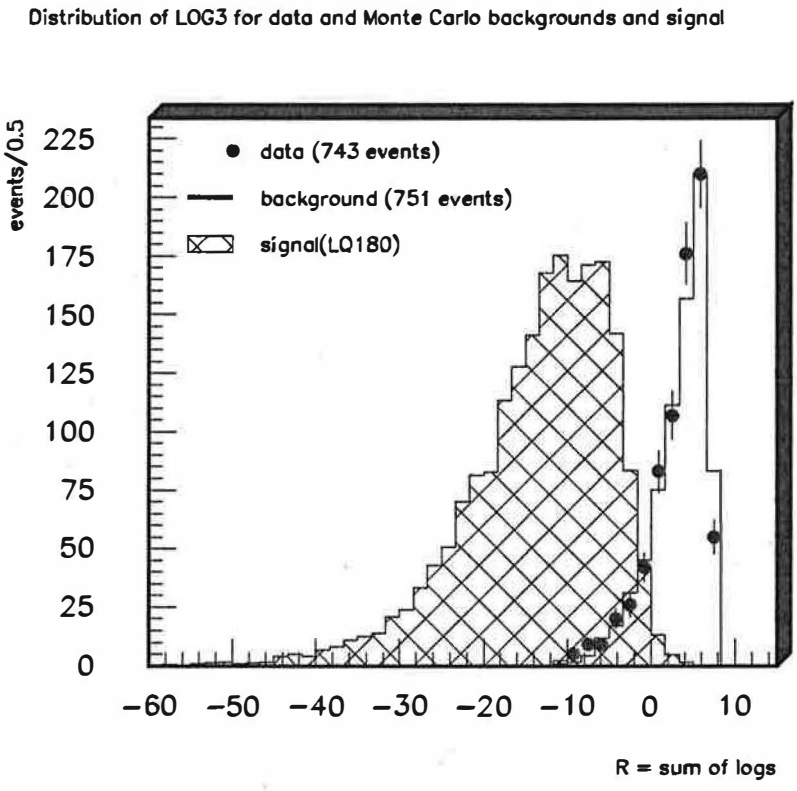

Figure 5.13: *Distributions of the variable LOG3 for leptoquark events* ($M_{S1} = 180$ GeV/c^2, *dashed histogram), background and real data (dots).*

CUT	140 GeV/c^2	150 GeV/c^2	160 GeV/c^2	170 GeV/c^2
E_T(e1)> 30 GeV	(71.4 ± 1.6)%	(73.7 ± 1.6)%	(74.1 ± 1.6)%	(76.3 ± 1.6)%
$\not\!\!E_T$ >20 GeV	(66.7 ± 1.5)%	(69.1 ± 1.5)%	(70.7 ± 1.6)%	(73.3 ± 1.6)%
anti B-tagging	(66.0 ± 1.5)%	(68.0 ± 1.5)%	(69.9 ± 1.5)%	(71.8 ± 1.6)%
E_T(j1,j2)> 30,15 GeV	(52.5 ± 1.3)%	(54.4 ± 1.3)%	(56.4 ± 1.3)%	(57.5 ± 1.4)%
$\not\!\!E_T$ significance	(49.2 ± 1.2)%	(50.8 ± 1.2)%	(52.2 ± 1.3)%	(54.0 ± 1.3)%
E_T(jets) and $\not\!\!E_T$	(48.5 ± 1.2)%	(50.3 ± 1.2)%	(51.7 ± 1.3)%	(53.7 ± 1.3)%
LOG3< -10.5	(18.8 ± 0.7)%	(20.4 ± 0.7)%	(23.7 ± 0.8)%	(28.1 ± 0.8)%
$\varepsilon_{\rm ID}^{el}$ + no 2nd ℓ	(12.3 ± 0.5)%	(12.9 ± 0.5)%	(15.0 ± 0.6)%	(17.6 ± 0.6)%

CUT	180 GeV/c^2	190 GeV/c^2	200 GeV/c^2	210 GeV/c^2
E_T(e1)> 30 GeV	(77.1 ± 1.0)%	(77.6 ± 1.7)%	(78.0 ± 1.7)%	(79.1 ± 1.7)%
$\not\!\!E_T$ >20 GeV	(73.9 ± 1.0)%	(74.7 ± 1.6)%	(74.8 ± 1.6)%	(76.4 ± 1.6)%
anti B-tagging	(72.7 ± 1.0)%	(73.0 ± 1.6)%	(73.2 ± 1.6)%	(74.9 ± 1.6)%
E_T(j1,j2)> 30,15 GeV	(58.9 ± 0.9)%	(59.5 ± 1.4)%	(59.9 ± 1.4)%	(60.7 ± 1.4)%
$\not\!\!E_T$ significance	(55.5 ± 0.8)%	(56.0 ± 1.3)%	(56.6 ± 1.3)%	(57.1 ± 1.3)%
E_T(jets) and $\not\!\!E_T$	(55.1 ± 0.8)%	(55.8 ± 1.3)%	(56.3 ± 1.3)%	(56.9 ± 1.3)%
LOG3 < -10.5	(30.6 ± 0.6)%	(33.5 ± 0.9)%	(36.6 ± 1.0)%	(38.0 ± 1.0)%
$\varepsilon_{\rm ID}^{el}$ + no 2nd ℓ	(18.9 ± 0.4)%	(20.8 ± 0.7)%	(21.5 ± 0.7)%	(23.0 ± 0.7)%

Table 5.4: *Listed here are the efficiencies of the different cuts of the selection for different leptoquark masses. Statistical errors only.*

The efficiencies of the selection cuts have been evaluated on the Monte Carlo's of the signal and are summarized in Table (5.4) for each M_{S1} and in Figure (5.14) before and after applying the electron-ID cuts. These efficiencies have been used to determine the limits on the cross section as will be done in Chapter 7 by using the Bayesian approach explained in Appendix D.

5.1.2. Other sources of background: contribution from fake electrons

Jets produced by the strong interactions of the remnant partons from the initial collision can mimic electrons and in events with high missing transverse energy can constitute a source of background in the leptoquarks search in the $e\nu jj$ decay channel.

The contamination from this kind of background in the signal region has been evaluated from data, using the whole high p_T inclusive electron sample. A fundamental assumption to apply in this procedure is that the distribution of the electron isolation variable for QCD jets that fake electrons is independent of the value of the $\not\!\!E_T$ of the event. This method has a systematic uncertainty of about 30% [99], and consists in subdividing the plane "isolation variable" versus "$\not\!\!E_T$" in four regions:

(a) Region with $\not\!\!E_T < 10$ GeV and $Iso < 0.1$: this region contains events with low missing transverse energy and with at least one isolated electron. These events can be Z/γ

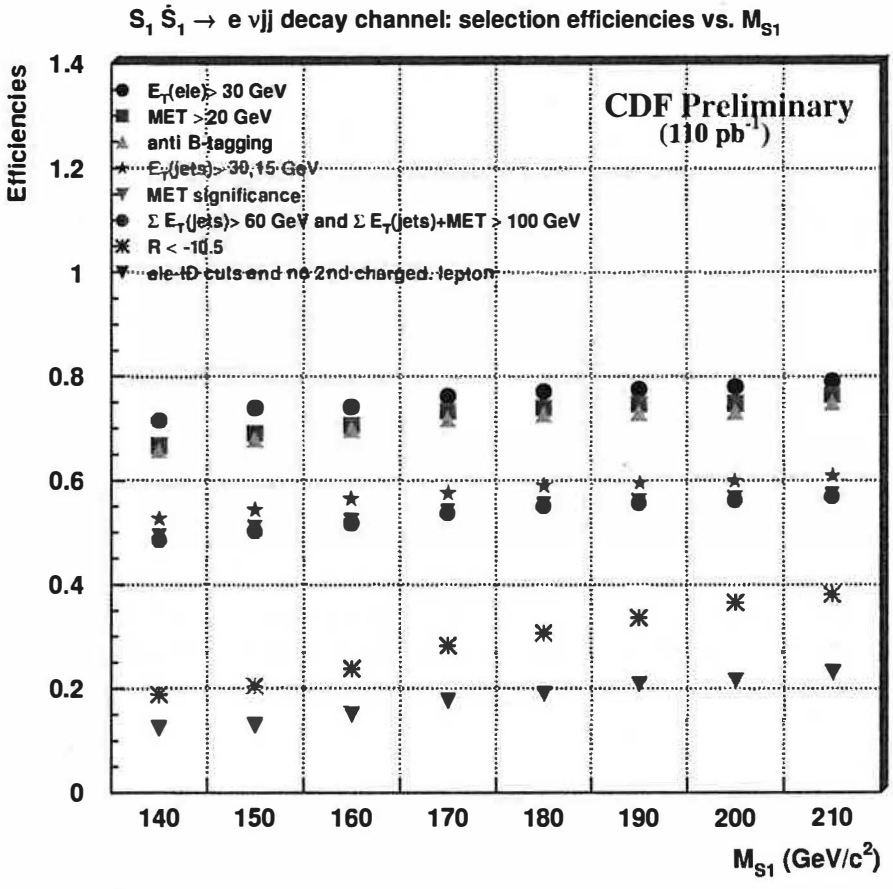

Figure 5.14: *Efficiencies of the selection cuts applied at different stages of the search in the $e\nu jj$ decay channel as a function of* M_{S1}.

Number of events	1a	1b	
PROCESSED	26853	128761	
In (a) after ele-ID, no-2^{nd} lepton, jets cuts	401	2427	$\Rightarrow N_{QCD}^{(a)} = 2828$
In (b) after ele-ID, no-2^{nd} lepton, jets cuts	162	1199	$\Rightarrow N_{QCD}^{(b)} = 1361$
In (c) after all selection cuts	0	0	$\Rightarrow N_{QCD}^{(c)} = 0$

Table 5.5: *Number of events passing the selection requirements in the regions (a), (b) and (c) of the isolation variable Iso versus $\not\!\!E_T$ plane to evaluate the QCD background contribution in the signal region.*

Drell-Yan events going into dielectron plus jets from initial state radiation, or can be QCD events;

(b) Region with $\not\!\!E_T < 10$ GeV and $Iso > 0.1$: this region contains events with low missing transverse energy and non-isolated electrons. These are typically QCD events;

(c) Region with $\not\!\!E_T > 20$ GeV and $Iso > 0.1$: this region contains events with high missing transverse energy and non-isolated electrons. These are also QCD events;

(d) Region with $\not\!\!E_T > 20$ GeV and $Iso < 0.1$: this is the signal region and it contains W + jets, top and QCD events.

The estimation of the number of QCD events in region (d) after all selection requirements applied gives the expectation from this source of background and is estimated in the following way.

First, are calculated the numbers $N_{QCD}^{(a)}$ and $N_{QCD}^{(b)}$ of events in the regions (a) and (b) after applying: (1) the electron-ID cuts, except the isolation, (2) the requirement of no second charged lepton in the event, which eliminates the Drell-Yan contribution from region (a), and (3) the requirement of at least two energetic jets in the event with $E_T > 30, 15$ GeV. After these cuts only the QCD events remain in these two regions: therefore the ratio $N_{QCD}^{(a)}/N_{QCD}^{(b)}$ gives an estimate of the percentage of QCD events surviving after the isolation cut.

If all the selection requirements of the $e\nu jj$ analysis are applied in the region (c), giving as result the number $N_{QCD}^{(c)}$, then thanks to the knowledge of the ratio $N_{QCD}^{(a)}/N_{QCD}^{(b)}$ it is possible to estimate how many QCD events remain in the signal region. This estimation is evaluated by doing the following calculation:

$$N_{QCD}^{(d)} = \frac{N_{QCD}^{(a)}}{N_{QCD}^{(b)}} \times N_{QCD}^{(c)}$$

The results are reported in Table (5.5): the estimated number of QCD events in the signal region is equal to zero.

5.1.3. Systematics uncertainties for the "relative likelihood" analysis

The selection requirements are based on the use of variables which are defined according to algorithms, like the one which defines the jets, or on settings used in the generation of the events. Different choices give different results in terms of selection efficiency, and should be considered as sources of systematic uncertainties. Moreover, in the evaluation of the limit on production cross section, the systematic uncertainties on the luminosity should also be taken into account. Listed here, and in Table (5.6), are the sources of systematics for the acceptance and luminosity evaluated for the search in the $e\nu jj$ channel on leptoquark events with $M_{S1} = 180$ GeV/c^2, and taken also as systematics for the other masses [5]:

1. **Jet energy scale.** The definition of the jets in the event is made using a cone algorithm which is based on the energy deposition in a region delimited by a cone with radius $R = \sqrt{\eta^2 + \phi^2}$ that in this analysis has been chosen equal to 0.7. Relative and absolute corrections have been applied on this measurement as well as corrections which take into account possible contributions from the out of cone energy and the underlying event, as outlined in Section (3.8). This model introduces a systematic effect $\mathcal{S}_{\rm jet}$ which is usually calculated as:

$$\mathcal{S}_{\rm jet} = (|\varepsilon_{+10\%} - \varepsilon| + |\varepsilon_{-10\%} - \varepsilon|)/2 \tag{5.3}$$

   where $\varepsilon_{\pm 10\%}$ are the efficiencies of the selection calculated after modifying the jets energies by $\pm 10\%$ and ε is the nominal selection efficiency.

2. **Monte Carlo statistics.** The limited statistics of simulated signal events used to evaluate the selection efficiencies produces a systematic uncertainty $\mathcal{S}_{\rm MC}$ given by:

$$\mathcal{S}_{\rm MC} = \sqrt{\frac{\varepsilon(1+\varepsilon)}{N_{generated}}}, \quad \text{with } \varepsilon = \frac{\rm N_{passed}}{\rm N_{generated}}$$

   where $N_{generated}$ and N_{passed} are the number of events generated and passing the selection.

3. **Gluon radiation.** The leptoquark events have been generated by turning on the initial or final gluon radiation in Pythia, to simulate jets coming from gluon showering. The uncertainty $\mathcal{S}_{\rm gluon}$ coming from this choice has been determined as the half of the difference between the efficiencies calculated setting the radiation on and off in Pythia.

4. **Choice of the pdf.** The signal events have been generated by using the CTEQ4L [91] parton distribution function, and consequently a systematic effect related with this choice must be taken into account. As uncertainty $\mathcal{S}_{\rm pdf}$ it has been considered the difference between the nominal selection efficiency and the value calculated by generating the events with the CTEQ2L parton distribution function.

[5] It has been verified that the result on the limit production cross section is not sensitive to large variations of the systematics.

Systematics	%
Jet energy	10.0
Monte Carlo	3.5
Gluon radiation	4.0
pdf choice	7.0
Q^2 scale	2.0
ε_{ID}^{el}	6.0
luminosity	4.1
TOTAL	15.0

Table 5.6: *This table lists all the relative systematic uncertainties on the selection efficiency which, added in quadrature with the error on the luminosity, gives the total systematic for the calculation of the limit production cross section. The calculations have been performed on the sample of leptoquark events with* $M_{S1} = 180$ GeV/c^2, *and taken also as systematics for the other masses. It has been verified that the result on the limit production cross section is not sensitive to large variations of the systematics.*

5. Q^2 **scale.** The Q^2 of the event is the parton momentum scale which in the analysis has been set equal to M_{S1}^2. To evaluate the systematics $\mathcal{S}_{Q^2}$ associated to this choice, the Q^2 has been scaled by a factor 1/4 and the difference between the selection efficiencies has been quoted as a sytematic uncertainty.

6. ε_{ID}^{el}. The electron identification efficiency has been calculated on both Monte Carlo and data events, and the former has been used for the calculation of the limit on the production cross section. The results of the two evaluation criteria differ as explained in Section (4.4.1), and an error $\mathcal{S}_{\varepsilon-ID}$ calculated as half of the difference between efficiency of the ID-cuts calculated on Monte Carlo and on data events has been assigned as a systematic uncertainty.

7. **Luminosity.** The measurement of the luminosity is affected by an error $\mathcal{S}_{\mathcal{L}}$ equal to 3.6% in run 1a and to 4.1% in run 1b [100]. It has been considered a systematic uncertainty of 4.1%.

The total signal efficiency can be written as $\varepsilon \pm \mathcal{S}_\varepsilon$, with the relative error expressed as the sum in quadrature of all relative contributions:

$$\frac{\mathcal{S}_\varepsilon}{\varepsilon} = \sqrt{\frac{\mathcal{S}_{jet}^2 + \mathcal{S}_{MC}^2 + \mathcal{S}_{gluon}^2 + \mathcal{S}_{pdf}^2 + \mathcal{S}_{Q^2}^2 + \mathcal{S}_{\varepsilon-ID}^2}{\varepsilon^2}}$$

and by adding $\mathcal{S}_\varepsilon/\varepsilon$ in quadrature with the relative error on the luminosity $\mathcal{S}_{\mathcal{L}}/\mathcal{L}$ one gets the total systematic uncertainty which must be quoted when measuring the limit cross section $\sigma_{lim} = N_{lim}/\mathcal{L} \cdot Br \cdot \varepsilon$ as will be done in Chapter (7):

$$\mathcal{S}_\sigma/\sigma = \sqrt{(\frac{\mathcal{S}_\varepsilon}{\varepsilon})^2 + (\frac{\mathcal{S}_{\mathcal{L}}}{\mathcal{L}})^2} = 15\% \qquad (5.4)$$

5.2. Selection requirements in the $eejj$ decay channel

In the $eejj$ decay channel a search is made for two high energy electrons and two high energy jets, coming from the pairs of produced leptoquarks, as shown in Figure (4.1). The production rate in this decay channel is equal to β^2.

The production mechanism of Standard Model events which can be misidentified as signal events in this analysis is shown in Figure (4.2) and explained in Section (4.1). The main source of background is represented by Drell-Yan events where a Z or a photon from quark-antiquark annihilation, produced in association with a gluon which fragments into jets, decays into electrons. A second, important source of background is represented by events where $t\bar{t}$'s are produced, both decaying semileptonically into electrons. Other backgrounds, from $b\bar{b}$ and Z$\rightarrow \tau^+\tau^-$ events, are negligible due to the electron isolation and large transverse energy requirements on the electron and jets [37].

The selection cuts can be summarized as follows:

1. one *tight* electron with $E_T > 40$ GeV
2. one *loose* electron with $E_T > 15$ GeV
3. $M_{e1,e2} \notin [76, 106]$ GeV/c^2
4. $E_T^C(e1) + E_T^C(e2) > 85$ GeV
5. $E_T^C(jet1) + E_T^C(jet2) > 85$ GeV
6. $\sqrt{(E_T^C(e1) + E_T^C(e2))^2 + (E_T^C(jet1) + E_T^C(jet2))^2} > 200$ GeV

1. and 2. Events are selected only if there are at least two electrons, the most energetic one identified by using the tight requirements of Table (4.1) and the second most energetic one by using the loose criteria of the same table. The two electrons are not required to have opposite electric charge since at very high p_T the charge determination is not reliable. In the selection are applied cuts on the uncorrected transverse energy of the two electrons at 40 and 15 GeV.

3. As already stated in Section (4.1), an important contribution to the background is given by Drell-Yan events with electrons coming from the reaction $q\bar{q} \rightarrow$Z$\rightarrow e^+e^-$, whose invariant mass (M_{ee}) should be distributed around the Z resonance peak. To eliminate this background, only events outside the mass window [76, 106] GeV/c^2 are taken.

4., 5. and 6. The most important requirements in this analysis involve combinations of the corrected transverse energies of the electrons and of the jets. These combinations have been chosen to minimize the background contribution by maintaining an high selection efficiency. The corrections applied on the transverse energies of the electrons come from test-beam results and from the W mass measurement on data, while jets, whose cone radius has been set equal to 0.7, have transverse energies corrections based on underlying events and on calorimetry/clustering effects. The variable $\sqrt{(E_T^C(e1) + E_T^C(e2))^2 + (E_T^C(jet1) + E_T^C(jet2))^2}$ represents, in the plane $E_T^C(e1) + E_T^C(e2)$ versus $E_T^C(jet1) + E_T^C(jet2)$, the radius of a circle centered in the origin.

CUT	run 1a	run 1b
Inclusive Sample	26882	128761
2nd electron $E_T > 15$ GeV	1452	14189
good run requirement	1245	13514
$E_{T_{e1,e2}} > 40, 15$ GeV	60	3131
$\geq$2 jets	14	852
$M_{ee} \notin [76, 106]$ GeV/c^2	8	94
$\sum E_{T_e}, \sum E_{T_j} > 85$ GeV	1	2
$\sqrt{\sum {E_{T_e}}^2 + \sum {E_{T_j}}^2} > 200$ GeV	0	0

Table 5.7: *Events passing the selection cuts on run 1a and run 1b. The presample has been created using the cuts listed in Section (4.2); it has been furtherly reduced by requiring a second electron with* $E_T > 15$ *GeV and bad run removal. On the surviving events the electron-ID cuts and the selection cuts have been applied: no events remain.*

Plots of the distributions of some kinematic variables are shown in Figure (5.15) for signal and background events. The Drell-Yan and $t\bar{t}$ events distributions have been normalized to the luminosity on data: the normalization factor for $t\bar{t}$ events has been estimated by using the theoretical value $\sigma_{t\bar{t}} = (4.75^{+0.73}_{-0.62})$ pb calculated in [97], while the one for the Drell-Yan events has been calculated by normalizing the dielectron invariant mass distribution to data inside the Z mass window, as shown in Figure (5.16). The normalization region is excluded by the selection requirements of the analysis, so it allows a correction which does not affect the presence of an eventual signal on data.

Using simulated signal and background events, in Figure (5.17) the sum of the corrected transverse energies of the two selected electrons is plotted versus the sum of the corrected transverse energies of the two jets: the backgrounds are represented in red (dark) dots, while the signal, leptoquarks with $M_{S1} = 220$ GeV/c^2, is drawn with green circles. The two right lines in the figure represent the cuts on the two variables separately at 85 GeV, while the arc of a circle with center in (0,0) and radius
$R = \sqrt{(E_T^C(e1) + E_T^C(e2))^2 + (E_T^C(jet1) + E_T^C(jet2))^2}$ illustrates the cut on R at 200 GeV.
On Table (5.7) the events on data passing different stages of the selection are listed. No events survive after these requirements are applied on data, while (1.8 ± 0.6) are expected as background. Since there is no evidence of a signal, upper limits on the leptoquark production cross section can be set also for this channel using the final selection efficiencies of Table (5.8) and plotted in Figure (5.18) for different leptoquark masses at different stages of the selection. The determination of the 95% confidence level limits will be described in Chapter 7, calculated according to a Bayesian statistical method detailed in Appendix D.

The sources of systematic effects found in the $e\nu jj$ channel search are present in the $eejj$ channel as well and their corresponding uncertainties are evaluated as explained in Section (5.1.3). They come from: jet energy scale (2.0%), Monte Carlo statistics (2.5%), gluon radiation (2.5%), choice of the parton distribution function (5.0%), Q^2 scale (2.0%), electron identification efficiency (7.0%) and must be added in quadrature to the 4% systematics in

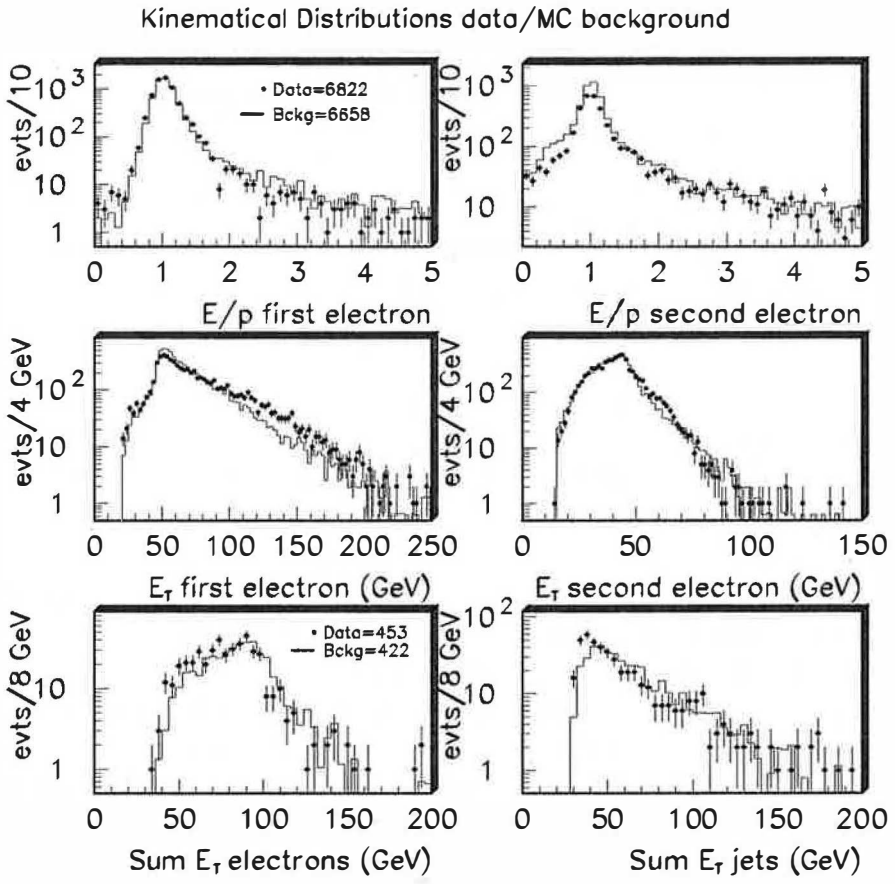

Figure 5.15: *Distributions of kinematical variables for data, represented by dots, and for simulated background events, Drell-Yan and $t\bar{t}$ normalized to run 1 luminosity. Shown are the ratio E/p for the two most energetic electrons, the corresponding transverse energies, and the sum of the electrons and of the jets E_T's.*

the luminosity measurement, giving a total of 10% evaluated for $M_{S1} = 220$ GeV/c^2.

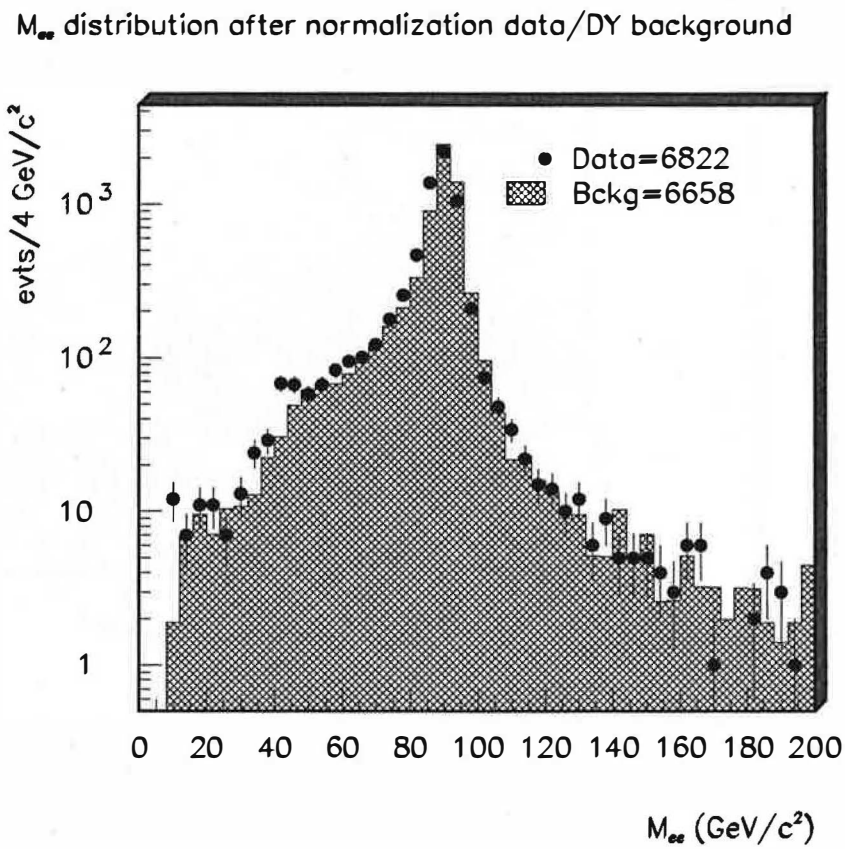

Figure 5.16: *Invariant mass distribution of the dielectrons selected in this search for background and data events. Data and generated events distributions have been normalized each other inside the Z mass window* $[76, 106]$ $\mathrm{GeV/c^2}$ *to take into account both the different luminosities and the different cross sections of the processes, which are Drell-Yan plus jets from ISR/FSR in the Monte Carlo and inclusive Drell-Yan on data.*

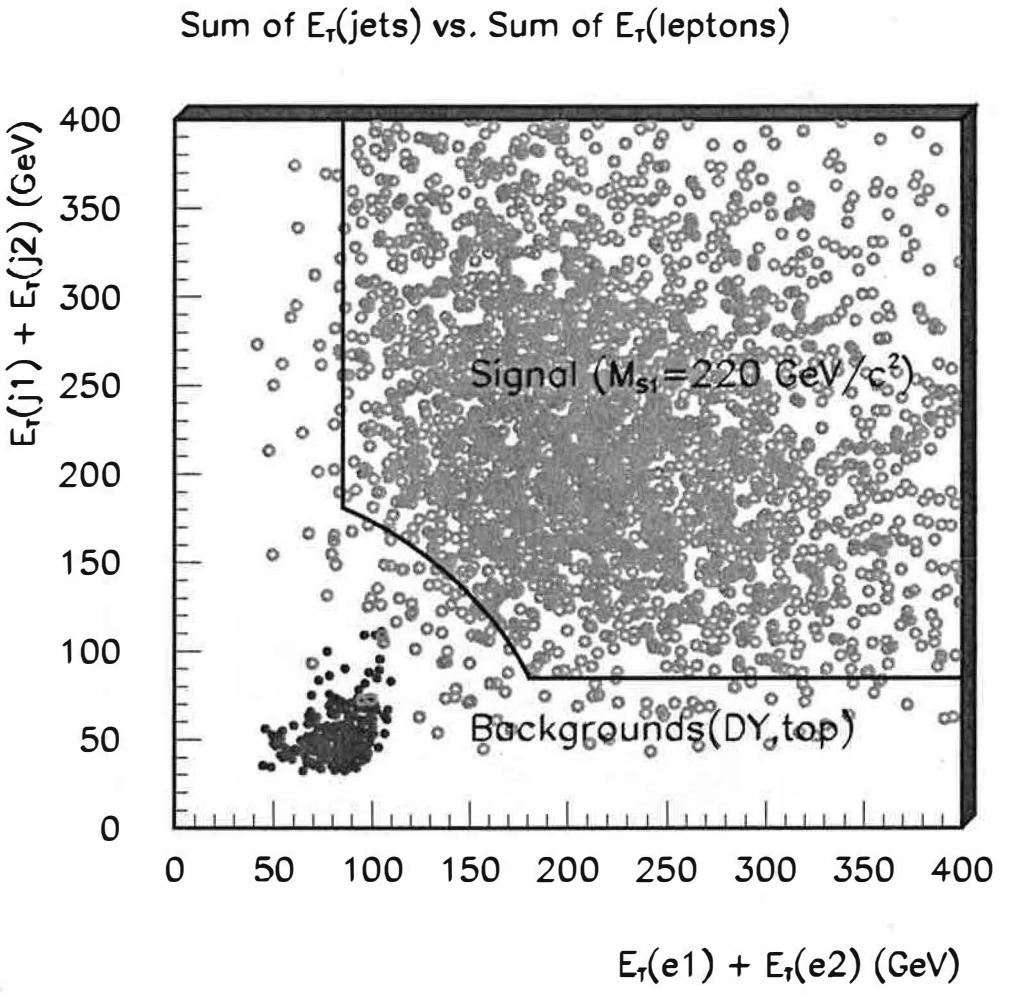

Figure 5.17: *This plot shows the distribution of the sum of the corrected E_T's of the two most energetic electrons versus the sum of the corrected E_T's of the two most energetic jets for simulated signal (leptoquarks events with $M_{S1} = 220$ GeV/c^2) and for backgrounds (Drell-Yan and $t\bar{t}$ events). The blue right lines show the cuts at 85 GeV in the sums of the leptonic and jet energies, while the arch of circle shows the cut at 200 GeV on the variable $\sqrt{(E_T^C(e1) + E_T^C(e2))^2 + (E_T^C(jet1) + E_T^C(jet2))^2}$, which is the radius of a circle centered in (0,0).*

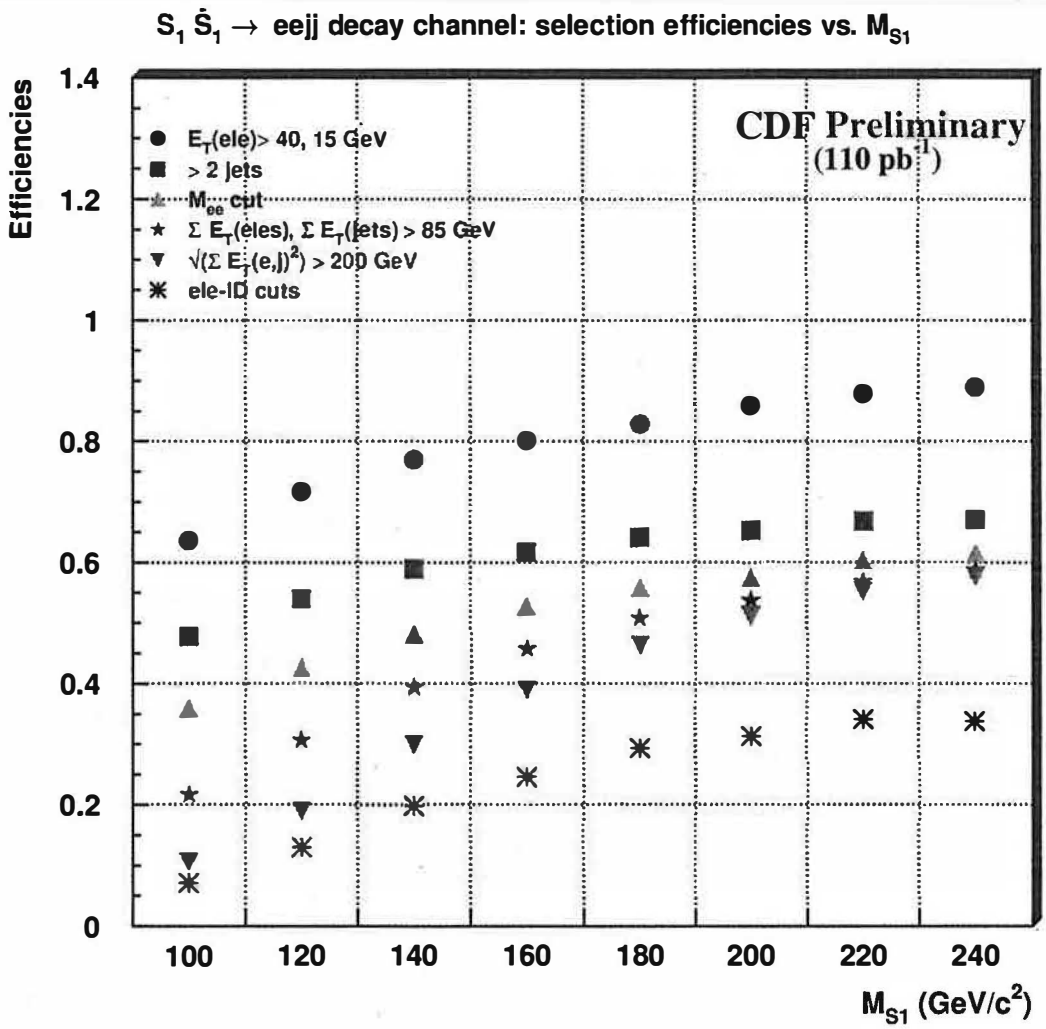

Figure 5.18: *Efficiencies evaluated at different stages of the selection for different leptoquark masses.*

$M_{S1}(GeV/c^2)$	100	120	140	160
$E_{T_e} > 40$, 15 GeV	$(63.6 \pm 1.3)\%$	$(71.8 \pm 1.4)\%$	$(77.0 \pm 1.5)\%$	$(80.2 \pm 1.5)\%$
≥ 2 jets	$(50.0 \pm 1.1)\%$	$(55.4 \pm 1.2)\%$	$(60.5 \pm 1.3)\%$	$(63.0 \pm 1.3)\%$
M_{ee} cut	$(36.8 \pm 0.9)\%$	$(43.6 \pm 1.0)\%$	$(49.3 \pm 1.1)\%$	$(53.8 \pm 1.2)\%$
$\sum E_{T's} > 85$ GeV	$(22.0 \pm 0.7)\%$	$(31.2 \pm 0.8)\%$	$(40.1 \pm 1.0)\%$	$(46.4 \pm 1.1)\%$
$\sqrt{\sum {E_{T's}}^2} > 200$ GeV	$(10.6 \pm 0.4)\%$	$(19.2 \pm 0.6)\%$	$(30.3 \pm 0.8)\%$	$(39.4 \pm 1.0)\%$
ε_{ID}^{el}	$(7.2 \pm 0.4)\%$	$(13.1 \pm 0.5)\%$	$(20.0 \pm 0.6)\%$	$(24.9 \pm 0.7)\%$

$M_{S1}(GeV/c^2)$	180	200	220	240
$E_{T_e} > 40$, 15 GeV	$(82.9 \pm 1.6)\%$	$(86.0 \pm 1.6)\%$	$(87.8 \pm 1.6)\%$	$(88.7 \pm 1.7)\%$
≥ 2 jets	$(65.3 \pm 1.3)\%$	$(66.4 \pm 1.3)\%$	$(68.2 \pm 1.4)\%$	$(68.3 \pm 1.4)\%$
M_{ee} cut	$(57.0 \pm 1.2)\%$	$(58.6 \pm 1.2)\%$	$(61.6 \pm 1.3)\%$	$(62.7 \pm 1.3)\%$
$\sum E_{T's} > 85$ GeV	$(51.5 \pm 1.1)\%$	$(54.5 \pm 1.2)\%$	$(57.8 \pm 1.2)\%$	$(59.8 \pm 1.3)\%$
$\sqrt{\sum {E_{T's}}^2} > 200$ GeV	$(46.9 \pm 1.1)\%$	$(52.0 \pm 1.1)\%$	$(56.3 \pm 1.2)\%$	$(58.5 \pm 1.2)\%$
ε_{ID}^{el}	$(29.6 \pm 0.8)\%$	$(31.8 \pm 0.8)\%$	$(34.6 \pm 0.9)\%$	$(34.2 \pm 0.9)\%$

Table 5.8: *The efficiency of each kinematical cut applied in the selection, and the total efficiency after the electron-ID cuts for different values of* M_{S1}. *The errors on the efficiencies are only statistical.*

Chapter 6

Search for vector leptoquarks in the $e\nu jj$ and $eejj$ decay channels

Introduction- *The analyses performed in the search for scalar leptoquarks in the two decay channels $e\nu jj$ and $eejj$ are adapted here to the search for vector leptoquarks. Even if the production cross section for the vector case is different from the scalar case, the decay features remain the same and the kinematics of the processes remains unchanged. For this reason the analysis approach of previous searches is used, and the same selection requirements are applied giving new efficiencies. These are calculated on Monte Carlo samples of the signal, generated with Pythia, which has been modified to include the production of vector leptoquarks. Limits on the vector leptoquark production cross sections can be then determined on the same run 1 data sample used for the scalar search.*

6.1. Vector leptoquarks production at Tevatron

According to their spin, leptoquarks can be scalar (spin=0) or vector (spin=1). For these latter, the production cross section depends on all possible spin orientations and on the unknown gauge-boson couplings: vector leptoquarks are either the fundamental gauge bosons with Yang-Mills couplings or composite particles with anomalous couplings. In the second case the anomalous couplings are described by the two parameters k_A and λ_A, where A indicates the gauge boson and in general can be the photon, the gluon, the $W^{\pm}$ or the Z, but in a $p\bar{p}$ collision can be represented only by the gluon (see the gluon couplings on Figure (2.4)) and the parameters are k_G and λ_G. As mentioned in the theoretical overview in Section (2.7), usually one refers to particular values of these couplings that are the Yang-Mills couplings $k_G = 0$ and $\lambda_G = 0$ and the minimal vector couplings $k_G = 1$ and $\lambda_G = 0$. The theoretical calculations of the cross sections exist only at the Leading Order [33, 101]: compared with the values of scalar leptoquark production cross sections, the ones for minimal vector coupling are about ten times larger, while the Yang-Mills ones are larger by a factor of about five.

6.2. Efficiency of the selection requirements

The so called "relative likelihood analysis" in the search for scalar leptoquarks in the $e\nu jj$ channel, while leaving unchanged the results on data and on background expectations, gives new selection efficiencies when applied on the Monte Carlo samples for the vector leptoquark signal. The requirements are recalled below and explained in Section (5.1):

- one electron *tight* with $E_T > 30$ GeV
- at least two jets with $E_T^C > 30, 15$ GeV
- $\not\!\!E_T > 20$ GeV
- no events with 2^{nd} charged lepton ($e^{\pm}, \mu^{\pm}$)
- no B-tagged events
- no events with $\Delta\phi(\not\!\!E_T, jet) < 10°$ if $\not\!\!E_T/\sqrt{\sum E_T} < 4$ GeV$^{1/2}$

CUT	200 GeV/c^2	280 GeV/c^2	360 GeV/c^2	400 GeV/c^2
E_T(e1)> 30 GeV	(79.2 ± 2.7)%	(81.5 ± 2.7)%	(86.9 ± 2.9)%	(84.4 ± 2.8)%
$\not\!\!E_T$ >20 GeV	(77.3 ± 2.7)%	(80.2 ± 2.6)%	(85.5 ± 2.9)%	(83.1 ± 2.8)%
anti B-tagging	(75.8 ± 2.6)%	(77.2 ± 2.6)%	(80.7 ± 2.7)%	(79.8 ± 2.7)%
E_T(j1,j2)> 30,15 GeV	(60.2 ± 2.2)%	(62.1 ± 2.2)%	(65.1 ± 2.3)%	(62.5 ± 2.2)%
$\not\!\!E_T$ significance	(56.4 ± 2.1)%	(59.7 ± 2.1)%	(62.6 ± 2.3)%	(60.4 ± 2.2)%
E_T(jets) and $\not\!\!E_T$	(56.1 ± 2.1)%	(59.6 ± 2.1)%	(62.4 ± 2.3)%	(60.3 ± 2.2)%
LOG3 < -10.5	(36.7 ± 1.6)%	(50.2 ± 1.9)%	(56.5 ± 2.1)%	(54.9 ± 2.1)%
$\varepsilon_{\rm ID}^{el}$ + no 2nd ℓ	(22.6 ± 1.2)%	(24.6 ± 1.2)%	(28.2 ± 1.4)%	(25.3 ± 1.3)%

Table 6.1: *Efficiency of the selection requirements applied in the search for vector leptoquarks in the $e\nu jj$ channel for different vector leptoquark masses.*

- $E_T^C(jet1) + E_T^C(jet2) > 60$ GeV
- $E_T^C(jet1) + E_T^C(jet2) + \not\!\!E_T > 100$ GeV
- $LOG3 < -10.5$

In the $eejj$ channel the cuts are the following, as in Section (5.2):

- one *tight* electron with $E_T > 40$ GeV
- one *loose* electron with $E_T > 15$ GeV
- $M_{e1,e2} \notin [76, 106]$ GeV/c^2
- $E_T^C(e1) + E_T^C(e2) > 85$ GeV
- $E_T^C(jet1) + E_T^C(jet2) > 85$ GeV
- $\sqrt{(E_T^C(e1) + E_T^C(e2))^2 + (E_T^C(jet1) + E_T^C(jet2))^2} > 200$ GeV

The leptoquark masses for which the efficiency has been calculated range between 200 and 400 GeV/c^2 for both channels, having based this choice on the limits found from other experiments [41]. The results are summarized in Table (6.1) and illustrated in Figure (6.1) for the search in the $e\nu jj$ channel and in Table (6.2) and Figure (6.1) for the search in the $eejj$ channel. It has been assumed a total systematic uncertainty of 15% and 10% as in the scalar case for the electron-neutrino and dielectron cases respectively. The values found for the selection efficiency are used in Chapter 7, to calculate the 95% confidence level upper limits on the production cross sections, from which are then determined the lower limits on M_{V1} from the two decay channels and from their combination.

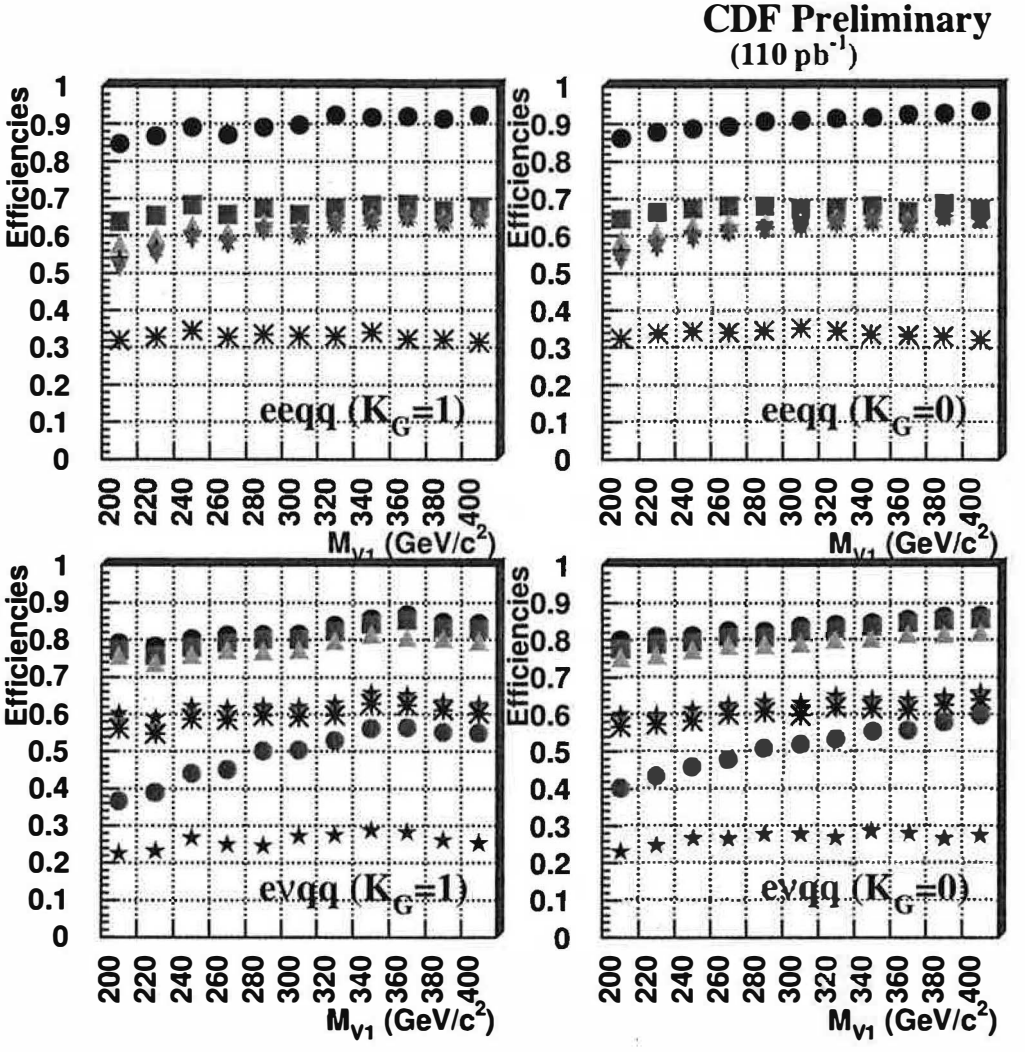

Figure 6.1: *Selection efficiency of the cuts applied in the vector leptoquark search in the $eejj$ channel (top) and in the $e\nu jj$ channel (bottom) for different values of* M_{V1} *for leptoquarks with Yang-Mills anomalous couplings ($k_G = 0, \lambda_G = 0$) and minimal couplings ($k_G = 1, \lambda_G = 0$).*

CUT	200 GeV/c^2	280 GeV/c^2	360 GeV/c^2	400 GeV/c^2
E_{T_e} > 40, 15 GeV	(84.8 ± 2.0)%	(89.2 ± 2.0)%	(92.0 ± 2.1)%	(92.5 ± 2.1)%
≥2 jets	(63.8 ± 1.6)%	(67.5 ± 1.7)%	(68.5 ± 1.7)%	(67.8 ± 1.7)%
M_{ee} cut	(57.8 ± 1.5)%	(63.5 ± 1.6)%	(65.9 ± 1.7)%	(65.5 ± 1.6)%
$\sum E_{T's}$ >85 GeV	(53.8 ± 1.4)%	(61.8 ± 1.6)%	(64.7 ± 1.6)%	(64.3 ± 1.6)%
$\sqrt{\sum E_{T's}{}^2}$ >200 GeV	(51.6 ± 1.4)%	(61.2 ± 1.6)%	(64.5 ± 1.6)%	(64.1 ± 1.6)%
ε_{ID}^{el}	(31.9 ± 1.0)%	(33.6 ± 1.0)%	(32.3 ± 1.0)%	(31.5 ± 1.0)%

Table 6.2: *Efficiency of the selection requirements applied in the vector leptoquark search in the eejj channel for different masses.*

Chapter 7

Limits on leptoquarks production from searches in the individual channels and from their combination

Introduction- *The analyses explained in the previous chapters all gave a negative result in the search for leptoquarks, since no events passed the selection requirements on data, in agreement with expectations from the dominant sources of Standard Model background. Therefore, based on the calculation of the 95% confidence level limit on the number of observed events, explained in Appendix D and performed by applying a Bayesian approach, the upper limits on the first generation scalar and vector leptoquarks pair-production cross section as a function of the mass are calculated for each decay channel. From comparisons with theoretical calculations at the Next-to-Leading Order in the scalar case [31] and Leading Order [33, 101] in vector case, the corresponding lower limits on the leptoquark mass can be obtained in particular for $\beta = 0.5$ in the $e\nu jj$ and for $\beta = 1.0$ in the $eejj$ decay channels and in general for $\beta \in [0., 1.]$ for each analysis. The results of the searches in the $e\nu jj$ and $eejj$ decay channels are finally combined, giving 95% lower limits on scalar and vector leptoquark masses as a function of β and, in the vector case, of the anomalous couplings.*

7.1. Limits for the existence of pairs of leptoquarks decaying in $e\nu jj$ and in $eejj$

The production cross section σ of a particle decaying with branching ratio Br in the investigated channel, can be expressed as:

$$\sigma = \frac{N_{obs}}{\varepsilon \cdot Br \cdot \int \mathcal{L}dt} \tag{7.1}$$

where N_{obs} is the number of observed events, ε the selection efficiency and $\int \mathcal{L}dt$ the integrated luminosity.

In all the analyses performed in this thesis the number of events surviving after the selection requirements is always consistent with the expected number of background events and is equal to zero. The conclusion of all these searches is that there is no new signal: what can be derived from the non-observation is an upper limit on the number of observed events, and therefore on the leptoquark production cross section, at a certain confidence level, here chosen to be 95%. It tells in which direction to continue the search to eventually find some hint of signal.

The limit cross section is expressed as a function of the leptoquark mass M_{Lq} in the following formula:

$$\sigma_{95}(M_{Lq}) = \frac{N_{95}(M_{Lq})}{\varepsilon(M_{Lq}) \cdot Br \cdot \int \mathcal{L}dt} \tag{7.2}$$

where $Br = 2\beta(1-\beta)$ when it is considered as the branching ratio of the decay $Lq\bar{L}q \to e\nu qq$, since β has been defined as $Br(\mathrm{S1, V1} \to \mathrm{eq})$, and $Br = \beta^2$ for the decay $Lq\bar{L}q \to eeqq$. $N_{95}(M_{Lq})$ is the upper limit on the number of observed events for each leptoquark mass, in this case the 95% confidence level limit of zero events, independently of the value of M_{Lq}, evaluated according to the Bayesian statistical approach explained in Appendix D and $\varepsilon(M_{Lq})$ is the selection efficiency evaluated for each leptoquark mass on the Monte Carlo.

M_{S1} (GeV/c^2)	95%C.L. σ (pb) ($e\nu jj$)	$\sigma_{theor} \times 2\beta(1-\beta)$ CTEQ4M (pb) $Q^2 = M^2_{S1}/4$	$Q^2 = 4M^2_{S1}$
140	0.226	5.338	7.091
150	0.214	1.902	2.487
160	0.182	0.765	0.991
170	0.160	0.339	0.434
180	0.146	0.160	0.205
190	0.133	0.079	0.101
200	0.132	0.040	0.051
210	0.123	0.021	0.027

Table 7.1: *Values of the upper limits at 95% of confidence level of the production cross sections of first generation scalar leptoquarks decaying in the $e\nu jj$ channel as a function of M_{S1} and considering a systematic effect of 15%. Last two columns on the right report the results of theoretical calculations at Next-to-Leading order [31] with the CTEQ4M pdf for $Q^2 = M^2_{S1}/4$ and $Q^2 = 4M^2_{S1}$ multiplied by a factor $2\beta(1-\beta)$=0.5 .*

7.1.1. Results from single channels in the scalar case

The values of the upper limits on the scalar leptoquark production cross sections calculated for the search in the $e\nu jj$ and $eejj$ channels as a function of M_{S1}, and taking into account a 15% and 10% systematic uncertainty respectively, are listed in Tables (7.1) and (7.2), where are also reported the results of the theoretical calculations done at the Next-to-Leading Order [31] with the CTEQ4M pdf for $Q^2 = M^2_{S1}/4$ and $Q^2 = 4M^2_{S1}$ scaled by $\beta = 0.5$ and $\beta = 1.0$ respectively.

In the Figures (7.1) and (7.2) are indeed plotted the values of the limit cross sections as a function of the leptoquark mass, represented by dots, compared with the theoretical values represented by the bands corresponding to different choices of Q^2. The intersection points between the experimental and the lower theoretical curves give the lower limits on the scalar leptoquark masses: the values found are 182 GeV/c^2 for $\beta = 0.5$ in the $e\nu jj$ channel and 220 GeV/c^2 for $\beta = 1.0$ in the $eejj$ channel.

7.1.2. Results from single channels in the vector case

Same kind of results have been found from the searches in the vector case, where a few more distinctions must be noted, since for each channel two sets of values for the anomalous couplings, $k_G = 0, \lambda_G = 0$ (Yang-Mills type couplings) and $k_G = 1, \lambda_G = 0$ (minimal couplings), have been considered. In the four plots of Figure (7.3) are shown, for $\beta = 1$ in the $eejj$ channel and for $\beta = 0.5$ in the $e\nu jj$ channel, the experimental limits and the theoretical values at the Leading Order [33, 101] of the cross sections as a function of the vector leptoquark mass, from which have been obtained the lower limits on M_{V1}. They are 300 GeV/c^2 and 250 GeV/c^2 for the search in the electron-neutrino channel with $\beta = 0.5$ and are 330 GeV/c^2 and 280 GeV/c^2 for the search in the dielectron channel with $\beta = 1.0$ for Yang-Mills and minimal couplings respectively.

M_{S1} (GeV/c^2)	95%C.L. σ (pb) ($eejj$)	$\sigma_{theor} \times \beta^2$ CTEQ4M (pb) $Q^2 = M_{S1}^2/4$	$Q^2 = 4M_{S1}^2$
100	0.385	10.677	14.182
120	0.219	3.805	4.975
140	0.138	1.537	1.982
160	0.109	0.678	0.869
180	0.093	0.320	0.409
200	0.087	0.158	0.202
220	0.080	0.080	0.102
240	0.081	0.041	0.053

Table 7.2: *Values of the upper limits at 95% confidence level of the production cross sections of first generation leptoquarks decaying in the $eejj$ channel as a function of M_{S1} and considering a systematic effect of 10%. Last two columns on the right report the results of theoretical calculations at Next-to-Leading order [31] with the CTEQ4M pdf for $Q^2 = M_{S1}^2/4$ and $Q^2 = 4M_{S1}^2$ scaled by a factor $\beta^2 = 1$.*

7.1.3. Results from single channels for $\beta \in [0, 1]$

For both the scalar and vector case it is possible to extend the results of the searches to the general case $\beta \in [0, 1]$. The lower limits on M_{S1} and M_{V1} have been calculated as a function of the value of the branching ratio β, and the results are represented for the scalar search in the $e\nu jj$ channel in Figure (7.4), for the scalar search in the $eejj$ channel in Figure (7.5) and for the vector searches in the two channels, for different anomalous couplings, in the plots of Figure (7.6). In these representations the excluded regions from these analyses at the 95% confidence level are drawn as shadowed areas.

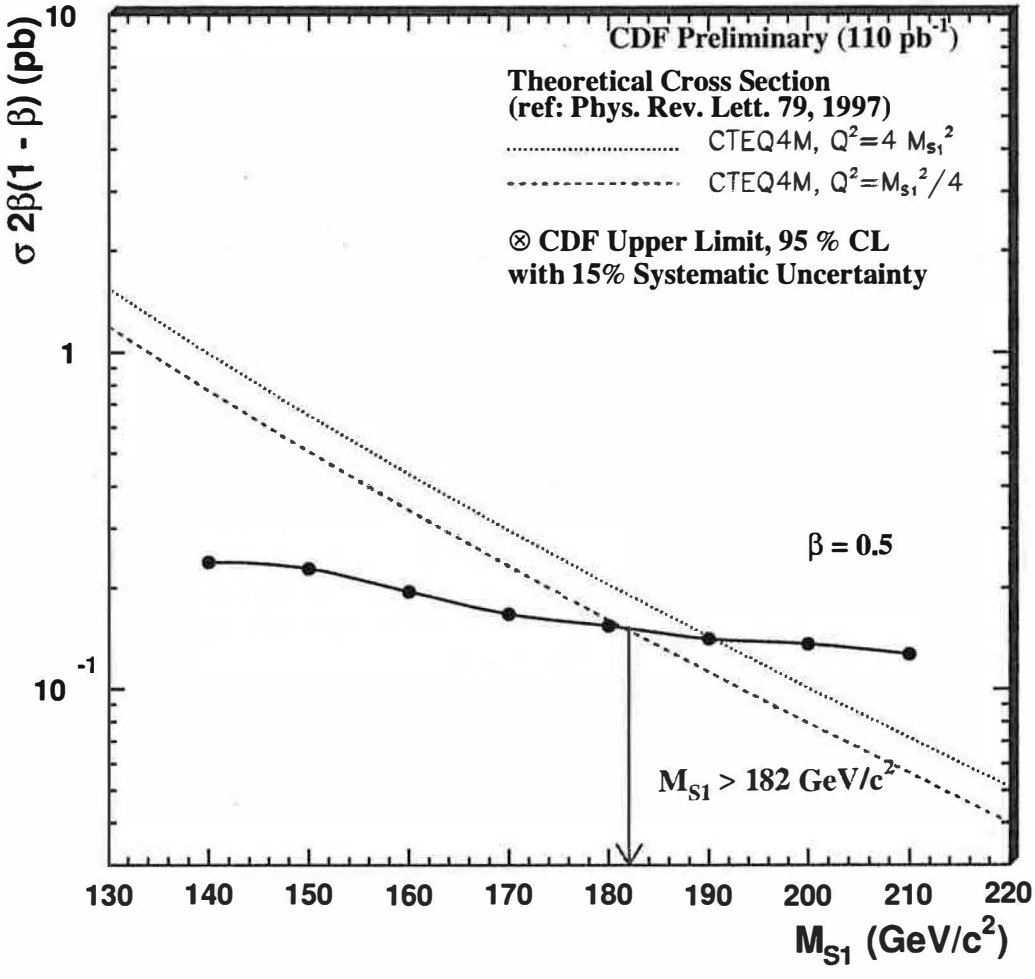

Figure 7.1: *Limit cross sections as a function of* M_{S1} *(black dots) compared with the theoretical expectations calculated at the Next-to-Leading order [31] for* $\beta = 0.5$. *At the intersection point between experimental and theoretical curves it is found a lower limit on* M_{S1} *at 182* GeV/c^2.

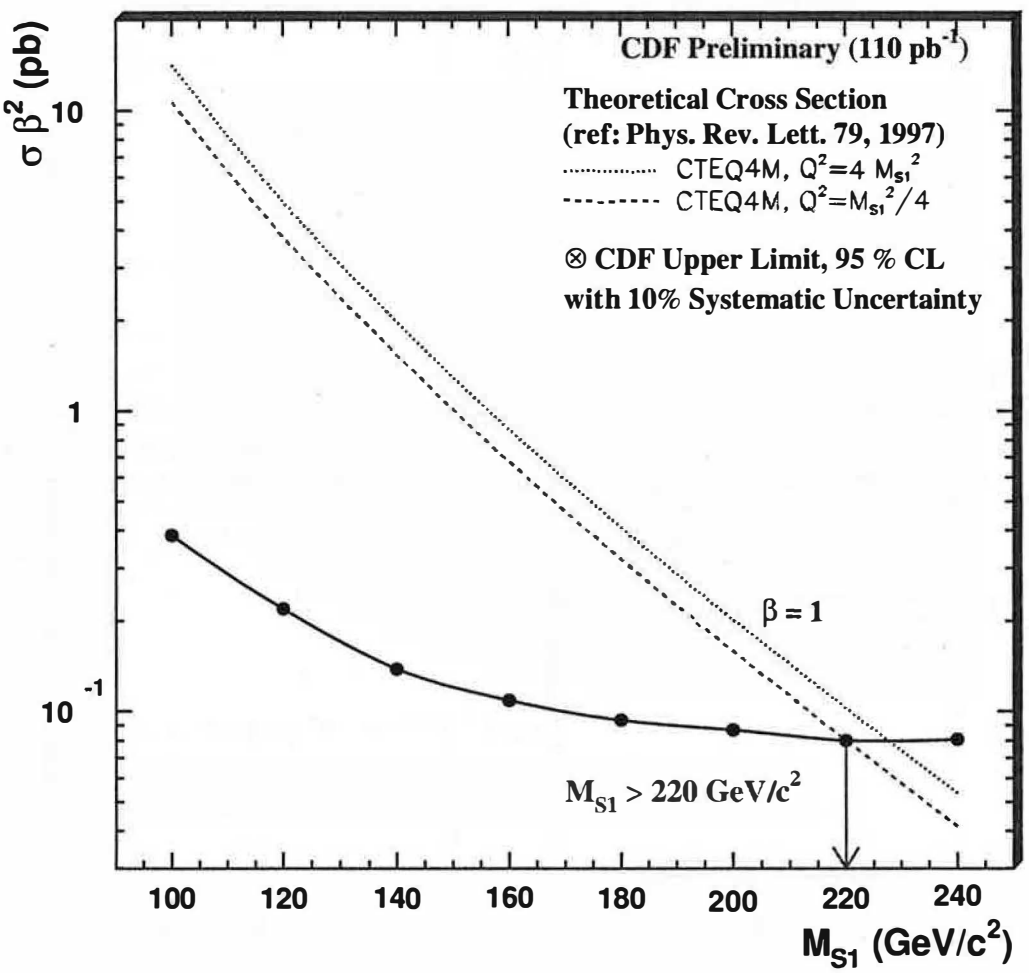

Figure 7.2: *Limit cross sections as a function of* M_{S1} *(black dots) compared with the theoretical expectations calculated at the Next-to-Leading order [31] for* $\beta = 1.0$ *in the search for scalar leptoquarks in the dielectron channel. At the intersection point between experimental and theoretical curves it is found a lower limit on* M_{S1} *at 220* GeV/c^2.

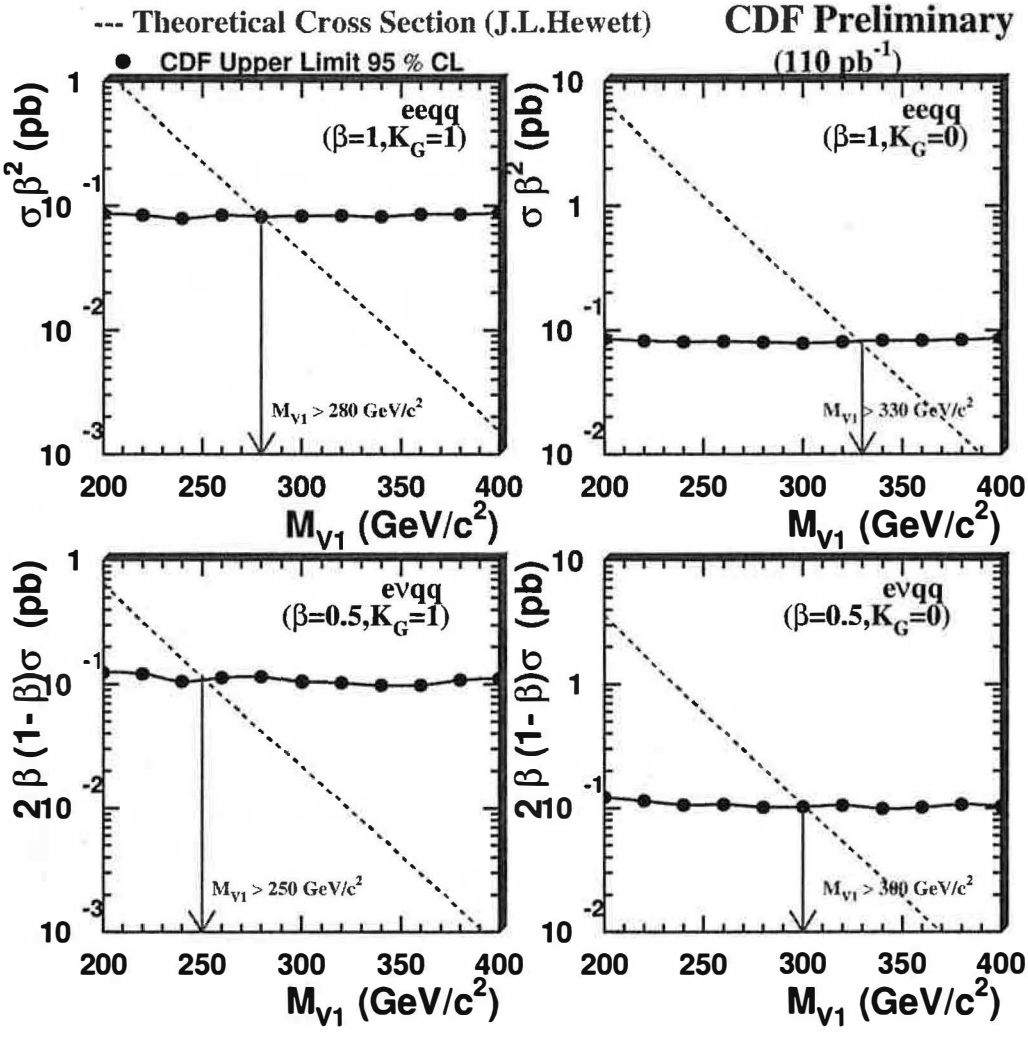

Figure 7.3: *Results of the searches for vector leptoquarks in the two decay channels and with $\beta = 0.5$ and $\beta = 1.0$ with different choices of anomalous couplings. The experimental upper limits on the production cross section are compared with the theoretical expectations calculated at the Leading Order (from Hewett, private Comm. [101]): their intersections give the lower limits on* M_{V1}.

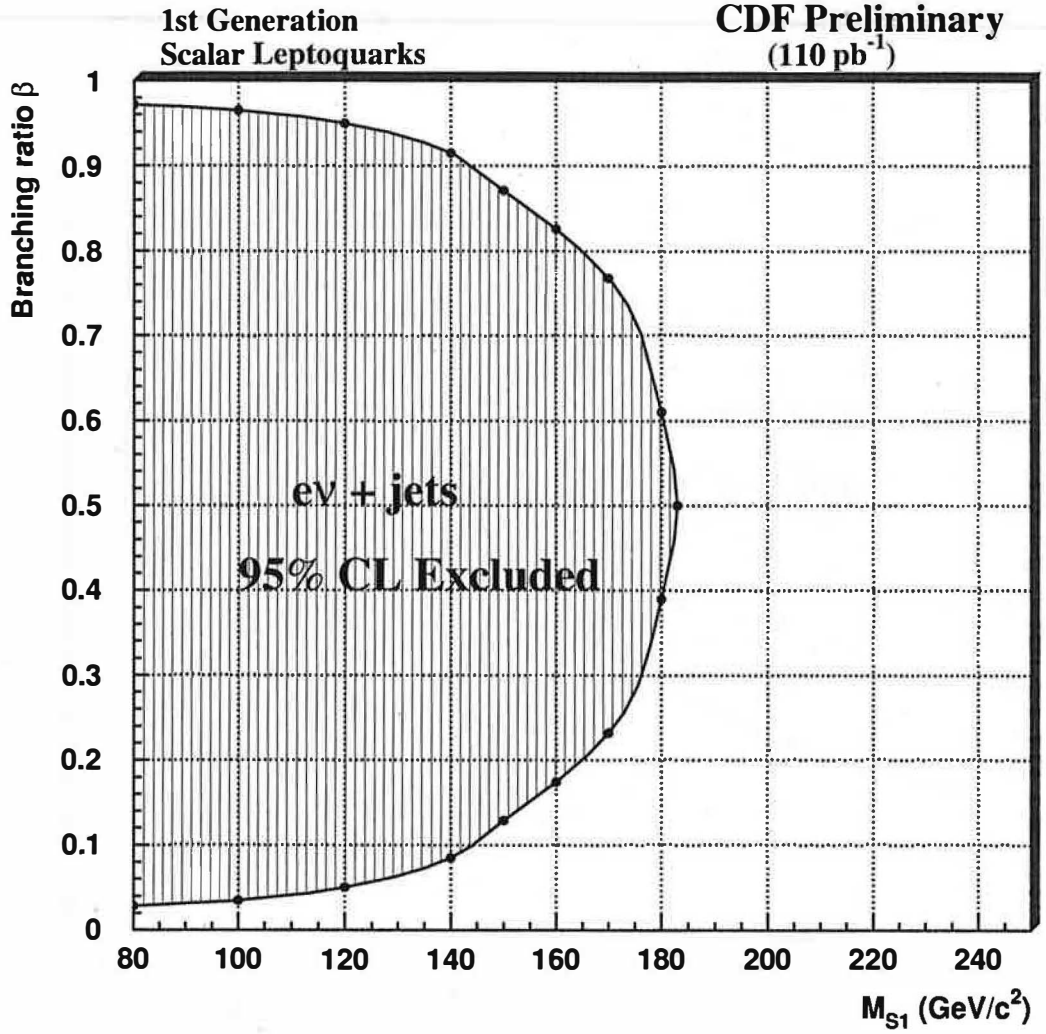

Figure 7.4: *In this plot is shown the lower limit on* M_{S1} *(black dots) as a function of the value of* β *in the search for scalar leptoquarks in the electron-neutrino channel: the shadowed area is excluded at 95% C.L. by this analysis.*

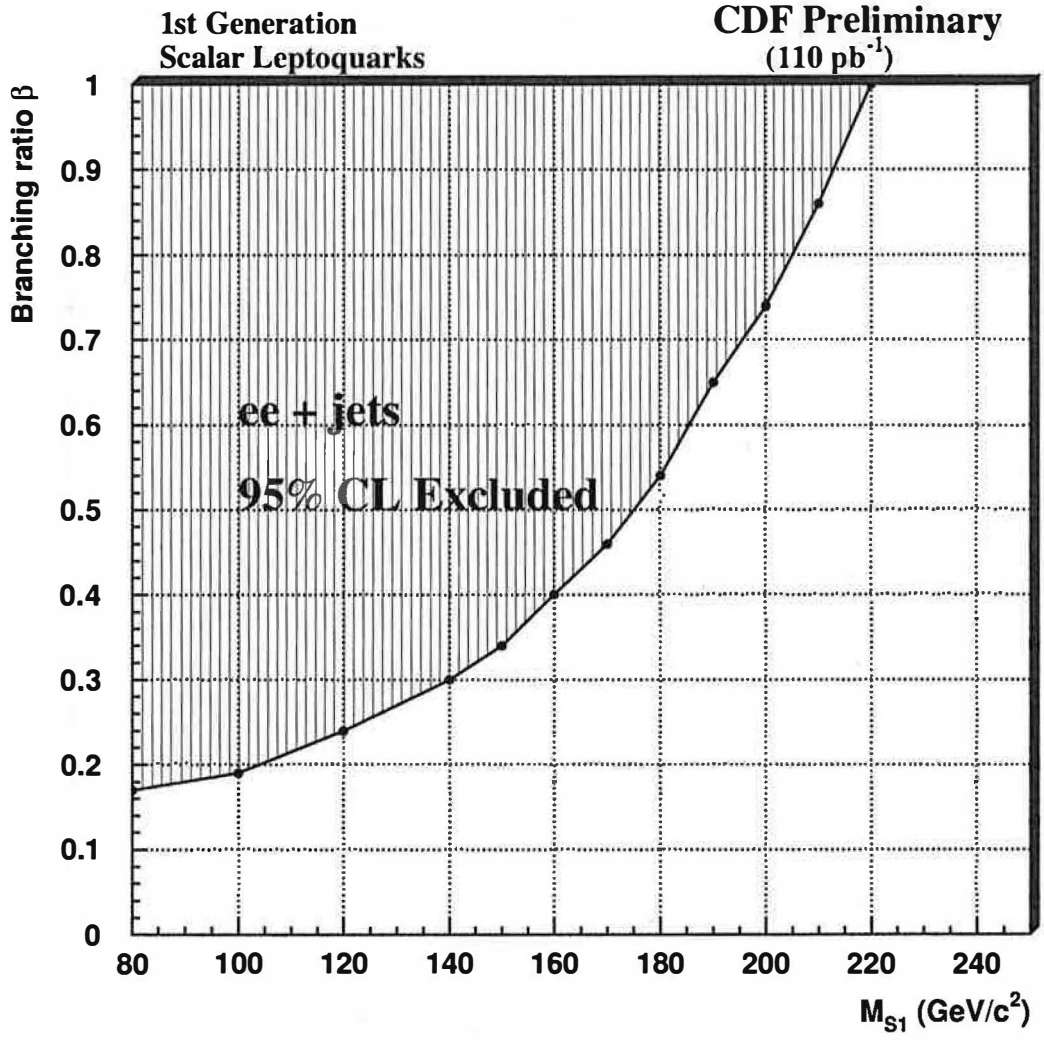

Figure 7.5: *In this plot is shown the scalar leptoquark mass limit as a function of β as found from the search for scalar leptoquarks in the dielectron channel: the shadowed area is excluded at 95% C.L. by this analysis.*

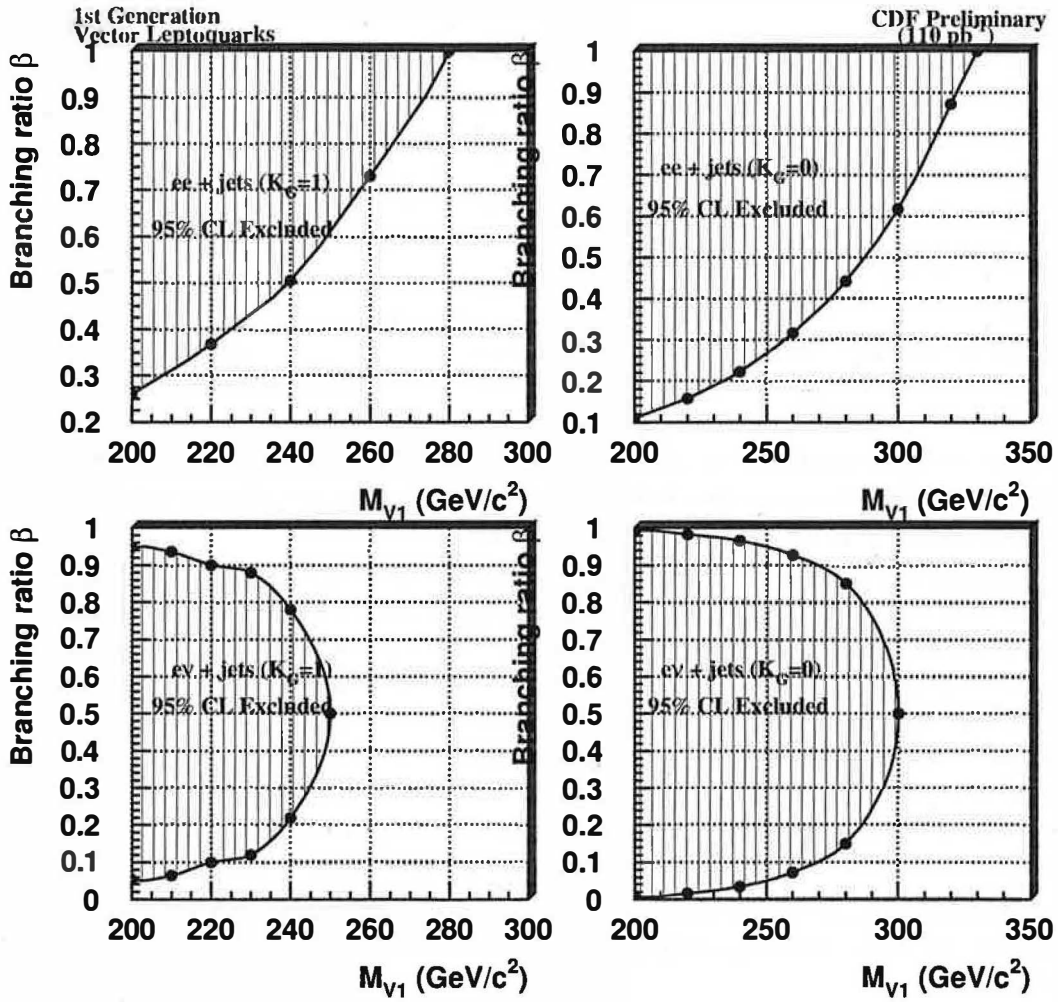

Figure 7.6: *Vector leptoquarks mass limits in the $e\nu jj$ and in the $eejj$ decay channel as a function of β. The regions excluded at 95% confidence level are shadowed in the plots.*

Experiment	β	M_{S1}	M_{V1} (Minimal)	M_{V1} (YM)
CDF	1	> 220 GeV/c^2	> 280 GeV/c^2	> 330 GeV/c^2
	0.5	> 204 GeV/c^2	> 265 GeV/c^2	> 310 GeV/c^2

Table 7.3: *Lower limits on scalar and vector leptoquark masses from the combination of the results of the analyses in the $e\nu jj$ and $eejj$ decay channels for the values of branching ratio $\beta = 0.5$ and $\beta = 1$.*

7.2. Combination of the results of the searches in the two channels

The results of the analyses in the two decay channels $e\nu jj$ and $eejj$ can be combined to give mass limits as a function of β: this limit is, in general, better than the corresponding one in each single channel. The procedure followed to combine limits from different analyses has been explained in Section (D.4). As far as concerns the systematic uncertainties, a few of them are common in the two searches, since changes in a definition or in a way to perform a measurement can affect both channels, a few are not: it has been taken about 3% and 4% as uncorrelated systematics in the electron-neutrino and dielectron channels and 15% as common uncertainty. The common part comes from correlation of the uncertainties on the jet energy measurement, on the choice of the parton density function and of the Q^2 in the Monte Carlo generation, on the electron identification efficiency calculation and on the decision of turning on the gluon radiation in the simulation.

The graphical representations of the results express the lower limits on the mass calculated, for each value of β, by using the Bayesian approach. In Figure (7.7) is shown, in the plane β versus M_{S1}, the limit on the mass obtained by the combination of the scalar search in the $e\nu jj$ and $eejj$ channels as a function of β. The largest curve is the exclusion region at 95% confidence level from the combination, while the two curves contained inside represent the areas eliminated by the single analyses. The Figures (7.8) and (7.9) show the same kind of results for the searches in vector case for Yang-Mills type and minimal couplings respectively. In Table (7.3) are listed the mass limits, for scalar and vector case, obtained by the combined channels for the branching ratio values $\beta = 1$ and $\beta = 0.5$.

The conclusive remarks of the analysis, the comparisons of the results with the current limits from D$\emptyset$ and from other experiments and the projections for the future will be detailed in next chapter.

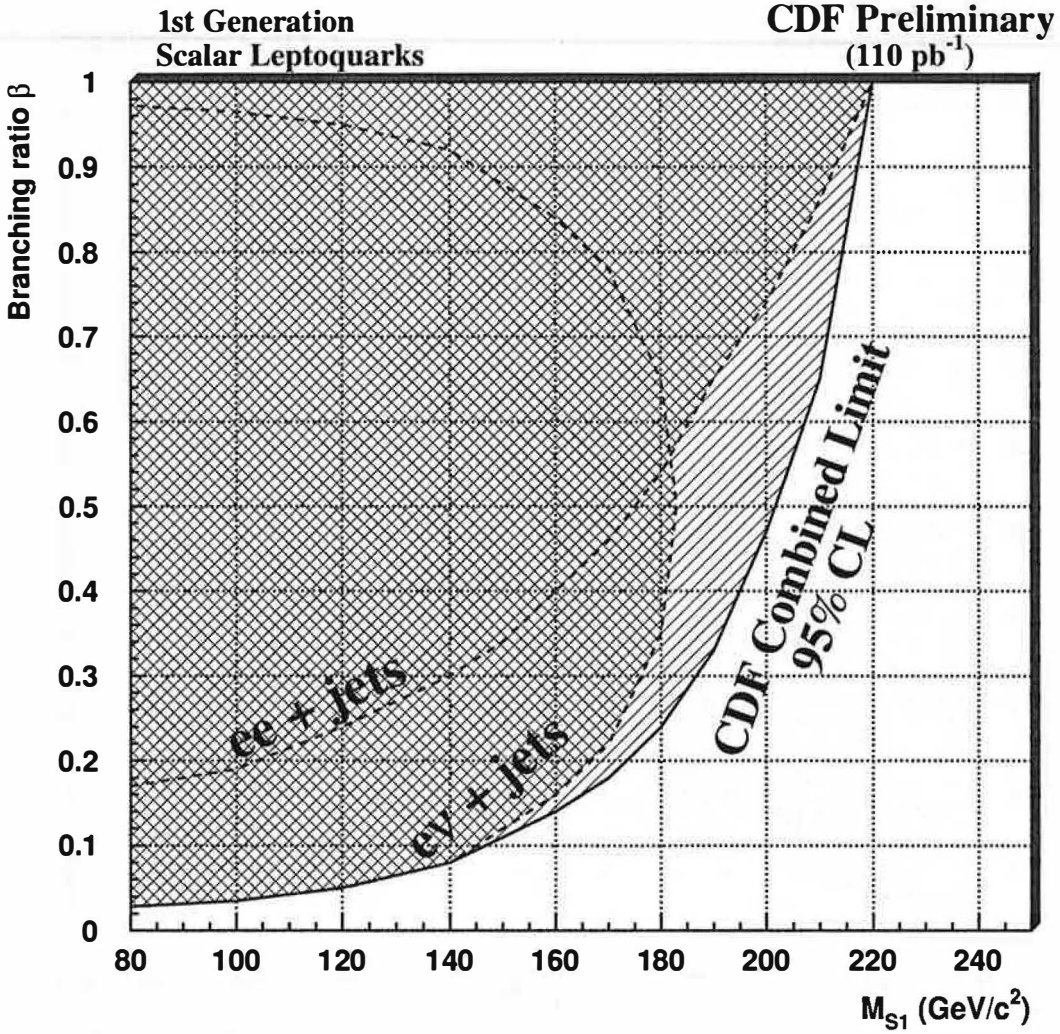

Figure 7.7: *In this plot are summarized all the results found from the searches for pair produced, scalar leptoquarks in the $e\nu jj$ and $eejj$ decay channels performed in this thesis. The shadowed regions represent the exclusion contours at 95% confidence level from single channels and from their combination.*

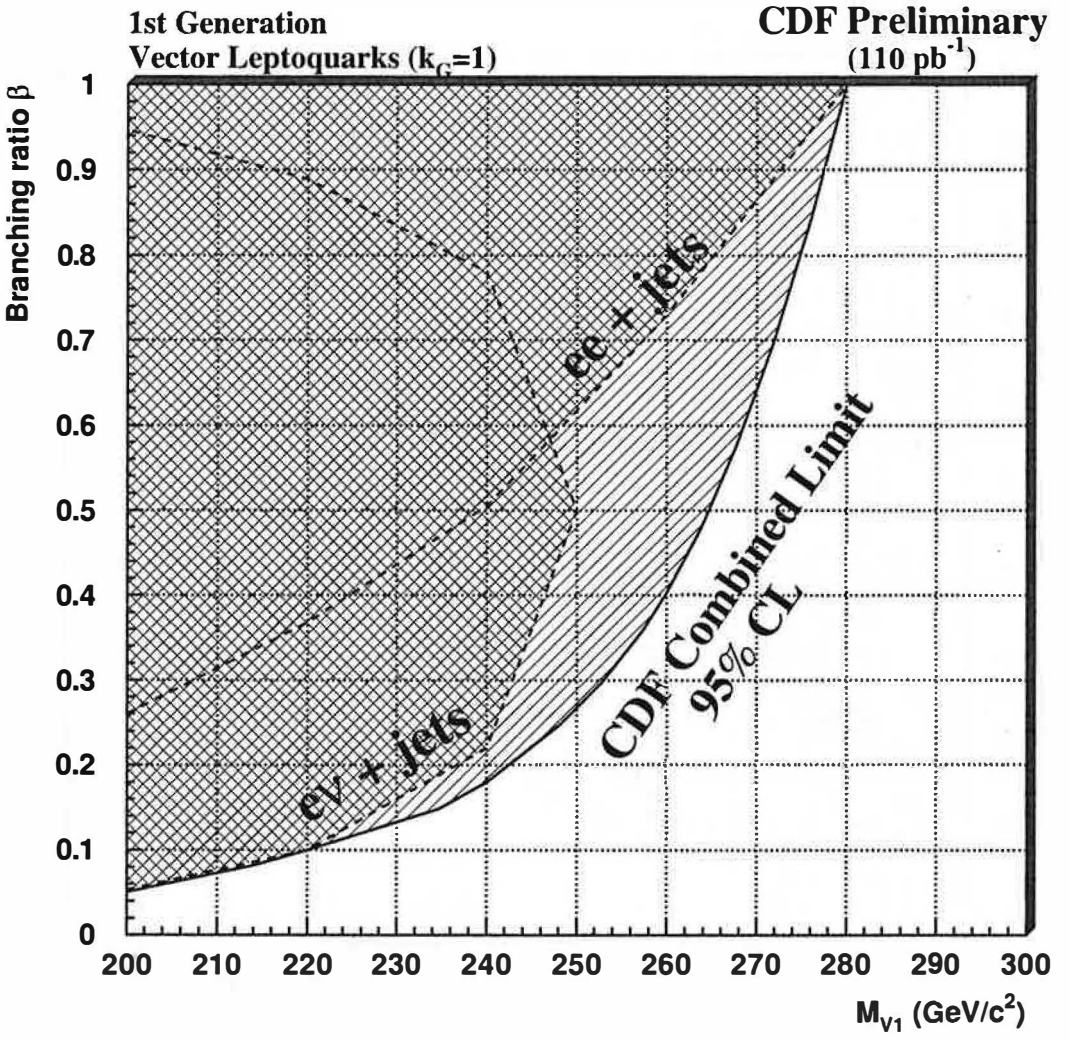

Figure 7.8: *This plot shows the results of the vector searches in the case of anomalous couplings $k_G = 1, \lambda_G = 0$. There are plotted the exclusion regions from the individual channels and their combination at 95% confidence level.*

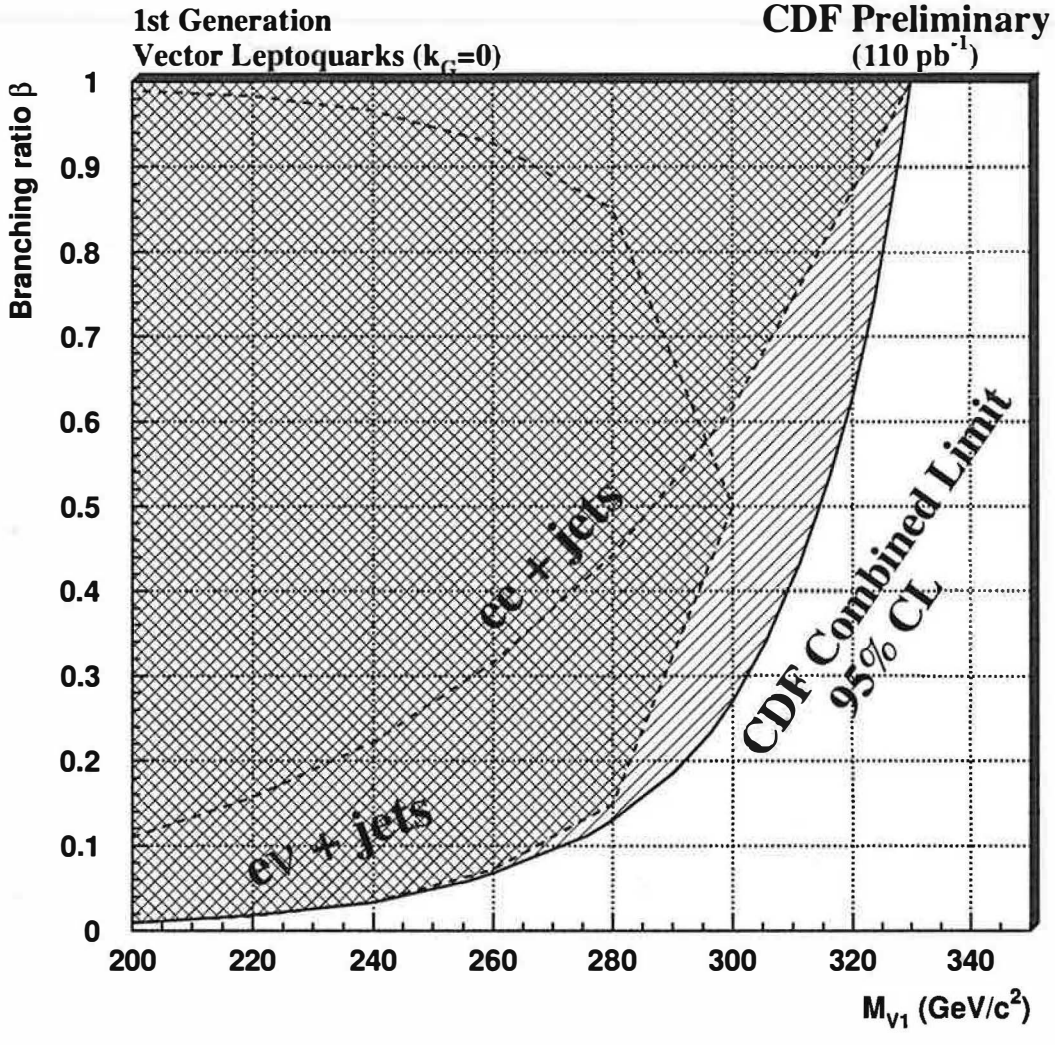

Figure 7.9: *This plot concentrates the results of the vector searches as well, here in the case of anomalous couplings $k_G = 0, \lambda_G = 0$: there are plotted the exclusion regions from single channel and their combination at 95% confidence level.*

Chapter 8

Epilogue

8.1. Conclusions

The first phase of Tevatron has finished running in 1996, and since then all data collected have been analyzed to look for signals of new physics beyond the Standard Model. In particular the Hadron Collider Group at the Geneva University has done much work in the leptoquark sector, for first and second [102] generation searches.

The most recent results for pair produced first generation leptoquarks performed at CDF are documented and detailed in this thesis, as well as in a paper which is in preparation.

In this analysis, leptoquarks have been searched for in the $e\nu jj$ and in the $eejj$ decay channels, by requiring events with one or two high energy, isolated electrons identified in the central ($e\nu jj$) or in the central and central/plug ($eejj$) regions of the electromagnetic calorimeter and at least two high energy jets.

In the search in the $e\nu jj$ channel the analysis, which is 19% efficient for a scalar leptoquark mass equal to 180 GeV/c^2, is based on the "relative likelihood" variable $LOG3$, which expresses the relative probability for the event being background with respect to signal. It is constructed by finding the expressions of the functions fitting the background and signal distributions of the $M_T(e,\nu)$, $\not\!\!E_T$ and $\sqrt{(E_T^C(j1)+E_T^C(j2))^2+(E_T(e1)+\not\!\!E_T)^2}$ variables: no events pass this selection on data, in agreement with the background expectation of (1.0 ± 0.6) W + jets and $t\bar{t}$ events. The same analysis has been repeated for the search of vector leptoquarks as well, since they have the same kinematical features of scalar leptoquarks.

In the search in the $eejj$ channel, the requirements of the selection are tight kinematic cuts on the transverse energies of the electrons and of the jets: the most important one is on the variable $\sqrt{(E_T^C(j1)+E_T^C(j2))^2+(E_T^C(e1)+E_T^C(e2))^2}$, which represents the radius of a circle centered in the origin of the plane $(E_T^C(j1)+E_T^C(j2)$ versus $(E_T^C(e1)+E_T^C(e2))$. The total efficiency of this selection is 35% on scalar leptoquark masses of 220 GeV/c^2, no events survive on real data while (1.8 ± 0.6) Drell-Yan and $t\bar{t}$ events are expected from background studies. Also in this case it has been possible to apply the selection requirements on samples of vector leptoquark events, whose selection efficiencies are roughly the same as in the scalar case.

For all the studied decay channels it has been possible to estimate, following a Bayesian approach, the 95% confidence level upper limits on the leptoquark production cross sections as a function of the leptoquark mass. By comparison with theoretical calculations of the cross section lower limits on leptoquark mass have been determined. These limits can be directly compared with the current DØ limits illustrated in Section (2.7.4) and in Figures (2.12) and (2.13), also found by using a Bayesian method.

First generation scalar leptoquarks decaying in the channel $e\nu jj$ have been excluded at 95% confidence level up to masses of 182 GeV/c^2 for a branching ratio for the leptoquark decay into electron and quark $\beta = 0.5$, value for which the limit takes its higher value in this case. This result is compatible with the values found at DØ, $M_{S1} > 175$ GeV/c^2 from the search in the $e\nu jj$ channel only [41]. Mass limits from this search as a function of β ranging in the interval [0.,1.] have been also found.

The same search has been repeated in the vector case, where the results depend on

Experiment	β	M_{S1}	M_{V1} (Minimal)	M_{V1} (YM)
CDF	1	> 220 GeV/c^2	> 280 GeV/c^2	> 330 GeV/c^2
	0.5	> 204 GeV/c^2	> 265 GeV/c^2	> 310 GeV/c^2

Table 8.1: *Lower limits on scalar and vector leptoquark masses from the combination of the results of the analyses in the $e\nu jj$ and $eejj$ decay channels for the values of branching ratio $\beta = 0.5$ and $\beta = 1$.*

Decay channel	Scalar Lq's Searches - TEVATRON Current Limits		
	CDF	DØ	CDF + DØ
$eejj$ ($\beta = 1$)	213 GeV/c^2 [37] **220** GeV/c^2	225 GeV/c^2 [38]	242 GeV/c^2 [39]
$e\nu jj$ ($\beta = 0.5$)	**182** GeV/c^2	175 GeV/c^2 [41]	
$\nu\nu jj$ ($\beta = 0$)		79 GeV/c^2 [40]	
All 3 channels ($\beta = 1$)	($ee + e\nu$) **220** GeV/c^2	225 GeV/c^2 [41]	
All 3 channels ($\beta = 0.5$)	($ee + e\nu$) **204** GeV/c^2	204 GeV/c^2 [41]	
All 3 channels ($\beta = 0$)		79 GeV/c^2 [41]	

Table 8.2: *Values of the 95% Confidence Level lower limits on the masses of first generation scalar leptoquarks from CDF [37] and DØ [38], [39], [41]. It is also indicated where this analysis will insert new limits or improve the previous ones.*

the choice of the so called anomalous coupling k_G, usually assumed equal to 0 (Yang-Mills coupling) or to 1 (minimal coupling). The results are lower limits on the mass at 250 GeV/c^2 (300 GeV/c^2) for $k_G = 1$ ($k_G = 0$) and for $\beta = 0.5$, compatible with the DØ values of 260 GeV/c^2 (315 GeV/c^2) [41].

The search in the $eejj$ channel has excluded scalar leptoquarks with masses lower than 220 GeV/c^2 for $\beta = 1$, which is the value of branching ratio which gives the highest limit from this search, and which is comparable with the DØ limit at 225 GeV/c^2 [38]. Also in this case the result has been generalized to each possible value of β in the range [0.,1.].

When the same cuts are applied in the vector case, the lower limits found on M_{V1} are 280 GeV/c^2 (330 GeV/c^2) for $k_G = 1$ ($k_G = 0$) for $\beta = 1$, to be compared with the DØ limits at 290 GeV/c^2 (340 GeV/c^2) [41].

Both in scalar and in vector case the results from single channels have been combined, giving the values listed in Table (8.1) as lower limits on the mass for $\beta = 0.5$ and $\beta = 1$. In particular $M_{S1} > 204$ GeV/c^2 and $M_{V1} > 310$ GeV/c^2(265 GeV/c^2) for Yang-Mills (minimal) anomalous couplings and for $\beta = 0.5$.

The Tables (8.2) and (8.3) are the same presented at the beginning of the thesis, in Section (2.7.4): they now contain all the numerical results found in this analysis and compare them with the current DØ limits.

Decay channel	Vector Lq's Searches - TEVATRON Current Limits	
	DØ	CDF
$eejj$ ($\beta = 1$)	340 GeV/c^2(K$_G$ = 0) [41]	**330** GeV/c^2
	290 GeV/c^2(K$_G$ = 1) [41]	**280** GeV/c^2
$e\nu jj$ ($\beta = 0.5$)	315 GeV/c^2(K$_G$ = 0) [41]	**300** GeV/c^2
	260 GeV/c^2(K$_G$ = 1) [41]	**250** GeV/c^2
$\nu\nu jj$ ($\beta = 0$)	206 GeV/c^2(K$_G$ = 0) [41]	
	154 GeV/c^2(K$_G$ = 1) [41]	
All 3 ($\beta = 1$)	345 GeV/c^2(K$_G$ = 0) [41]	($ee + e\nu$) **330** GeV/c^2
	292 GeV/c^2(K$_G$ = 1) [41]	($ee + e\nu$) **280** GeV/c^2
All 3 ($\beta = 0.5$)	337 GeV/c^2(K$_G$ = 0) [41]	($ee + e\nu$) **310** GeV/c^2
	282 GeV/c^2(K$_G$ = 1) [41]	($ee + e\nu$) **265** GeV/c^2
All 3 ($\beta = 0$)	206 GeV/c^2(K$_G$ = 0) [41]	
	159 GeV/c^2(K$_G$ = 1) [41]	

Table 8.3: *Values of the 95% Confidence Level lower limits on first generation vector leptoquarks from DØ [41]. The analysis performed in this thesis will give the first CDF limits on vector leptoquark searches.*

It will be necessary to wait the new data, taken with higher luminosity and energy, to be able to improve this analysis or eventually to have the evidence of a signal.

8.2. Future searches

During the next decade several high-energy colliders will start running and thanks to the available energies and luminosities it will be possible to perform searches for signals of new physics beyond the Standard Model. The leptoquark searches will continue at Tevatron and HERA, while new colliders like LHC will boost the limits on their masses and discovery reaches to the TeV region. A detailed general review on leptoquarks production at the future colliders can be found in [103].

The Tevatron has started running in 2001 at a center of mass energy $\sqrt{s} = 2.0$ TeV and expects to collect about 2 fb^{-1} total luminosity during the first two years and possibly 10 fb^{-1} before LHC turns on in 2005 [104], [105]. This will allow an improvement in the leptoquark mass limits, assuming that they are not discovered: if one considers a 25% selection efficiency at high mass and without candidate events surviving the selection requirements, then the CDF and DØ experiments should be able to set a lower limit on the scalar leptoquark mass at the 95% confidence level of approximately 300 GeV/c^2 (375 GeV/c^2) for 1 fb^{-1} (10 fb^{-1}) of data. These limits are calculated by comparing the expected experimental results with the Next-to-Leading Order calculations of the production cross section made by Krämer [31] for a center of mass energy of 2.0 TeV. The plots of the leading order cross sections as a function of the leptoquark mass are shown in Figures (8.1) and (8.2), as they have been calculated by [30]. The ten-event discovery reach is about 235 GeV/c^2 (325 GeV/c^2) for 1 fb^{-1} (10 fb^{-1}). In this way the leptoquark searches at Tevatron during

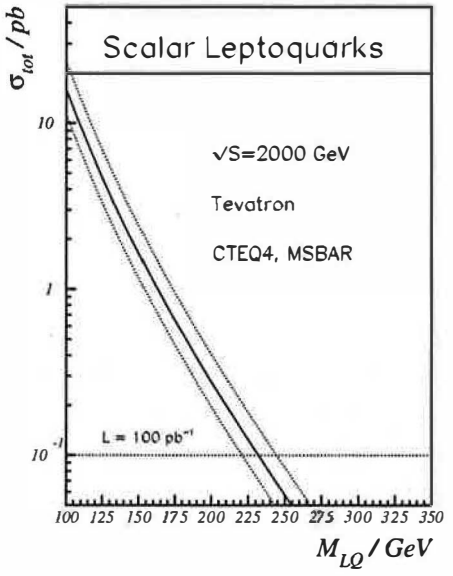

Figure 8.1: *Cross sections for pair produced scalar leptoquarks at the new Tevatron centre-of-mass energy $\sqrt{s} = 2$ TeV. The full line represents the cross section evaluated for the choice $Q^2 = \mathrm{M_{S1}}$ for the factorization scale, while the dotted lines contain the range of the scale variation $Q^2 \in [\mathrm{M_{S1}}/2, 2\mathrm{M_{S1}}]$ (from [30]).*

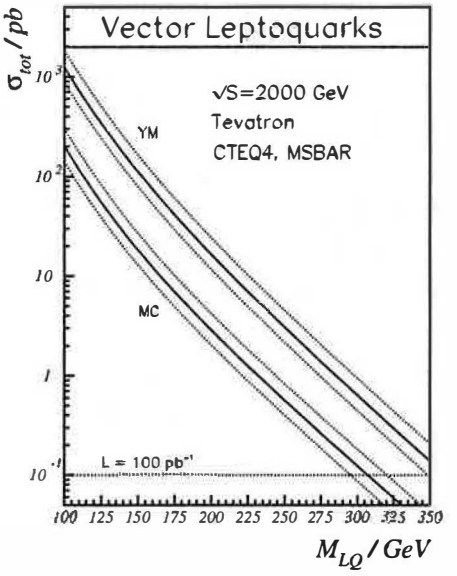

Figure 8.2: *Cross sections for pair produced vector leptoquarks at the new Tevatron centre-of-mass energy $\sqrt{s} = 2$ TeV for the Yang-Mills type coupling (YM) and minimal coupling (MC). The full line represents the cross section evaluated for the choice $Q^2 = \mathrm{M_{V1}}$, while the dotted lines contain the range of the scale variation $Q^2 \in [\mathrm{M_{V1}}/2, 2\mathrm{M_{V1}}]$ (from [30]).*

next run should cover the entire phase space of the future HERA searches, regardless of the strength of the unknown Yukawa coupling.

In fact, the HERA machine at DESY has been upgraded with the installation of dual-purpose superconducting magnets that focus and bend the beam particles installed within the detectors very close to the collision point and has started the new run at the end of July 2001 [106]. Along with several other improvements to the machine, the delivered luminosity should be approximately 170 pb^{-1} per year per experiment. Accumulated data samples should approach 1 fb^{-1} by 2005. Future searches for leptoquarks are expected to probe masses up to about 300 GeV/c^2 for Yukawa couplings of the order of one-tenth electromagnetic strength.

The Large Hadron Collider (LHC) machine is currently under construction at CERN: starting in 2005, it will provide pp collisions at a center of mass energy $\sqrt{s} = 14$ TeV and 100 fb^{-1} of data each year [104], [107]. The ATLAS and CMS experiments are likely to be the most important high energy physics experiments of the decade, precisely because they will be the first experiments whose energy is clearly in the regime of new physics. In Figures (8.3) and (8.4) are shown the scalar and vector leptoquarks pair production cross sections calculated at the LHC energy, $\sqrt{s} = 14$ TeV [30]. The most important contribution to the cross section is given by the gluon fusion, whereas the quark term becomes important for large masses. Detailed studies of the pair production of first-generation leptoquark signals and backgrounds have been performed at the event-generator level with energy smearing to mimic the response of the calorimeters. Both ATLAS and CMS expect a mass reach at the 95% confidence level for the pair production of first generation scalar leptoquarks at 1.3 TeV/c^2 (1.7 TeV/c^2) for 10 fb^{-1} (100 fb^{-1}) of data, assuming no events are observed and $\beta = 0.5$. The topology of the searched events is similar to the one studied at Tevatron, and the main background sources are Z events, reduced by applying tight requirements on the dilepton invariant mass value, and $t\bar{t}$ events, partially eliminated through kinematical cuts to variables like $\sum E_T$, the sum of all transverse energies of the event. These estimations are done by optimizing signal to noise ratio on simulated signal and background events for different leptoquark masses. The efficiencies are about 30% for leptoquark masses higher than 1.4 TeV/c^2 [108], [109].

Other more futuristic studies have been performed, and a few examples are summarized in Table (8.4), where the search reaches for first generation scalar and vector leptoquarks are compared for different hadron colliders [110], and in Table (8.5) for leptoquark searches at linear colliders like TESLA or the still under study American Linear Collider and the CERN $\mu^+\mu^-$ collider [111], [112], [113], [114]. The strength of the linear collider is in the determination of the leptoquark's electroweak quantum numbers and the strength of its Yukawa couplings once it is discovered. The possibility of measuring their production rate and polarized left-right asymmetry could completely determine the leptoquark's electroweak properties and identify its type in both the pair and single production channels, up to the kinematic limit.

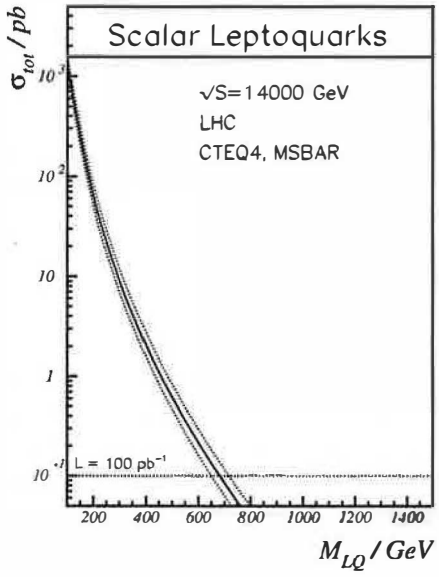

Figure 8.3: *Production cross section for pair-produced scalar leptoquarks at LHC for center of mass energy equal to 14 TeV. The full line represents the theoretical calculation for the choice* $Q^2 = \mathrm{M_{S1}}$ *for the factorization scale, while the dotted lines contain the range of the scale variation* $Q^2 \in [\mathrm{M_{S1}}/2, 2\mathrm{M_{S1}}]$ *(from [30]).*

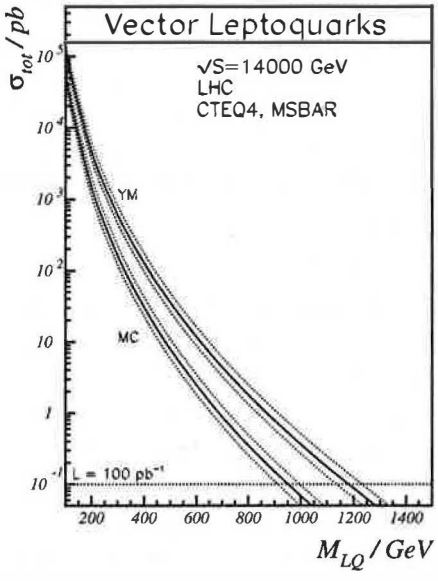

Figure 8.4: *Production cross sections for vector leptoquarks pair production at LHC for the Yang-Mills type coupling (YM) and minimal coupling (MC) at 14 TeV. The full line represents the theoretical calculation for* $Q^2 = \mathrm{M_{V1}}$*, while the dotted lines contain the range of the scale variation* $Q^2 \in [\mathrm{M_{V1}}/2, 2\mathrm{M_{V1}}]$ *(from [30]).*

Machine	$\mathcal{L}$ fb^{-1}	Scalar	Vector
LHC	100	1.34 (1.27)	2.1 (2.0)
60 TeV (pp)	100	4.9 (4.4)	7.6 (7.0)
60 TeV ($p\bar{p}$)	100	5.7 (5.2)	9.6 (9.0)
200 TeV (pp)	1000	15.4 (14.1)	24.2 (23.3)
200 TeV ($p\bar{p}$)	1000	18.1 (16.2)	31.1 (29.0)

Table 8.4: *Search reaches in TeV for Scalar and Vector leptoquarks at future hadron colliders assuming a branching fraction into a charged lepton plus a jet of 1 (1/2). For vector leptoquarks* $k_G = 1$ *has been assumed and in both cases the MRSA' parton densities have been employed. These results are based on the assumption of 10 signal events. The estimation obtained for the LHC is somewhat smaller than that given by the analyses mentioned in [108] and [109].*

$\sqrt{s}$ (TeV)	$\mathcal{L}$ fb^{-1}	Scalar	Vector
		e^+e^- Colliders	
0.5	50	490 GeV/c^2	490 GeV/c^2
1.0	200	980 GeV/c^2	980 GeV/c^2
1.5	200	1.4 TeV/c^2	1.5 TeV/c^2
5.0	1000	4.7 TeV/c^2	4.8 TeV/c^2
		$e\gamma$ Colliders	
0.5	50	450 GeV/c^2	450 GeV/c^2
1.0	200	900 GeV/c^2	910 GeV/c^2
1.5	200	1.4 TeV/c^2	1.4 TeV/c^2
5.0	1000	4.5 TeV/c^2	4.5 TeV/c^2
		$\mu^+\mu^-$ Colliders	
0.5	0.7	250 GeV/c^2	310 GeV/c^2
0.5	50	400 GeV/c^2	440 GeV/c^2
5.0	1000	3.6 TeV/c^2	3.7 TeV/c^2

Table 8.5: *Leptoquark discovery limits for the e^+e^-, $e\gamma$ and $\mu^+\mu^-$ colliders. The discovery limits are based on the production of 100 leptoquarks for the energies and integrated luminosities given in first and second columns [113].*

Merci !

Je voudrais remercier tous ceux qui, avec leur compétence, chaleur et soutien, m'ont aidé à parvenir au but de ce travail.
Je remercie le Professeur Allan Clark, pour m'avoir donné l'opportunité de participer à une expérience très formative et intéressante, pour avoir été là dans les moments difficiles ainsi que pour avoir partagé avec moi les joies et les satisfactions des ces années.
Je remercie les Professeurs Maria Kienzle et Thomas Müller pour avoir gentillement accepté de faire partie du jury.
Je remercie Xin Wu, Lorenzo Moneta et John Conway pour l'aide et les conseils qu'ils m'ont donné et sans lesquelles cette recherche n'aurait pas pu être menée au terme.
Le soulagement de la fin d'un travail parfois exigeant laisse un peu de place à la tristesse du départ: je dis au revoir à mon bureau, au couloirs du DPNC, à la cafétéria où j'ai passé mes pauses avec les collegues, et, bien sûr, à tous les gens qui ont animé ces lieux: Thomas, Lorenzo, Didier, Xin, Daniela, Andras, Annie, Eric, Gerard, Bertrand, Daniel, Philippe, Sam, Federica, Yanwen, Cristina, Monica, Saverio, Patrick, Markus, Philipp, Pablo, Catherine, Peggy, les deux dames du café et la dame de la réception, Jean-Claude, Mr. Joly, les ingénieurs et les techniciens que je croise tout le temps, mais dont j'ignore encore le nom.

Grazie, Simona e Patrizia, per il bellissimo legame che siamo riuscite ad instaurare anche se un Oceano ci separa. Grazie, Manu e Christine, per quella serata indimenticabile passata in un vecchio cineforum di legno di un villaggio vicino a Batavia, raggiunto quasi per caso in una serata nevosa, a vedere "Les demoiselles de Rochefort" in francese. Grazie, Fabrizio e Titti, per dimostrarci in tutti i modi che in fondo la lontananza da casa non conta. Grazie, Claralberta, Gino e Francesco, per avermi accolta nella vostra bella famiglia molto unita e molto romagnola di Chêne-Bougeries. Grazie, mamma e babbo, per avermi spinta a partire con le lacrime agli occhi e con il desiderio di vedermi felice.
Dedico questa tesi a Daniele, coraggioso e abile timoniere della barchetta Michelini-Strumia, che condivide con me gioie e frustrazioni della vita. E la dedico a Matteo, che in questo periodo ha lavorato tanto ottenendo strepitosi risultati, e' riuscito a sedersi senza cadere quando stavo cominciando il capitolo teorico, ha detto babbo a quello sul rivelatore, ha cominciato a mangiare le pappine durante quello sulla electrons selection, ha avuto il primo dentino mentre spiegavo i sistematici, ha battuto le mani alle reti neurali, ha detto "broum-broum" alle conclusioni e oggi e' venuto qua con me dandomi la mano e chiamandomi mamma.

Part IV

Appendices

Appendix A

The electron identification efficiency

CUT	Tight (Central)	Loose (Central or Plug)
Had/Em	< 0.05	< 0.1
E/p	< 1.8	< 4.0
Isolation	< 0.1	< 0.1
$\|\Delta x\|$	≤ 1.5 cm	*none*
$\|\Delta z\|$	≤ 3.0 cm	*none*
Lshr	< 0.2	*none*
χ^2_{str}	< 10.0	*none*
$\chi^2_{3\times3}$	*none*	≤ 3.0
$\|Z_v - Z_e\|$	≤ 5.0 cm	*none*
$\|Z_v\|$	≤ 60.0 cm	*none*
Conversion	yes	yes
Fiducial	yes	*none*

Table A.1: *Electron-ID cuts applied in this analysis: the requirements are a central electron passing the tight cuts in the $e\nu jj$ analysis and a central electron passing tight cuts and a central or plug electron passing looser cuts in the $eejj$ analysis.*

A.1. Electron identification efficiency calculated on real data

The electron identification efficiencies evaluated on Monte Carlo simulated leptoquark events listed in Table (A.2) have been compared with the values obtained from calculations done on a data sample of $Z \rightarrow ee$ events from run 1b. To build this sample, events have been selected by requiring, as first leg (leg1) of the Z decay, one central electron passing the tight cuts of the selection (see Table (A.1)) and, as a second leg (leg2), a second electromagnetic bank in the central or plug region with an associated track in the CTC, opposite charge with respect to leg1 if in the central region and such that the invariant mass $M_{leg1,leg2}$ be in the Z mass window $[76, 106]$ GeV/c^2. On these second legs the tight and loose selection cuts have been then applied to calculate the efficiencies for dielectron identification for the

M_{S1}(GeV/c^2)	ε_e "$e\nu jj$"	M_{S1}(GeV/c^2)	ε_{ee} "$eejj$"
140	$(72.2 \pm 2.2)\%$	**100**	$(65.9 \pm 1.9)\%$
150	$(72.0 \pm 2.1)\%$	**120**	$(65.2 \pm 1.8)\%$
160	$(72.0 \pm 2.1)\%$	**140**	$(63.7 \pm 1.7)\%$
170	$(70.9 \pm 2.1)\%$	**160**	$(60.3 \pm 1.6)\%$
180	$(69.7 \pm 2.0)\%$	**180**	$(62.9 \pm 1.7)\%$
190	$(70.1 \pm 2.1)\%$	**200**	$(60.8 \pm 1.6)\%$
200	$(67.7 \pm 2.0)\%$	**220**	$(60.3 \pm 1.6)\%$
210	$(69.7 \pm 2.0)\%$	**240**	$(58.5 \pm 1.5)\%$

Table A.2: *Electron-identification efficiencies evaluated on Monte Carlo leptoquark events for the two analyses in the scalar case.*

analysis in the $ee\gamma jj$ channel and for the single electron identification in the $e\nu jj$ channel. In Figure A.1 is represented the distribution of $M_{leg1,leg2}$ with the two legs obtained with the above criteria, except of the cut on $M_{leg1,leg2}$. The second leg can belong to the following

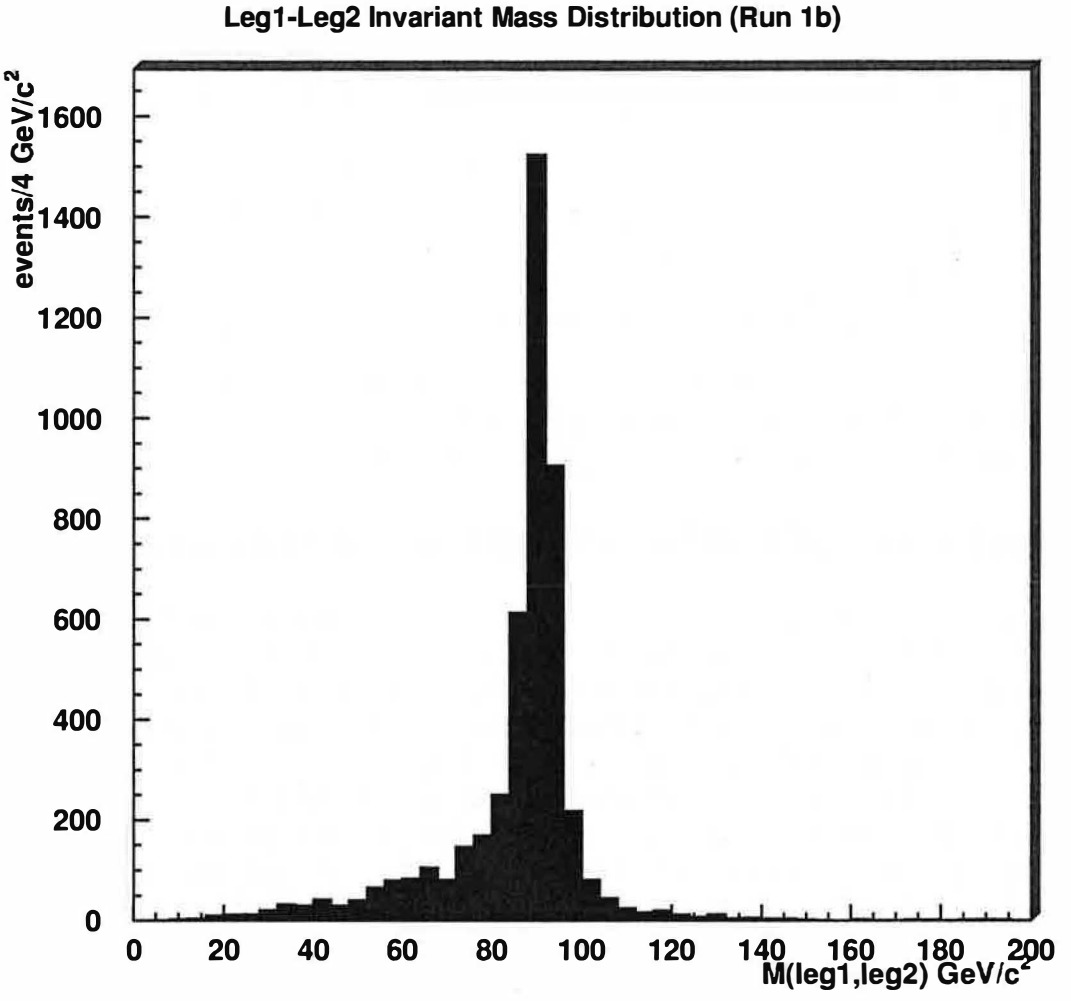

Figure A.1: *Distributions of the leg1-leg2 invariant mass according to the selection criteria enounced in Section 4.4 before the cut on* $M_{leg1,leg2}$.

categories:

1. central, in the fiducial volume;
2. central, not in the fiducial region;
3. plug

Leg2's of category 1. can satisfy both tight and loose selection cuts, of category 2. and 3. only the loose-central and loose-plug selection cuts respectively. So for the electron-electron

F=f-f	N=f-nf	P=f-p
F_t=(f+t)-f	N_t=(f+t)-nf	P_t=(f+t)-p
F_{tl}=(f+t)-(f+l)	N_{tl}=(f+t)-(nf+l)	P_{tl}=(f+t)-(p+l)
F_{tt}=(f+t)-(f+t)	N_{tt}=(f+t)-(nf+t)= $\emptyset$	P_{tt}=(f+t)-(p+t)= $\emptyset$

Table A.3: *Grid with the variables defined for the electron-identification efficiencies (f: fiducial, nf: non-fiducial, t: tight, l: loose, p:plug).*

analysis all of three are involved, while for the electron-neutrino analysis only the first one will be taken into account.

• Electrons-ID efficiency in the dielectron analysis

The combinations of categories which are involved by the selection are summarized in Table (A.3): F is the number of events with two electrons in the central region and in the fiducial volume; N is the number of events with two electrons in the central region, one in the fiducial volume and the other in the non fiducial; P is the number of events with one electron in the central region, in the fiducial volume and the other in the plug region. Among these events the number of events with one leg passing tight cuts are F_t, N_t or P_t and the number of events with both legs passing tight-loose or tight-tight cuts are F_{tl}, N_{tl} or P_{tl} and F_{tt}, N_{tt} or P_{tt} respectively. One remark: the two categories N_{tt} and P_{tt} are empty, because the second leg, being in the central,non fiducial or in the plug region, does not satisfy the tight cuts. After defining with ε_t the efficiency of tight cuts for one leg and with ε_l^F, ε_l^N and ε_l^P the efficiency of loose cuts for events of the categories F, N and P, the following relations can be found:

$$F_t = 2\varepsilon_t F - \varepsilon_t^2 F \quad \text{(A.1)}$$

$$N_t = \varepsilon_t N \quad \text{(A.2)}$$

$$P_t = \varepsilon_t P \quad \text{(A.3)}$$

$$F_{tl} = 2\varepsilon_t \varepsilon_l^F F - \varepsilon_t^2 F \quad \text{(A.4)}$$

$$N_{tl} = \varepsilon_t \varepsilon_l^N N \quad \text{(A.5)}$$

$$P_{tl} = \varepsilon_t \varepsilon_l^P P \quad \text{(A.6)}$$

$$F_{tt} = \varepsilon_t^2 F \quad \text{(A.7)}$$

from which can be calculated:

$$\varepsilon_t = 2\frac{F_{tt}}{F_t + F_{tt}} \quad \text{(A.8)}$$

$$\varepsilon_l^F = \frac{F_{tt} + F_{tl}}{F_t + F_{tt}} \quad \text{(A.9)}$$

$$\varepsilon_l^N = \frac{N_{tl}}{N_t} \quad \text{(A.10)}$$

$$\varepsilon_l^P = \frac{P_{tl}}{P_t} \quad \text{(A.11)}$$

and the efficiencies of the dielectron selection:

$$\varepsilon_{tl_f} = (2\varepsilon_l^F - \varepsilon_t)\varepsilon_t \quad \text{(A.12)}$$

ε_t	68.0%
ε_l^F	88.6%
ε_l^N	84.1%
ε_l^P	77.2%
ε_{tl_f}	74.2%
ε_{tl_n}	57.1%
ε_{tl_p}	52.4%

$M_{S1}(GeV/c^2)$	A	B	C	ε_{ee}
100	0.57	0.17	0.26	$(65.6 \pm 4.0)\%$
120	0.56	0.17	0.25	$(65.7 \pm 3.5)\%$
140	0.55	0.18	0.27	$(65.1 \pm 3.3)\%$
160	0.55	0.20	0.25	$(65.3 \pm 3.3)\%$
180	0.54	0.21	0.25	$(65.2 \pm 3.1)\%$
200	0.54	0.21	0.25	$(65.1 \pm 3.0)\%$
220	0.54	0.20	0.26	$(65.1 \pm 3.0)\%$
240	0.55	0.22	0.23	$(65.4 \pm 3.1)\%$

Table A.4: *Partial efficiencies evaluated from data (see Equations from A.8 to A.14), Monte Carlo coefficients A, B and C and total dielectron identification efficiency ε_{ee} for different scalar leptoquark masses.*

$$\varepsilon_{tl_{nf}} = \varepsilon_t \varepsilon_l^N \tag{A.13}$$

$$\varepsilon_{tl_p} = \varepsilon_t \varepsilon_l^P \tag{A.14}$$

The last three relations give the dielectron efficiencies when the loose cuts are applied on the second leg in the fiducial volume of the central region, in the non-fiducial volume of the central region and in the plug region respectively. The combination of these three efficiencies, to get the total dielectron identification efficiencies, is done by summing them according to the following formula:

$$\varepsilon_{ee} = A \times \varepsilon_{tl_f} + B \times \varepsilon_{tl_{nf}} + C \times \varepsilon_{tl_p} \tag{A.15}$$

where A, B and C are the proportions, evaluated on Monte Carlo samples of leptoquarks for different masses, in which are present these three kind of categories on the events. The values obtained range between 65.1 and 65.7 %, with a statistical error of about 3%, comparable with what has been obtained from Monte Carlo events. In Table (A.4) are reported the values of the partial efficiencies used to evaluate the global one and the weights A, B and C used in the Equation (A.15) evaluated from Monte Carlo for different leptoquark masses and the result for the total dielectron efficiency ε_{ee}.

- Electron-ID efficiency in the electron-neutrino analysis

In this channel only the F_t and the F_{tt} categories of Table (A.3) are important because the electron must satisfy the tight cuts, and as consequence it cannot be accepted in the central non-fiducial region, or in the plug region. The identification efficiency for a single electron can be then defined as in Equation (A.8) as:

$$\varepsilon_e = 2\frac{F_{tt}}{F_t + F_{tt}} \tag{A.16}$$

giving a value of $\varepsilon_e = (67.2 \pm 1.6)\%$, in agreement with what obtained from the Monte Carlo.

Appendix B

The fits over background and signal in the "relative likelihood analysis"

B.1. Fits on kinematical distributions with $P_S(x)$ and $P_B(x)$

The fits on the kinematical distributions plotted in Figures (5.11) and (5.10) have been performed with the functions $P_S(x)$ and $P_B(x)$ listed below, which have been normalized to one in the same interval for background and for signal. For signal events the fits are done with the following functions:

- $x = \not{E}_T$:
  - $P_S(x) = 248.21 \cdot e^{-0.5 \cdot \frac{(x-75.677)^2}{37.202^2}}$ if $x \leq 125$,
  - $P_S(x) = e^{7.9096-0.22965E-01x}$ elsewhere
- $x = M_T(e, \nu)$:
  - $P_S(x) = 10. + 182.69 \cdot e^{-0.5 \cdot \frac{(x-138.48)^2}{96.734^2}}$
- $x = E_T(jet1) + E_T(jet2) + E_T(electron)$:
  - $P_S(x) = 206.71 \cdot e^{-0.5 \cdot \frac{(x-282.04)^2}{55.273^2}}$ if $x \leq 330$,
  - $P_S(x) = 16374. \cdot e^{-0.5 \cdot \frac{(x+557.50)^2}{290.62^2}}$ elsewhere
- $x = E_T(electron) + \not{E}_T$:
  - $P_S(x) = 135.36 \cdot e^{-0.5 \cdot \frac{(x-141.57)^2}{35.892^2}}$ if $x \leq 160$,
  - $P_S(x) = 205.94 \cdot e^{-0.5 \cdot \frac{(x-24.492)^2}{150.37^2}}$ elsewhere
- $x = E_T(jet1) + E_T(jet2) + E_T(electron) + \not{E}_T$:
  - $P_S(x) = 216.22 \cdot e^{-0.5 \cdot \frac{(x-369.86)^2}{66.278^2}}$ if $x \leq 410$,
  - $P_S(x) = 475.13 \cdot e^{-0.5 \cdot \frac{(x-125.28)^2}{204.53^2}}$ elsewhere
- $x = \sqrt{(E_T(jet1) + E_T(jet2))^2 + (E_T(electron) + \not{E}_T)^2}$:
  - $P_S(x) = 195.39 \cdot e^{-0.5 \cdot \frac{(x-265.25)^2}{47.099^2}}$ if $x \leq 285$,
  - $P_S(x) = 485.98 \cdot e^{-0.5 \cdot \frac{(x-54.335)^2}{166.68^2}}$ elsewhere

In an analogous way the functions fitting the background distributions have the following form:

- $x = \not{E}_T$:
  - $P_B(x) = 280.47 \cdot e^{-0.5 \cdot \frac{(x-38.285)^2}{11.867^2}}$ if $x \leq 60$,

  - $P_B(x) = 85852. \cdot e^{-0.5 \cdot \frac{(x+152.66)^2}{55.281^2}}$ elsewhere

- $x = M_T(e, \nu)$:
  - $P_B(x) = 22.355 + 302.77 \cdot e^{-0.5 \cdot \frac{(x-72.629)^2}{14.810^2}}$ if $x \leq 120$,
  - $P_B(x) = e^{(9.0761 - 0.47914E-01x)}$ elsewhere

- $x = E_T(jet1) + E_T(jet2) + E_T(electron)$:
  - $P_B(x) = 122.15 \cdot e^{-0.5 \cdot \frac{(x-106.26)^2}{13.866^2}}$ if $x \leq 115$,
  - $P_B(x) = e^{(7.1371 + 0.18383E-01x)}$ elsewhere

- $x = E_T(electron) + \not{E}_T$:
  - $P_B(x) = 163.69 \cdot e^{-0.5 \cdot \frac{(x-81.408)^2}{15.064^2}}$ if $x \leq 90$,
  - $P_B(x) = e^{(8.9868 + 0.45685E-01x)}$ elsewhere

- $x = E_T(jet1) + E_T(jet2) + E_T(electron) + \not{E}_T$:
  - $P_B(x) = 182.15 \cdot e^{-0.5 \cdot \frac{(x-141.25)^2}{7.6379^2}}$ if $x \leq 150$,
  - $P_B(x) = e^{(8.0306 - 0.18075E-01x)}$ elsewhere

- $x = \sqrt{(E_T(jet1) + E_T(jet2))^2 + (E_T(electron) + \not{E}_T)^2}$:
  - $P_B(x) = 276.41 \cdot e^{-0.5 \cdot \frac{(x-105.43)^2}{7.7976^2}}$ if $x \leq 100$,
  - $P_B(x) = 19150. \cdot e^{-0.5 \cdot \frac{(x+362.98)^2}{152.707^2}}$ elsewhere

Appendix C

The Neural Network analysis in the $e\nu jj$ decay channel

C.1. The Neural Network analysis

Introduction- *The analysis techniques which involve neural network algorithms are used more and more often in the community of high-energy physics. They are based on the way the information is transmitted between neurons in our brain and on the way it makes decisions. As our brain is able to distinguish a black dog from a white cat, a program based on the same kind of structure used in high-energy physics would be able, in principle, to discriminate a signal event from a background event. These techniques have been successfully used in analyses performing B-tagging of jets, trigger definitions, searches for new particles or reconstruction of resonances [115], since they often improve the signal-to-noise ratio with respect to the usual algorithms. In the following sections the entire procedure of creating a neural network, of training it and of using it to discriminate leptoquark events from (W+ jets) and $t\bar{t}$ background events in the $e\nu jj$ decay channel will be reviewed and its preliminary results compared with the results of the "relative likelihood" analysis.*

C.2. Neural Network and human brain

The idea of creating programs whose architecture represents the human brain's cell behaviour, even if they don't try to be biologically realistic in the details, was initially suggested by Von Neumann [116].

Our brain contains *neurons* (= nerve cells) of different types ($\sim 10^{11}$) which have transmitting ends called *synapses* to communicate information to other neurons. The effect of the transmission is to raise or lower the electrical potential inside the body of the receiving neuron [117], [118]. Each neuron may, in general, receive inputs from many other neurons, carrying each one a different information. Since each information is transmitted as an electric signal, when the total potential reaches a threshold a pulse is sent towards the nucleus: the cell has fired, that is equivalent to saying that the cell has recognized a known pattern. To model this kind of behaviour it is important to individualize the most important variables entering in the definition of the object to discriminate. This criterion is based on the comparison between the desired object and its negation, for example between a signal and a background. The neural network must be trained, like the brain, to understand what it is looking for by comparisons with what it is not.

On the basis of the above approach, the first step in the construction of a neural network algorithm is the choice of its architecture, that is the choice of all the input variables to give to the net. Moreover, once the structure is chosen, it is important to train the net as long as possible to separate the features of signal and backgrounds. The second step after the neural network is built, is the testing phase, during which the capability of the net to distinguish signal from background, that is its efficiency, will be determined.

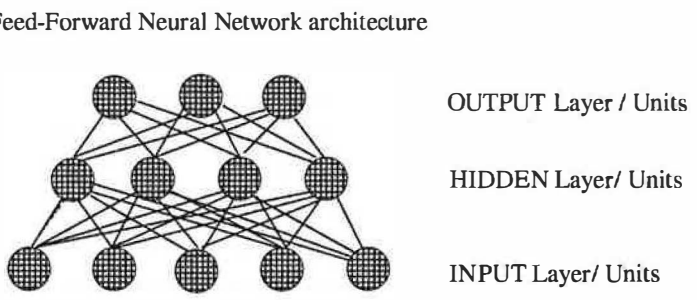

Figure C.1: *Architecture of a feed-forward neural network. In this example there are 5 input units, 3 output units, one hidden layer and a total of 3 layers. In a feed-forward network every unit of every layer feeds only units in the next layer and there are no contacts with units in the previous layer or in the same layer.*

C.3. Strategy for a neural network architecture in the leptoquark search

The search for leptoquarks in the $e\nu jj$ channel by using neural networks has been performed to compare the results of a standard procedure with those obtained using the hand-made "relative likelihood" analysis. The architecture of the neural network, as sketched, for example, in Figure (C.1), is characterized by the number of input and output variables and by its internal structure. This is chosen by considering that:

a) if the input variables are correlated this does not improve the information of the neural network, as would be in the case of totally independent variables;

b) the number of input variables, as well as the number of inner layers of the neural network, should be " neither too big, nor too small". A neural network with only a few input variables will have less initial information than a neural network with many. But, on the other side, if these input variables are "too many", then the neural network risks to be overtrained, that is the informations in input will be too detailed to allow a clear separation between signal and background. The distinction between a black dog and a white cat is based on a few features: colour and race. If one adds many other features, like number of feets, of eyes, of hears and so on, then the number of common features overcomes the number of differences, and the two "objects" become indistinguishable.
The same effects result if a complicated inner structure for the net, with many hidden layers, is used. Usually the choice of a net with only a few layers is considered a good choice.
A decision on the best architecture to use can be made by performing a systematic search in the space of all possible architectures. This is quite an unreal way, because of the enormous CPU power and time required before finding a good answer. An alternative approach can be to proceed incrementally either by starting with many units, and eventually eliminating some of them, or by starting with a few units, incrementing new units. This latter approach has been used to perform the analysis described here.

C.4. The feed-forward neural network

The schema represented in Figure (C.1) illustrates a simple structure of a neural network: it is constitued by many *units*, which are the bullets in the plot and which are grouped in different *layers*, that is the horizontal groupings. In the figure there are three layers: from bottom to top there are: the input layer, constitued by 5 units, one inner, or hidden, layer, and the output layer, which here is constitued by 3 units.

Each unit can be thought as modeling the behaviour of one neuron, which receives inputs from other units and gives as output one or zero according to whether the sum of the input pulses is above or below a certain threshold. The output n_i of the i^{th} unit can be represented by the following equation:

$$n_i = g(\sum_i w_{ij} n_j - \mu_i) \tag{C.1}$$

It represents the status of the unit "i" after the inputs n_j's have been elaborated. The w_{ij}'s are called the *weights* and are related to each possible connection between the units n_i and n_j; they say the relative strength of a kind of variable with respect to the others in the evaluation of n_i. It is during the training phase that these weights, which are all the same at the beginning, are computed. They can be positive or negative, corresponding to excitatory or inhibitory synapses respectively. The parameter μ_i is called the *threshold* or *bias* of the unit i: the unit fires if the weighted sum of the input reaches or exceeds the value of μ_i. The function g is a nonlinear function that is called the activation function. It can be represented by the hyperbolic function $g(x) = 1/(1+e^{-2x})$ sketched in Figure (C.2). The kind of neural network chosen in this analysis has the "feed-forward" structure: it is the simplest class of neural networks, based on the idea that, in every layer, every unit feeds only the units in the next layer and that there are no contacts with units in the previous layer or between units in the same layer.

TRAINING OF THE NEURAL NETWORK - The training, or learning, phase represents the moment in which different architectures are tested. Once the best one has been chosen, it calculates the best set of values to assign to each weight. For each training different sets of events are given as input to the net: in this analysis they are the simulated leptoquark events with mass equal to 180 GeV/c^2 [1] and simulated (W + jets) and $t\bar{t}$ events to represent the signal and the background respectively.

The program which implements the neural network [119] requires that all the input variables range between 0 and 1, both for signal and for background. It is also necessary that the events given in input come randomly from signal or from background: the frequency with which are taken the different background events must also respect the relative ratio between the cross sections.

The neural network knows which must be the response of the output layer, because it knows if the input event is signal or background, and makes iteratively, by back-propagation,

[1] The precedure of the analysis with the neural networks was first been tried with this value for the leptoquarks mass, since the aim was to compare its results with the ones of the relative likelihood analysis. Of course, if this method were chosen to perform the search, the training of the network would have been done for each different leptoquark mass.

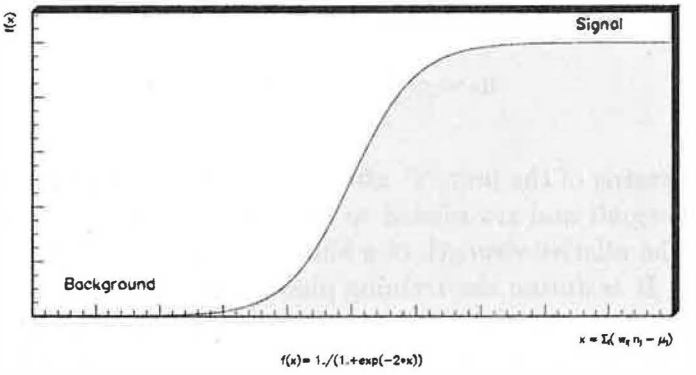

Figure C.2: *Shape of the function $g(x) = 1/(1+e^{-2x})$ which is used in the neural computation to evaluate the answer of each unit of the net. It depends on the input informations, and on the corresponding weights, and it interprets the event as background or signal according to if its value is low or high.*

small adjustments so that the weights converge to a set of values which will be used during the testing phase. For this analysis the net output layer contains only one unit, since in this simple case what is asked to the net is if, yes or not, the event is a signal.

A loose preselection has been applied before the training and testing of the network, which requires at least one electron in the central electromagnetic calorimeter passing the usual tight identification cuts listed in Table (4.4), uncorrected $\not\!\!E_T > 25$ GeV, $M_T(e,\nu) > 40$ GeV/c^2 and two jets (jet1 and jet2) with $E_T^C > 20, 15$ GeV. Plots of the kinematical distributions for backgrounds and real data can be found in Figure (C.3). The architecture used here is summarized below:

- 10 input units corresponding to the following kinematical variables:
  - $E_T(electron)$,
  - $E_T(jet1)$,
  - $E_T(jet2)$,
  - $E_T(electron) + E_T(jet1) + E_T(jet2) + \not\!\!E_T$,
  - $M_T(e,\nu)$,

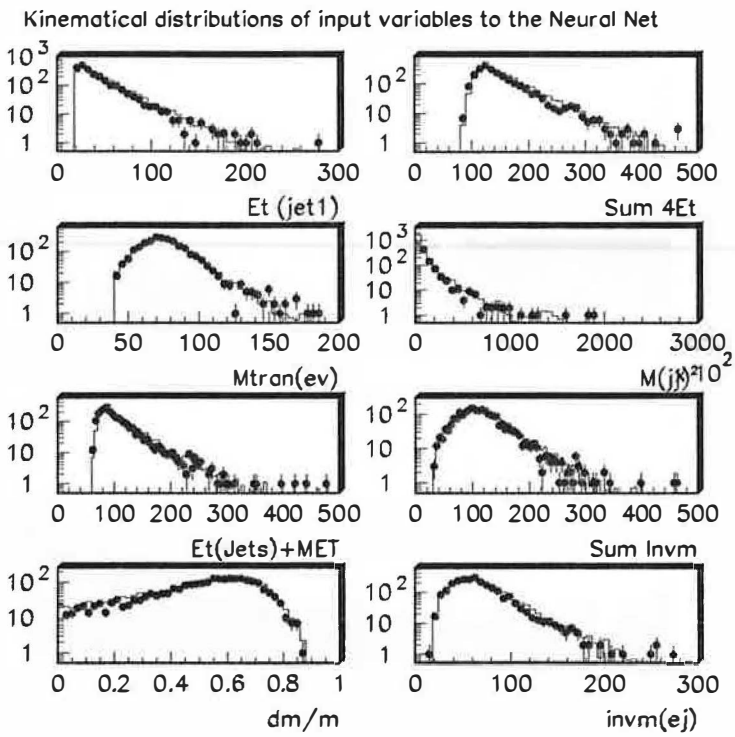

Figure C.3: *Kinematical distributions of some of the input variables to the neural network for the Monte Carlo of the backgrounds compared with data. A loose preselection is applied before passing them to the net. The simulated events have been normalized to the luminosity on data.*

- $M^2(jet1, jet2)$,
- $E_T(jet1) + E_T(jet2) + \not{E}_T$,
- $M_T(e,\nu) + M(e,$ other jet$)$ in the combination which gives the smallest difference of invariant masses,
- $M(e, jet)$,
- $min(\frac{|M_{e,j1}-M_{nom}|}{M_{nom}}, \frac{|M_{e,j2}-M_{nom}|}{M_{nom}})$, where M_{nom} is the nominal leptoquark mass (M_{S1} = 180 GeV/c^2), $M_{e,j1}$ and $M_{e,j2}$ are the invariant masses electron-jets, with j1 and j2 the two most energetic jets in the event;

- 18 units in the hidden layer;
- 1 output unit whose response should be equal to 1. if the event is signal or 0 if the event is background.

The sets of events generated to train the neural network are:

- 13000 scalar leptoquarks with M_{S1} = 180 GeV/c^2 generated with Pythia [88];
- 37000 (W + 2 jets) events generated with Vecbos;

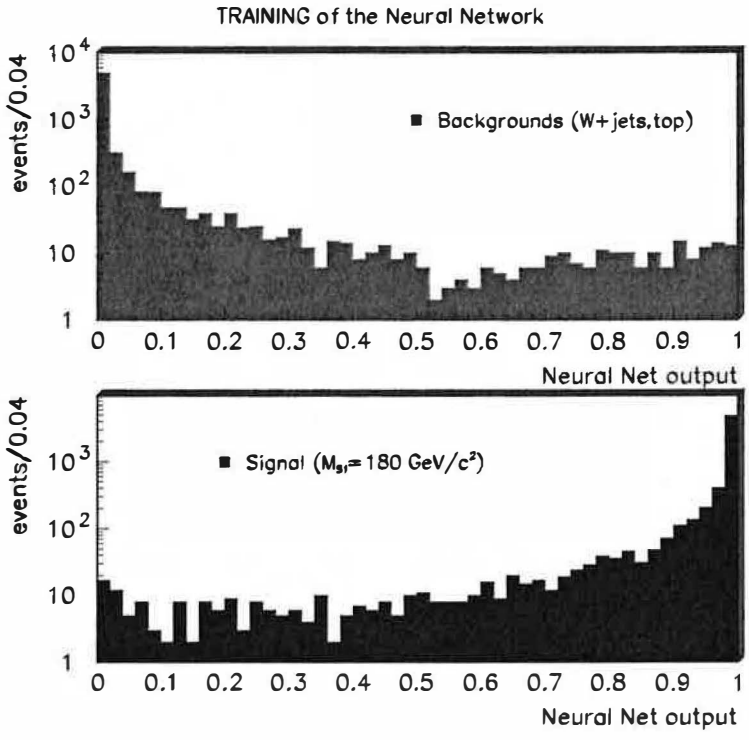

Figure C.4: *The Neural Network must be able to distinguish between background and signal events by giving output values close to 1 for the signal and close to zero for the backgrounds. These plots show the result of a check performed on the net after the training phase: the input events to the net are the same used for the training. A testing phase will follow, in which the net output will be evaluated on different samples from those used to train it.*

- 15000 (W + 3 jets) events generated with Vecbos;
- 6000 $t\bar{t}$ events generated with Isajet [120].

The outputs of the neural network when the training samples are given as input are plotted in Figure (C.4). On the top is represented the output when as input are given kinematical variables of background events, and it is spread around zero; on the bottom plot is shown the output of the signal, peaked around one.

TESTING THE NEURAL NETWORK - The network built in the previous paragraph is now ready to use with real data to eventually obtain the evidence of a leptoquark signal on data as a bump around one in its outputs.

For the neural network analysis the data sample of the "relative likelihood" analysis has again been used, that is the whole run 1 data sample, corresponding to $\int \mathcal{L}dt \sim 110$ pb^{-1}, equivalent to the about 160000 events of the high p_T inclusive electron sample. As Monte Carlo samples for the signal and background new sets of events have been generated, constitued by:

- 12000 scalar leptoquark events with $M_{S1} = 180$ GeV/c^2 (Pythia);

CUT	1a	1b	Expected background
$NN_{output} > 0.80$	4	18	(29.0 ± 2.5)
$NN_{output} > 0.85$	3	13	(22.3 ± 2.1)
$NN_{output} > 0.90$	3	10	(14.4 ± 1.7)
$NN_{output} > 0.95$	2	6	(7.1 ± 1.1)

Table C.1: *Events surviving to the cuts on the Neural Network output on data and expectations on background.*

- 79000 (W + 2 jets) events (Vecbos);
- 88000 (W + 3 jets) events (Vecbos);
- 84000 $t\bar{t}$ events (Isajet).

These samples must obviously be different from the ones used for the training: they are unkown to the net. After passing the loose preselection requirements, the kinematical variables are passed to the network. The output for the backgrounds is shown on the top of Figure (C.5) after its normalization to the luminosity of the experiment. It is also put as comparison the output on data, represented by the red stars, which confirm a good agreement between Standard Model expectations and experimental results. In the Table (C.1) are shown a comparison between the number of events passing the selection requirements on data and the background expectations when the cut applied to the neural network output has the values 0.80, 0.85, 0.90 and 0.95. The good agreement confirms, again, that there are no signal events hidden inside the neural network black-box. This is a cross check of the conclusion given in the "relative likelihood" analysis, whih remains, on the other hand, the selection used in this thesis for the reasons explained below.

With the "neural network" analysis it has not been possible to find a better selection than with the "relative likelihood" analysis, giving a lower expected limit on the cross section. With a cut on the net output at 0.99, corresponding to a signal efficiency of about 19%, a number of background expected events of (1.9 ± 0.3) and a total systematic of 15%, the expected limit $\sigma^{lim}_{exp}(180) \times Br$, calculated as in Equation (5.2), would be 0.25 pb as in the "relative likelihood analysis", where:

$$\sigma^{lim}_{exp} = \frac{(int(N_{bckg}) - N_{bckg})^{lim}}{\int \mathcal{L}dt \cdot \varepsilon \cdot 2\ \beta\ (1-\beta)} \tag{C.2}$$

This preliminary studies have been interpreted as a confirmation that, based on comparisons between the expected limits, this analysis cannot improve the "relative likelihood" one, therefore it has not been pursued further.

The following section has been reported for completeness. It contains the description of the method to apply for the determination of the upper limit on the leptoquark production cross section. The usual procedure to calculate the 95% confidence level upper limit on the cross section is illutrated in the following expression:

$$\sigma_{lim}(M_{S1}) = \frac{N^{lim}}{\int \mathcal{L}dt\ \varepsilon 2\ \beta\ (1-\beta)} \tag{C.3}$$

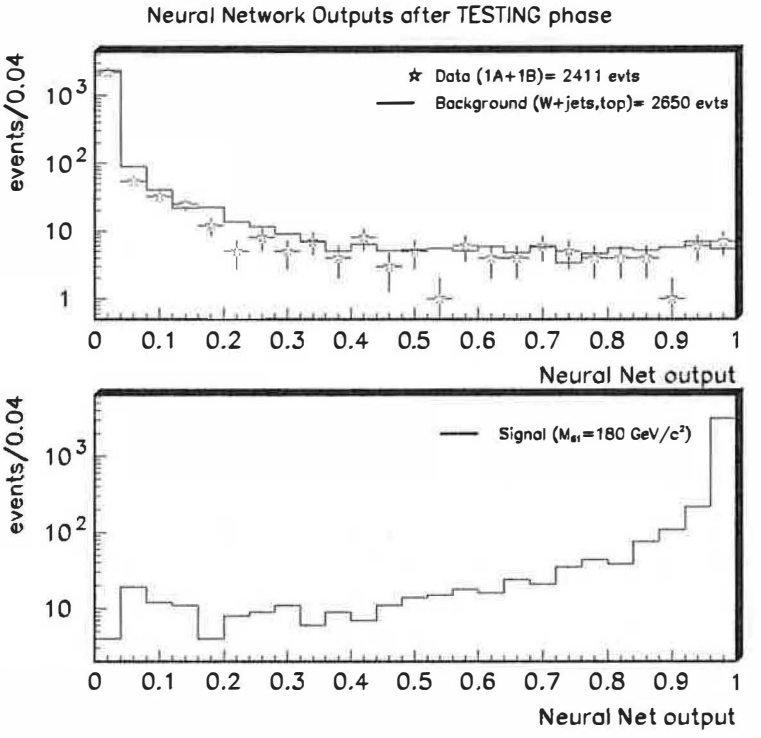

Figure C.5: *On a different set of events the Neural Network is able to well discriminate signal from background. Data are plotted as well, as stars in the first figure, superposed to the background.*

where N^{lim} is the Bayesian upper limit on the number of real events passing the cut evaluated in Appendix D. Another procedure to calculate $\sigma_{lim}(\mathrm{M_{S1}})$, is explained in the following section.

C.5. Likelihood fit on neural network output

An elegant way to determine the upper limit σ_{lim} from the result of the neural network analysis is by the use of a binned log-likelihood fit of the background to the data on the neural network output distribution of Figure (C.5) performed with Minuit [98]. This distribution can be subdivided in a number "nbin" of bins: in each bin, using the Monte Carlo samples, the following quantities can be counted:

- n_i^{S1} = number of signal events,
- n_i^{W2j} = number of (W + 2 jets) background events (not normalized to data),
- n_i^{W3j} = number of (W + 3 jets) background events (not normalized to data),
- $n_i^{t\bar{t}}$ = number of $t\bar{t}$ background events (not normalized to data)

Moreover, one can define:

- $N_{S1}, N_{W2j}, N_{W3j}, N_{t\bar{t}}$ = total number of generated events for the signal and the backgrounds given as input to the neural network, and
- $nsgnl, nwjets, ntop$ = the real contributions of these three possible sources to the distribution on data.

The three latter variables will be the free parameters of the fit, and in particular if $nsgnl$ will be consistent with zero, then this will mean that there is no evidence for a leptoquark signal.
For each bin the Poissonian probability of having the n_i events seen on data if μ_i are expected as background can be defined:

$$\mathcal{P}(n_i|\mu_i) = \frac{\mu_i^{n_i} exp(-\mu_i)}{n_i!} \tag{C.4}$$

with:

$$\mu_i = \frac{n_i^{S1}}{N_{S1}} \cdot nsgnl + \frac{n_i^{w2j} + n_i^{w3j}}{N_{wj}} \cdot nwjets + \frac{n_i^{t\bar{t}}}{N_{t\bar{t}}} \cdot ntop \tag{C.5}$$

The likelihood function, which is minimized to fit background to data, is defined as:

$$\mathcal{L}ik = -log\mathcal{L}^* = -\sum_{i=1}^{nbin} \mathcal{P}_i + \frac{(n_{top} - \mu_{top})^2}{2\sigma_{top}^2} + \frac{(\varepsilon_{S1} - \mu_\varepsilon)^2}{2\sigma_\varepsilon^2} + \frac{(\mathcal{L} - \mu_\mathcal{L})^2}{2\sigma_\mathcal{L}^2} \tag{C.6}$$

In this expression the variables $n_{top}, \varepsilon_{S1}$ and $\mathcal{L}$ are also free in the fit, in particular to take into account the systematic effects in the calculation of the limit, while $\mu_{top}, \mu_\varepsilon$ and $\mu_\mathcal{L}$ are the expected values and $\sigma_{top}, \sigma_\varepsilon$ and $\sigma_\mathcal{L}$ their uncertainties.
The 95% confidence level upper limit on the cross section is calculated, according to the ideas explained in Appendix D, by integration of the likelihood function over the fit parameter $nsgnl$, opportunely parametrized with a real number f:

$$\frac{\int_{f_{95}}^{+\infty} \mathcal{L}ik(f')df'}{\int_0^{+\infty} \mathcal{L}ik(f')df'} = \varepsilon = 0.05 \tag{C.7}$$

where $\mathcal{L}ik$, given in Equation (C.6), contains the Poisson probability expressed in Equation (C.4) with a number of expected events μ_i for each bin given by the sum of Equation (C.5): the variable $nsgnl$ has been parametrized as $nsgnl(f) = f \cdot nsgnl^{exp}$, if $nsgnl^{exp}$ is the theoretical expected number of leptoquark events.
The plot on top of Figure (C.6) illustrates the neural network output distribution on data compared with the histogram, which contains signal plus background predictions from the likelihood fit: the variable $nsgnl$ obtained by the fit has a value which is compatible with zero. The plot on the bottom shows the distribution of the likelihood functions calculated with the values determined by the fit versus the production cross section. The shaded area represents the 95% of the global area intercepted by the curve and corresponds to $\sigma_{lim} = 0.25$ pb.

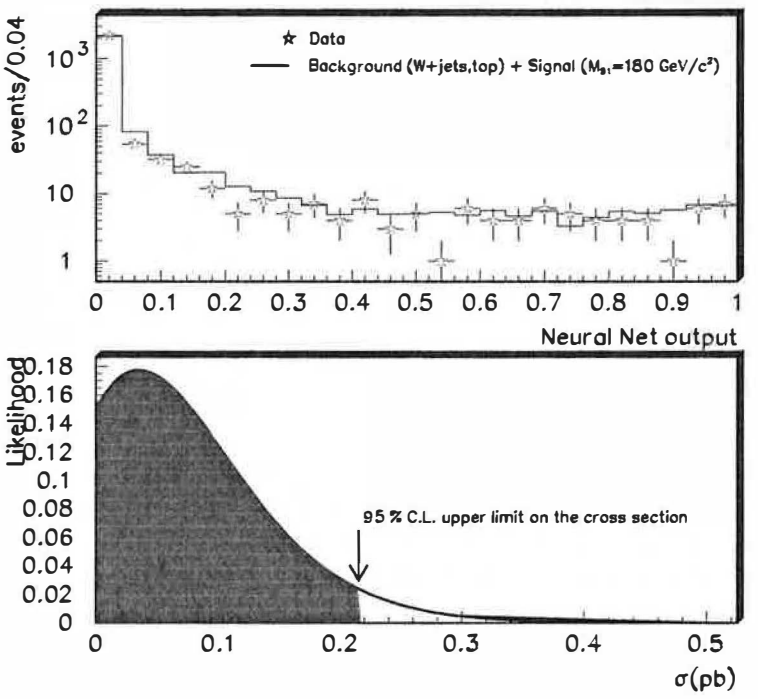

Figure C.6: *The figure on top of this plot shows the output of the Neural Network after a binned likelihood fit of data to a combination of signal and background events. In case there would be a signal on data, this would result in a sort of peak for some values of the cross section in the likelihood shown in the second figure.*

Appendix D

The Bayesian Statistical Method to calculate Confidence Level Limits

Introduction- *"...There are apple and pear trees in a garden, and usually pears fall during the night from the trees. One morning the farmer, who is interested in apples, looks through the window: it is still dark, he wouldn't be able to distinguish apples from pears, but he sees that during the night no fruits did fall in his garden. His conclusion is that the upper limit on the number of falling apples in the night is 2.3 at* 90% *confidence level. His wife, who is a classical statistician, tells him that the limit is too high because he should subtract the expected pears background. He argues "there are no pears", but she insists and explains him that he cannot ignore the pears that could have been there but weren't. If he would have expected 2 pears, for zero apples seen the limit on the number of falling apples would have become 0.3 at* 90% *confidence level, much lower than the 2.3 calculated without considering the pears..."* (G. Zech, "Confronting Classical and Bayesian Confidence Limits to Examples" [121]). *The choice of the statistical method to use for the calculation of confidence limits has always been controversal, and it has been the subject of many debates during last few years [121]. This example shows that, according to the classical statistics, the limits on the signal can be different for two experiments with exactly the same evidence relative to the signal and different interpretations of the background.*

In this thesis the Bayesian approach for the calculation of upper limits on the number of expected leptoquark events has been chosen. The reasons for this choice are threefold: first, the idea of a posterior probability expressed by Bayes' theorem as likelihood modified by the result of the experience itself is a beautiful concept, less abstract than the more formal definition of classical probability seen as limit of the observation rate for an infinite number of experiments; second, the upper limits obtained by the use of Bayesian method with uniform prior probability density functions are however more conservative than the frequentist limits; third, the Bayesian approach allows the combination between the results of different analyses in a very elegant way.

D.1. Bayes' theorem: the principle of learning by experience

The subject of statistical inference is concerned with the problem of making predictions, or inferences, on a parameter from a set of observations. There are two different approaches to the statistical inference, that have been developed in the past in high energy physics as well as in other scientific fields, and are the so called frequentist and Bayesian methods [123]. In the frequentist, or classical, method the probability to measure x_i from an experiment is seen as the limit of the frequency N_i of that result when the number of identical experiments N is very large, that is:

$$P(x_i) = \lim_{N\to\infty} \frac{N_i}{N} \tag{D.1}$$

In this expression $P(x_i)$ is not just a property of the experiment, it also depends on the "ensemble", or on the N repetitions of the same experiment. Therefore, the experiment must be repeatable under identical conditions and with different possible outcomes.

The Bayesian approach is based on the idea of a subjective probability of observing an event in the sense of *degree of belief*. The degree of belief can be modified by observations, as expressed in Bayes' theorem, which is based on the definition of the *prior* probability

density function (pdf) of getting certain results, from which is possible to determine the *posterior* pdf as the conditional pdf given the result of the measurement.

Suppose one has a certain hypothesis H and knows the probability P(H) for this hypothesis before doing an experiment [1]. If the event A is verified after the experiment, then Bayes' theorem tells us how to modify the probability of the hypothesis H having observed A:

$$P(H|A)P(A) = P(A|H)P(H) \quad (D.2)$$

$$P(H|A) = \frac{P(A|H)}{P(A)}P(H) \quad (D.3)$$

This relation should be read as the belief in the hypothesis H after having observed the result A, which is the posterior pdf for H, P(H|A), is given by the ratio between the probability of getting the result A if the hypothesis H is true, P(A|H) and the probability of getting A independently of the fact that the result is true or not, P(A), multiplied by the prior probability for H, P(H), that is the belief of the hypothesis H before doing the experiment. Thanks to this theorem, the posterior pdf can be modelled according to the results of the experiments, it is not an untouchable function which tells us how things should be, independently of the experience of the scientist who is performing it. The experiment itself changes the probability of the result. Bayes' theorem must be used with caution: the dangerous point in it is the occurence of the prior probability P(H). In some applications $P(H)$ is known, but the problem becomes particularly acute when there is minimal prior information about the parameters to be estimated, or total lack of knowledge about them. The criticism by the non bayesians is that the choice of prior probabilities is subjective and arbitrary and, therefore, so too are the inferences derived from the same. Bayesians answer by saying that the results are usually not sensitive to the choice of the prior pdf: in many applications one sets P(H) equal to a constant (uniform pdf), even if there is no indication which suggests a preference on its form. This is the choice that has been made for the limits calculations in this thesis, as it will explained in next section.

D.2. Confidence belts and Bayesian intervals

The result of a measurement is always associated to an uncertainty, or confidence interval, which tells the known precision of the parameter which represents the unknown true value of the variable which has been measured. Consider an experiment in which the quantity x_o is measured and the expected mean value $\bar{x}$ is unknown. The probability density function for that observation is given by $f(x_o|\bar{x})$, that is the probability of observing x_0 given the expectation value $\bar{x}$: for simplicity, one can imagine that the variable is distributed according to a gaussian with unknown mean $\bar{x}$. Since the value of the mean $\bar{x}$ is not a priori known, there are many possible gaussians with different mean values which can describe the result of this measurement: they are all the gaussians for which the difference between the true value and the observed value is less than or equal to the established precision of the measurement.

[1] What is being enunciated here can be generalized to the case of a set of theories or hypotheses H_i with known probabilities $P(H_1)$,$P(H_2)$,...$P(H_N)$.

All the possible values for the expected value $\bar{x}$ constitute the so called confidence interval at the desired confidence level. The procedure to draw it following a classical approach is explained below [124], while the Bayesian way will be introduced as a variant of this method.

1. If the desired confidence level is fixed to $1-\varepsilon$, then for each physically allowed value of $\bar{x}$ the interval $[x_1, x_2]$ is determined, such that:

$$P(x_1 < x_o < x_2|\bar{x}) = \int_{x_1}^{x_2} f(x_o'|\bar{x})dx_o' = 1-\varepsilon \tag{D.4}$$

$$\text{with} \quad P(x_o < x_1) = P(x_o > x_2) = \varepsilon/2 \tag{D.5}$$

   Since the condition of coverage given by Equation (D.4) would not determine x_1 and x_2 uniquely, the criterium which is usually adopted is to choose central intervals such that the area of the excluded tail on either side is $\varepsilon/2$, as expressed in Equation (D.5). In this interval the results of the measurements fall with an occurency of $(1-\varepsilon)$.
   With such a procedure a region is built in the plane $(x, \bar{x})$ containing all points satisfying the conditions above. The region is represented graphically in Figure (D.1) by the area $D(\varepsilon)$. To each value $\bar{x}$ on the ordinate corresponds an interval $[x_1(\bar{x},\varepsilon), x_2(\bar{x},\varepsilon)]$ on the horizontal axis: the probability that the observed value x_o falls between x_1 and x_2 is 1-ε. The representation of the probability density function, in this example the gaussian distribution, which is function of each particular choice of $\bar{x}$, should be thought as coming out of the page. The union of all intervals $[x_1(\bar{x},\varepsilon), x_2(\bar{x},\varepsilon)]$ for all values of $\bar{x}$ is known as the *confidence belt.*

2. Once the confidence belt has been defined, it is possible to draw the *confidence interval* for the expected value $\bar{x}$ related with the measured value x_o. It is obtained by drawing the vertical line passing by x_o and crossing the boundaries of $D(\varepsilon)$ in the points $\bar{x}_1$ and $\bar{x}_2$ delimiting it.

In particular one talks about upper and lower limits for $\bar{x}$ when considering one-sided confidence intervals for the variable under study, usually when the measured value is close to a physical boundary. This case can be represented with a confidence belt constructed like the one of Figure (D.1) but with one of the two curves to ∞, found when either x_2 tends to $+\infty$ or x_1 to $-\infty$. For example in this thesis the *upper* limit on the number of observed leptoquark events is calculated , which corresponds to the particular case where x_2 tends to $+\infty$, which also implies that the value of x_1 is uniquely determined.

Looking more into detail at the leptoquark search, if all the x's are substituted by n's in Figure (D.1), then n_o indicates the number of candidate leptoquark events on data and if with μ_{Lq} is indicated the corresponding expected number of leptoquark events, then, according to the description given above, it is possible to define for μ_{Lq} a one-sided confidence interval $[0, n_{Lq}^{lim}]$ at the established confidence level $1-\varepsilon$ (68%, 90%, 95% ...).
The confidence interval for the parameter μ_{Lq} determined from the measurement of n_o means that for each value of μ_{Lq} in that interval $[\mu_1, \mu_2] = [0, n_{Lq}^{lim}]$ the measurement which has been done, n_o, has 1-ε as probability, or confidence level, to fall in the corresponding interval $[n_1(\mu_{LQ},\varepsilon), n_2(\mu_{LQ},\varepsilon)]$.

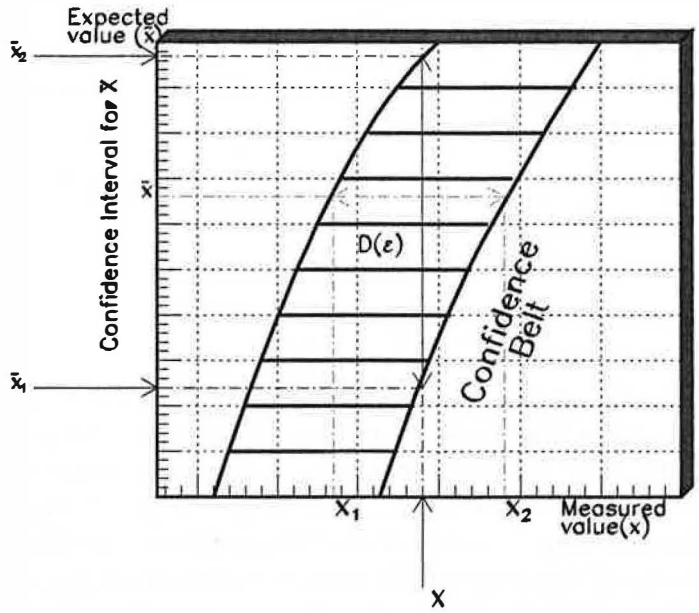

Figure D.1: *Confidence intervals for a single, unknown parameter $\bar{x}$ as a function of its measured value. The construction of the confidence belt is described in the text: the probability density function $f(x_0|\bar{x})$ can be imagined as plotted in the third dimension, sorting from the paper, as a function of x along each horizontal line of $\bar{x}$ constant. The domain $D(\varepsilon)$ contains a fraction $1-\varepsilon$ of the area under each of these functions.*

An high-energy physics experiment consists in a large number T of trials, for example proton-antiproton collisions, in which a search is conducted to find n interesting outcomes predicted by the hypothesis one wants to test. It is assumed the repeatibility of the trials, that is the collisions happen in the same conditions, their order is not important and each interesting outcome occurs with equal probability. In these kinds of experiments the condition which is usually satisfied is $n \ll T$: at the Tevatron, for example, more than a trillion collisions were needed to find the top quark in a few events. The probability to assign to this sample of n final events, assuming that q is the probability of success, that q is the same for each trial and that the order of the collisions is not important, is given by the following combinatorial formula:

$$P(n|q,T) = \left(\begin{array}{c} T \\ n \end{array} \right) q^n (1-q)^{T-n} \tag{D.6}$$

This expression is rigorously correct, but it can be modified to take into account that T is usually much greater than n. Since by definition the number of expected events $n_{exp} = qT$, one can write:

$$P(n|q,T) = P(n|n_{exp},T) = \frac{T!}{(T-n)!n!} \frac{n_{exp}^n}{T^n} (1 - \frac{n_{exp}}{T})^{T-n} \tag{D.7}$$

which becomes, for $T >> n$, the Poisson distribution:

$$\mathcal{P}(n|n_{exp}) = \frac{n_{exp}^n e^{-n_{exp}}}{n!} \tag{D.8}$$

which is the standard likelihood for a counting experiment for the observed number of favourable events for a certain hypothesis. Therefore in this case, the probability density function $f(n_o|\mu_{Lq})$ of observing n_o events given μ_{Lq} leptoquark events expected for that mass is the Poisson distribution with mean μ_{Lq} $\mathcal{P}(n_o|\mu_{Lq}) = \mu_{Lq}^{n_o} e^{-\mu_{Lq}}/n_o!$.
In a Bayesian approach the way to define a confidence interval is slightly different, in the sense that the likelihood function for the expected parameter μ_{Lq} is a dynamically constructed function which depends on the value of the observed number of events n_o and is modified as n_o changes. The confidence interval is built by ranging the variable μ_{Lq} in the physically allowed interval $[0, +\infty[$. For each value, and according to Bayes' theorem, there is a prior pdf $P(\mu_{Lq})$ from which the posterior pdf $P(\mu_{Lq}|n_o)$ can be determined, after the experiment, according to the Equation (D.3) as:

$$P(\mu_{Lq}|n_o) = \frac{\mathcal{L}ik(n_o|\mu_{Lq})}{\int_0^{+\infty} \mathcal{L}ik(n_o|\mu'_{Lq}) P(\mu'_{Lq}) d\mu'_{Lq}} P(\mu_{Lq}) \tag{D.9}$$

The integral in the denominator can be seen as normalization term for $P(\mu_{Lq}|n_o)$. In this calculation the fundamental assumption of *uniform* prior pdf is taken into account [2]. This

[2] As mentioned earlier, this is not the only possible assumption, since usually one doesn't know much about prior pdf's. It is interesting to see where are the differences when one, for example, determines a confidence interval by applying the frequentist, the Bayesian with prior uniform in μ_{Lq} and the Bayesian with prior $1/\mu_{Lq}$ definitions in a Poisson process. He will find [121] that the 90% confidence level upper limits are the same for classical and uniform prior, while the 90% confidence level lower limits are the same for classical and $1/\mu_{Lq}$ prior. It is a common belief that one reason to accord so much interest in the uniform prior pdf is due to the fact that usually physicists calculate upper limits.

allows simplifications in Equation (D.9):

$$P(\mu_{Lq}|n_o) = \frac{\mathcal{L}ik(n_o|\mu_{Lq})}{\int_0^{+\infty} \mathcal{L}ik(n_o|\mu'_{Lq})d\mu'_{Lq}} \tag{D.10}$$

which becomes, after the substitution of the Poisson distribution in the likelihood $\mathcal{L}ik$:

$$P(\mu_{Lq}|n_o) = \frac{\mu_{Lq}^{n_o} e^{-\mu_{Lq}}}{n_o!} \frac{1}{\int_0^{+\infty} \frac{\mu_{Lq}^{'n_o} e^{-\mu'_{Lq}}}{n_o!} d\mu'_{Lq}} \tag{D.11}$$

Therefore in this case the way to find the confidence interval for μ_{Lq}, or, in a more Bayesian jargon, the *Bayesian interval*, is to equalize the integral of the posterior pdf over μ_{Lq} to the desired confidence level $1 - \varepsilon$ as follows:

$$\frac{\int_0^{n_{Lq}^{lim}} P(\mu'_{Lq}|n_o)d\mu'_{Lq}}{\int_0^{+\infty} P(\mu'_{Lq}|n_o)d\mu'_{Lq}} = 1 - \varepsilon \tag{D.12}$$

or, equivalently:

$$\frac{\int_{n_{Lq}^{lim}}^{+\infty} P(\mu'_{Lq}|n_o)d\mu'_{Lq}}{\int_0^{+\infty} P(\mu'_{Lq}|n_o)d\mu'_{Lq}} = \varepsilon \tag{D.13}$$

which should be compared to the frequentist way used to calculate the confidence interval expressed in Equation (D.5). The integrals are calculated in a range of positive values to take into account the physical meaning of the free-parameter μ_{Lq}, which must be a positive, real number. One should remark that the likelihood function is not a pdf for μ_{Lq}, so in general it is meaningful to integrate the likelihood function with respect to its parameters. But it should be remembered that $P_{posterior} \sim \mathcal{L}ik(n_o|\mu_{Lq}) \times P_{prior}$ and that if the prior pdf is uniform, integrating the posterior pdf may seem like integrating $\mathcal{L}ik$. It is the prior pdf which gives the density, which in this case is constant.

From a technical point of view, the integration variable μ_{Lq} must be parametrized to range from zero to a reasonable high number. It can be chosen a real value f to parametrize μ_{Lq} in the form $\mu_f = \mu_{Lq}(f) = f \cdot \mu_{th}$, where μ_{th} is the number of predicted signal events according to the theory, and it can be calculated the corresponding likelihood function for each f. In a search for new particles the distribution of the posterior pdf as a function of f will have a maximum at $f = 0$ if there is no signal, while a peak around $f = 1$, corresponding to the case of $\mu_{Lq} = \mu_{th}$, would be found in case of discovery. By performing an integration over f it can be found the value $f_{1-\varepsilon}$ satisfying the Equation (D.13) which can be rewritten as:

$$\frac{\int_0^{f_{1-\varepsilon}} P(\mu_{f'}|n_o)df'}{\int_0^{+\infty} P(\mu_{f'}|n_o)df'} = 1 - \varepsilon \tag{D.14}$$

If in the experiment there is no agreement between what is observed, for example the number of events passing the selection requirements in the leptoquark analysis, and what is expected in terms of signal, for example μ_{th}, that is the number of predicted leptoquark events from the theory, and if the result of the measurement is consistent with the background expectations, then the conclusion is that there is no new signal in the events and from the

result can be derived an information about the upper limit on the number of expected signal events.

The limit can be calculated by following the procedure explained above and understood with the help of the plots of Figure (D.2). In the horizontal axis of these plots it is represented the variable f, which parametrizes the number of expected signal events which then ranges from zero to infinity. A critical value for this variable is 1, since for $f = 1$ the parameter μ_f equals the theoretical expectation μ_{th}, where:

$$\mu_{th} = \int \mathcal{L}dt \cdot \sigma_{th} \cdot Eff \cdot Br \tag{D.15}$$

where $\int \mathcal{L}dt$ is the integrated luminosity of the experiment, Br the branching ratio in the channel where are searched leptoquarks, σ_{th} is the theoretical cross section for a certain value of the leptoquark mass and Eff is the selection efficiency for that mass. On the vertical axis of each plot, for every value of f is taken the corresponding value of the likelihood as given in Equation (D.11). To solve the Equation (D.14) means to find that value of f, called $f_{1-\varepsilon}$, for which the integral of the likelihood calculated from zero to that $f_{1-\varepsilon}$ over the integral from zero to infinity equals the established confidence level.

The value of $f_{1-\varepsilon}$ can be lower, equal or higher than 1: that means that the $(1-\varepsilon)\%$ confidence level upper limit on the number of expected events can be lower, equal or higher than the expected value from the theory. In other words, if that value of $f_{1-\varepsilon}$ is equal to 1, then the corresponding μ_f is the upper limit calculated at $(1-\varepsilon)\%$ confidence level, if $f_{1-\varepsilon} >$ (or $<$)1, then the upper limit is calculated at a confidence level that is $< (1-\varepsilon)\%$ (or $> (1-\varepsilon)\%$). These observations could be referred to Figures (7.1) and (7.2), where the upper limits on the leptoquark production cross section are plotted as a function of the leptoquark mass and compared with the theoretical predictions for the scalar leptoquark searches in the $e\nu jj$ and $eejj$ decay channels. If one trusts the predictions of the theory, then the value of the mass for which the two curves cross each other represents the lower limit on the leptoquark mass. In fact, when the experimental values are lower than the theoretical curves, this means that prediction and experiment don't agree, within the uncertainties, for that mass: the experiment gives a result which represents a $(1-\varepsilon)\%$ confidence level upper limit on the cross section. Should there be a signal for that mass, the corresponding cross section would fall, the $(1-\varepsilon)\%$ of the times, in the interval $[0, \sigma^{lim}(\mathrm{M_{Lq}})]$. Only $\varepsilon\%$ of the times the cross section would fall outside that interval. Therefore that limit on the cross section does not represent an acceptable value when compared with theory, and that mass does not represent the lower limit on the leptoquark mass.

On the other side, when the experimental value is higher than the theoretical one, the comparison becomes meaningless, since the experimental result is no more sensitive to the theory prediction. The confidence interval in this case contains the theoretical prediction, and some values of the interval are higher than the theoretical cross section, with the consequence that the experiment allows a cross section which can be higher than the predicted one, which is a nonsense. In other terms, in this case one could set an upper limit on the cross section at a lower confidence level, for example at 60% instead of 95%, that means that the experiment result would gives less precise information, or that the corresponding confidence interval is smaller.

The crossing point between the theory and the experiment is where the upper limit on the expected production cross section equals its theoretical value: it is the limit case where the agreement between result and prediction can still exist, and for which it is calculated the lower limit on the leptoquark mass.

To improve the limits, the experimental conditions should be improved, for example by increasing the luminosity, or the selection efficiency, or by combining either the results of the searches of different counting experiments in the same decay channel or different decay channels each other.

The four plots in the Figure (D.2) can also explain in which way the Figures (7.4) and (7.5) have been built. By definition:

$$\mu_f = \mu_{Lq}(f) = f \cdot \mu_{th} = f \cdot \int \mathcal{L}dt \cdot Eff \cdot \sigma_{th} \cdot Br \tag{D.16}$$

The branching ratio Br is equal to $2\beta(1-\beta)$ and to β^2 in the $e\nu jj$ and in the $eejj$ decay channels respectively, if β is equal to $Br(Lq \to eq)$. If the value of β ranges from 0. to 1., this allows to calculate, for each value of β and for M_{Lq} fixed, the upper limit on the cross section, therefore the lower limit on the leptoquark mass. This is well represented in the Figures (7.4) and (7.5) and four possible situations are depicted in the plots of Figure (D.2) according to the values of M_{Lq} and β. The four plots show four different choices, that is different points in the (M_{Lq}, β) plane. For each one it is calculated the corresponding value of $f_{1-\varepsilon}$. If $f_{1-\varepsilon} \geq$ or < 1, the corresponding point of the (M_{Lq}, β) plane will be outside, inside or on the boundary of the excluded region at that confidence level. The dashed regions in the plots represent the excluded region, the boundaries the limits on the mass for each β, and the external region couldn't be explored by the experiment, so for the moment is not excluded.

D.3. Limits with background estimation and uncertainties

There are still two points to consider before concluding the interpretation of the result of the counting experiment which gave n_o leptoquark observed events with μ_{Lq} expected:

1. it should be taken into account the systematic uncertainty determined on the signal efficiency in the evaluation of μ_{Lq};

2. among the n_o events it can be eventually estimated the contribution relative to the background, $\mu_B \pm \sigma_B$, where σ_B indicates the uncertainties on μ_B.

1. The variable μ_{Lq} has been defined in the previous section as the number of expected events passing the selection requirements, given the n_o observed in the experiment. The observation is affected by systematics effects due to the different sources listed in Section (5.1.3), which imply that, in a more realistic way, μ_{Lq} should be thought as the mean value of a gaussian probability distribution with standard deviation equal to the systematic uncertainty on the selection efficiency. This means that the likelihood function entering in the Equation (D.10), which is a function of μ_{Lq}, should be convoluted with a gaussian

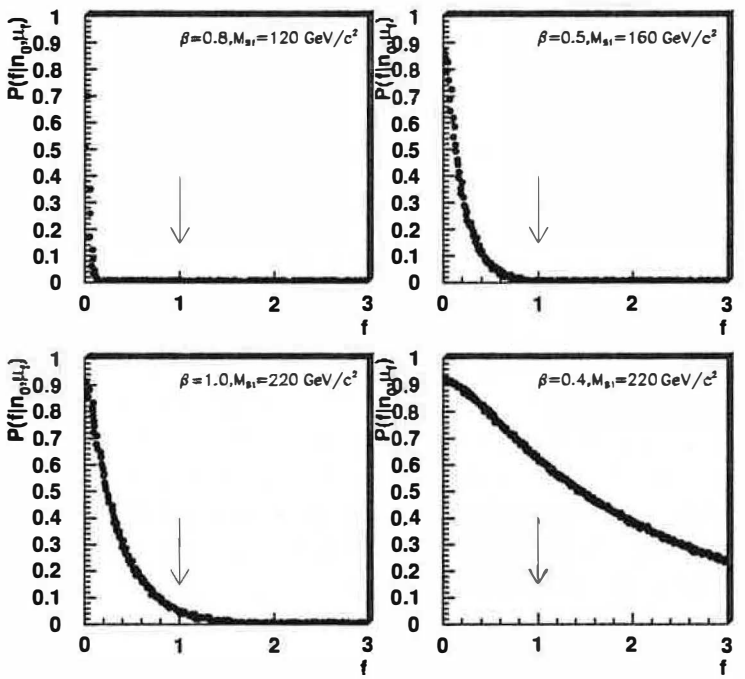

Figure D.2: *In this plot are represented four distributions of the posterior pdf* $\mathcal{P}(\mathrm{f}|\mathrm{n}_0, \mu_\mathrm{f})$, *defined in Equation (D.11), expressed here as a function of the real parameter f. It has been evaluated for different choices of points in the* β,$\mathrm{M_{LQ}}$ *plane. The two figures on the top represent the case where the integral* $\int_1^\infty \mathcal{P}\mathrm{df}'$ *is less than 5%:it also means that the value of* $f_{1-\varepsilon}$, *here called* f_{95}, *as given in Equation (D.14) is less than 1. In the bottom figure on left this ratio is exactly 5%* ($f_{95} = 1$) *and in the bottom figure on the right it is greater than 5%* ($f_{95} > 1$). *This means that the two first sets of* (β,$\mathrm{M_{LQ}}$) *points are representing points excluded by the corresponding analysis at a Confidence Level that is greater than 95%, that is these points are well inside the exclusion contour at 95% C.L.. In the third case the* (β,$\mathrm{M_{LQ}}$) *point is excluded at 95% C.L. by the corresponding analysis, while in the fourth case it is not excluded.*

distribution $G(\mu_{Lq}|\sigma_S)$, where $\sigma_S = (S_\varepsilon/\varepsilon)\mu_{Lq}$, which gives, after the parametrization with f:

$$\mathcal{L}ik'(\mathrm{n_0}|\mu'_\mathrm{f}, \sigma_\mathrm{S}) = \mathcal{L}\mathrm{ik}(\mathrm{n_o}|\mu'_\mathrm{f}) \otimes \mathrm{G}(\mu'_\mathrm{f}|\mu_\mathrm{f}, \sigma_\mathrm{S}) \tag{D.17}$$

where the symbol $\otimes$ represents the convolution between $\mathcal{L}ik$ and the Gaussian distribution. This new likelihood function should replace the one of Equation (D.10). The negative values of μ'_f are not taken into account, because they are physically not allowed, and this restriction implies a different normalization for the likelihood $\mathcal{L}ik'$ with respect to $\mathcal{L}ik$. This does not affect the results, since they are always expressed in terms of ratio of posterior pdf's.

2. The evaluation of the number of background events μ_B can, if enough precise, improve the limits: in this case the μ_{Lq} is expressed as sum of μ_S and μ_B, and the Equation (D.9) becomes:

$$P(\mu_{Lq}|n_o, \mu_B) = \frac{\mathcal{L}ik(n_o|\mu_{Lq}, \mu_B)}{\int_0^{+\infty} \mathcal{L}ik(n_o|\mu'_{Lq} + \mu_B)P(\mu'_{Lq})d\mu'_{Lq}} P(\mu_{Lq}) \tag{D.18}$$

which gives, for uniform prior $P(\mu_{Lq})$:

$$P(\mu_{Lq}|n_o, \mu_B) = \frac{\mathcal{L}ik(n_o|\mu_{Lq}, \mu_B)}{\int_0^{+\infty} \mathcal{L}ik(n_o|\mu'_{Lq}, \mu_B)d\mu'_{Lq}} \tag{D.19}$$

and where:

$$\mathcal{L}ik(n_o|\mu'_{Lq}, \mu_B) = \frac{e^{-(\mu_{Lq}+\mu_B)} \cdot (\mu_{Lq} + \mu_B)^{n_o}}{n_o!} \tag{D.20}$$

To take into account σ_B, one should proceed, as for the signal uncertainties, by convoluting the likelihood function with a gaussian distribution with mean μ_B and standard deviation σ_B.

After taking into account the uncertainties on the selection efficiency and the possibility of background subtraction from n_o, the global expression for the posterior pdf is given by:

$$P(\mu_{Lq}|n_o, \mu_B) = \frac{1}{2\pi\sigma_B\sigma_S} \int_0^{\infty} \int_0^{\infty} \mathcal{L}ik(n_o|\mu'_{Lq}, \mu'_B) e^{-\frac{(\mu_B-\mu'_B)^2}{2\,\sigma_B^2}} e^{-\frac{(\mu_S-\mu'_S)^2}{2\,\sigma_S^2}} d\mu'_B d\mu'_S \tag{D.21}$$

With this new expression of posterior pdf, one can easily come back to Equation (D.12) to find the upper limit on μ_{Lq} as:

$$\frac{\int_0^{n_{Lq}^{lim}} P(\mu'_{Lq}|n_o, \mu_B)d\mu'_{Lq}}{\int_0^{+\infty} P(\mu'_{Lq}|n_o, \mu_B)d\mu'_{Lq}} = \varepsilon \tag{D.22}$$

In general, the upper limits obtained using this method exceed those obtained with the frequentist approach: that is, the Bayes intervals "overcover" the frequentist ones. This is regarded as a shortcoming by some authors, and as laudably "conservative" by others.

D.4. Combination of limits from different analyses

The same method used to evaluate limits from the result of a counting experiment can be also applied when two different counting experiments combine their results in the same

decay channel or, as in this thesis, the results of the same search in two different channels. The case treated in this thesis is quite easy to represent [125]: the combination is made between the results of scalar or vector leptoquarks search in the two decay channels $e\nu jj$ and $eejj$, for which the posterior pdf's are:

$$P(\mu_f^{e\nu}|n_{e\nu}) = \frac{\mathcal{L}ik(n_{e\nu}|\mu_f^{e\nu})}{\int_0^{+\infty}\mathcal{L}ik(n_{e\nu}|\mu'_{fe\nu})d\mu'_{fe\nu}} \tag{D.23}$$

$$P(\mu_f^{ee}|n_{ee}) = \frac{\mathcal{L}ik(n_{ee}|\mu_f^{ee})}{\int_0^{+\infty}\mathcal{L}ik(n_{ee}|\mu'_{fee})d\mu'_{fee}} \tag{D.24}$$

Through these two probability distributions it has been defined the joint likelihood as:

$$\mathcal{P}(f|n_{ee},\mu_{f,ee},n_{e\nu},\mu_{f,e\nu}) = \prod_{i=ee,e\nu}\mathcal{P}(f|n_i,\mu_{f,i}) \tag{D.25}$$

Each likelihood has been convoluted with a gaussian distribution with mean $\mu_{f,e\nu(f,ee)}$ and standard deviation σ_S to take into account the systematics uncertainties on the selection efficiencies.

The two searches use common criteria for the two channels, and they apply sometimes to the same kind of requirements. The systematic uncertainties in the two channels can be correlated, when for example changes on a variable used in the selection on one channel imply the transformation of the same variable in the other channel as well, or uncorrelated, that means that what happens in one channel does not influence the result on the other one. To take into account these different contributions, the likelihood of Equation (D.25) is convoluted with three gaussians: one smears the expected value in the $e\nu jj$ channel with the uncorrelated contributions coming from that channel and therefore uses a gaussian with standard deviation equal to $\sigma_{e\nu}$; the other makes the same thing in the other channel, using a gaussian with standard deviation equal to σ_{ee}. The correlated systematics are considered only once for the two analyses by convoluting the rest with a gaussian having standard deviation equal to the uncorrelated systematic.

List of Tables

List of Figures

Bibliography

[1] "History of Original Ideas and Basic Discoveries in Particle Physics", edited by H. B. Newman and T. Ypsilantis, NATO ASI Series B: Physics Vol.352 (1996)

[2] J. J. Thomson, "Cathode Rays", Philosophical Magazine 44, 293 (1897)

[3] J. Perrin, "New experiments on kathode rays", Nature, Vol. 53, 298-299 (1896)

[4] J. J. Thomson, "On the Masses of the Ions in Gases at Low Pressures", Philosophical Magazine Series 5, Vol. 48, N. 295, 547-567 (1899)

[5] E. Rutherford, "The scattering of alpha and beta particles by matter and the structure of the atom", Philosophical Magazine volume 21 (1911) 669-688

[6] J. Chadwick, "Possible Existence Of A Neutron", Nature **129** (1932) 312

[7] M. Gell-Mann, "A Schematic Model Of Baryons And Mesons", Phys. Lett. **8** (1964) 214

[8] J. J. Aubert *et al.*, "Experimental Observation Of A Heavy Particle J," Phys. Rev. Lett. **33** (1974) 1404

[9] J. E. Augustin *et al.*, "Total Cross-Section For Hadron Production By Electron - Positron Annihilation Between 2.4-Gev And 5.0-Gev Center-Of-Mass Energy", Phys. Rev. Lett. **34** (1975) 764

[10] S. W. Herb *et al.*, "Observation of a Dimuon Resonance at 9.5 GeV in 400-GeV Proton-Nucleus Collisions", Phys. Rev. Lett. 39 (1977) 252; W. R. Innes *et al.*, "Observation of Structure in the υ Region", Phys. Rev. Lett. 39 (1977) 1240

[11] F. Abe *et al.*, the CDF Collaboration, "Evidence for top quark production in $p\bar{p}$ collisions at $\sqrt{s}$ = 1.8 TeV", Phys. Rev. D 50 (1994) 2966; S. Abachi *et al.*, the DØ Collaboration, "Observation of the top quark," Phys. Rev. Lett. **74** (1995) 2632 [hep-ex/9503003]

[12] W. Pauli Address to Group on Radioactivity (Tübingen, December 1930) (unpublished); Rappts. Septieme Conseil Phys. Solvay, Bruxelles, 1933 (Gautier-Villars, Paris 1934); E. Fermi, Z.Physik 88 (1934) 161

[13] K. Kodama *et al.*, the DONUT Collaboration, "Observation of tau neutrino interactions," Phys. Lett. B **504** (2001) 218 [hep-ex/0012035]

[14] G. B. Mills, for the LSND Collaboration, "Neutrino oscillation results from LSND", Nucl. Phys. Proc. Suppl. **91** (2001) 198

[15] Y. Fukuda *et al.*, the Super-Kamiokande Collaboration, "Evidence for oscillation of atmospheric neutrinos", Phys. Rev. Lett. **81** (1998) 1562 [hep-ex/9807003]

[16] D. E. Groom et al, the Particle Data Group, "The Review of Particle Physics", The European Physical Journal C15 (2000) **1**

[17] The LEP Collaborations and the LEP Electroweak working Group, as reported by J. Mnich at the International Europhysics Conference, Tampere, Finland (July 1999),

[18] T. Affolder *et al.*, the CDF Collaboration, "Search for a fourth-generation quark more massive than the Z boson in $p\bar{p}$ collisions at $s^{1/2} = 1.8$ TeV", Phys. Rev. Lett. **84** (2000) 835 [hep-ex/9909027]

[19] K. Eggert, the UA1 Collaboration, "Observation Of The Neutral Intermediate Vector Boson At The Cern Anti-P P Collider", Print-83-1038 (Aachen) *In Brighton 1983, Proceedings, High Energy Physics, 447-460*; G. Arnison *et al.*, the UA1 Collaboration, "Observation Of The Muonic Decay Of The Charged Intermediate Vector Boson", Phys. Lett. B **134** (1984) 469; P. Bagnaia *et al.*, the UA2 Collaboration, "Evidence For $Z \to e^+e^-$ At The Cern Anti-P P Collider", Phys. Lett. B **129** (1983) 130; M. Banner *et al.*, the UA2 Collaboration, "Observation Of Single Isolated Electrons Of High Transverse Momentum In Events With Missing Transverse Energy At The Cern Anti-P P Collider", Phys. Lett. B **122** (1983) 476

[20] S. L. Glashow, Nucl. Phys. **22** 579 (1961)

[21] S. Weinberg, Phys. Rev. Lett. **19** 1264 (1967)

[22] A. Salam, in "Elementary Particle Theory", edited by N. Svartholm, Almquist and Wiksells, Stockholm (1969)

[23] Suggested readings: E. Leader and E. Predazzi, "An introduction to gauge theories and modern particle physics", edited by Cambridge monographs on Particle Physics, Nuclear Physics and Cosmology; F. Halzen and A. D. Martin, "Quarks and Leptons: an introductory course in modern particle physics", edited by John Wiley and Sons; I. J. R. Aitchison and A. J. G. Hey, "Gauge theories in particle physics", Graduate Students Series in Physics edited by Adam Hilger Ltd; P. Renton, "Electroweak interactions, an introduction to the physics of quarks and leptons", edited by Cambridge University Press; J. P. Derendinger, "Théorie Quantique des Champs", edited by Troisième Cycle de la Physique en Suisse Romande (1995)

[24] G. G. Ross, "Grand Unified Theories", Reading, Usa: Benjamin/cummings (1984) 497 (Frontiers In Physics, 60)

[25] M. B. Wise, H. Georgi and S. L. Glashow, "SU(5) And The Invisible Axion", Phys. Rev. Lett. **47** (1981) 402; S. Dimopoulos and H. Georgi,"Softly Broken Supersymmetry And SU(5)", Nucl. Phys. B **193** (1981) 150

[26] see for example R. S. Chivukula, "Lectures on technicolor and compositeness", hep-ph/0011264

[27] see for example H. E. Haber and G. L. Kane, "The search for supersymmetry: probing physics beyond the Standard Model", Physics Reports (Review Section of Phys. Lett.) **117**, N. 2-4 (1985) 75-263; P. Fayet and S. Ferrara, "Supersymmetry", Physics Report (Section C of Phys. Lett.) **32**, N. 5 (1977) 249-334. Both papers can be found in the Volume "Supersymmetry and Supergravity", edited by M. Jacob for the North-Holland / World Scientific (1991)

[28] W. Buchmuller, R. Ruckl and D. Wyler, "Leptoquarks In Lepton Quark Collisions", Phys. Lett. B **191** (1987) 442 [Erratum-ibid. B **448** (1987) 320]

[29] J. Blümlein and R. Rückl, Phys. Lett. B304 (1993) 337

[30] J. Blümlein, E. Boos and A. Kryukov, "Leptoquark pair production in hadronic interactions", Z. Phys. C **76** (1997) 137 [hep-ph/9610408]; J. Blümlein, E. Boos and A. Kryukov, "Leptoquark pair production cross-sections at hadron colliders," hep-ph/9811271

[31] M. Kramer, T. Plehn, M. Spira and P. M. Zerwas, "Pair production of scalar leptoquarks at the Tevatron", Phys. Rev. Lett. **79** (1997) 341 [hep-ph/9704322]; M. Kramer, "Leptoquark production at the Tevatron", hep-ph/9707422

[32] J. L. Hewett and S. Pakvasa, "Leptoquark Production In Hadron Colliders", Phys. Rev. D **37** (1988) 3165; J. L. Hewett and T. G. Rizzo, Phys. Rev. D36, 3367 (1988); J. L. Hewett, T. G. Rizzo, S. Pakvasa, H. E. Haber and A. Pomarol, "Vector leptoquark production at hadron colliders", hep-ph/9310361

[33] W. Beenakker, R. Höpker, M. Spira and P. M. Zerwas, Phys. Rev. Lett. **74** (1995) 2905 and Nucl. Phys. **B492** (1997) 51

[34] C. Adloff *et al.*, the H1 Collaboration, "Observation of events at very high Q^2 in ep collisions at HERA", Z. Phys. C **74** (1997) 191 [hep-ex/9702012]

[35] J. Breitweg *et al.*, the ZEUS Collaboration, "Comparison of ZEUS data with standard model predictions for $e^+p \to e^+X$ scattering at high x and Q^2", Z. Phys. C **74** (1997) 207 [hep-ex/9702015]

[36] A. Amadon, C. Grosso-Pilcher and F. Strumia, "First Generation Leptoquark search in Run 1A and 1B", CDF Internal Note 4126 (1997)

[37] F. Abe *et al.*, the CDF Collaboration, "Search for first generation leptoquark pair production in p anti-p collisions at $s^{1/2} = 1.8$ TeV", Phys. Rev. Lett. **79** (1997) 4327 [hep-ex/9708017]

[38] B. Abbott *et al.*, the DØ Collaboration, "Search for first generation scalar leptoquark pairs in p anti-p collisions at $s^{1/2} = 1.8$ TeV", Phys. Rev. Lett. **80** (1998) 2051 [hep-ex/9710032]

[39] C. Grosso-Pilcher, G. Landsberg and M. Paterno, the CDF and DØ Collaborations, "Combined limits on first generation leptoquarks from the CDF and D0 experiments", hep-ex/9810015

[40] V. M. Abazov *et al.*, the DØ Collaboration, "Search for leptoquark pairs decaying to $\nu\nu$ + jets in p anti-p collisions at $s^{1/2} = 1.8$ TeV", hep-ex/0106065

[41] V. M. Abazov et al., the DØ Collaboration "Search for First-Generation Scalar and Vector Leptoquarks", FERMILAB-PUB-01-057-E, hep-ex/0105072, submitted to Phys.Rev.D (2001)

[42] C. Adloff et al., the H1 Collaboration, Eur. Phys. J. C **11** (1999) 447 [Erratum-ibid. C **14** (1999) 553] [hep-ex/9907002]

[43] C. Adloff et al., the H1 Collaboration, "A Search for Leptoquark Bosons in e^-p Collisions at HERA", hep-ex/0107038, Submitted to Phys. Lett. B (2001)

[44] J. Breitweg et al., the ZEUS Collaboration, "Search for resonances decaying to $e^+ - jet$ in e^+p Interactions at HERA", Eur. Phys. J. C **16** (2000) 253 [hep-ex/0002038]

[45] J. Breitweg et al., the ZEUS Collaboration, Phys. Rev. D **63** (2001) 052002 [hep-ex/0009059]

[46] U. F. Katz, for the H1 and ZEUS Collaborations, "New HERA results on deep-inelastic e^+p scattering at very high Q^2", Prepared for 26^{th} SLAC Summer Institute on Particle Physics: Gravity, From the Hubble Length to the Planck Length (SSI 98), Stanford, California, 3-14 Aug 1998

[47] P. P. Allport et al., the DELPHI Collaboration, Phys. Lett. **B446** (1999) 62

[48] G. Abbiendi et al., the OPAL Collaboration, "Search for single leptoquark and squark production in electron-photon scattering at $\sqrt{s_{ee}} = 189$ GeV at LEP", hep-ex/0106031, Submitted to Eur. Phys. J. C (2001)

[49] F. Abe *et al.*, the CDF Collaboration, "The Collider Detector at Fermilab", a compilation of articles reprinted from Nuclear Instruments and Methods in Physics Research - A, Vol. A267 (1988) 249-366, Vol. A268 (1988) 24-104, Vol. A269 (1988) 33-100 and Vol. A271 (1988) 387-403, edited by North-Holland (1988)

[50] F. Abe et al., the CDF Collaboration, "Evidence for top quark production in $\bar{p} - p$ collisions at $\sqrt{s} = 1.8$ TeV", Phys. Rev. D50, 2966 (1994)

[51] F. Abe et al., the CDF Collaboration, "Measurement of the $\bar{t}t$ production cross section in $\bar{p} - p$ collisions at $\sqrt{s} = 1.8$ TeV", Phys. Rev. Lett. 80, 2773 (1998)

[52] T. Affolder et al., the CDF Collaboration, "Measurement of the W boson mass with the Collider Detector at Fermilab", Phys. Rev. D64 (2001)

[53] F. Abe et al., the CDF Collaboration, "Measurement of B hadron lifetimes using J/ψ final states at CDF", Phys. Rev. D57, 5382 (1998); T. Affolder et al., the CDF Collaboration, "A measurement of $\sin 2\beta$ from $B \to J/\psi\, K^0_S$ with the CDF detector", Phys. Rev. D61 (2000)

[54] The Operations department of the Fermi National Accelerator Laboratory, "The Concepts Rookie Book", actually at the URL http://www-bdnew.fnal.gov/operations/rookie_books/rbooks.html

[55] S. D. Holmes, "Tevatron performance goals for the coming decade", Proceedings of the 1999 Particle Accelerator Conference

[56] The CDF II Collaboration, " The CDF II Detector: Technical Design Report", Fermilab-Pub-96/390-E, November 1996

[57] D. Amidei *et al.*, "The Silicon Vertex Detector of the Collider Detector at Fermilab", Nuclear Instruments and Methods in Physics Research A 350 (1994), 73-130

[58] P. Azzi *et al.*, "SVX', the new CDF silicon vertex detector", Nuclear Instruments and Methods in Physics Research A 360 (1995), 137-140

[59] M. Binkley *et al.*, "The CDF vertex time projection chamber system", Nuclear Instruments and Methods in Physics Research A 268 (1988) 75-91

[60] F. Bedeschi *et al.*, "Design and construction of the CDF central tracking chamber", Nuclear Instruments and Methods in Physics Research A 268 (1988) 50-74

[61] L. Balka *et al.*, "The CDF central electromagnetic calorimeter", Nuclear Instruments and Methods in Physics Research A 267 (1988) 272-279

[62] K. Byrum *et al.*, "Shower maximum trigger for electrons and photons at CDF", Nuclear Instruments and Methods in Physics Research A364, 144 (1995)

[63] Y. Seya, "CDF Calorimeter and its Upgrade", Proceedings of 1994 Beijing Calorimetry Symposium at IHEP

[64] S. Bertolucci *et al.*, "The CDF central and endwall hadron calorimeter", Nuclear Instruments and Methods in Physics Research A 267 (1988) 301-314

[65] Y. Fukui *et al.*, "CDF end plug electromagnetic calorimeter using conductive plastic proportional tubes", Nuclear Instruments and Methods in Physics Research A 267 (1988) 280-300

[66] W. C. Carithers *et al.*, "The CDF end plug hadron calorimeter", submitted to Nuclear Instruments and Methods (1988)

[67] G. Brandenburg *et al.*, "An electromagnetic calorimeter for the small angle regions of the Collider Detector at Fermilab", Nuclear Instruments and Methods in Physics Research A 267 (1988) 257-271

[68] S. Cihangir *et al.*, "The CDF forward/backward hadron calorimeter", Nuclear Instruments and Methods in Physics Research A 267 (1988) 249-256

[69] G. Ascoli *et al.*, CDF central muon detector, Nuclear Instruments and Methods in Physics Research A 268 (1988) 33-40

[70] Nuclear Instruments and Methods in Physics Research A271 (1988) 387-403

[71] G. Foster *et al.*, A fast hardware track-finder for the CDF Central Tracking Chamber, Nucl. Inst. Meth. Phys. Res., A269, 93, 1988

[72] D. Cronin-Hennessy et al., Measurement of $Z \rightarrow e^+e^- + Njets$ Cross Sections in 1.8 TeV $p\bar{p}$ Collisions, Internal CDF Note 3360, 1996

[73] X. Wu, "Detections at hadron colliders", Cours pour la Troisième Cycle de la Physique en Suisse Romande (1999)

[74] L. Nodulman, "Preliminary 1b CEM calibration to the february shutdown", CDF Internal Note 3048

[75] Y. K. Kim, "PEM energy scale corrections for Run 1b", CDF Internal Note 3424

[76] R. K. Ellis, W. J. Stirling and B. R. Webber, "QCD and collider physics", Cambridge monographs on particle physics, Nuclear physics and cosmology (1996)

[77] S. Bethke *et al.*, the JADE Collaboration, Phys. Lett. **B213** (1988) 235

[78] J. Huth *et al.*, "Proceedings 1990 Summer Study on High Energy Physics", ed. E. Berger Singapore: World Scientific, 134 (1992)

[79] B. Flaugher and G. Blazey, "Inclusive Jet and Dijet Production at the Tevatron", CDF Internal Note 4915, FERMILAB-PUB-99/038-E and in the Annual Review of Nuclear and Particle Science Vol. 49 (1999)

[80] G. Blazey *et al.*, "Run II jet physics", CDF Internal Note 5293 (2000)

[81] N. Eddy, "New relative jet corrections for Run 1a and 1b data", CDF Internal Note #3534 (1996)

[82] The CDF II Coll., Update to proposal P-909, Physics Performance of the CDF II with an Inner Silicon Layer and a Time Of Flight detector, 1999

[83] S. Belforte *et al.*, "Silicon Vertex Tracker Technical Design Report", CDF Internal Note #3108 (1994)

[84] T. Affolder *et al.*, the CDF Collaboration, "Search for Second and Third Generation Leptoquarks Including Production via Technicolor Interactions in $p\bar{p}$ Collisions at $s^{1/2}$ = 1.8 TeV", Phys. Rev. Lett. 85, 2056 (2000)

[85] F. Abe *et al.*, the CDF Collaboration, Phys. Rev. **D 49** 1 (1994)

[86] The Top Group at CDF, "Sample selection for Run 1B Top Search", CDF Internal Note # 2966 (1996)

[87] D. Gerdes, "Study of Conversion removal for the lepton + jets sample", CDF Internal Note # 2903 (1994)

[88] T. Sjöstrand, "PYTHIA 5.7 and JETSET 7.4: Physics and manual", Computer Physics Communication **82** (1994) 74 and [hep-ph/9508391] (1995)

[89] F. A. Berends, W. T. Giele and H. Kuijf, "Exact Expressions For Processes Involving A Vector Boson And Up To Five Partons", Nucl. Phys. B **321** (1989) 39; F. A. Berends, H. Kuijf, B. Tausk and W. T. Giele, "On the Production of a W and Jets at Hadron Colliders", Nucl. Phys. **B357**, 32 (1991)

[90] A. D. Martin, W. J. Stirling and R. G. Roberts, Phys. Rev. **D 47** 867 (1993); Phys. Lett. **B306** 145 (1993)

[91] J. Botts, J. G. Morfin, J. F. Owens, J. Qiu, W. Tung and H. Weerts, the CTEQ Collaboration, "CTEQ parton distributions and flavor dependence of sea quarks", Phys. Lett. B **304** (1993) 159 [hep-ph/9303255]

[92] B. Andersson, G. Gustafson, G. Ingelman and T. Sjostrand, "Parton Fragmentation And String Dynamics", Phys. Rept. **97** (1983) 31

[93] G. Marchesini, B. R. Webber, G. Abbiendi, I. G. Knowles, M. H. Seymour and L. Stanco, "HERWIG: A Monte Carlo event generator for simulating hadron emission reactions with interfering gluons. Version 5.1 - April 1991", Comput. Phys. Commun. **67** (1992) 465

[94] M. Shapiro *et al.*, "A user's guide to QFL", CDF Internal Note # 1810

[95] D. Glezinski *et al.*, "A detailed study of the SECVTX algorithm", CDF Internal Note #2925 (1994)

[96] B. Winer *et al.*, "SVX and SLT tags in the Z sample", CDF Internal Note #2342 (1993)

[97] S. Catani *et al.*, Phys.Lett. **B378**, 329 (1996)

[98] F. James, "MINUIT, Minimization package, Reference Manual", Version 94.1, Computing and Networks Division (CERN)

[99] J. Dittmann, "Measurement of the W + $\geq$ 1 Jet Cross Section in Proton-Antiproton Collisions at $\sqrt{s}$ = 1.8 TeV", Ph.D. Thesis, CDF Internal Note #5512 (1998)

[100] D. Cronin-Hennessy *et al.*, "Luminosity Monitoring and Measurement at CDF", CDF Internal Note #4956 (1999)

[101] J. L. Hewett, private communication

[102] L. Moneta, "Searches for Second Generation Leptoquarks in $\mu\nu qq$ channel", CDF Internal Note #5572 (2001); H. Kambara, "Second Generation Leptoquark Search at CDF", Ph.D. Thesis, CDF Internal Note #4649 (1998)

[103] A. Djouadi, J. Ng and T. G. Rizzo, "New particles and interactions", hep-ph/9504210

[104] B. Dion, L. Marleau and G. Simon, "Scalar and vector leptoquark pair production at hadron colliders: Signal and backgrounds", Phys. Rev. D **59** (1999) 015001 [hep-ph/9808413]; O. J. P. Eboli and A. V. Olinto, Phys. Rev. **D38** 3461 (1998); J. L. Hewett and S. Pakvasa, Phys. Rev. **D37** 3165 (1998); J. Blümlein, E. Boos and A. Krykov, hep-ph/9610408; M. Krämer et al., Phys. Rev. Lett. **79** 341 (1997); J. L. Hewett and T. Rizzo, hep-ph/9703337; T. Rizzo, hep-ph/9609267

[105] R. Blair et al., the CDF II Collaboration, "The CDF II Detector", Technical Design Report, Fermilab-Pub-96/390-E; the DØ Collaboration, "The DØ upgrade: the detector and its physics", Fermilab-Pub-96/357-E

[106] W. Buchmüller, R. Rückl and D. Wyler, Phys. Lett. **B191** 442 (1987)

[107] B. Dion, L. Marleau, G. Simon and M. de Montigny, Eur. Phys. J. C2, 497 (1998); O. J. P. Eboli, R. Z. Funchal and T. L. Lungov, Phys. Rev. **D57** 1715 (1998)

[108] G. Wrochna, "First look at leptoquarks in CMS", CMS Note CMS CR 1996/003 (1996)

[109] S. Abdullin et al., "Study of leptoquark pair production at the LHC with the CMS detector", CMS Note 1999/027 (1999)

[110] T. G. Rizzo, "Searches for Scalar and Vector Leptoquarks at Future Hadron Colliders", Proceedings of the 1996 DPF/DPB Summer Study on New Directions for High Energy Physics-Snowmass96, hep-ph/9609267

[111] J. L. Hewett and T. Rizzo, Phys. Rev. **D36** 3367 (1987); J. L. Hewett and S. Pakvasa, Phys. Lett. **B227** 178 (1987); J. Blümlein and R. Rückl, Phys. Lett. **B304**, 337 (1993); J. Blümlein, E. Boos and A. Krykov, Phys. Lett. **B392**, 150 (1997); M. S. Berger, hep-ph/9609517

[112] T. Abe *et al.*, the Americal Linear Collider Working Group, "Linear collider physics resource book for Snowmass 2001. Part 3: Studies of exotic and Standard Model physics", hep-ex/0106057

[113] M. A. Doncheski and S. Godfrey, "Leptoquark production and identification at high energy lepton colliders," hep-ph/9807290

[114] TESLA Technical Design Report (2001)

[115] E. Moore *et al.*, "Optimization and Testing of an Artificial Neural Network for a $t\bar{t}$ Cross Section Measurement", CDF Internal Note #5680 (2001); M. Tanaka *et al.*, "Soft Electron Identification with Neural Net", CDF Internal Note #5252 (2000); F. Strumia, A. G. Clark, L. Moneta and X. Wu, "Search for First Generation Scalar Leptoquarks in the $e\nu jj$ channel using Neural Networks", CDF Internal Note #5230 (2000)

[116] J. von Neumann, "Probabilistic Logics and the Synthesis of Reliable Organisms from Unreliable Components", in Automata Studies, edited by C. E. Shannon and J. McCarthy, 43-98 (1956)

[117] J. Hertz, A. Krogh, R. G. Palmer "Introduction to the theory of neural computation", Addison-Wesley Publishing Company (1991)

[118] R. Beale, T. Jackson "Neural computing: an introduction", Institute of Physics Publishing Bristol and Philadelphia (1994)

[119] The code which implements architectures of feed-forwards Neural Networks has been courtesly given by John Conway

[120] F. E. Paige, S. D. Proto pescu, H. Baer and X. Tata, "ISAJET 7.40: A Monte Carlo event generator for $pp, \bar{p}p$, and e^+e^- reactions", hep-ph/9810440

[121] "Workshop on Confidence Limits", CERN Yellow Report CERN 2000-005 30 May 2000

[122] G. Feldman and R. Cousins, "Unified approach to the classical statistical analysis of small signals", Phys. Rev. D 57 (1998) 3873-3889; C. Giunti, "A new ordering principle for the classical statistical analysis of Poisson processes with background", Phys. Rev. D 59 (1999) 053001 1-6 [hep-ph 9808240]; un libro di statistica, corso di xin, corso di Pohl,

[123] G. D'Agostini, "Bayesian reasoning in High-Energy Physics: Principles and applications", CERN Yellow Report 99-03; R. Cousins, "Why isn't every physicist a Bayesian", Am. J. Phys. 63 (1995) 398-410

[124] H. B. Prosper, "Statistical Issues in Data Analysis", in Techniques and Concepts of High-Energy Physics IX, edited by T. Ferbel, Plenum Press, New York (1997)

[125] F. Strumia and J. Conway, "Combined Limits from Searches for First Generation Scalar Leptoquarks in $eeqq$ and $e\nu qq$ channels", CDF Internal Note #4921 (1999)